Argonne NATIONAL LABORATORY

ANL-11/03

MONTE CARLO MODELING AND ANALYSES OF YALINA BOOSTER SUBCRITICAL ASSEMBLY

PART III: LOW ENRICHED URANIUM CONVERSION ANALYSES

Nuclear Engineering Division

About Argonne National Laboratory
Argonne is a U.S. Department of Energy laboratory managed by UChicago Argonne, LLC under contract DE-AC02-06CH11357. The Laboratory's main facility is outside Chicago, at 9700 South Cass Avenue, Argonne, Illinois 60439. For information about Argonne, see www.anl.gov.

Availability of This Report
This report is available, at no cost, at http://www.osti.gov/bridge. It is also available on paper to the U.S. Department of Energy and its contractors, for a processing fee, from:

U.S. Department of Energy
Office of Scientific and Technical Information
P.O. Box 62
Oak Ridge, TN 37831-0062
phone (865) 576-8401
fax (865) 576-5728
reports@adonis.osti.gov

Disclaimer
This report was prepared as an account of work sponsored by an agency of the United States Government. Neither the United States Government nor any agency thereof, nor UChicago Argonne, LLC, nor any of their employees or officers, makes any warranty, express or implied, or assumes any legal liability or responsibility for the accuracy, completeness, or usefulness of any information, apparatus, product, or process disclosed, or represents that its use would not infringe privately owned rights. Reference herein to any specific commercial product, process, or service by trade name, trademark, manufacturer, or otherwise, does not necessarily constitute or imply its endorsement, recommendation, or favoring by the United States Government or any agency thereof. The views and opinions of document authors expressed herein do not necessarily state or reflect those of the United States Government or any agency thereof, Argonne National Laboratory, or UChicago Argonne, LLC.

ANL-11/03

MONTE CARLO MODELING AND ANALYSES OF YALINA BOOSTER SUBCRITICAL ASSEMBLY PART III: LOW ENRICHED URANIUM CONVERSION ANALYSES

by
Alberto Talamo and Yousry Gohar
Nuclear Engineering Division, Argonne National Laboratory

January 2011

MONTE CARLO MODELING AND ANALYSES OF YALINA BOOSTER SUBCRITICAL ASSEMBLY

PART III: LOW ENRICHED URANIUM CONVERSION ANALYSES

Table of Contents

Contents Page

Abstract 1

1. Introduction 2

2. 90% Enriched Uranium Fuel Configuration 2

3. 90% and 36% Enriched Fuels Configurations – From Deep Subcritical to Near-Critical Configurations 6

4. 36% Enriched Fuel Configuration 7

5. 21% Enriched Fuel Configuration 10

6. 21% Enriched Fuel Configurations with Square and Circular Arrangement of the Absorber Interface between the Fast and the Thermal Zones 11

7. Conclusions 13

Acknowledgments 15

References 15

MONTE CARLO MODELING AND ANALYSES OF YALINA BOOSTER SUBCRITICAL ASSEMBLY

PART III: LOW ENRICHED URANIUM CONVERSION ANALYSES

List of Figures

Figure No. Page

Figure 1. Three-dimensional view of YALINA Booster subcritical assembly.....23

Figure 2. Horizontal section of YALINA Booster subcritical assembly with 90% 24

Figure 3. 3He(n,p) reaction rate in EC6T for 90% enriched fuel..... 25

Figure 4. ^{235}U(n,f) reaction rate in EC6T for 90% enriched fuel..... 25

Figure 5. ^{235}U(n,f) reaction rate in EC2B for 90% enriched fuel..... 26

Figure 6. ^{197}Au(n,γ) reaction rate in EC6T for 90% enriched fuel..... 26

Figure 7. ^{55}Mn(n,γ) reaction rate in EC6T for 90% enriched fuel 27

Figure 8. In(n,γ) reaction rate in EC5T for 90 enriched % fuel..... 27

Figure 9. In(n,γ) reaction rate in EC6T for 90% enriched fuel..... 28

Figure 10. In(n,γ) reaction rate in EC7T for 90% enriched fuel..... 28

Figure 11. In(n,γ) reaction rate in EC10R for 90% enriched fuel..... 29

Figure 12. Neutron spectrum in fast zone for 90% enriched fuel and 902 fuel rod configuration..... 29

Figure 13. Neutron spectrum in thermal and reflector zones for 90% enriched fuel and 902 fuel rod configuration..... 30

Figure 14. Neutron spectrum in fast zone for 90% enriched fuel and 1141 fuel rod configuration..... 31

Figure 15. Neutron spectrum in thermal and reflector zones for 90% enriched fuel and 1141 fuel rod configuration..... 32

Figure 16. ^{3}He(n,p) reaction rate in EC1B for 90% enriched fuel and Cf source 33

Figure 17. ^{3}He(n,p) reaction rate in EC2B for 90% enriched fuel and Cf source 33

Figure 18. ^{3}He(n,p) reaction rate in EC3B for 90% enriched fuel and Cf source 34

Figure 19. ^{3}He(n,p) reaction rate in EC5T for 90% enriched fuel and Cf source 34

Figure 20. ^{3}He(n,p) reaction rate in EC6T for 90% enriched fuel and Cf source 35

Figure 21. Normalized reaction rates for 90% enriched fuel, D-D neutron source, and 902 EK10 fuel rods 35

Figure 22. Normalized reaction rates for 90% enriched fuel, D-T neutron source, and 902 EK10 fuel rods 36

Figure 23. Normalized reaction rates for 90% enriched fuel, D-D neutron source, and 1141 EK10 fuel rods 36

Figure 24. Normalized reaction rates for 90% enriched fuel, D-T neutron source, and 1141 EK10 fuel rods 37

Figure 25. Correction factor on reactivity for 90% enriched fuel 37

Figure 26. Corrected and uncorrected experimental multiplication factors and MCNPX multiplication factor obtained by criticality calculations for 90% enriched fuel configuration; the experimental reactivity has been corrected by the dynamic correction factor 38

Figure 27. k_{eff} calculated by MONK and MCNPX as function of EK10 rod numbers for 90 and 36% enriched fuels 39

Figure 28. k_{eff} calculated by MCNPX and from experimental measurements as function of EK10 rods; long detectors (EC5T and EC6T; EC6T and EC7T) 39

Figure 29. Horizontal section of the fuel zone of YALINA Booster assembly with 36% enriched fuel in fast zone and 1185 EK10 fuel rods in thermal zone.. 40

Figure 30. ^{3}He(n,p) reaction rate in EC6T for 36% enriched fuel..... 41

Figure 31. ^{235}U(n,f) reaction rate in EC6T for 36% enriched fuel..... 41

Figure 32. ^{235}U(n,f) reaction rate in EC2B for 36% enriched fuel..... 42

Figure 33. ^{197}Au(n,γ) reaction rate in EC6T for 36% enriched fuel..... 42

Figure 34. ^{55}Mn(n,γ) reaction rate in EC6T for 36% enriched fuel 43

Figure 35. ^{115}In(n,γ) reaction rate in EC5T for 36% enriched fuel 43

Figure 36. ^{115}In(n,γ) reaction rate in EC6T for 36% enriched fuel 44

Figure 37. ^{115}In(n,γ) reaction rate in EC7T for 36% enriched fuel 44

Figure 38. ^{115}In(n,γ) reaction rate in EC10R for 36% enriched fuel..... 45

Figure 39. Neutron spectrum in fast zone for 36% enriched fuel 45

Figure 40. Neutron spectrum in thermal and reflector zones for 36% enriched fuel 46

Figure 41. Normalized reaction rates for 36% enriched fuel and D-D neutron source..... 47

Figure 42. Normalized reaction rates for 36% enriched fuel and D-T neutron source..... 47

Figure 43. Normalized ^{3}He (n,p) reaction rate in EC5T for 36% enriched fuel; L refers to 25-cm long detectors; maximum of experimental data has been multiplied by 0.61; Δt = 2 and 10 μs for experiment and MCNP, respectively 48

Figure 44. Normalized ^{3}He(n,p) reaction rate in EC6T for 36% enriched fuel; L refers to 25-cm long detectors; maximum of experimental data has been multiplied by 0.95; Δt = 2 and 10 μs for experiment and MCNP, respectively 48

Figure 45. Normalized ^{3}He (n,p) reaction rate in EC5T for 36% enriched fuel; L and S refer to 25- and 1-cm long detectors, respectively; maximum of experimental data has been multiplied by 1.3; Δt = 2 and 10 μs for experiment and MCNP, respectively 49

Figure 46. Normalized ^{3}He (n,p) reaction rate in EC6T for 36% enriched fuel; L and S refer to 25- and 1-cm long detectors, respectively; maximum of experimental data has been multiplied by 1.1; Δt = 2 and 10 μs for experiment and MCNP, respectively 49

Figure 47. Normalized ^{3}He (n,p) reaction rate in measurement channel MC5 for 36% enriched fuel; L and S refer to 25- and 1-cm long detectors, respectively; maximum of experimental data has been multiplied by 1.05; Δt = 2 and 10 μs for experiment and MCNP, respectively 50

Figure 48. Correction factor for 36% enriched fuel from static MCNPX simulations with D-D neutron source and 902 EK10 fuel rods 50

Figure 49. Correction factor for 36% enriched fuel from static MCNPX simulations with D-T neutron source and 902 EK10 fuel rods..... 51

Figure 50. Correction factor for 36% enriched fuel from MCNPX simulations with D-D neutron source and 1185 EK10 fuel rods..... 51

Figure 51. Correction factor for 36% enriched fuel from static MCNPX simulations with D-T neutron source and 1185 EK10 fuel rods 52

Figure 52. CIEMAT[16] and ANL correction factors for D-T neutron source in different EK10 fuel configurations; the results have been calculated using the CIEMAT definition of the correction factor[16] 52

Figure 53. Corrected and uncorrected experimental multiplication factors and MCNPX 53

Figure 54. Horizontal section of YALINA Booster fuel zone with 21% enriched fuel in fast zone and 1185 EK10 fuel rods in thermal zone (Configuration 4).. 54

Figure 55. Vertical section of YALINA Booster subcritical assembly with 21% enriched fuel in fast zone..... 55

Figure 56. Technical specifications of the fuel rod with 21% enriched uranium oxide, dimensions in mm 56

Figure 57. ^{3}He(n,p) reaction rate in EC6T for 21% enriched fuel..... 57

Figure 58. ^{235}U(n,f) reaction rate in EC6T for 21% enriched fuel 57

Figure 59. ^{235}U(n,f) reaction rate in EC2B for 21% enriched fuel..... 58

Figure 60. ^{197}Au(n,γ) reaction rate in EC6T for 21% enriched fuel..... 58

Figure 61. ^{55}Mn(n,γ) reaction rate in EC6T for 21% enriched fuel 59

Figure 62. ^{115}In(n,γ) reaction rate in EC5T for 21% enriched fuel 59

Figure 63. ^{115}In(n,γ) reaction rate in EC6T for 21% enriched fuel 60

Figure 64. ^{115}In(n,γ) reaction rate in EC7T for 21% enriched fuel 60

Figure 65. ^{115}In(n,γ) reaction rate in EC10R for 21% enriched fuel..... 61

Figure 66. Neutron spectra in fast zone for 21% enriched fuel 61

Figure 67. Neutron spectra in thermal and reflector zones for 21% enriched fuel 62

Figure 68. Normalized reaction rates for 21% enriched fuel and D-D neutron source..... 63

Figure 69. Normalized reaction rates for 21% enriched fuel and D-T neutron source..... 63

Figure 70. Spatial correction factor calculated with MCNPX simulations for 21% enriched fuel configuration and D-D neutron source 64

Figure 71. Corrected and uncorrected experimental multiplication factors and MCNPX multiplication factor obtained from criticality calculations for 21% enriched fuel configuration; the experimental reactivity has been corrected by the static correction factor Experiments were performed with D-D neutron source 65

Figure 72. Horizontal section of configuration 5 of Table I 66

Figure 73. Fuel zone of configuration 5 of Table I 67

Figure 74. Fast zone of configuration 5 of Table I at z = 0 cm 68

Figure 75. Fast zone of configuration 5 of Table I between z = 25 and z = 30.2 cm.... 69

Figure 76. Fast zone of configuration 5 of Table I between z = 30.2 and z = 31 cm.... 70

Figure 77. Fast zone of configuration 5 of Table I between z = 31 and z = 32 cm..... 71

Figure 78. Fast zone of configuration 5 of Table I between z = 32 and z = 32.5 cm.... 72

Figure 79. Fast zone of configuration 5 of Table I between z = 32.5 and z = 33.7 cm 73

Figure 80. Fast zone of configuration 5 of Table I between z = 33.7 and z = 34.1 cm 74

Figure 81. Fast zone of configuration 5 of Table I between z = 34.1 and z = 43.6 cm (steel grid ends at z = 42 cm) 75

Figure 82. Vertical section of configuration 5 of Table I at y = 0.88 cm 76

Figure 83. Vertical section of configuration 5 of Table I at y = 0 cm 77

Figure 84. Top zoom of vertical section of configuration 5 of Table I; axial positions are relative at bottom surface of copper disk (z = 0 cm); in this configuration, offset (relative to bottom surface of copper disk) of active fuel length of 21% enriched fuel has not been taken into account..... 78

Figure 85. Bottom zoom of vertical section of configuration 5 of Table I 79

Figure 86. Zoom of target zone of configuration 5 of Table I 80

Figure 87. Vertical section of target zone (8 x 82 cm) of configuration 5 of Table I when the Cf beam tube is removed and replaced by a lead block; only the upper lead block has a hole; this arrangement was used only for calculations of Figures 123 and 124 81

Figure 88. Fast zone of annular configuration 6 of Table I at z = 0 cm 82

Figure 89. Fast zone of annular configuration 7 of Table I at z = 0 cm 83

Figure 90. Fast zone of annular configuration 8 of Table I at z = 0 cm; 44 polyethylene rods in outer fast zone 84

Figure 91. Vertical section of fast zone of annular configuration 8 of Table I; 44 polyethylene rods in outer fast zone 85

Figure 92. Geometry specifications of 90%, 36% enriched, and natural uranium fuel rods. Cross hatched yellow area highlights the polyethylene rod used in configuration 8 of Table I, dimensions in mm 86

Figure 93. Fuel zone of (annular) configuration 9 of Table I at z = 0 cm; 538 polyethylene rods in thermal zone 87

Figure 94. Geometry specifications of 10% enriched uranium rod. Cross hatched yellow area highlights the polyethylene rod used in configuration 9 of Table I. Cross hatched pink area highlights the steel region replaced by air when the polyethylene rod is used configuration 9 of Table I, dimensions in mm 88

Figure 95. Fuel zone of annular configuration 10 of Table I at z = 0 cm; 100 21% enriched fuel rods in thermal zone 89

Figure 96. Axial flux distribution from criticality calculation for square configuration 5 90

Figure 97. Axial flux axial distribution from Cf neutron source for square configuration 5 90

Figure 98. Axial flux profile from D-D neutron source for square configuration 5..... 91

Figure 99. Axial flux distribution from D-T neutron source for square configuration 5 91

Figure 100. Radial flux distribution for square configuration 5 92

Figure 101. Thermal flux profile from criticality calculation for square configuration 5... 92

Figure 102. Fast flux profile from criticality calculation for square configuration 5 93

Figure 103. Total flux profile from criticality calculation for square configuration 5 93

Figure 104. Thermal flux profile from Cf neutron source for square configuration 5 94

Figure 105. Fast flux profile from Cf neutron source for square configuration 5 94

Figure 106. Total flux profile from Cf neutron source for square configuration 5 95

Figure 107. Thermal flux profile from D-D neutron source for square configuration 5 ... 95

Figure 108. Fast flux profile from D-D neutron source for square configuration 5 96

Figure 109. Total flux profile from D-D neutron source for square configuration 5 96

Figure 110. Thermal flux profile from D-T neutron source for square configuration 5.... 97

Figure 111. Fast flux profile from D-T neutron source for square configuration 5..... 97

Figure 112. Total flux profile from D-T neutron source for square configuration 5..... 98

Figure 113. Normalized neutron spectrum in EC1B for square configuration 5..... 98

Figure 114. Normalized neutron spectrum in EC2B for square configuration 5..... 99

Figure 115. Normalized neutron spectrum in EC3B for square configuration 5..... 99

Figure 116. Normalized neutron spectrum in EC4B for square configuration 5..... 100

Figure 117. Normalized neutron spectrum in EC5T for square configuration 5..... 100

Figure 118. Normalized neutron spectrum in EC6T for square configuration 5..... 101

Figure 119. Normalized neutron spectrum in EC7T for square configuration 5..... 101

Figure 120. Normalized neutron spectrum in EC8R for square configuration 5..... 102

Figure 121. Normalized neutron spectrum in EC9R for square configuration 5..... 102

Figure 122. Normalized neutron spectrum in EC10R for square configuration 5..... 103

Figure 123. ^{3}He(n,p) reaction rate in experimental channels of fast zone for square configuration 5 from Cf neutron source; beam tube replaced by lead block 103

Figure 124. ^{3}He(n,p) reaction rate in experimental channels of thermal zone for square configuration 5 from Cf neutron source; beam tube replaced by lead block 104

Figure 125. ^{3}He(n,p) reaction rate in the experimental channel EC2B (25-cm long detector) for square configuration 5 from D-D neutron source 104

Figure 126. ^{3}He(n,p) reaction rate in the experimental channel EC6T (1-cm long detector) for square configuration 5 from D-D neutron source 105

Figure 127. Flux axial distribution from criticality calculation for annular configuration 6 105

Figure 128. Flux axial distribution from Cf neutron source for annular configuration 6 106

Figure 129. Flux axial distribution from D-D neutron source for annular configuration 6 106

Figure 130. Flux axial distribution from D-T neutron source for annular configuration 6 107

Figure 131. Flux radial distribution for annular configuration 6 107

Figure 132. Thermal flux profile from criticality calculation for annular configuration 6 108

Figure 133. Fast flux profile from criticality calculation for annular configuration 6 108

Figure 134. Total flux profile from criticality calculation for annular configuration 6 109

Figure 135. Thermal flux profile from Cf neutron source for annular configuration 6 ... 109

Figure 136. Fast flux profile from Cf neutron source for annular configuration 6 110

Figure 137. Total flux profile from Cf neutron source for annular configuration 6 110

Figure 138. Thermal flux profile from D-D neutron source for annular configuration 6 111

Figure 139. Fast flux profile from D-D neutron source for annular configuration 6 111

Figure 140. Total flux profile from D-D neutron source for annular configuration 6 112

Figure 141. Thermal flux profile from D-T neutron source for annular configuration 6. 112

Figure 142. Fast flux profile from D-T neutron source for annular configuration 6..... 113

Figure 143. Total flux profile from D-T neutron source for annular configuration 6..... 113

Figure 144. Normalized neutron spectrum in EC1B for annular configuration 6..... 114

Figure 145. Normalized neutron spectrum in EC2B for annular configuration 6..... 114

Figure 146. Normalized neutron spectrum in EC3B for annular configuration 6..... 115

Figure 147. Normalized neutron spectrum in EC4B for annular configuration 6..... 115

Figure 148. Normalized neutron spectrum in EC5T for annular configuration 6 116

Figure 149. Normalized neutron spectrum in EC6T for annular configuration 6 116

Figure 150. Normalized neutron spectrum in EC7T for annular configuration 6 117

Figure 151. Normalized neutron spectrum in EC8R for annular configuration 6..... 117

Figure 152. Normalized neutron spectrum in EC9R for annular configuration 6..... 118

Figure 153. Normalized neutron spectrum in EC10R for annular configuration 6..... 118

MONTE CARLO MODELING AND ANALYSES OF YALINA BOOSTER SUBCRITICAL ASSEMBLY

PART III: LOW ENRICHED URANIUM CONVERSION ANALYSES

List of Tables

Table No. Page

Table I. YALINA Booster subcritical assembly loading pattern, *S* and *A* in 4th column indicate square and annular arrangement of absorber rods, respectively, Italics and 0% indicate pure polyethylene rods (used only in configurations 8 and 9) 17

Table II. (n,γ) reaction rates [reactions/sp·10^{24}] (sp = source particle) in EC2B experimental channel for different nuclides, external neutron sources, and EK10 fuel rod numbers 17

Table III. (n,γ) reaction rate standard deviations [%] in EC2B experimental channel for different nuclides, external neutron sources, and EK10 fuel rod numbers 17

Table IV. Kinetic parameters of YALINA booster subcritical assembly with different fuel enrichments in the fast zone; square interface zone; ENDF/B-VI.6 nuclear data library for configurations 1, 2; ENDF/B-VII.0 nuclear data library for configurations 3, 4; the delayed neutron fraction has been calculated by the one-run method 18

Table V. Technical specifications of pulsed neutron source experiments. Helium detector has 0.45 cm radius; length is 25 cm for long (L) detectors and 1 cm for short (S) detectors; the colors for 36% enriched fuel label the experimental data plot in Figure 53 19

Table VI. Fuel composition of YALINA Booster subcritical assembly (weight fractions) 20

Table VII. Effective multiplication factor calculated by MCNPX and MONK codes for 90% and 36% enriched fuels as a function of EK10 fuel rods 21

Table VIII. Superhistory parameter for MONK for calculations of Table VII 21

Table IX. k_{eff} and k_{src} (D-T) for 36% enriched fuel as functions of EK10 fuel rods; MCNPX calculations with ENDF/B-VI.6 21

Table X Multiplication factor for 21% enriched fuel 22

Table XI. Effective multiplication factor for configuration 5 (L = long detector and S = short detector) obtained from numerical simulations 22

MONTE CARLO MODELING AND ANALYSES OF YALINA BOOSTER SUBCRITICAL ASSEMBLY

PART III: LOW ENRICHED URANIUM CONVERSION ANALYSES

Abstract

This study investigates the performance of the YALINA Booster subcritical assembly, located in Belarus, during operation with high (90%), medium (36%), and low (21%) enriched uranium fuels in the assembly's fast zone. The YALINA Booster is a zero-power, subcritical assembly driven by a conventional neutron generator. It was constructed for the purpose of investigating the static and dynamic neutronics properties of accelerator driven subcritical systems, and to serve as a fast neutron source for investigating the properties of nuclear reactions, in particular transmutation reactions involving minor-actinides. The first part of this study analyzes the assembly's performance with several fuel types. The MCNPX and MONK Monte Carlo codes were used to determine effective and source neutron multiplication factors, effective delayed neutron fraction, prompt neutron lifetime, neutron flux profiles and spectra, and neutron reaction rates produced from the use of three neutron sources: californium, deuterium-deuterium, and deuterium-tritium. In the latter two cases, the external neutron source operates in pulsed mode.

The results discussed in the first part of this report show that the use of low enriched fuel in the fast zone of the assembly diminishes neutron multiplication. Therefore, the discussion in the second part of the report focuses on finding alternative fuel loading configurations that enhance neutron multiplication while using low enriched uranium fuel. It was found that arranging the interface absorber between the fast and the thermal zones in a circular rather than a square array is an effective method of operating the YALINA Booster subcritical assembly without downgrading neutron multiplication relative to the original value obtained with the use of the high enriched uranium fuels in the fast zone.

MONTE CARLO MODELING AND ANALYSES OF YALINA BOOSTER SUBCRITICAL ASSEMBLY

PART III: LOW ENRICHED URANIUM CONVERSION ANALYSES

1. Introduction

The YALINA Booster is a zero-power subcritical assembly driven by a conventional neutron generator. It was constructed for the purpose of investigating the static and dynamic neutronics properties of accelerator driven subcritical systems, and to serve as a fast neutron source for measuring reaction rates involving minor-actinides.[1-2] This assembly was previously analyzed by Monte Carlo codes, as described in earlier reports.[3,4] The present report is divided into two parts: the first covers the IAEA benchmark calculations using high (90%), medium (36%), and low (21%) enriched uranium fuels in the fast zone and 10% enriched uranium fuel in the thermal zone. The second part investigates the assembly loaded only with 21% and 10% enriched uranium fuels in order to determine alternative fuel loading configurations that preserve the booster feature (operation with thermal and fast zones) and obtain neutron reactivity similar to the value obtained with 90% enriched uranium fuel in the fast zone.

2. 90% Enriched Uranium Fuel Configuration

Two previous reports[3,4] illustrated the calculational methods used to analyze the YALINA Booster subcritical assembly loaded with high enriched (90%) uranium fuel. All numerical results in this section were obtained by the MCNPX code[5] utilizing nuclear data libraries based on the ENDF/B-VI.6 nuclear data library.[6] Figures 1 and 2 illustrate the subcritical assembly overview and the horizontal section with labeling of the experimental channels. Features of the configurations using the 90% enriched uranium fuel are summarized in the first two rows of Table I (configurations 1 and 2); they differ only in the number of EK10 fuel rods (10% enriched uranium fuel) in the thermal zone of the assembly (902 or 1141 fuel rods). The high and natural enriched fuels consist of metallic uranium; the medium (36%) and the low (21%) enriched fuels consist of uranium oxide; the low (10%) enriched fuel loaded only in the thermal zone consists of uranium oxide mixed.

Figures 3-11 repeat the same plots of Figures 61-69 in Ref. 3, with the addition of results obtained from the californium (Cf) neutron source. Tables II and III report the results of Tables III and IV in Ref. 3, with the addition of results obtained from the Cf neutron source. Because the Cf neutron source has a fission neutron spectrum, the results are very similar to those obtained from the deuterium-deuterium (D-D) neutron source. In all 90% enriched fuel calculations, the indium reaction rate refers to natural indium.

Figures 12-15 repeat the plots of Figures 43-56 in Ref. 3, with the addition of results obtained from the Cf neutron source. In all the neutron spectrum plots, the neutron spectrum was first normalized to 1 and then to lethargy. The three external neutron sources, Cf, D-D, and deuterium-tritium (D-T), have very similar spectra, other than the peak located at the source energy for the D-D and D-T sources.

MCNPX results and experimental results for the ^{3}He(n,p) reaction rate obtained with the Cf neutron source are illustrated in Figures 16-20. In these calculations and experiments, the beam tube was removed from the assembly and replaced by a lead block. The thermal fuel zone was loaded with 1141 EK10 fuel rods. Reaction rates were tallied over a volume with a 0.45 cm radius and 1 cm height, matching the dimensions of the detector active volume. The irradiation samples were located at the center of the axial positions indicated in the figures by ticks on the z-axis. The MCNPX calculations were performed with (i.e., self-shielding) and without (i.e., no self-shielding) modeling the irradiation samples. The maximum value of the experimental reaction rate has been set equal to the maximum value from the MCNPX calculations because source intensity was not measured. There is a good match between the MCNPX and experimental results, with the exception of those near the boundary in the experimental channels of the fast zone. This mismatch may be caused by neutron reflection from the room walls and the YALINA Thermal facility (both the YALINA Booster and the YALINA Thermal facilities are located next to each other in the same room).[1]

Table IV summarizes the multiplication factor of the YALINA Booster subcritical assembly loaded with 90% enriched fuel (configurations 1 and 2 of Table I). The effective multiplication factor (first data row of Table IV) obtained by using ENDF/B-VII.0 nuclear data library[7] is very similar to that obtained by using the ENDF/B-VI.6 nuclear data library. The source multiplication factor set by the Cf neutron source (second data row of Table IV) is close to the value obtained by the D-D neutron source (third data row of Table IV), since the two neutron sources emit neutrons with similar average energies. Inclusion of the energy-angle distribution of the D-D and D-T source neutrons (plotted in Figures 34-37 of Ref. 8) does not significantly change the source multiplication factor, as shown by the results obtained for the configuration with 902 EK10 fuel rods (configuration 2 of Table I). This configuration was investigated because of the lower reactivity (relative to that of configuration 1), which enhances the contribution of source neutrons to the fission chains. Unless otherwise specified, all D-D and D-T calculations referring to 90% enriched fuel were performed with isotropic angular distribution and mono-energetic energy equal to 2.45 and 14.1 MeV for the D-D and D-T neutron sources, respectively. The Cf neutron source is isotropic and therefore does not require special attention in MCNP modeling.

Inclusion of the (n,xn) reactions in the source multiplication factor affects only the D-T source multiplication factor[8], which results in 10 and 80 pcm for configurations 1 and 2, respectively. The threshold energy of the (n,2n) reaction is more than 5.5 MeV for both ^{235}U and ^{238}U, which is higher than D-D neutrons energy. When the facility operates closer to criticality (configuration 1), most of the neutrons are from fission reactions and the contribution of (n,xn) reactions from the external neutron source diminishes.

For the configuration with 1141 EK10 fuel rods, the effective delayed neutron fraction calculated by MCNP4C[9] with nuclear data from ENDF/B-VII.0 is 717±1 pcm. This result was obtained with one MCNP simulation.[3,10] The value obtained with the nuclear data from ENDF/B-VI.6 is slightly higher, the value is 752 ± 2 pcm.[3]

The calculated β_{eff} of configuration 2 is 762 ± 2, 10 pcm more than the corresponding value of configuration 1. The delayed neutron fraction from ^{238}U increases slightly with the decrease of the neutron energy (Figure 38 of Ref. 8), which explains the difference between the β_{eff} values for configurations 1 and 2. Configuration 2 has less fuel but the same amount of moderator relative to configuration 1. Similar results were obtained also in Section 5 of Ref. 8.

The $^{235}U(n,f)$ and $^{3}He(n,p)$ reaction rates obtained with D-D and D-T neutron sources in EC1B, EC2B, EC3B, EC6T, and EC8R are plotted in Figures 21 and 22 for the configuration with 902 fuel rods and in Figures 23 and 24 for the configuration with 1141 fuel rods. The ^{235}U fission rate is scored in the experimental channels of the fast zone while the ^{3}He (n,p) rate is scored in the experimental channels of the thermal and the reflector zones. The reaction rates are normalized to their respective maximum values in each experimental channel. The results shown in Figures 21-24 are similar to the results shown in Figures 24-28 of Ref. 4, however the present results are for a single neutron source pulse with 5 μs duration.

Figure 25 illustrates the dynamic and the static correction factors[8] calculated by MCNPX in different experimental channels for the D-D and D-T neutron sources for configuration 1. The correction factor has been calculated according to Equation 1.[8,11]

$$c \equiv \frac{\rho_{cri}}{\rho_{src}} = -\frac{A_d}{A_p \cdot \beta_{eff}} \frac{k_{eff} - 1}{k_{eff}} \qquad (1)$$

In Equation 1, ρ_{cri} is the reactivity calculated by MCNPX in criticality mode and ρ_{src} is the reactivity calculated by MCNPX in source mode with an external neutron source. Using the area method[12] the latter parameter (in unit of dollars) can be expressed as the ratio between the prompt (A_p) and the delayed (A_d) areas. The statistical error calculation of the correction factor and the difference between the static and the dynamic correction factors is discussed in Section 11.D of Ref. 8.

In all the calculations of this report, the static correction factors have been obtained by MCNPX without modeling the detector and without any variance reduction technique. The reaction rates tallies have been sampled using a cylindrical volume with 25 cm length and the experimental channel radius.

For the D-T neutron source and the experimental channels of the fast zone, the dynamic correction factors have been calculated using the space-energy weight window for each single detector and the delayed neutrons bias variance reduction techniques. In the calculational model, three detectors were simultaneously loaded in EC1B, EC2B, and EC3B experimental channels and each detector has 1 cm height and 0.45 cm

radius active zone. Only the active zone of each detector is modeled for tallying the reaction rate.

For the D-D neutron source and the experimental channels of the thermal zone, the dynamic correction factor has been calculated with biasing the delayed neutrons to reduce the statistical error and without modeling the detectors. The reaction rate has been tallied using a cylindrical volume with 20 cm length and 1.2 cm radius.

For the EC8R experimental channel, the dynamic correction factor has been calculated using the weight window with single neutron energy range and biasing the delayed neutrons for reducing the statistical error. Two detectors were simultaneously loaded in EC6T and EC8R experimental channels. Each detector has active zone of 25 cm length and 0.45 cm radius.

The dynamic correction factors of Figure 25 differ from those reported in Table III of Ref. 4 due to the following improvements in the calculations of the present studies:

- Whenever a detector is modeled in the MCNPX source simulation for ρ_{src} calculation, ρ_{cri} calculation used the same calculational model. This is important for 25 cm long detectors because the 1 cm detectors do not impact the neutron multiplication value.
- The delayed neutron fraction value of 760 pcm has been changed to 752 pcm because the latter value has been obtained by the more accurate Meulenkamp and van der Marck method.[9,10]

The delayed neutrons bias is 1.2 delayed neutrons per fission. Of course, this does not change the effective multiplication factor.

Generally, there is a good agreement between static and dynamic correction factors when the statistical error value is small. It is not the case in the fast zone, where the statistical error is large. The channels close to the neutron source have a correction factor smaller than one. The uncorrected and corrected criticality multiplication factors from experimental measurements are shown in Figure 26. The corrected multiplication factor has been calculated with Equation 2 using the dynamic correction factor.

$$\rho_c = c \cdot \rho_{\exp} \qquad (2)$$

The technical details of the experiments are given in Table V. The detectors have equal radius of 0.45 cm but different length, 1 or 25 cm. The S and L characters at the end of the experimental channels labels refer to the short and the long detectors, respectively. The EC8RL experiment was performed using two long detectors at the same time; the other long detector was placed in EC6T. The spatial correction factor equalizes the experimental reactivity values measured in the different channels. The average corrected experimental value of the effective neutron multiplication is 450 pcm lower than the valued calculated by MCNPX. However, the MCNPX numerical model did not take into account ^{234}U isotope and the fuel impurities. The impurities are

important for the EK10 fuel loaded in the thermal zone of the assembly, where neutron losses to impurities are significant. The examination of the 563 EK10 fuel rods has found that the average uranium mass in the EK10 fuel rods is 76.737 g. When the compositions of the 90%, 36%, and 10% fuels include ^{234}U, the difference between the experimental and the MCNPX numerical multiplication factors disappears. Table VI gives the fuel composition without and with ^{234}U isotope. The updated composition of the EK10 fuel includes impurities and it takes into account the average uranium mass per EK10 fuel rod, which is 76.737 g. The average uranium mass per EK10 fuel rod used in the present report differs from the 78.388 g value used in Reference 8 Section 11.D. Both in the present study and Reference 8, the EK10 fuel density[1] is 5.042 g/cm^3.

The experimental results for the 90% fuel configuration have not been corrected for the detector dead-time due to the lack of the experimental information. Usually, the dead-time correction reduces the experimental value of the multiplication factor.

3. 90% and 36% Enriched Fuels Configurations – From Deep Subcritical to Near-Critical Configurations

Table VII summarizes the effective multiplication factor as a function of the number of EK10 fuel rods for configurations with different fuel enrichments in the fast zone. The 90% enriched configurations have 132 90% enriched fuel rods in the inner fast zone and 563 36% enriched fuel rods in the outer fast zone. The 36% enriched configurations have 695 36% enriched fuel rods in the fast zone. The calculations were performed by the MCNPX code with the ENDF/B-VI.6 nuclear data and by the MONK code with the DICE semi-continuous nuclear data library from the ENDF/B-VI.3 nuclear data.[14] The MONK results differ by a few hundred pcm from the MCNPX results due to the different versions of the ENDF/B-VI nuclear data files and also due to the lack of carbon bound in graphite data in the DICE data library. The superhistory parameter of the MONK inputs is reported in Table VIII. It is important to set this parameter as high as possible to obtain accurate results. The results of Table VII are also plotted in Figure 27; the curves for 90% and 36% enriched fuels diverge as the EK10 fuel rod number diminishes. Source neutrons contribute more to the fission chains in deep subcritical configurations. Therefore, the contribution of the 90% enriched fuel located around the external neutron source to neutron multiplication is amplified in deep subcritical configurations. In the configurations with a high number of EK10 fuel rods, neutron multiplication is mainly contributed from the thermal zone rather than from the fast zone. Figure 28 shows the MCNPX and experimental results obtained with the 36% enriched fuel. The experimental results have been obtained by D-D pulsed neutron source using $^3He(n,p)$ detectors. The area method,[12] with and without Gozani correction,[13] has been used to calculate the experimental reactivity. Figure 28 show that when the facility approaches criticality, the difference between the experimental and MCNPX results diminishes. In a critical assembly, all experimental channels give the same reactivity value without any spatial dependence. For a critical assembly, the Bell and Glasstone correction factor[4,8,11] is 1.

The variation of the D-T source multiplication factor as a function of the EK10 fuel rod number, for some of the 36% enriched fuel configurations, is reported in Table IX. The D-T source multiplication factor is always higher than the effective multiplication factor, and the former converges to the latter when the assembly approaches criticality.[8] The inclusion of (n,xn) reactions into the source multiplication factor definition slightly increases k_{src} as discussed in Section 4.B of Ref. 8.

4. 36% Enriched Fuel Configuration

The calculations of the YALINA Booster subcritical assembly with the 36% enriched fuel were performed using 1185 EK10 fuel rods, as specified in Table I for configuration 3. The increased number of EK10 fuel rods compensates for the reactivity decrease from the inner fast zone with reduced fuel enrichment. Figure 29 plots the fuel loading pattern of configuration 3.

Figures 30-42 are similar to Figures 3-15 and 21-24 discussed for configuration 2 with 90% enriched fuel. In the 36% enriched fuel calculations with 1185 EK10 fuel rods, the energy-angle distribution of D-D and D-T source neutrons calculated by the DROSG code[15] has been taken into account using 180 energy-angle bins. In this Section, the MCNPX code used cross section library produced from ENDF/B-VII.0 nuclear data files unless otherwise specified. The ENDF/B-VI.6 nuclear data library was used only in the calculations for the pulsed neutron source analyses of Figures 43-47, the dynamic correction factors, the effective multiplication factor of configuration 3 of Table IV with d label, and the effective multiplication factor with fuel impurities of Figure 53.

The reaction rates for the 36% enriched fuel shown in Figures 30-38 are lower than those obtained with the 90% enriched fuel shown in Figures 3-11 because of the lower neutron multiplication. For the 36% fuel, the ^{115}In(n,γ) reaction rate has been tallied using ENDF/B-VII.0. The cross sections of the different indium isotopes are available in ENDF/B-VII.0 files, while ENDF/B-VI.6 has only the cross sections for natural indium. The configurations with 90% enriched uranium fuel used ENDF/B-IV.6. The neutron spectra in Figures 39 and 40 for the 36% enriched fuel are similar to those of the 90% enriched fuel in Figures 12-15. The reaction rates from a single D-D and D-T pulse in Figures 41 and 42 for the 36% enriched fuel are similar to those of the 1141 configuration with 90% enriched fuel in Figures 23-24 because these two configurations have similar effective multiplication factors. The k_{eff} vales are 0.97507 ± 9 and 0.97972 ± 4 for the 36% and 90% enriched fuels, respectively as given in Table IV.

Kinetic parameters for the configuration with 36% enriched fuel are given in Table IV, as well as the results for the configurations with 90% and 21% enriched fuels. The effective multiplication factor k_{eff} diminishes as either the fuel enrichment in the fast zone or number of EK10 fuel rods decreases. For the 36% enriched uranium fuel configuration, the use of ENDF/B-VI.6 and ENDF/B-VII.0 gives the same multiplication factor as shown in Table IV. The source multiplication factor k_{src} for the D-T external neutron source is always higher than the effective multiplication factor k_{eff} independently of the uranium fuel enrichment in the fast zone. The D-T neutrons reaching the thermal

zone increase the neutron multiplication. In addition, the number of fission neutrons increases with the increase of the incident neutron energy, which also enhances the D-T source multiplication factor relative to the D-D and Cf source multiplication factors. The k_{src} from Cf and D-D sources are higher than k_{eff} of configurations 1 and 2 (90% enriched fuel), similar to k_{eff} of configuration 3 (36% enriched fuel), and lower than k_{eff} of configuration 4 (21% enriched fuel). Lowering the fuel enrichment of the fast zone enhances the parasitic absorption of the source neutrons, thus reducing the Cf and D-D source multiplication factors (k_{src}). Unlike D-T neutrons, D-D and Cf source neutrons do not reach the thermal zone; the peaks of the neutron spectra in Figures 12-15, 39-40, and 66-67 corresponding to the external neutron source energy confirm this observation. For the analyzed configurations, the contribution of (n,xn) reactions to the source multiplication factor is less than 100 pcm for the D-T neutron source as given in Table IV.

The effective delayed neutron fractions β_{eff} (calculated by MCNP4c3 with the one-run method)[3,9,10] for configurations 3 and 4 obtained with the ENDF/B-VII.0 nuclear data, are slightly smaller than the corresponding values of configurations 1 and 2 obtained with the ENDF/B-VI.6 nuclear data. The effect of the different nuclear data libraries have been further investigated for a configuration with 1141 EK10 fuel rods in the thermal zone and 695 36% enriched fuel rods in the fast zone. For this configuration, the effective delayed neutron fraction calculated by the MCNPX code (using the k-ratio method, also referred to as the two-run method)[3] using the ENDF/B-VI.6 nuclear data is 766 ± 12 pcm, which is similar to the values obtained for the configurations with 90% enriched fuel using the ENDF/B-VI.6 nuclear data library. In addition, for configuration 1, the change of the nuclear data library from ENDF/B-VI.6 to ENDF/B-VII.0 lowers the β_{eff} value from 752 to 717 pcm as given in Table IV.

The prompt neutron lifetime l_p is similar for all configurations (55-60 μs) independently of the fuel enrichment in the fast zone as given in Table IV.

Figures 43 and 44 show a good agreement between the experimental and the calculated reaction rates in EC5T and EC6T experimental channels with 25 cm long and 0.45 cm radius detectors. In these experiments two detectors have been simultaneously used. The MCNPX results have been calculated using the ENDF/B-VI.6 nuclear data libraries, the weight window with a single energy range and the delayed neutron bias variance reduction techniques, the helium detectors with 0.45 cm active radius and 25 cm active length (only the active volume is modeled in MCNPX calculations), and the C program to superimpose the pulses.[4,8] The detector material is modeled as a mixture of 80% (atomic fraction) ^{3}He and 20% natural Kr with 8.143 mg/cm^3 density. The results have been normalized using an arbitrary factor since the absolute source strength is unknown. The time bins of the experimental counting system and the MCNPX calculations are 2 and 10 μs, respectively. The arbitrary factor does not affect the reactivity obtained by the area method since it is canceled in the reactivity calculations. The simultaneous use of two long (25 cm height) detectors in EC5T and EC6T decreases the multiplication factor from 0.97510±8 down to 0.97344±8. The insertion of

two short (1 cm height) detectors in EC5T and EC6T and a long (25 cm height) detector in MC5 does not change the multiplication factor.

Figures 45 - 47 show the measured and calculated ^{3}He(n,p) reaction rates in EC5T, EC6T, and MC5 experimental channels. In the experiment three detectors have been simultaneously used. Two short detectors have been inserted into EC5T and EC6T experimental channels and one long detector has been inserted into MC5 experimental channel. The MCNPX simulations have been performed with the delayed neutrons bias variance reduction technique with the three detectors. The agreement between experimental and numerical results is good. The experimental data of Figures 45 and 46 exhibit larger fluctuations relative to those of Figures 43 and 44 due to the difference in the detector length.

Figures 48 and 49 show the correction factor using Eq. 1 for the D-D and D-T neutron sources, respectively, when the assembly is loaded with 36% fuel in the fast zone and 902 EK10 fuel rods in the thermal zone (this configuration is not listed in Table I). The correction factor has been obtained using the static simulations[8] and a cylindrical tally volume using 25 cm of the experimental channel length without the MCNPX weight window and the delayed neutrons bias variance reduction techniques. In these plots, six different response functions have been considered: ^{238}U(n,f), ^{237}Np(n,f), ^{235}U(n,f), ^{3}He(n,p), ^{10}B(n,α), and constant integrating the neutron flux. The materials of the response functions have not been modeled in the MCNPX geometrical model. ^{238}U(n,f) tallies fast neutrons above 2 MeV; ^{237}Np(n,f) tallies fast neutrons above 0.5 MeV; the ^{235}U(n,f) mainly tallies neutrons in the thermal energy range; ^{3}He(n,p) and ^{10}B(n,α) tally only thermal neutrons, and the constant tallies the neutron flux neutron flux over the whole energy range. The Bell and Glasstone correction factor is calculated according to Equation 1 and the calculation of its statistical error used the methodology discussed in Section 11.D of Ref. 8.

The detectors with large thermal cross sections underscore the reaction rates from the fast source neutrons and consequently provide smaller prompt areas. Therefore, the correction factor increases as the average detector scoring energy decreases. The ranking order of the correction factor starting with the highest value follows the order of the previously listed response functions. The correction factors for the D-T neutron source are similar to those for the D-D neutron source.

Figures 50 and 51 show the correction factor for the D-D and D-T neutron sources, respectively, when the assembly is loaded with 36% enriched fuel in the fast zone and 1185 EK10 fuel rods in the thermal zone (configuration 3 of Table I). In Figure 50, the dynamic correction factor has been calculated for the D-D neutron source with ^{3}He(n,p) response function in EC5T and EC6T experimental channels. Two different variance reduction techniques were used: the weight window with a single energy range and the delayed neutron fraction biasing technique. Two long detectors were simultaneously inserted in the EC5T and the EC6T experimental channels. For the 36% enriched fuel, the experimental measurements have been performed with two or three helium detectors at the same time. The technical details of the experiments are reported in

Table V. All experiments have used D-D neutron source with 5 μs duration and 20 ms period.

Figure 52 plots the CIEMAT correction factors[16] and the correction factors using the CIEMAT definition of the static correction factor[16] using the MCNPX results in Figure 49. CIEMAT and ANL results are in good agreement.

The average value of the multiplication factor calculated from the corrected experimental results obtained from the use of three detectors at the same time based on static calculations is shown in Figure 53. This value is 700 pcm lower than the MCNPX criticality multiplication factor. If the very low natural fraction of ^{234}U isotope of the uranium and the K10 fuel impurities is included in the 36% and 10% enriched fuels compositions as listed in Table VI, the difference decreases to 250 pcm. The correction of the experimental results for the detector dead time decreases k_{eff} by 100 pcm.[17] This latter correction is important for long detectors placed in the thermal region as shown in Table V and Figure 53; the detector colors of Figure 53 are labeled in Table V.

5. 21% Enriched Fuel Configuration

The horizontal cross section of the fuel zone and the vertical cross section of the assembly of the YALINA Booster assembly loaded with 21% enriched fuel are shown in Figures 54 to 55. The 21% enriched fuel rod geometry is shown in Figure 56. Some fuel holes in the fast zone were left empty science the available number of the 21% enriched fuel rods is 601. The 21% enriched fuel rod is longer than the 36% enriched fuel rod and this shifts the borated polyethylene reflector on the side opposite to the beam tube. In addition, the active fuel zone center is shifted 0.7 cm relative to the copper target disk, which marks the center of the active fuel length of the 90%, the 36%, and the 10% enriched fuel rods. In the calculations of this Section, this offset was taken into account and the MCNPX code utilized an ENDF/B-VII.0 nuclear data library.

The reaction rates in the experimental channels for the 21% enriched fuel configuration are lower than those for the 36% enriched fuel configuration as shown in Figures 57 to 65 relative to Figures 30-38 for the 36% configurations because of the lower neutron multiplication as shown in the last two columns of Table IV.

The neutron spectra from 36% and 21% fuel enrichments are very similar as shown in Figures 66-67 and Figures 39-40, respectively. The reaction rates from the D-D and the D-T pulsed neutron sources shows that the delayed neutron background is slightly higher for the 36% enriched fuel relative to the 21% enriched fuel as shown in Figures 68-69 and Figures 41-42, respectively.

Figure 70 shows the static and the dynamic correction factors for the 21% enriched fuel configuration calculated by MCNPX. The dynamic correction factor has been calculated for $^{3}He(n,p)$ reaction rate in different experimental channels. The static correction factors were calculated by the same procedure used for 36% enriched fuel considering the remarks observed for Figure 48. The dynamic correction factor has

been calculated using the variance reduction technique of biasing the delayed neutrons fraction, 0.3 delayed neutrons per fission, and tallying within a cylinder with 20 cm height and a radius equal to the radius of the experimental channel without modeling the detector.

Figure 71 illustrates the comparison between the average value of the corrected experimental multiplication factor and the MCNPX criticality multiplication factor; the difference between the two values is 650 pcm. The experimental reactivity has been corrected using the static correction factors shown in Figure 70. Table V summarizes the technical details of the experiments; two detectors were simultaneously used with a D-D pulsed neutron source with 5 μs duration and 20 ms period. When the 21% and the 10% enriched fuels compositions are changed to take into account the ^{234}U and EK10 fuel impurities, as summarized in Table VI, the difference between the average of the corrected experimental and the MCNPX multiplication factors decreases to 250 pcm. When the detector dead time is taken into account,[17] the MCNPX results match the experimental results within 500 pcm range.

6. 21% Enriched Fuel Configurations with Square and Circular Arrangement of the Absorber Interface between the Fast and the Thermal Zones

The use of 21% enriched fuel reduces the effective neutron multiplication factor of the assembly relative to the values obtained with the 90% enriched fuel as shown in Table IV for configurations 1 and 4. In this Section, alternative fuel loading patterns of the 21% enriched fuel are examined to enhance the effective neutron multiplication factor of the assembly while using the same number of fuel rods. The numbers of the fuel rods are 651 and 1185 for the 21% and the 10% enriched fuels, respectively. In all MCNPX calculations of this Section, the 0.7 cm offset of the 21% fuel rods center relative to the center of the EK10 fuel active length, was not considered. ENDF/B-VII.0 nuclear data were used for the analyses.

Figures 72 to 95 plot the MCNPX geometry model used for the assembly loaded with the 21% and the 10% enriched fuels. In those figures, the correspondence between materials and colors is:

- yellow air
- pale-green borated polyethylene
- green stainless steel
- gold organic glass
- red iron
- light-blue water
- purple polyethylene
- pink lead
- blue 21% enriched uranium
- khaki 10% enriched uranium
- olive green natural uranium
- salmon boron carbide

- violet-red polystyrene
- wheat graphite
- magenta aluminum alloy
- orange copper

Figures 72 to 87 focus on configuration 5 of Table I. This configuration is the same as configuration 4 of Table I, except for the number of the 21% and the natural enriched fuel rods. Figure 88 shows the fast zone of configuration 6, which differs from configuration 5 in the circular rearrangement of the natural uranium and the B_4C absorber rods. Figure 89 shows the fast zone of configuration 7, which differs from configuration 6 in the reduced number of natural uranium rods. Figures 90 and 91 show the horizontal and vertical sections, respectively, of the fast zone of configuration 8. In this configuration, 44 natural uranium rods have been replaced by polyethylene rods with 0.35 cm radius, 61 cm length, and 0.859 g/cm^3 density, as shown in Figure 92. Figure 93 shows the fast zone of configuration 9. This configuration differs from configuration 6 because 538 polyethylene rods have been inserted in the thermal region. The polyethylene rods used in the thermal region have 0.5 cm radius, 57.6 cm length, and 0.859 g/cm^3 density, as shown in Figure 94. Figure 95 shows the fuel zone of configuration 10. In this configuration, relative to configuration 6:

1) 100 rods with 21% enriched uranium are replaced by air in the outer fast zone.
2) 100 EK10 fuel rods are replaced by 21% enriched fuel.

The multiplication factors of all the configurations are given in Table X. Arranging the natural uranium and absorber rods in an annular pattern increases the effective neutron multiplication factor by ~1900 pcm. For configurations 6 and 7, changing the number of the natural uranium rods from 152 to 108 results in a 150 pcm change in the k_{eff} value. The addition of 44 polyethylene rods in the outer fast zone or the addition of 538 polyethylene rods in the thermal zone has a small effect on k_{eff} of less than 100 pcm. For configuration 10, the replacement of 100 EK10 fuel rods with 100 21% enriched fuel rods of configuration 6 increases the neutron multiplication factor by 400 pcm. The 100 21% enriched fuel rods located outside the ring of the absorber rods experience a more thermalized neutron spectrum relative to the fuel rods inside the ring. This enhances the neutron multiplication because the ^{235}U fission cross section is much greater in the thermal energy range. In configuration 10, only 1085 EK10 fuel rods are used while the available EK10 fuel rods are 1185.

For the 21% enriched fuel, as already discussed in Section 4, the source multiplication factor for Cf and D-D neutron sources is lower than the effective multiplication factor as shown in Table X. The source multiplication factor for the D-T neutron source exhibits opposite behavior since D-T neutrons reach the thermal region of the assembly, which has higher neutron multiplication. Configurations 4 and 5 have similar neutron multiplication factors since both configurations have the same number of EK10 rods and most of the neutron multiplication occurs in the thermal zone. However, the source multiplication factor of configuration 5 is 90 to 140 pcm higher than that of configuration 4 because the fast zone is filled with fuel rods and this reduces neutron leakage.

The neutron flux profiles in the experimental channels of configuration 5 are plotted in Figures 96-100. These profiles have been calculated by MCNPX in critical and source modes; in the latter case Cf, D-D, or D-T neutron sources were used. In these plots 1185 x 651 x 152 x 116 represents the numbers of EK10 rods, the 21% fuel rods, the natural uranium rods, and the boron carbide rods, respectively.

The thermal, fast, and total neutron flux profiles at the midplane perpendicular to the fuel rods are illustrated in Figures 101 through 112 from the criticality and source-driven calculations. Generally, the first few rows of EK10 fuel rods have the highest thermal neutron flux. The Cf neutron source shows strong contributions to the peak value at the center of the target zone for the thermal and fast fluxes as shown in Figures 104 and 105, respectively. Also, the D-D and D-T neutron sources contribute to the fast flux at the center of the target zone as shown in Figures 108 and 111, respectively.

The neutron spectra in the experimental channels for the configuration 5 are plotted in Figures 113 through 122. These plots are similar to those of Figures 66 and 67 for configuration 4. Unlike the Cf and D-D source neutrons, the D-T source neutrons stream into the thermal zone of the assembly.

Figures 123 and 124 plot the ^{3}He(n,p) reaction rate in some of the experimental channels of the fast and thermal zones, respectively, for the Cf neutron source. These plots are similar to those of Figures 16 through 20 for configuration 1; however, the lower neutron multiplication of configuration 5 reduces the reaction rates.

The ^{3}He(n,p) reaction rate from the D-D pulsed neutron source is plotted in Figures 125 and 126 for the EC2B and EC6T experimental channels, respectively. In the configuration 5 calculations, the active zone of the detector has been modeled, the weight windows and delayed neutron bias variance reduction techniques have been used, and the pulse superimposition methodology has been applied.[4,8] The results shown in Figure 126 are similar to those in Figures 44 and 46 for configuration 3; however, the lower neutron multiplication of configuration 5 results in a smaller delayed neutron fraction. The effective multiplication factor from these calculations is reported in Table XI.

Figures 127 through 153 give the same results of Figures 96 through 122 but for configuration number 6. The flux profiles in the experimental channels from the source calculations are much higher for configuration 6 than for configuration 5 due to the much higher k_{eff} of configuration 6. The flux profiles in the experimental channels from the criticality calculations are approximately the same for configuration 5 and 6 because the flux is normalized per fission source neutron. These remarks hold also for the neutron flux profile of Figures 132 through 143.

7. Conclusions

The MCNPX analyses of the YALINA Booster subcritical assembly loaded with high, medium, and low enriched uranium fuels are presented in this report. The kinetic parameters, neutron flux and spectra in the experimental channels, and the ^{3}He(n,p),

$^{235}U(n,f)$, $^{55}Mn(n,\gamma)$, $^{115}In(n,\gamma)$, and $^{197}Au(n,\gamma)$ reaction rates due to the use of californium (Cf), D-D, and D-T neutron sources are included.

The effective neutron multiplication factor k_{eff} diminishes as the fuel uranium enrichment in the fast zone or the number of EK10 fuel rods in the thermal zone decreases. The neutron source multiplication factor k_{src} for the D-T external neutron source is always higher than the effective multiplication factor k_{eff} because D-T neutrons generate extra neutrons from (n,xn) reactions and reach the thermal zone of the assembly achieving higher neutron multiplication than in the fast zone. The k_{src} of the Cf and D-D neutron sources are higher than k_{eff} for the configurations with high and medium uranium enrichments. For the configuration with low uranium enrichment, the k_{src} values are lower than k_{eff} because the neutron multiplication is reduced in the fast zone and the source neutrons do not reach the thermal zone of the assembly. In addition, the contribution of (n,x) reactions from these source neutrons is negligible. When the facility approaches the critical status, k_{src} converges to k_{eff}.

As observed for the YALINA Thermal facility,[8] the effective delayed neutron fraction increases while the number of EK10 fuel rods in the thermal zone diminishes. This change is very small and can be detected only by the one-run method because of the large statistical error associated with the results from the k-ratio method. The delayed neutron fraction calculated with ENDF/B-VII.0 nuclear data is slightly lower than the value calculated with ENDF/B-VI.6 data. Prompt neutron lifetime and neutron spectra in the experimental channels are approximately the same for all the examined configurations.

The MCNPX $^{3}He(n,p)$ reaction rate from the Cf neutron source for the 90% enriched fuel configuration has been compared with experimental results and a good agreement was obtained. A mismatch occurs at the boundary of the experimental channels in the fast zone due to neutron reflection from the surrounding walls and the other hardware inside the experimental room.

The Bell and Glasstone correction factors were calculated by the dynamic and the static methods[8]; the two methods provide similar results within the statistical error. As already observed and discussed for the YALINA Thermal subcritical assembly,[8] the correction factor is smaller than 1 near the neutron source and higher than 1 away from the source. The Bell and Glasstone correction factor converges to 1 when the assembly approaches criticality. The correction factor strongly depends on the energy response function of the detector, especially when the measurement is performed close to the neutron source. The neutron source energy-angle distribution (D-D or D-T) has a very small influence on the correction factor. The correction factor also depends on the axial position of the detector.[18] The correction factor calculated for the medium uranium enriched fuel is in good agreement with other published results.[16]

The comparison between the corrected experimental reactivity and the MCNPX reactivity results shows a good agreement when the ^{234}U concentration in the uranium fuels, EK10 fuel impurities, and the dead time of the detectors are considered in the analyses. The experimental results from the use of the D-D pulsed neutron source with

the 36% enriched uranium fuel configuration were successfully compared with MCNPX results obtained by the pulse superimposition calculation methodology.

The use of low enriched uranium fuels in the fast zone reduces the multiplication factor of the assembly. Different loading configurations were investigated to restore the effective multiplication factor to the original value while using the same number of fuel rods. The annular arrangement of the interface zone, the natural uranium and the absorber rods enhances the effective neutron multiplication factor. Utilization of pure polyethylene rods, in either the fast or thermal zones results in small changes in the effective neutron multiplication factor. The arrangement of some of the 21% enriched fuel rods in the thermal zone next to the fast zone increases the effective neutron multiplication factor of the assembly.

Acknowledgments

This project is supported by the U.S. Department of Energy, National Nuclear Security Administration, Office of Global Nuclear Material Threat Reduction (NA213).

References

[1] Y. GOHAR and D. L. SMITH, "*YALINA, Facility, A Subcritical Accelerator-Driven System (ADS) for Nuclear Energy Research. Facility Description and Overview of the Research Program*," Argonne National Laboratory Report ANL-10/05, 2010; www.osti.gov/bridge.

[2] G. ALIBERTI and Y. GOHAR, "*YALINA Analytical Benchmark Analyses Using the Deterministic ERANOS Code System*," Argonne National Laboratory Report ANL-09/23, 2009; www.osti.gov/bridge.

[3] A. TALAMO and Y. GOHAR, "*Monte Carlo Modeling and Analyses of YALINA Booster Subcritical Assembly, Part I: Analytical Model and Main Neutronics Parameters*," Argonne National Laboratory Report ANL-NE-08/13, 2008; www.osti.gov/bridge.

[4] A. TALAMO and Y. GOHAR, "*Monte Carlo Modeling and Analyses of YALINA Booster Subcritical Assembly, Part II: Pulsed Neutron Source Analyses*," Argonne National Laboratory Report ANL-08/33, 2008; www.osti.gov/bridge.

[5] J. S. HENDRICKS et al., "*MCNPX, VERSION 2.6.B*," LA-UR-06-3248, 2006.

[6] http://t2.lanl.gov/data/data.html

[7] M. B. CHADWICK et al., "*ENDF/B-VII.0: Next Generation Evaluated Nuclear Data Library for Nuclear Science and Technology*," Nuclear Data Sheets 107/12, pp. 2931-3118, 2006.

[8] A. TALAMO and Y. GOHAR, "*Deterministic and Monte Carlo Modeling and Analyses of YALINA-Thermal Subcritical Assembly*," Argonne National Laboratory Report ANL-NE-10/17, 2010; www.osti.gov/bridge.

[9] J. F. BRIESMEISTER, "*A General Monte Carlo N-Particle Transport Code*, *Version 4c*," Los Alamos National Laboratory, LANL, LA-13709-M, 2002.

[10] R.K. MEULEKAMP and S. C. van der MARCK, "*Calculating the Effective Delayed Neutron Fraction with Monte Carlo*," Nuclear Science and Engineering 152, pp. 142-148, 2006.
[11] G. I. BELL and S. GLASSTONE, "*Nuclear Reactor Theory*," Van Nostrand Reinhold Company, 1970.
[12] N. SJÖSTRAND, "*Measurement on a Subcritical Reactor Using a Pulsed Neutron Source*," Arkiv för Fysik 11, 1956.
[13] T. GOZANI, "*A Modified Procedure for the Evaluation of Pulsed Source Experiments in Subcritical Reactors*," Nucleonik 4, 1962.
[14] ANSWERS SOFTWARE, "*MONK, User Guide for Version 9,*" 2006.
[15] http://homepage.univie.ac.at/manfred.drosg/drosg2000.htm
[16] C. BECARES et al., "*Correction Methods for Reactivity Monitoring Techniques in Pulsed Neutron Source (PNS) Measurements*", PHYSOR, Pittsburgh, PA, USA, 2010.
[17] Y. CAO and Y. GOHAR, "*YALINA-Booster Subcritical Assembly Pulsed-Neutron Experiments: Data Processing and Spatial Corrections*", Argonne National Laboratory, ANL-NE-10/22 2010; www.osti.gov/bridge.
[18] A. TALAMO et al., "*Axial Dependency of the Bell and Glasstone Correction Factor for Subcriticality Measurements"*, ANS Winter Meeting, Las Vegas, USA, 2010.

Table I. YALINA Booster subcritical assembly loading pattern, *S* and *A* in 4th column indicate square and annular arrangement of absorber rods, respectively, Italics and 0% indicate pure polyethylene rods (used only in configurations 8 and 9)

Configuration	**Inner Fast Zone** No. of Rods / Enrichment	**Outer Fast Zone** No. of Rods / Enrichment	**Absorber Zone** No. of U_{nat} Rods /No. of B_4C Rods /Shape	**Thermal Zone** No. of Rods / Enrichment
1	132 / 90%	563 / 36%	108 / 116 / S	1141 / 10%
2	132 / 90%	563 / 36%	108 / 116 / S	902 / 10%
3	132 / 36%	563 / 36%	108 / 116 / S	1185 / 10%
4	55 / 21%	546 / 21%	108 / 116 / S	1185 / 10%
5	132 / 21%	519 / 21%	152 / 116 / S	1185 / 10%
6	132 / 21%	519 / 21%	152 / 116 / A	1185 / 10%
7	132 / 21%	519 / 21%	108 / 116 / A	1185 / 10%
8	132 / 21%	44 / 0% 519 / 21%	108 / 116 / A	1185 / 10%
9	132 / 21%	519 / 21%	152 / 116 / A	*538 / 0%* 1185 / 10%
10	132 / 21%	419 / 21%	152 / 116 / A	1085 / 10% 100 / 21%

Table II. (n,γ) reaction rates [reactions/sp·10^{24}] (sp = source particle) in EC2B experimental channel for different nuclides, external neutron sources, and EK10 fuel rod numbers

Isotope or Material	**1141 EK10 Fuel Rods**			**902 EK10 Fuel Rods**		
	Cf	**D-D**	**D-T**	**Cf**	**D-D**	**D-T**
^{197}Au	0.008930	0.008380	0.011099	0.003370	0.002509	0.004987
In	0.010707	0.008770	0.014540	0.005066	0.004626	0.006641
^{55}Mn	0.000466	0.000416	0.000771	0.000190	0.000153	0.000282

Table III. (n,γ) reaction rate standard deviations [%] in EC2B experimental channel for different nuclides, external neutron sources, and EK10 fuel rod numbers

Isotope or Material	**1141 EK10 Fuel Rods**			**902 EK10 Fuel Rods**		
	Cf	**D-D**	**D-T**	**Cf**	**D-D**	**D-T**
^{197}Au	9.97	9.73	11.66	12.20	8.09	6.62
In	9.12	8.18	9.07	15.28	9.78	8.61
^{55}Mn	8.43	8.06	10.65	13.49	7.4	7.39

Table IV. Kinetic parameters of YALINA booster subcritical assembly with different fuel enrichments in the fast zone; square interface zone; ENDF/B-VI.6 nuclear data library for configurations 1, 2; ENDF/B-VII.0 nuclear data library for configurations 3, 4; the delayed neutron fraction has been calculated by the one-run method

Kinetic Parameter	**Configuration**			
	1	**2**	**3**	**4**
k_{eff}	0.97972±4 0.97953±5[c)]	0.92881±4 0.92838±4[c)]	0.97507±9 0.97510±8[d)]	0.96404±4
k_{src} Cf	0.98703 0.98705[b)]	0.95716 0.95722[b)]	0.97531 0.97534[b)]	0.95584 0.95588[b)]
k_{src} D-D	0.98686 0.98687[b)]	0.95635 0.95639[b)] 0.95599[a)] 0.95604[ab)]	0.97493[a)] 0.97495[ab)]	0.95587[a)] 0.95590[ab)]
k_{src} D-T	0.99143 0.99151[b)]	0.97118 0.97203[b)] 0.97126[a)] 0.97210[ab)]	0.98374[a)] 0.98403[ab)]	0.97101[a)] 0.97193[ab)]
β_{eff} [pcm]	752±2 717±2[c)]	762±2	717.1±1.4	720.8±1.4
l_p [μs]	54±2	54±2	57.9±1.5	60.0±0.7

Legend of Table IV	
a	Source modeling takes into account the energy-angle distribution of neutrons
b	k_{src} includes (n,xn) reactions
c	ENDF/B-VII.0 nuclear data library
d	ENDF/B-VI.6 nuclear data library

Table V. Technical specifications of pulsed neutron source experiments. Helium detector has 0.45 cm radius; length is 25 cm for long (L) detectors and 1 cm for short (S) detectors; the colors for 36% enriched fuel label the experimental data plot in Figure 53

Experimental Channels	Neutron Source	Pulse Duration [μs]	Pulse Period [ms]	Detector Voltage [V]
Fuel with 90% Enrichment				
EC1BS	DT	5	20	1600
EC2BS	DT	5	20	1600
EC3BS	DT	5	20	1600
EC5TS	DD	10	17.93	1600
EC6TS	DD	10	17.93	1600
EC7TS	DD	10	17.93	1600
EC8RL (EC6TL)	DD	5	20	1600
Fuel with 36% Enrichment				
EC5TL EC6TL	DD	5	20	—
MC5L EC5TL EC6TS	DD	5	20	1600 1600 1100
MC5L EC6TL EC7TS	DD	5	20	1600 1600 1100
MC5L EC7TL EC5TS	DD	5	20	1600 1600 1100
MC5L EC9RS EC8RL	DD	5	20	1600 1100 1600
MC5L EC9RL EC8RS	DD	5	20	1600 1600 1100
MC5L EC3BL EC6TS	DD	5	20	1600 1600 1100
MC5L EC2BL EC5TS	DD	5	20	1600 1600 1100
MC5L EC1BL EC6TS	DD	5	20	1600 1600 1100
MC5L EC6TS EC5TS	DD	5	20	1600 1600 1600
MC5L EC8RS EC7TS	DD	5	20	1600 1600 1600
MC5L EC7TS EC8RS	DD	5	20	1600 1600 1600
MC5L EC6TS EC5TS	DD	5	20	1600 1600 1600
Fuel with 21% Enrichment				
EC1BL EC5TL	DD	5	20	1600 1600
EC2BL EC6TL	DD	5	20	1600 1600
EC3BL EC7TL	DD	5	20	1600 1600
EC8RL EC9RL	DD	5	20	1600 1600

Table VI. Fuel composition of YALINA Booster subcritical assembly (weight fractions)

Fuel with 90% Enrichment ρ = 17.95 [g/cm^3]		
Isotope	**Without ^{234}U**	**With ^{234}U**
^{234}U	0	0.0089
^{235}U	0.9	0.8911
^{238}U	0.1	0.1000
Fuel with 36% Enrichment ρ = 9.694 [g/cm^3]		
Isotope	**Without ^{234}U**	**With ^{234}U**
^{234}U	0	0.002844436
^{235}U	0.31479	0.311945600
^{238}U	0.56624	0.566240000
^{16}O	0.11897	0.118970000
Fuel with 21% Enrichment ρ = 9.6735 [g/cm^3]		
Isotope	**Without ^{234}U**	**With ^{234}U**
^{234}U	0	1.377670E-3
^{235}U	0.185064	1.847491E-1
^{238}U	0.696194	6.951317E-1
^{16}O	0.118742	1.187415E-1
Fuel with 10% Enrichment ρ = 5.042 [g/cm^3]		
Isotope	**Without ^{234}U**	**With ^{234}U and Impurities**
^{234}U	0	6.954402E-4
^{235}U	0.079691	7.873928E-2
^{238}U	0.728557	7.115114E-1
^{16}O	0.142022	1.063647E-1
^{12}Mg	0.049730	1.024215E-1
^{10}B	0	3.142065E-8
^{11}B	0	1.391193E-7
C	0	8.975785E-5
^{14}N	0	8.940596E-6
^{15}N	0	3.518870E-8
^{28}Si	0	5.772447E-5
^{29}Si	0	3.027224E-6
^{30}Si	0	2.078800E-6
^{55}Mn	0	4.218619E-6
^{54}Fe	0	5.178804E-6
^{56}Fe	0	8.492974E-5
^{57}Fe	0	2.073506E-6
^{58}Fe	0	2.685306E-7
^{58}Ni	0	3.799817E-6
^{60}Ni	0	1.514147E-6
^{61}Ni	0	6.692201E-8
^{62}Ni	0	2.168258E-7
^{64}Ni	0	5.703287E-8
^{63}Cu	0	2.458623E-6
^{65}Cu	0	1.131691E-6

Table VII. Effective multiplication factor calculated by MCNPX and MONK codes for 90% and 36% enriched fuels as a function of EK10 fuel rods

No. of EK10 Fuel Rods	**MCNPX with ENDF/B-VI.6 data**		**MONK with ENDF/B-VI.3 data DICE Library**	
	90% ^{235}U	**36% ^{235}U**	**90% ^{235}U**	**36% ^{235}U**
127	0.66349±8	0.46713±7	0.66960±20	0.46840±20
183	0.68251±8	0.52214±7	0.68800±20	0.52290±20
379	0.76183±9	0.68762±8	0.76400±20	0.68670±20
538	0.82327±9	0.77811±8	0.82370±20	0.77680±20
754	0.89056±8	0.86380±7	0.88960±20	0.86080±20
902	0.92880±8	0.90870±9	0.92710±20	0.90570±20
1061	0.96591±8	-	-	-
1132	0.97879±9	-	-	-
1141	0.97956±9	0.96635±8	0.97710±20	0.96350±20 0.96310±20
1165	0.98418±7	0.97116±9	0.98170±20	0.96770±20
1177	0.98634±9	0.97356±9	0.98350±20	0.97030±20
1209	0.99218±7	0.98016±9	0.98970±20	0.97720±20 0.97670±20

Table VIII. Superhistory parameter for MONK for calculations of Table VII

No. of EK10 Rods	**90% ^{235}U**	**36% ^{235}U**
127	100	100
183	100	100
379	100	100
538	100	100
754	200	200
902	200	200
1141	400	300 400
1165	400	400
1177	400	400
1209	400	300 400

Table IX. k_{eff} and k_{src} (D-T) for 36% enriched fuel as functions of EK10 fuel rods; MCNPX calculations with ENDF/B-VI.6

No. of EK10 Rods	**k_{eff}**	**k_{src} (D-T)**	
		With (n,xn) reactions	**Without (n,xn) reactions**
1165	0.97116±9	0.98142	0.98104
1177	0.97356±9	0.98287	0.98255
1209	0.98016±9	0.98696	0.98678

Table X Multiplication factor for 21% enriched fuel

Configuration	Figures	Code	Multiplication Factor	
			With (n,xn) reactions	**Without (n,xn) reactions**
5	72-87	MCNP-5.1.14	0.96386±5 k_{eff} 0.95726 k_{src} Cf 0.95712 k_{src} DD 0.97276 k_{src} DT	0.95722 k_{src} Cf 0.95709 k_{src} DD 0.97191 k_{src} DT
		MCNPX-2.7a	0.95665 k_{src} Cf	
6	88	MCNP-5.1.14	0.98297±5 k_{eff} 0.98023 k_{src} Cf 0.98034 k_{src} DD 0.98734 k_{src} DT	0.98022 k_{src} Cf 0.98032 k_{src} DD 0.98716 k_{src} DT
		MCNPX-2.6e	0.98265±5 k_{eff}	
7	89	MCNPX-2.6e	0.98157±5 k_{eff}	
8	90-92	MCNPX-2.6e	0.98376±5 k_{eff}	
9	93-94	MCNPX-2.6e	0.98332±5 k_{eff}	
10	95	MCNPX-2.7a	0.98709±5 k_{eff}	

Table XI. Effective multiplication factor for configuration 5 (L = long detector and S = short detector) obtained from numerical simulations

Detector	Code	Multiplication Factor
None	MCNP-5.1.14	0.96386±5 k_{eff} Criticality Calculation
EC2BL	MCNPX-2.6b	0.96352±4 k_{eff} Criticality Calculation 0.94910 k_{eff} D-D Source Calculation (Area Method)
EC6TS	MCNPX-2.6b	0.96343±5 k_{eff} Criticality Calculation 0.96469 k_{eff} D-D Source Calculation (Area Method)

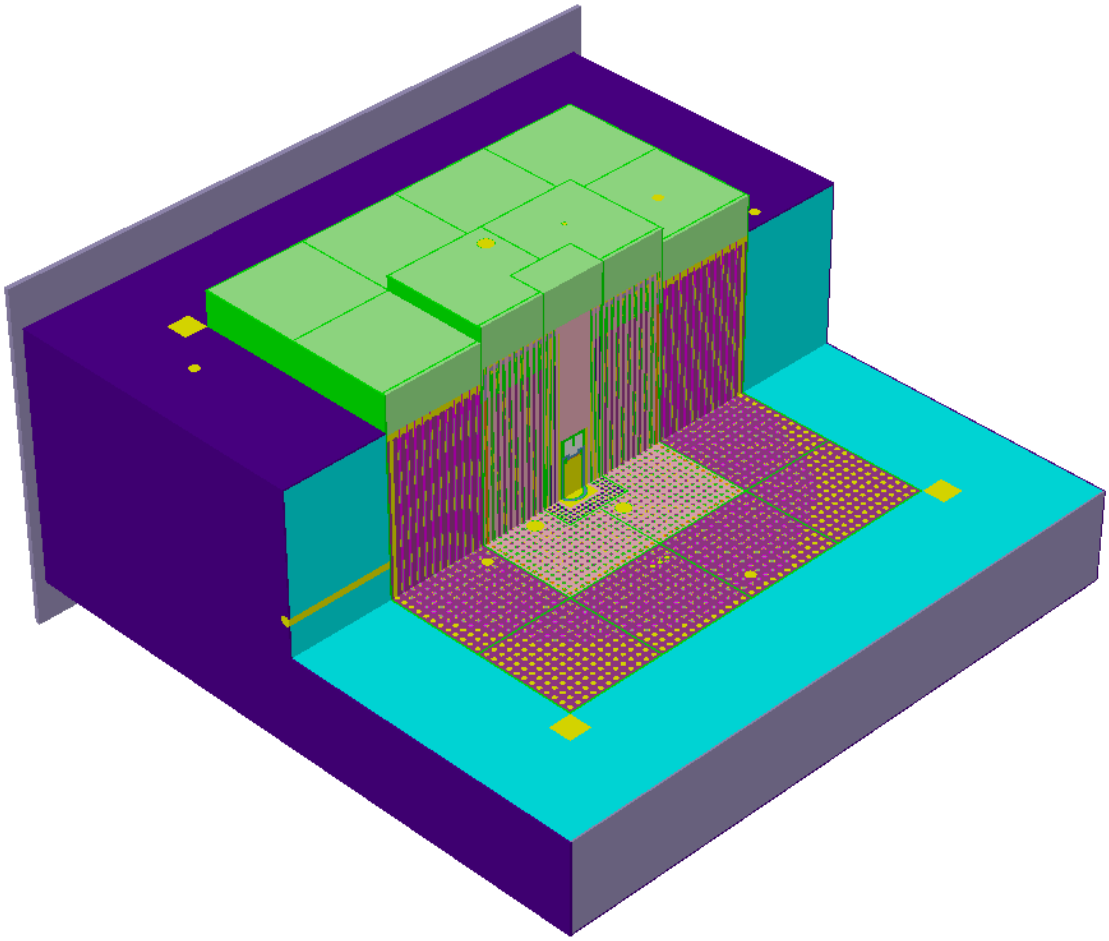

Figure 1. Three-dimensional view of YALINA Booster subcritical assembly

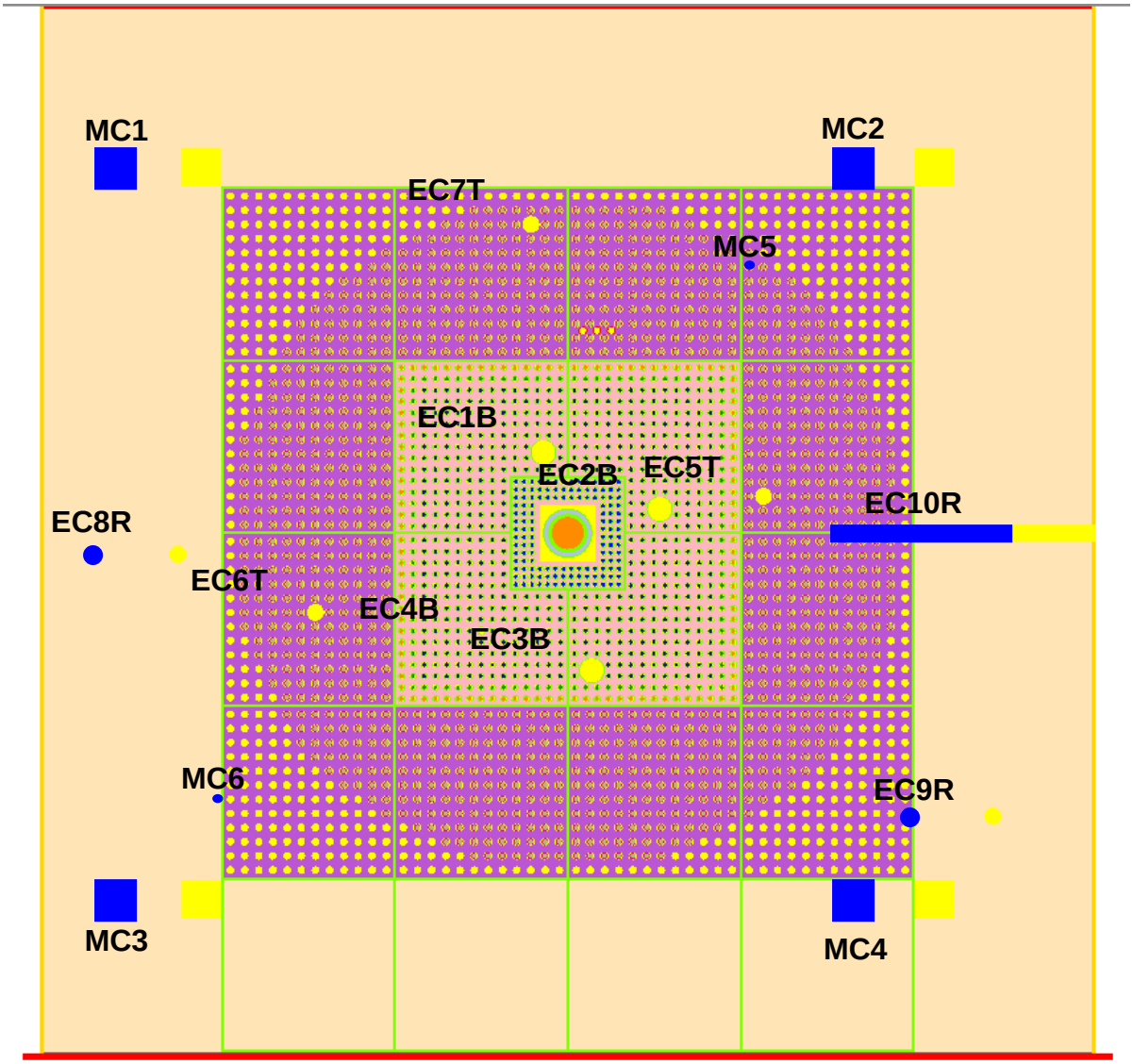

Figure 2. Horizontal section of YALINA Booster subcritical assembly with 90% fuel in the fast zone. Thermal fuel zone is moderated by polyethylene (purple color) loaded with EK10 fuel rods. Fast fuel zone is filled with lead matrix (pink color) loaded with 90%, 36%, or 21% enriched fuel

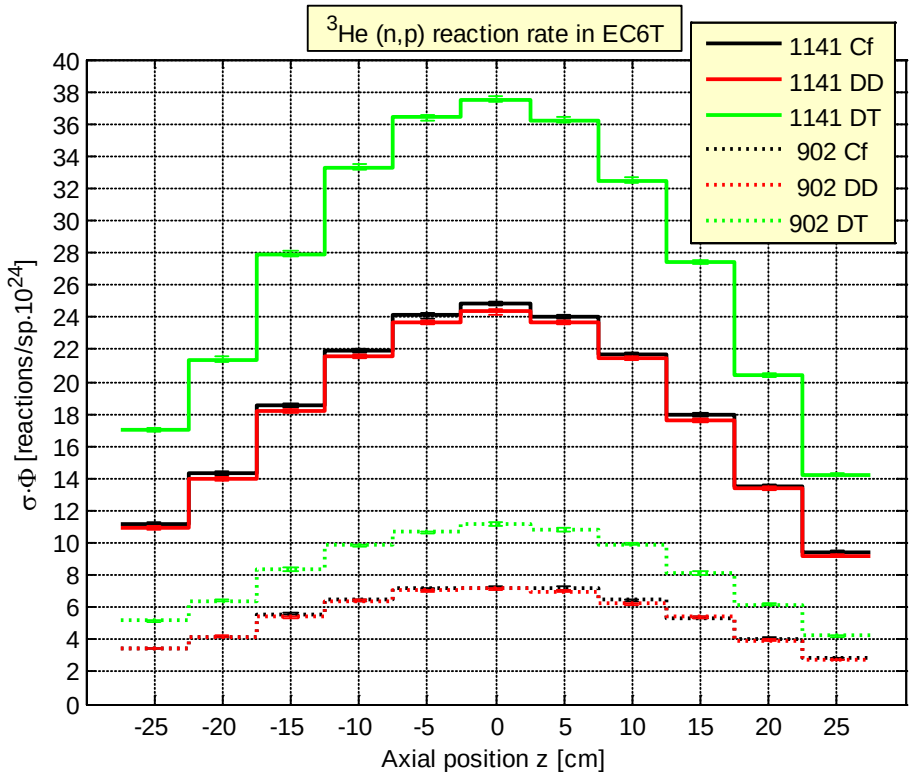

Figure 3. 3He(n,p) reaction rate in EC6T for 90% enriched fuel

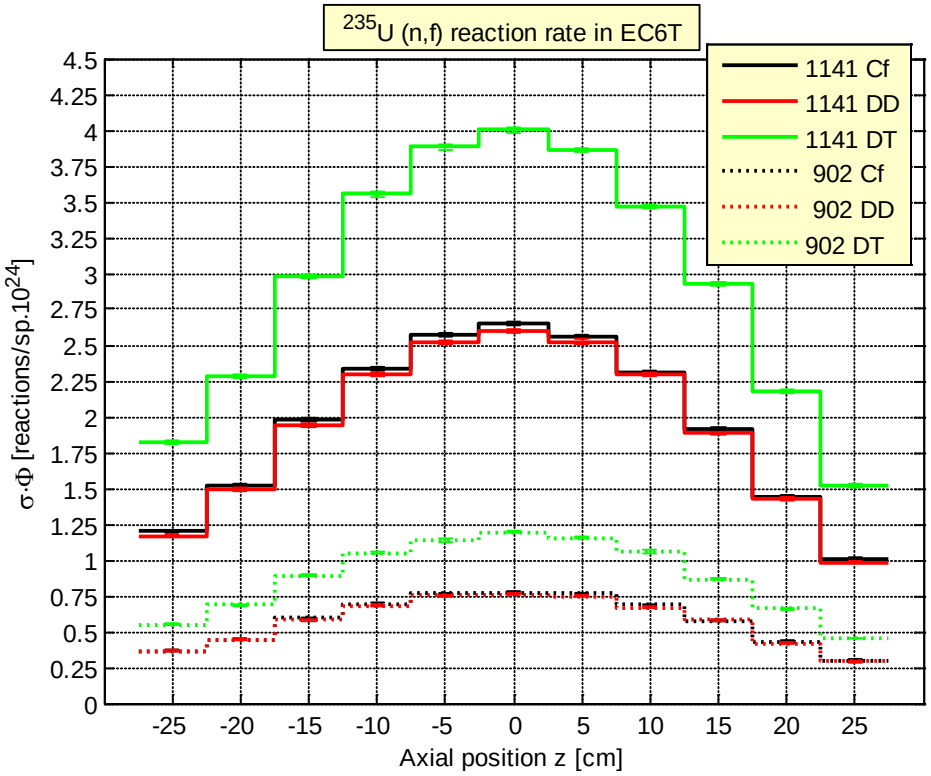

Figure 4. ^{235}U(n,f) reaction rate in EC6T for 90% enriched fuel

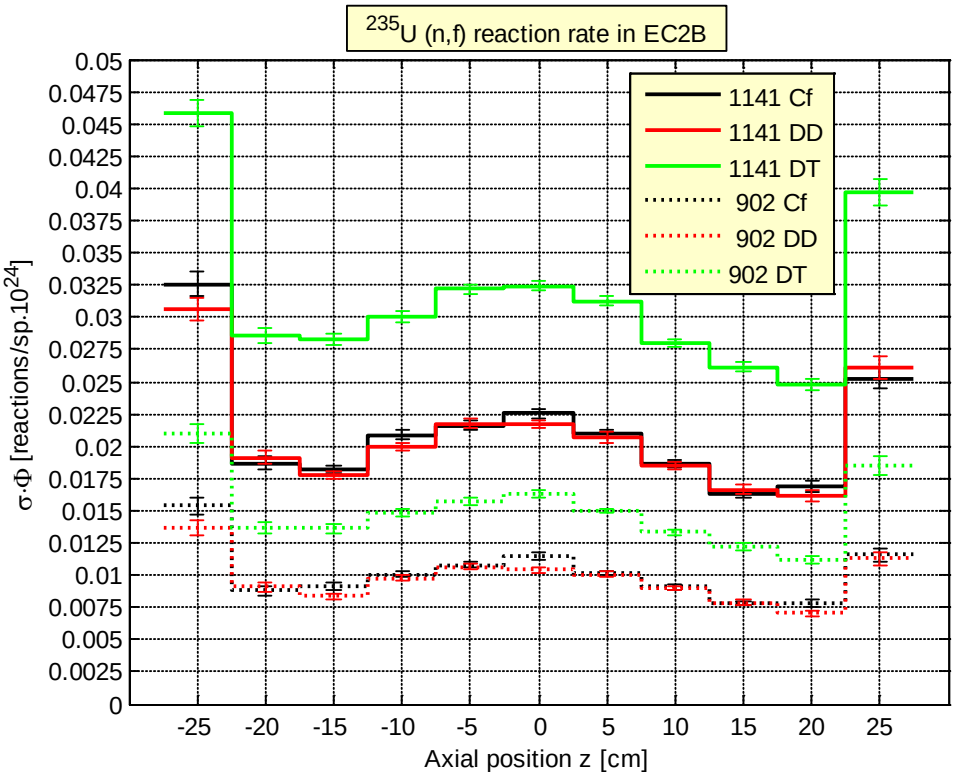

Figure 5. ^{235}U(n,f) reaction rate in EC2B for 90% enriched fuel

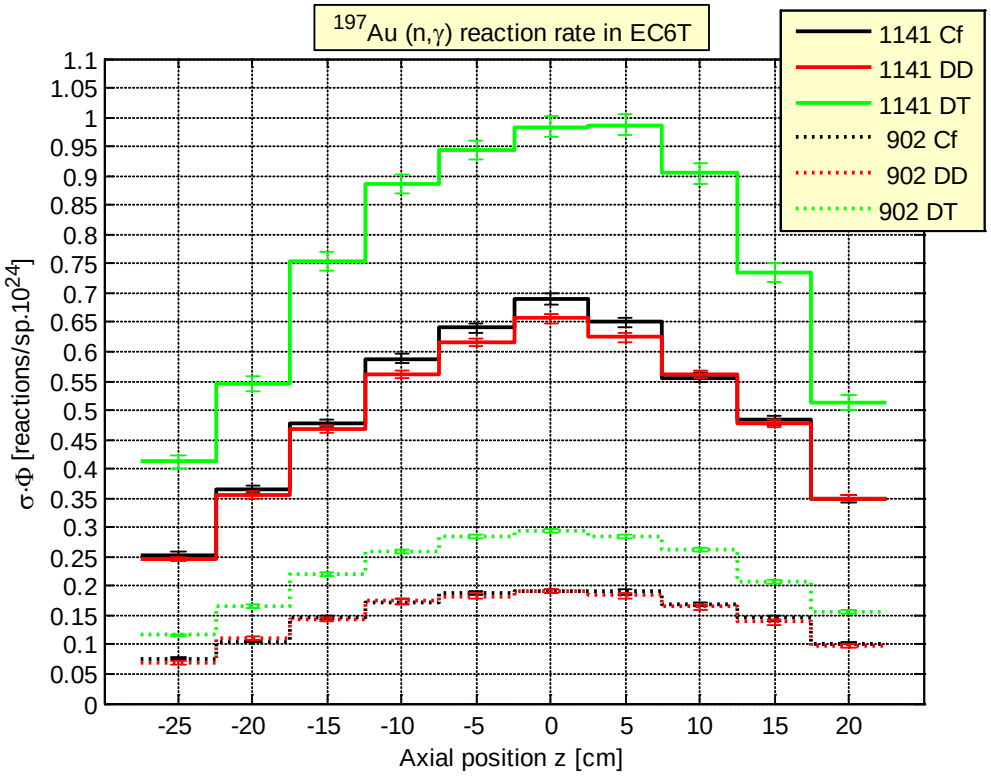

Figure 6. ^{197}Au(n,γ) reaction rate in EC6T for 90% enriched fuel

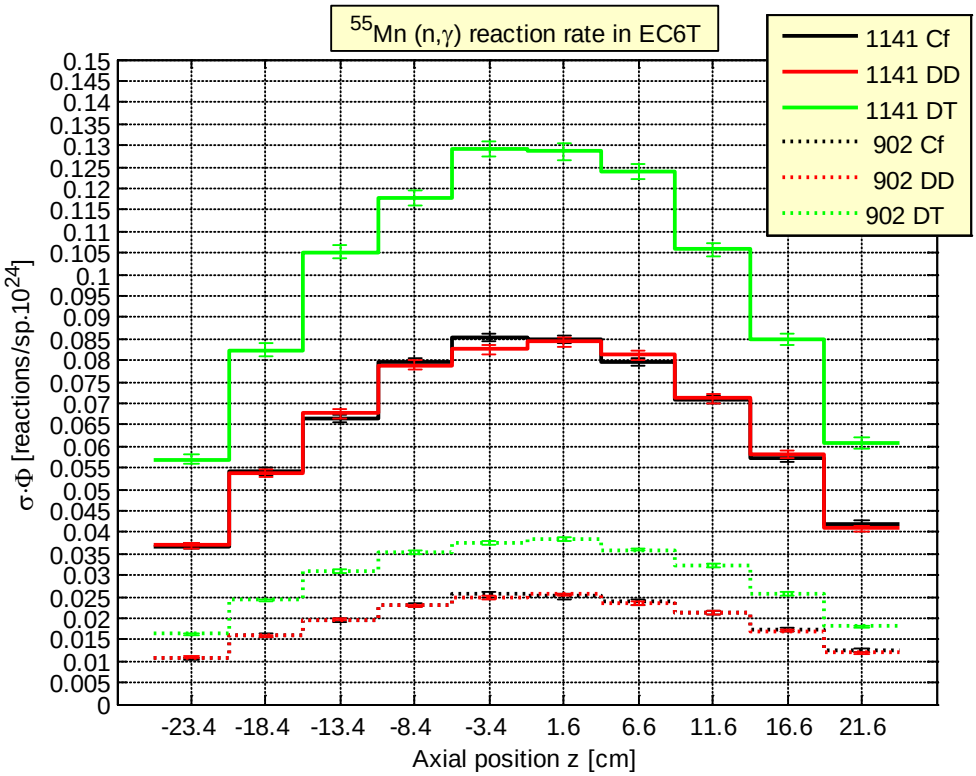

Figure 7. ^{55}Mn(n,γ) reaction rate in EC6T for 90% enriched fuel

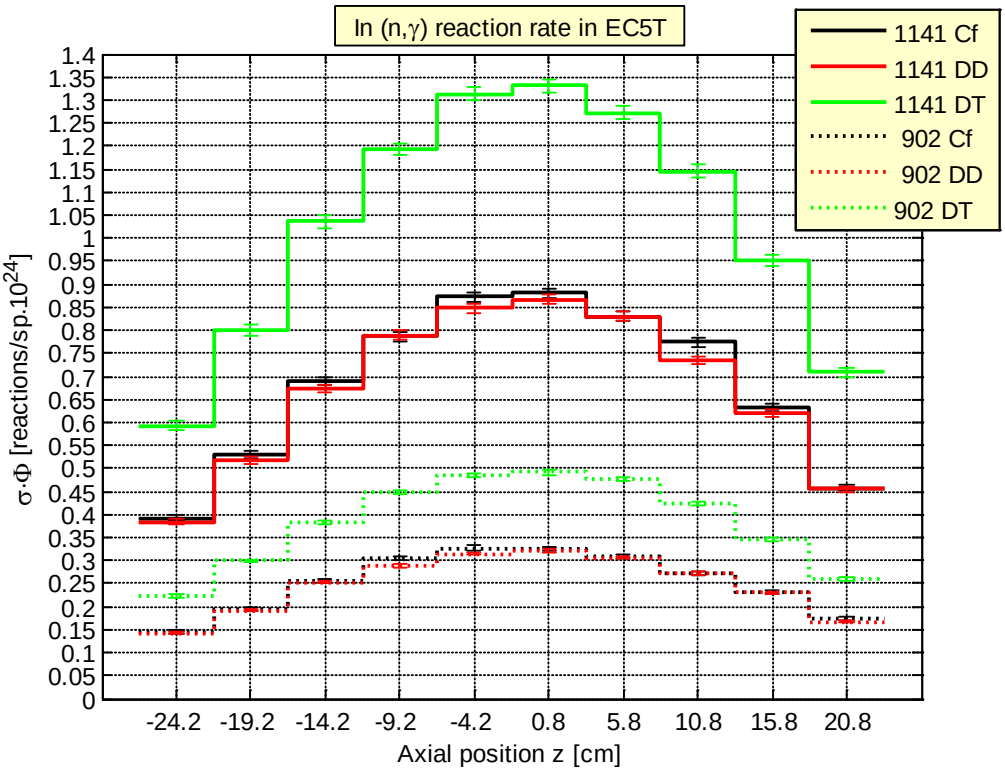

Figure 8. In(n,γ) reaction rate in EC5T for 90 enriched % fuel

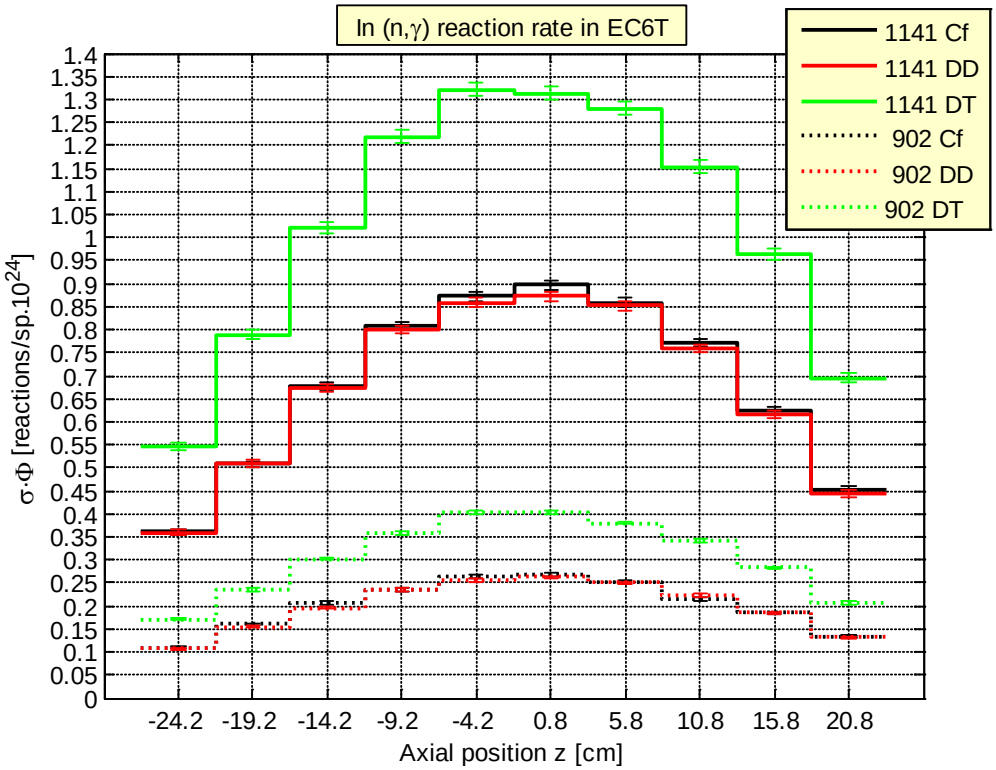

Figure 9. In(n,γ) reaction rate in EC6T for 90% enriched fuel

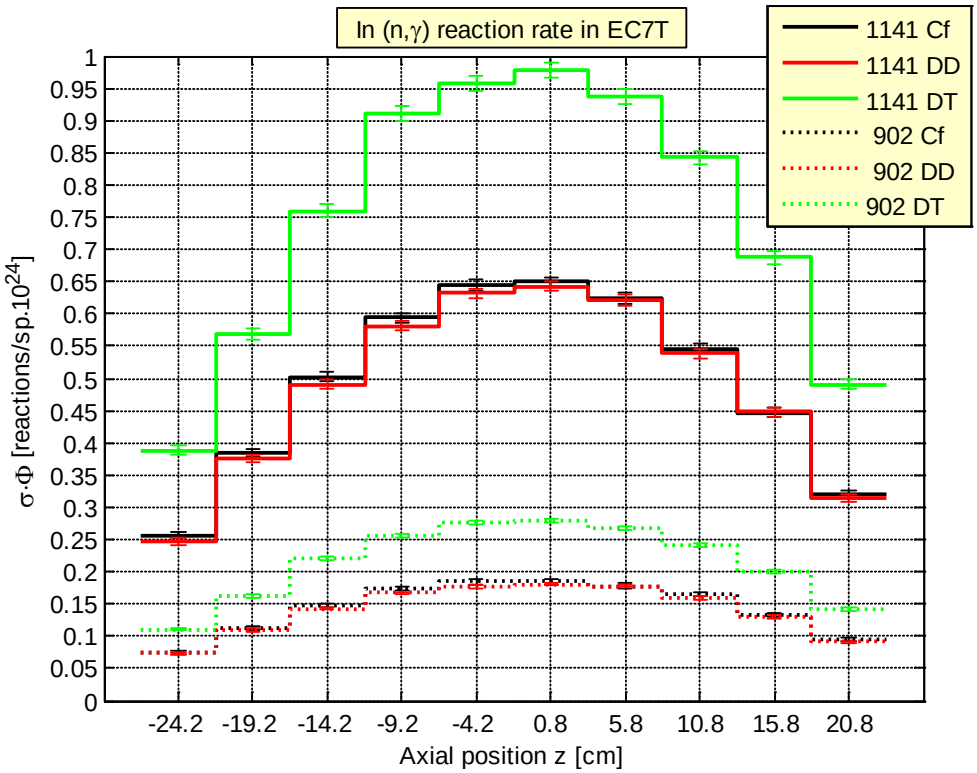

Figure 10. In(n,γ) reaction rate in EC7T for 90% enriched fuel

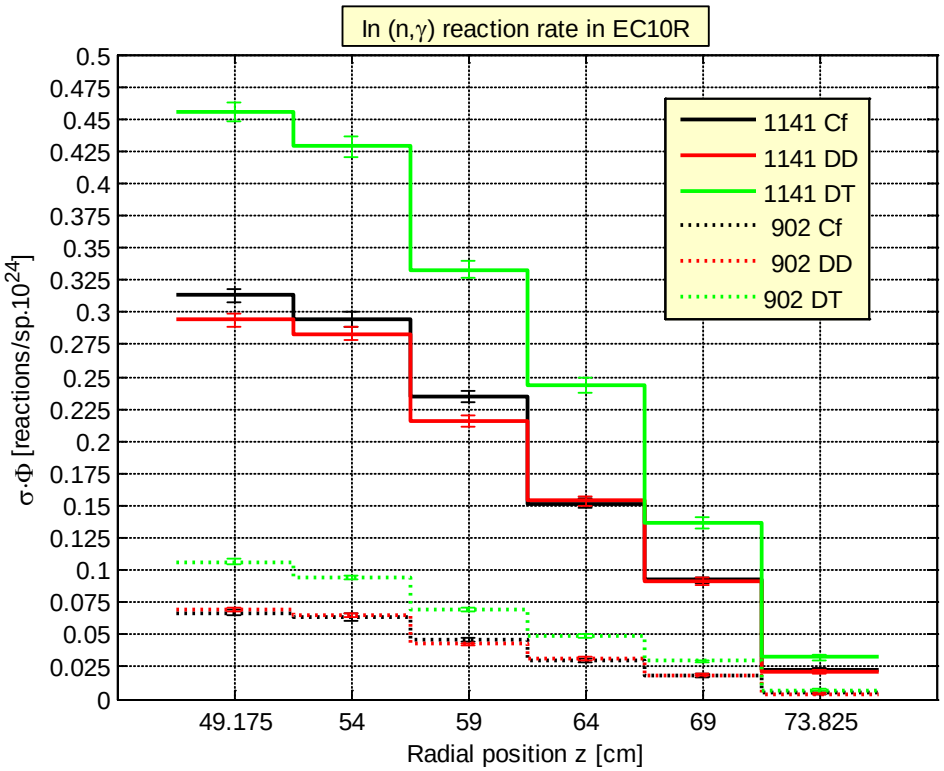

Figure 11. In(n,γ) reaction rate in EC10R for 90% enriched fuel

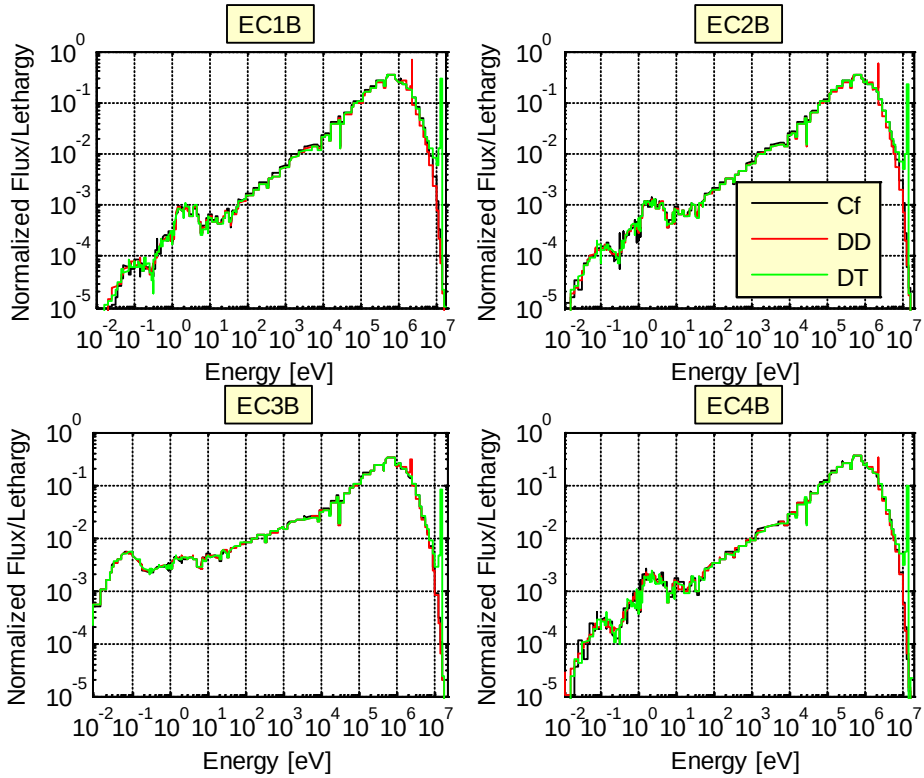

Figure 12. Neutron spectrum in fast zone for 90% enriched fuel and 902 fuel rod configuration

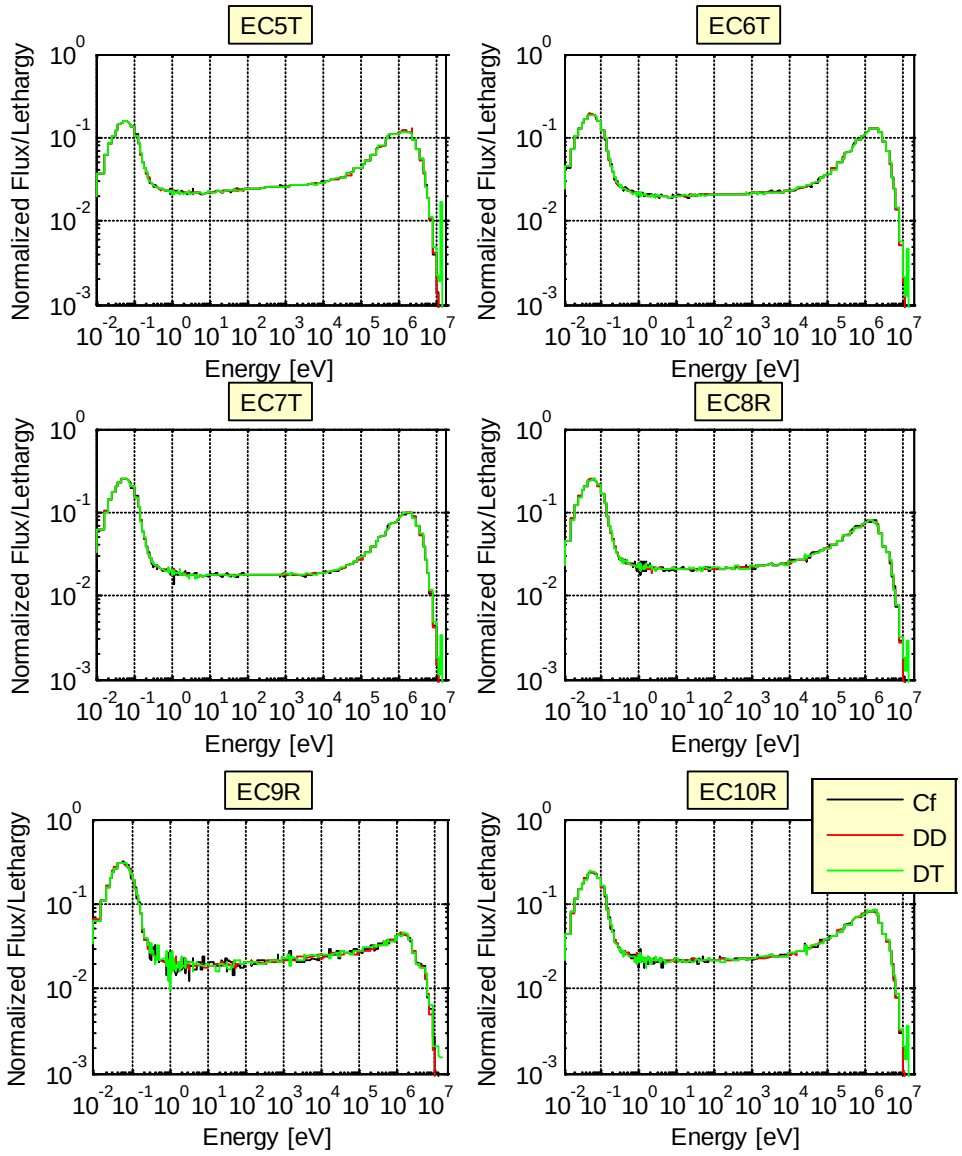

Figure 13. Neutron spectrum in thermal and reflector zones for 90% enriched fuel and 902 fuel rod configuration

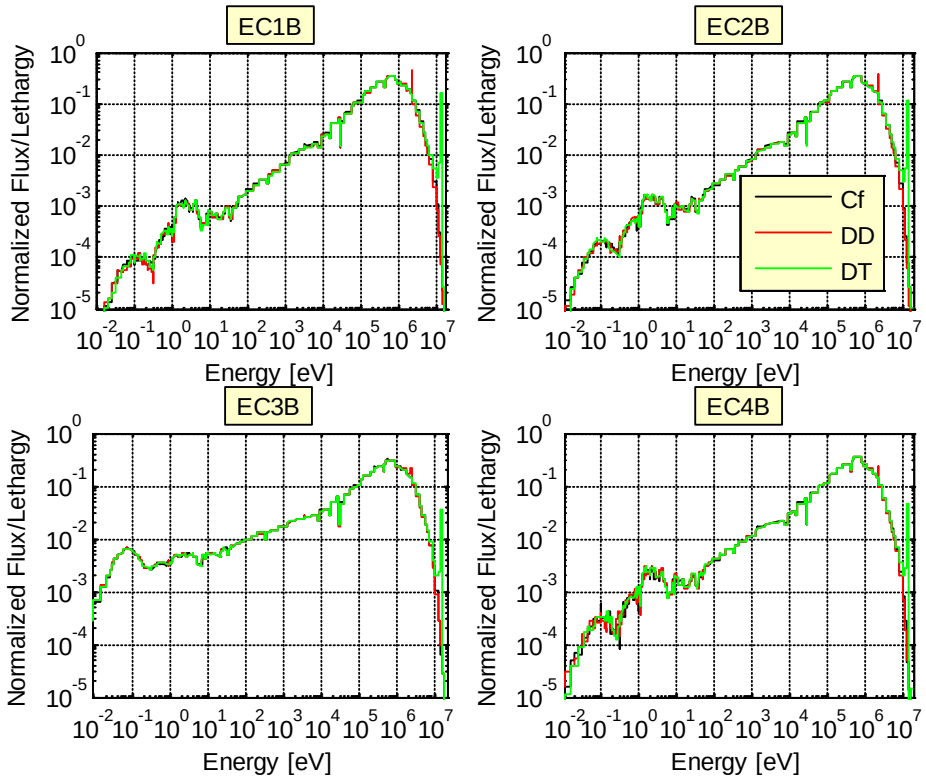

Figure 14. Neutron spectrum in fast zone for 90% enriched fuel and 1141 fuel rod configuration

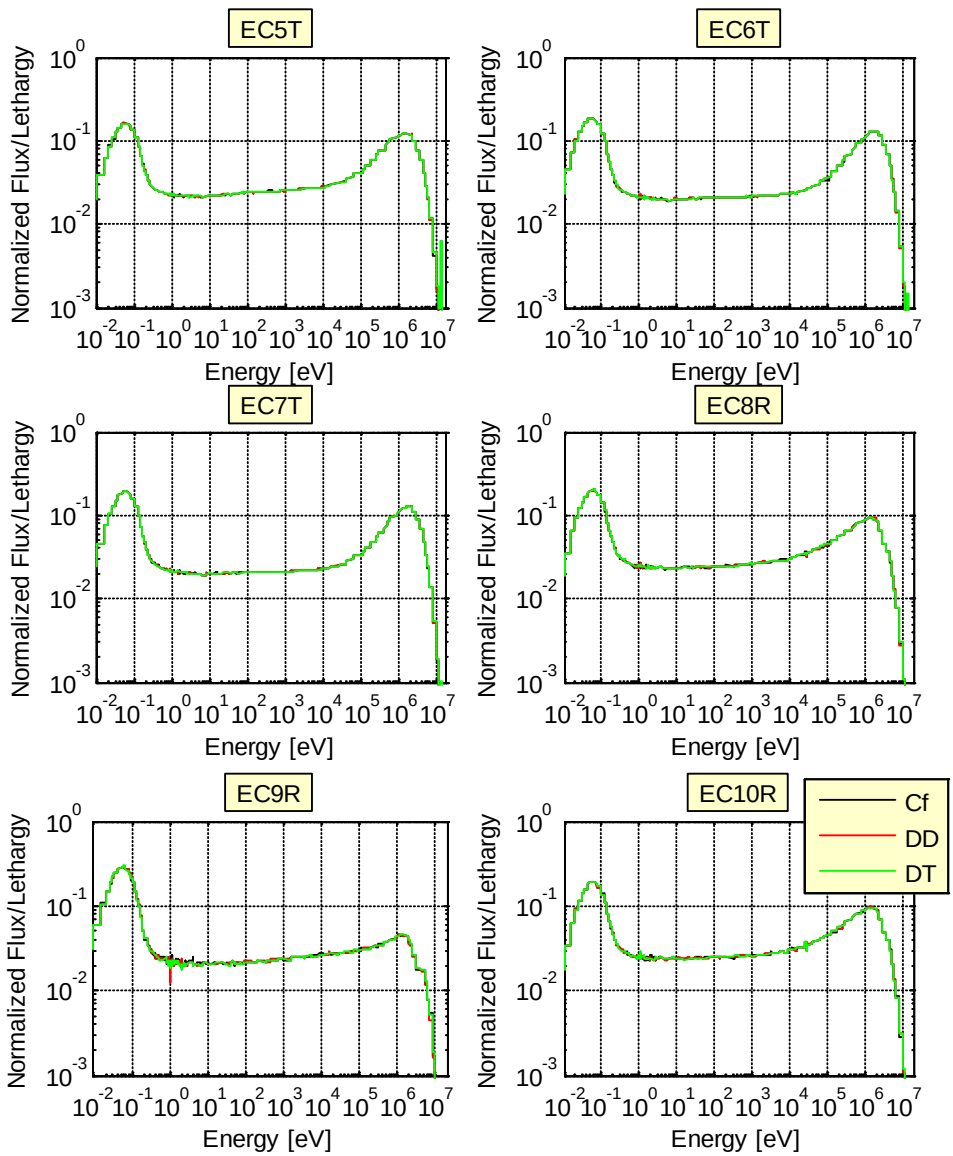

Figure 15. Neutron spectrum in thermal and reflector zones for 90% enriched fuel and 1141 fuel rod configuration

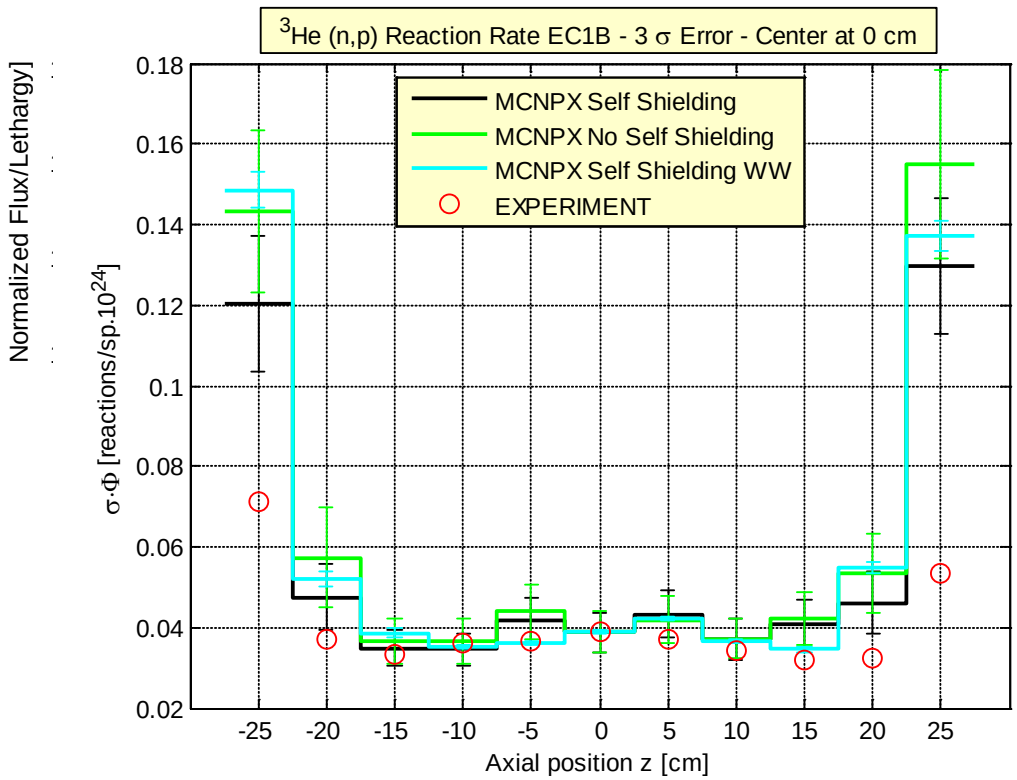

Figure 16. ^{3}He(n,p) reaction rate in EC1B for 90% enriched fuel and Cf source

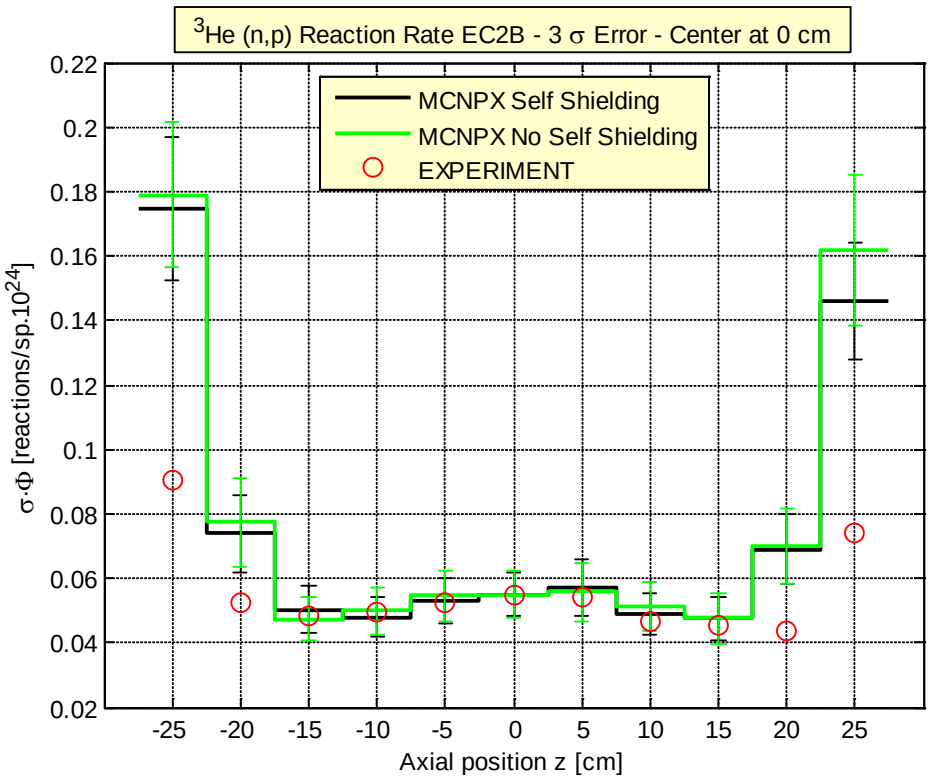

Figure 17. ^{3}He(n,p) reaction rate in EC2B for 90% enriched fuel and Cf source

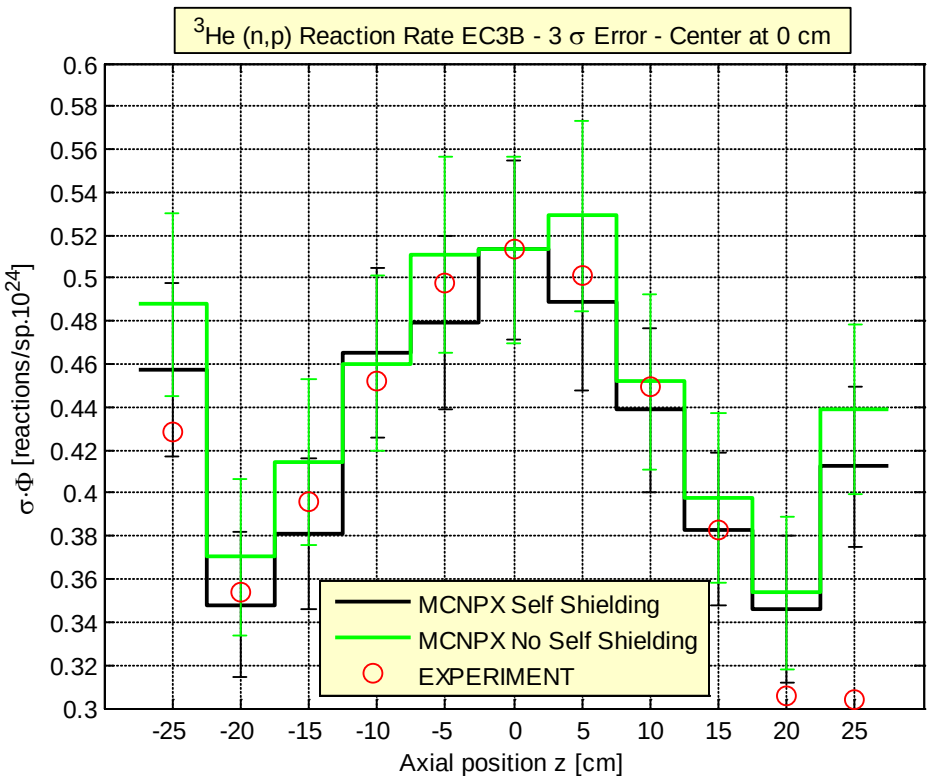

Figure 18. ^{3}He(n,p) reaction rate in EC3B for 90% enriched fuel and Cf source

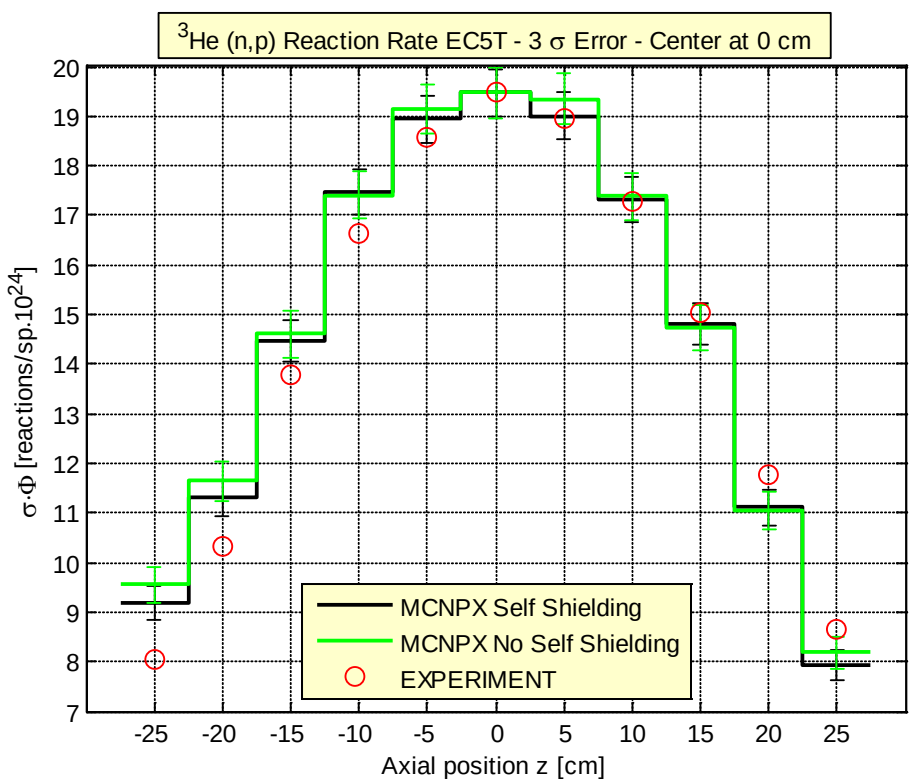

Figure 19. ^{3}He(n,p) reaction rate in EC5T for 90% enriched fuel and Cf source

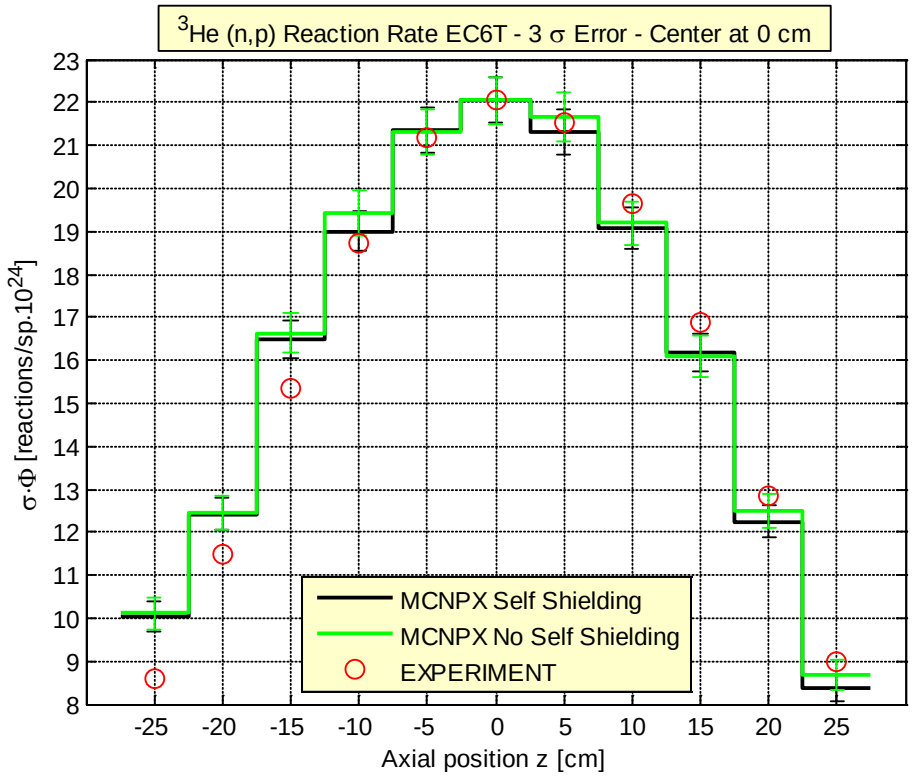

Figure 20. ^{3}He(n,p) reaction rate in EC6T for 90% enriched fuel and Cf source

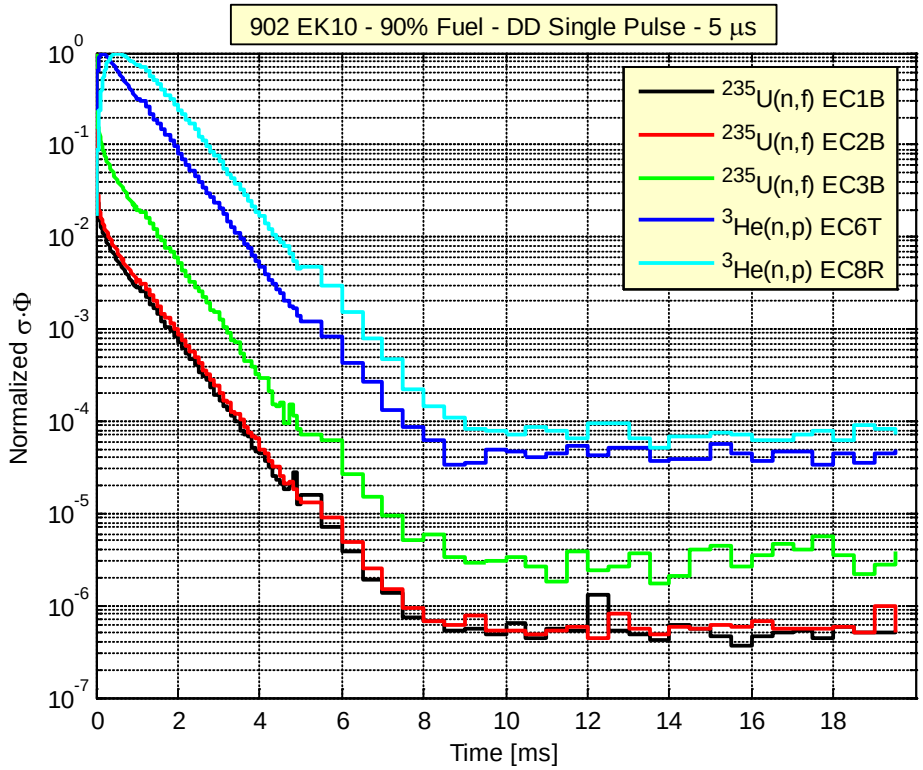

Figure 21. Normalized reaction rates for 90% enriched fuel, D-D neutron source, and 902 EK10 fuel rods

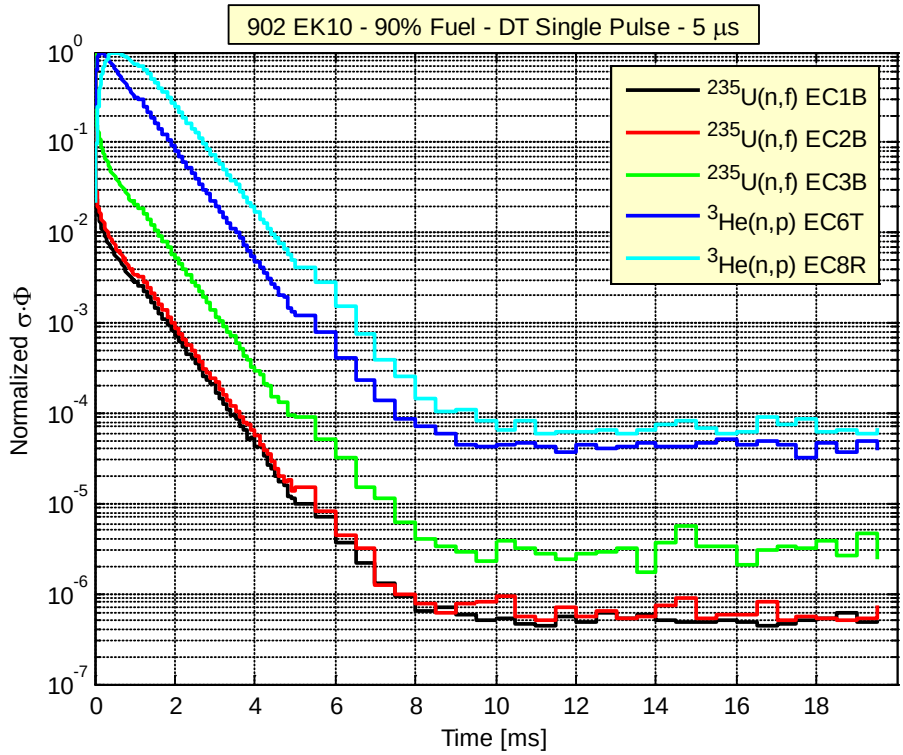

Figure 22. Normalized reaction rates for 90% enriched fuel, D-T neutron source, and 902 EK10 fuel rods

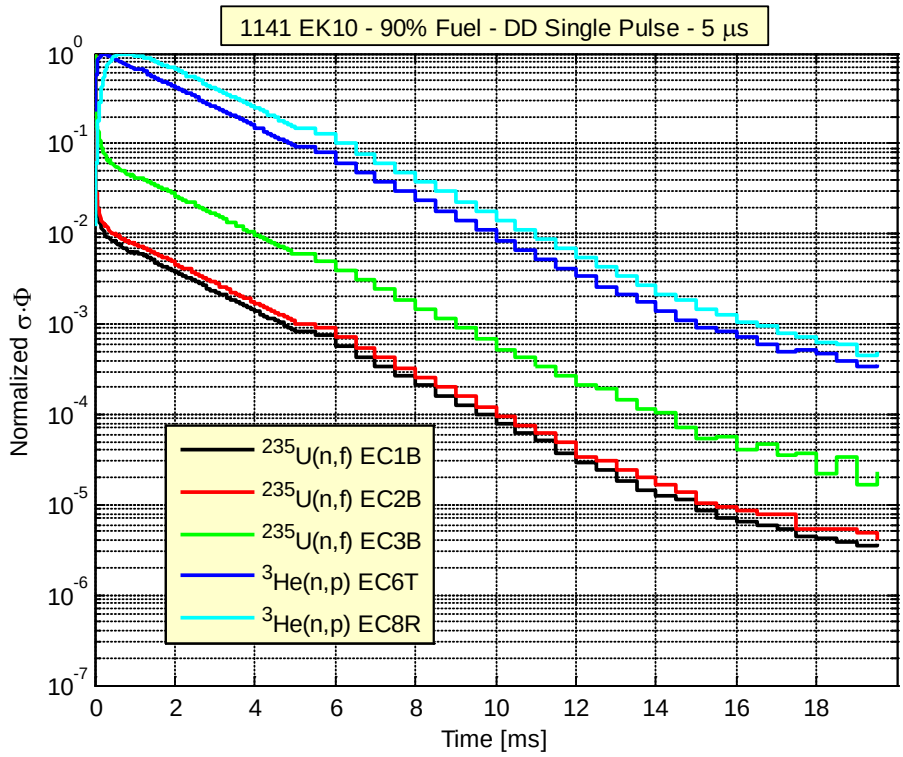

Figure 23. Normalized reaction rates for 90% enriched fuel, D-D neutron source, and 1141 EK10 fuel rods

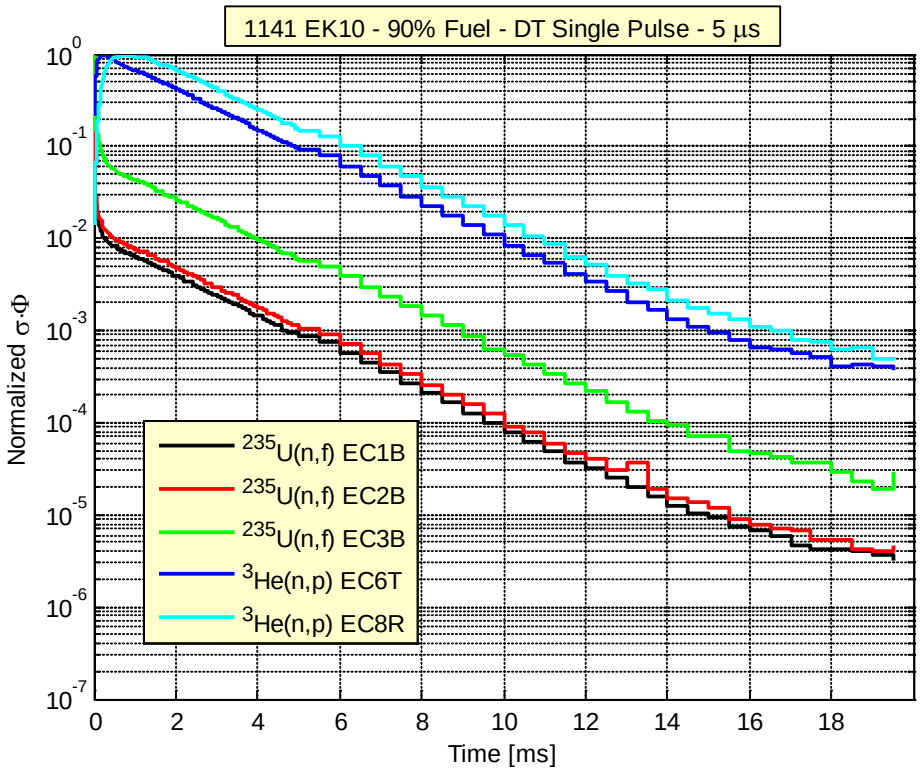

Figure 24. Normalized reaction rates for 90% enriched fuel, D-T neutron source, and 1141 EK10 fuel rods

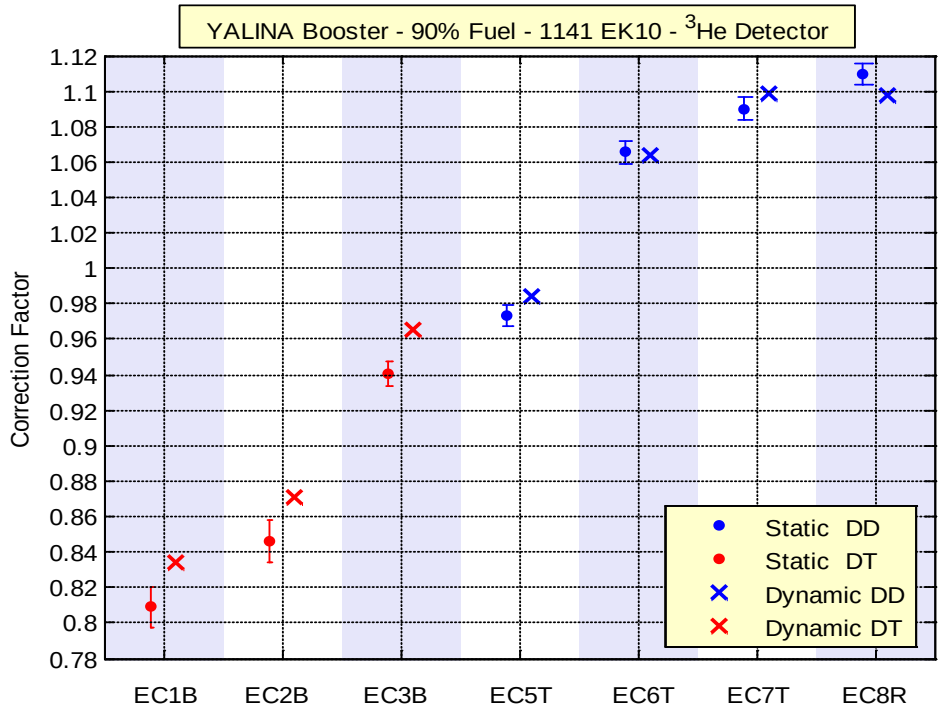

Figure 25. Correction factor on reactivity for 90% enriched fuel

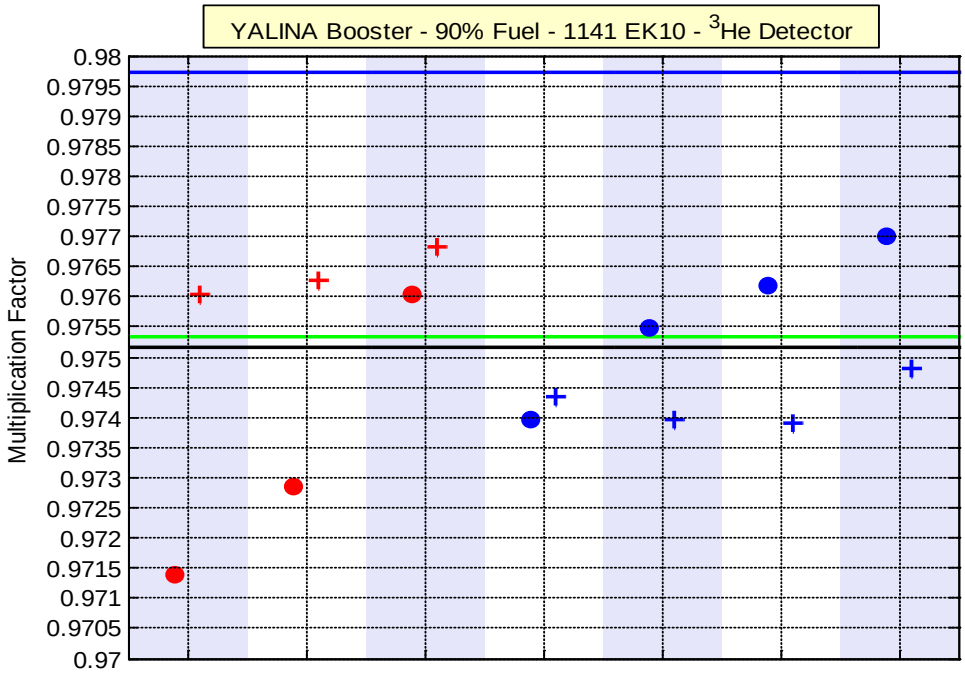

Figure 26. Corrected and uncorrected experimental multiplication factors and MCNPX multiplication factor obtained by criticality calculations for 90% enriched fuel configuration; the experimental reactivity has been corrected by the dynamic correction factor

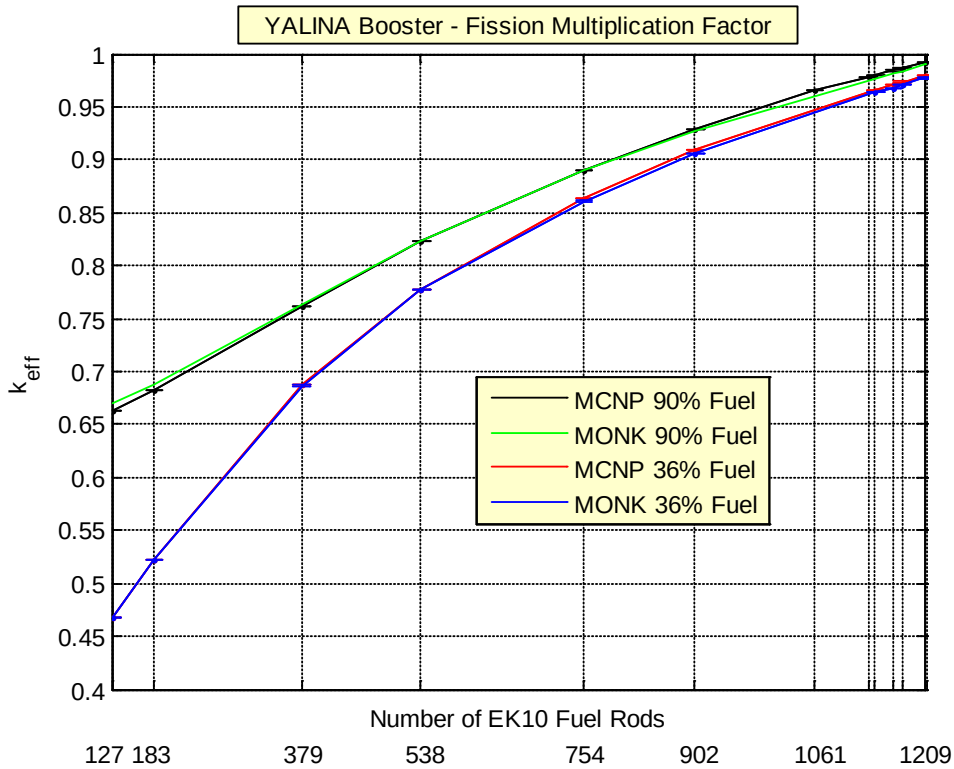

Figure 27. k_{eff} calculated by MONK and MCNPX as function of EK10 rod numbers for 90 and 36% enriched fuels

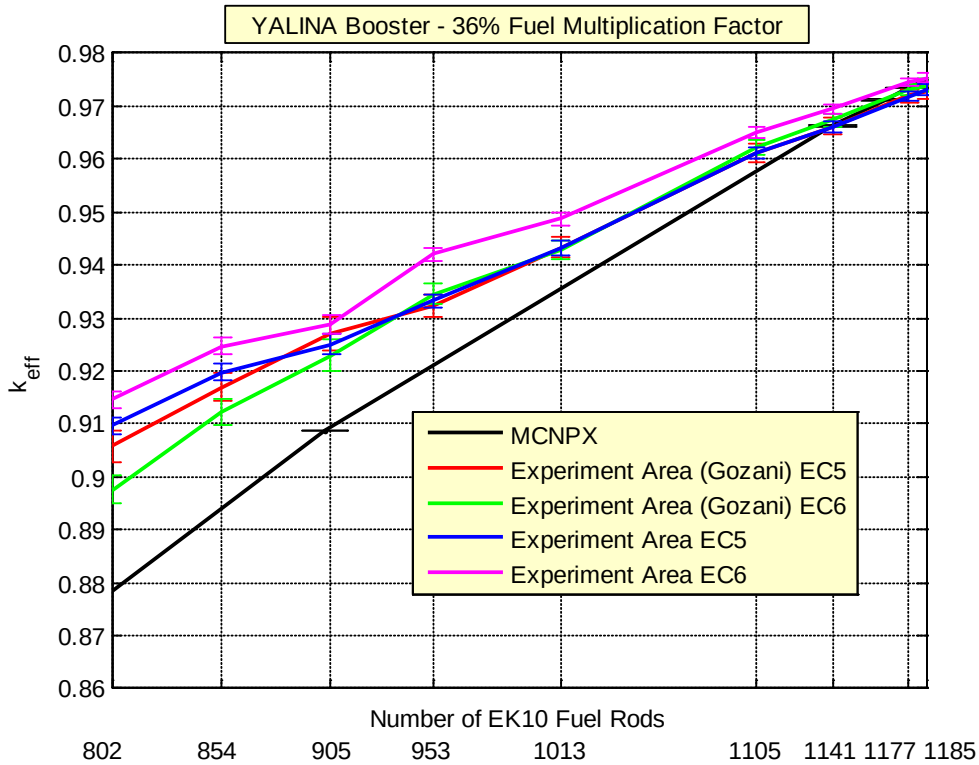

Figure 28. k_{eff} calculated by MCNPX and from experimental measurements as function of EK10 rods; long detectors (EC5T and EC6T; EC6T and EC7T)

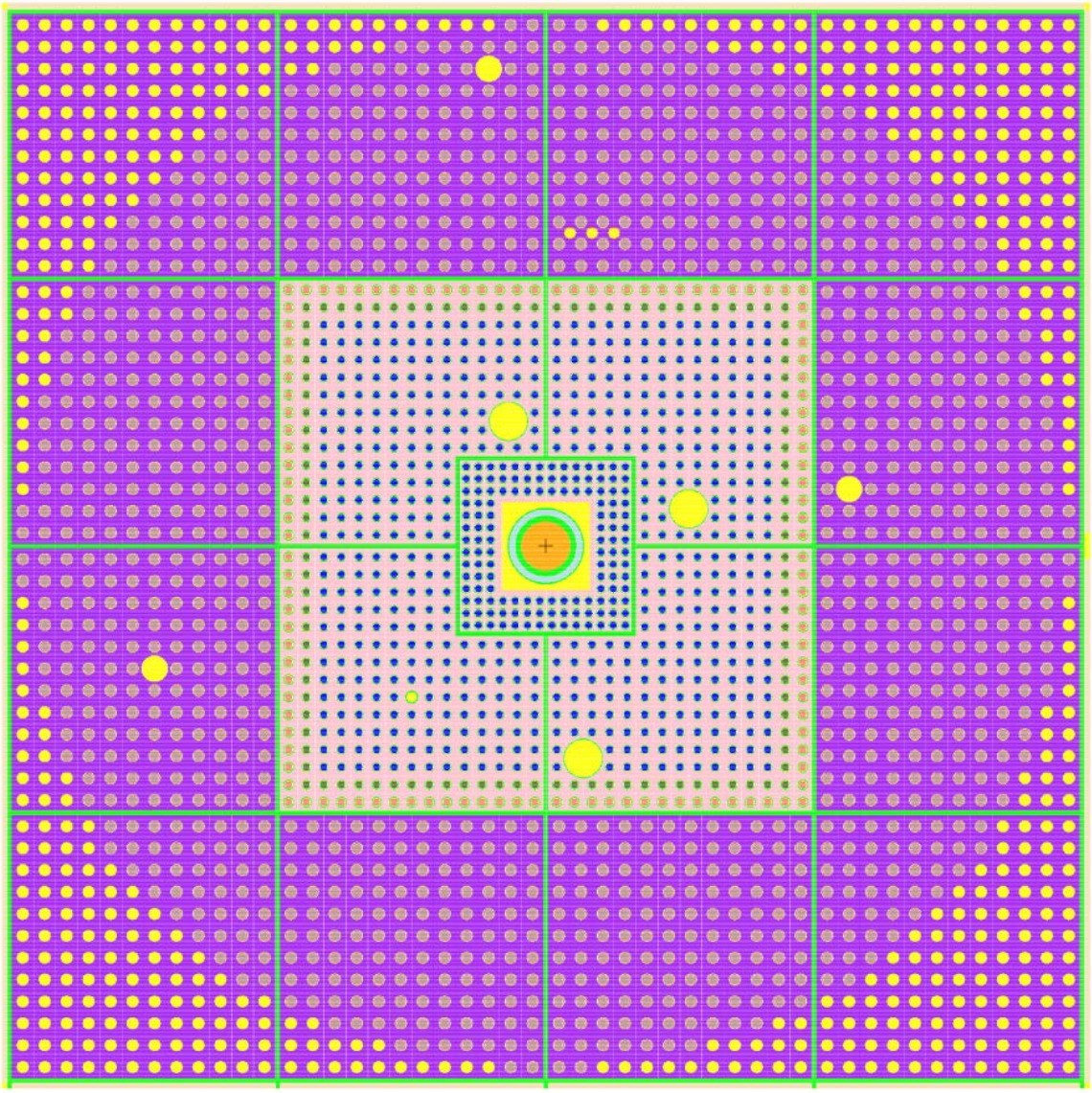

Figure 29. Horizontal section of the fuel zone of YALINA Booster assembly with 36% enriched fuel in fast zone and 1185 EK10 fuel rods in thermal zone

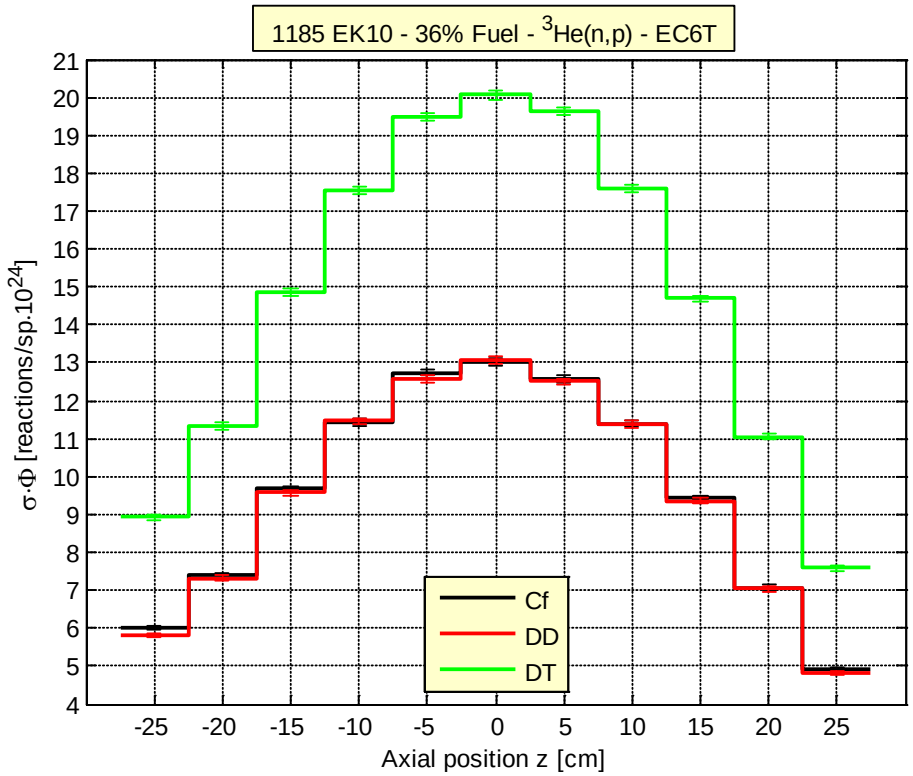

Figure 30. ^{3}He(n,p) reaction rate in EC6T for 36% enriched fuel

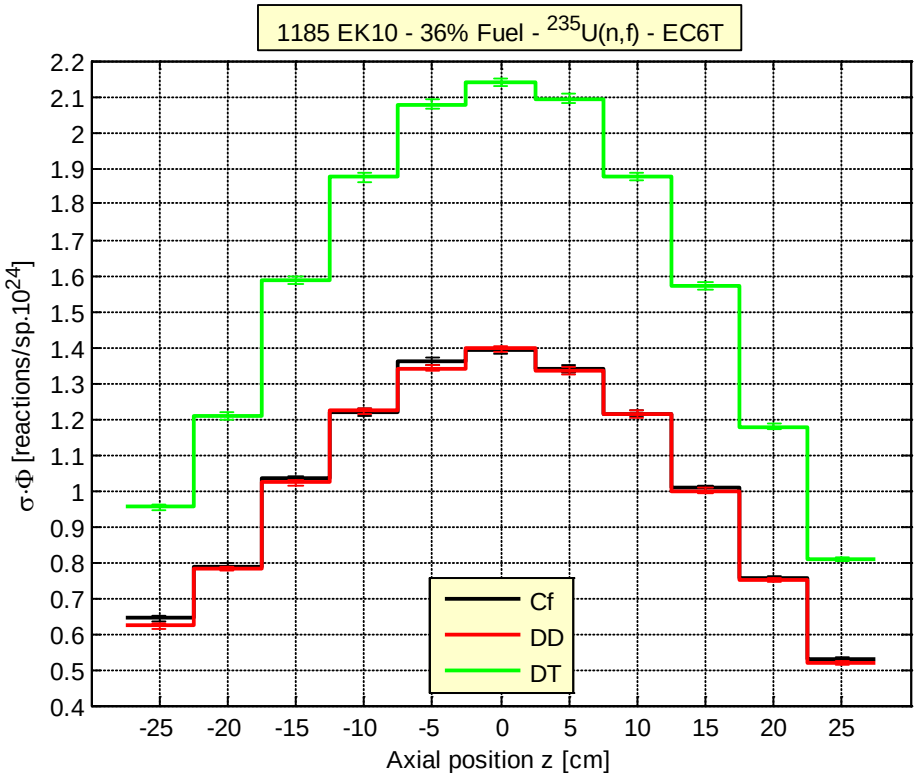

Figure 31. ^{235}U(n,f) reaction rate in EC6T for 36% enriched fuel

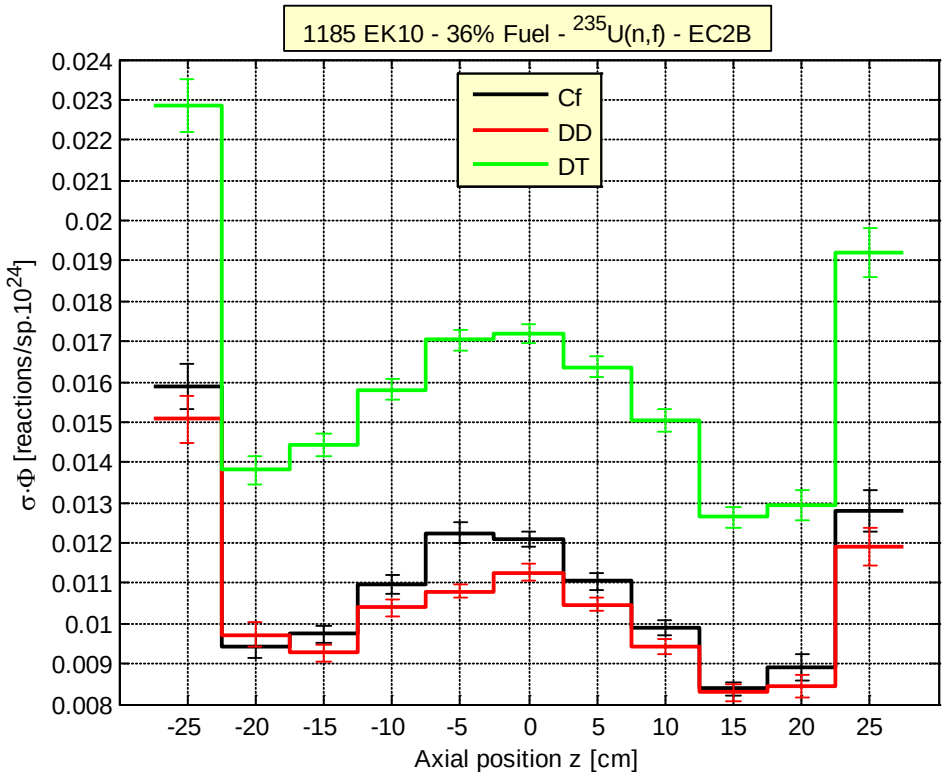

Figure 32. ^{235}U(n,f) reaction rate in EC2B for 36% enriched fuel

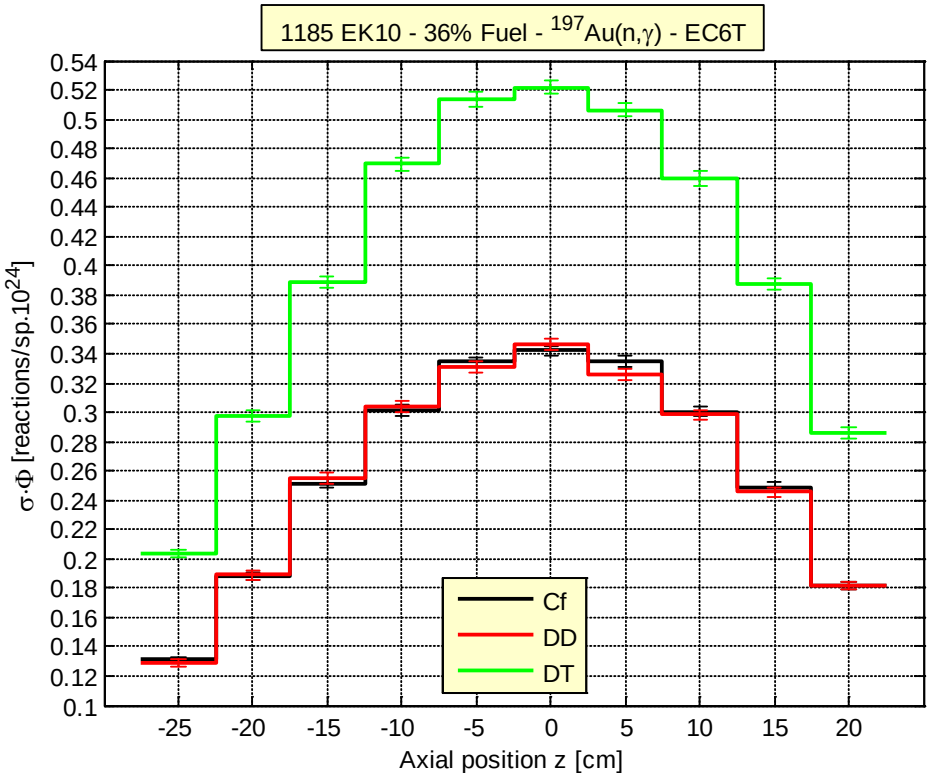

Figure 33. ^{197}Au(n,γ) reaction rate in EC6T for 36% enriched fuel

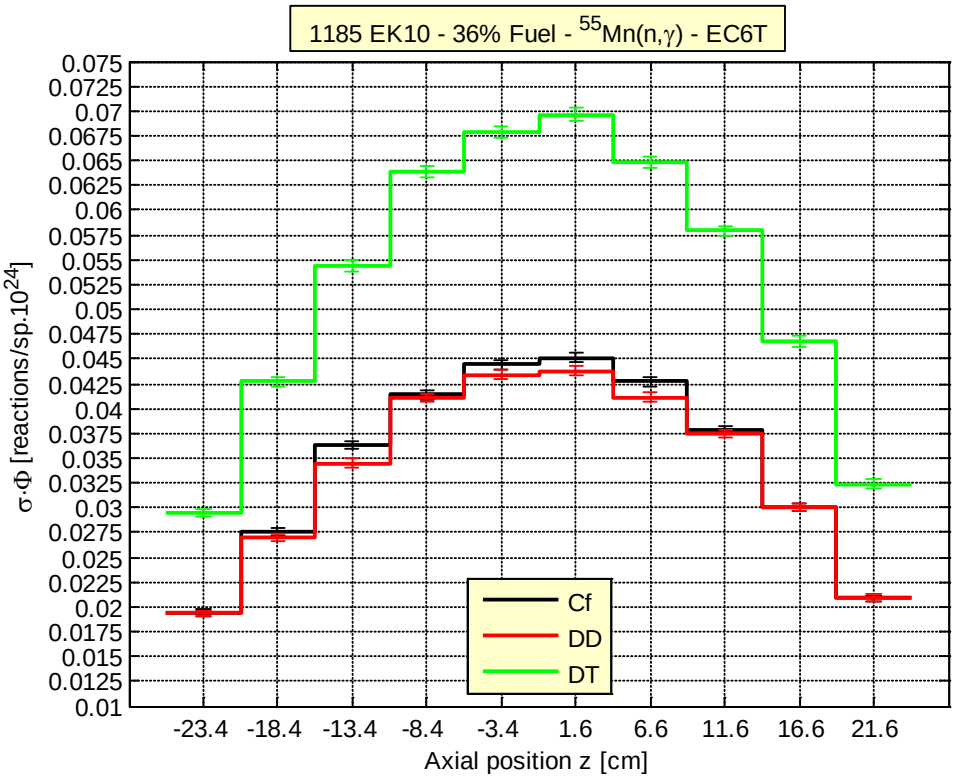

Figure 34. ^{55}Mn(n,γ) reaction rate in EC6T for 36% enriched fuel

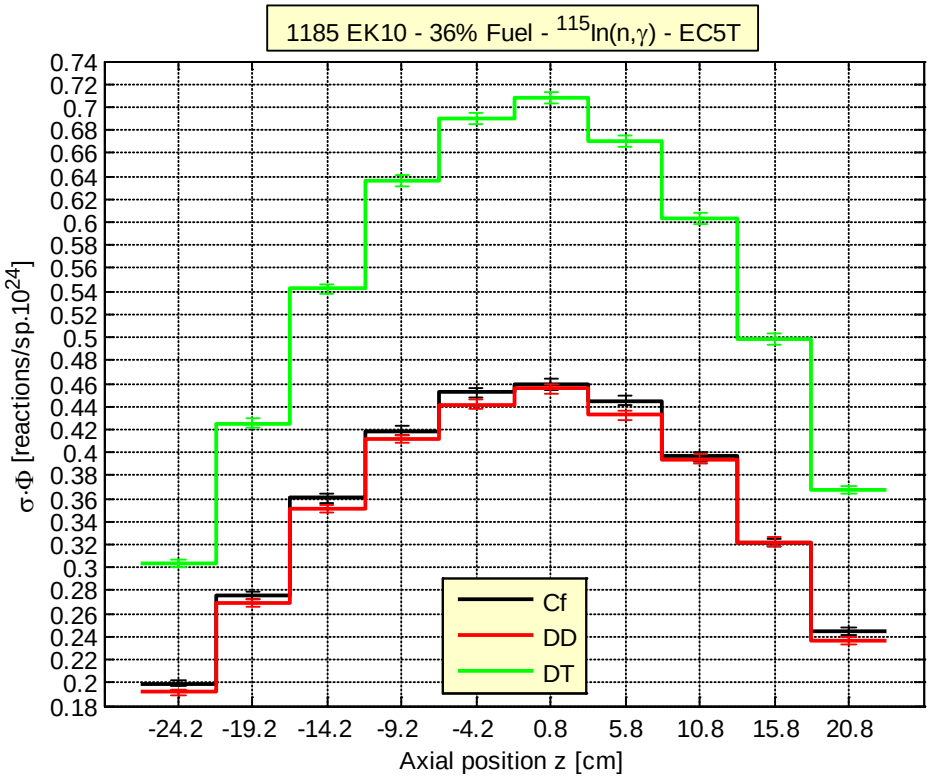

Figure 35. ^{115}In(n,γ) reaction rate in EC5T for 36% enriched fuel

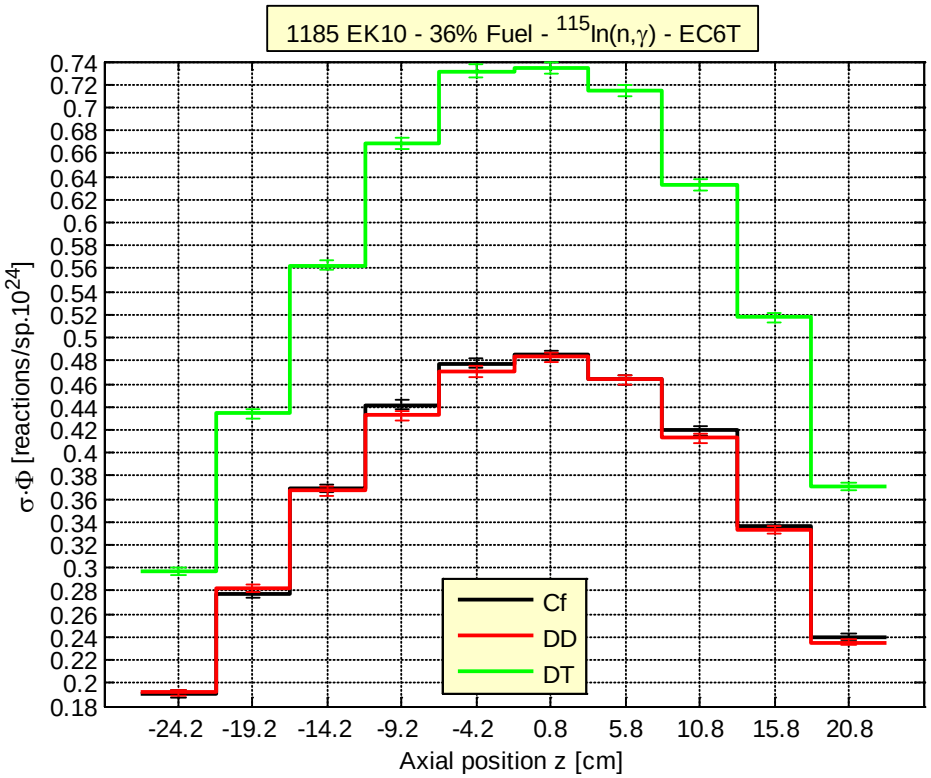

Figure 36. ^{115}In(n,γ) reaction rate in EC6T for 36% enriched fuel

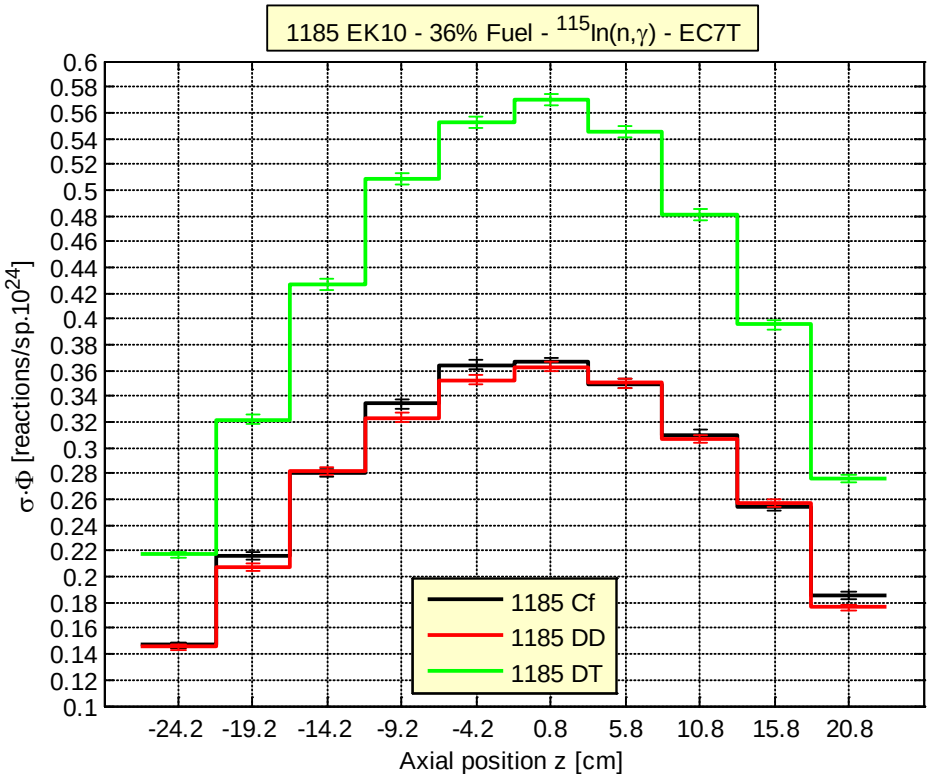

Figure 37. ^{115}In(n,γ) reaction rate in EC7T for 36% enriched fuel

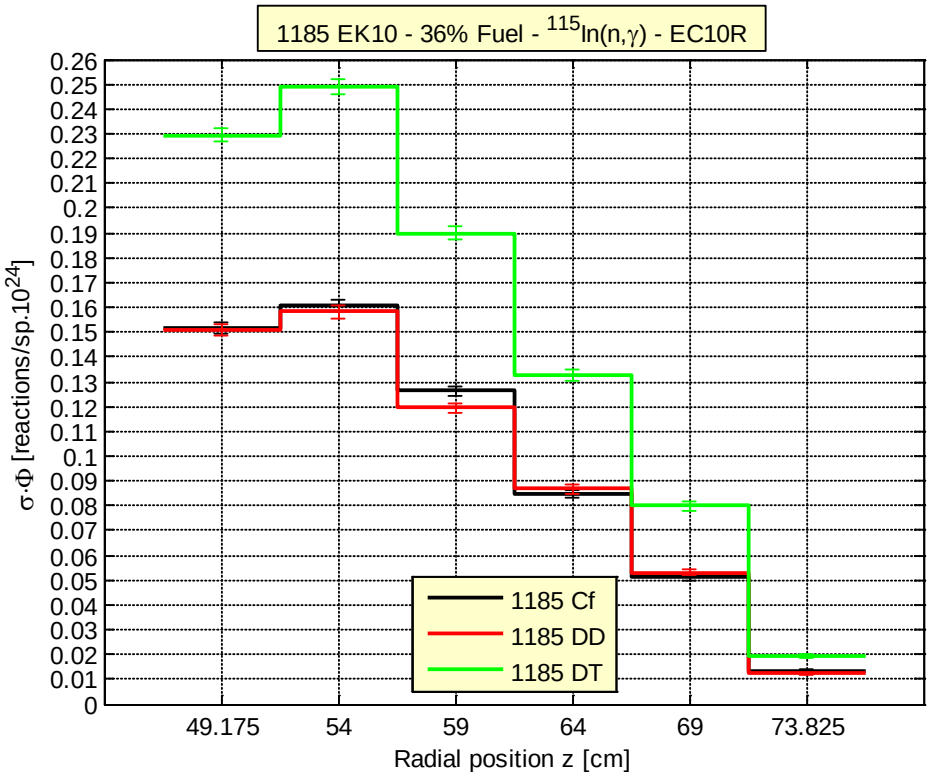

Figure 38. ^{115}In(n,γ) reaction rate in EC10R for 36% enriched fuel

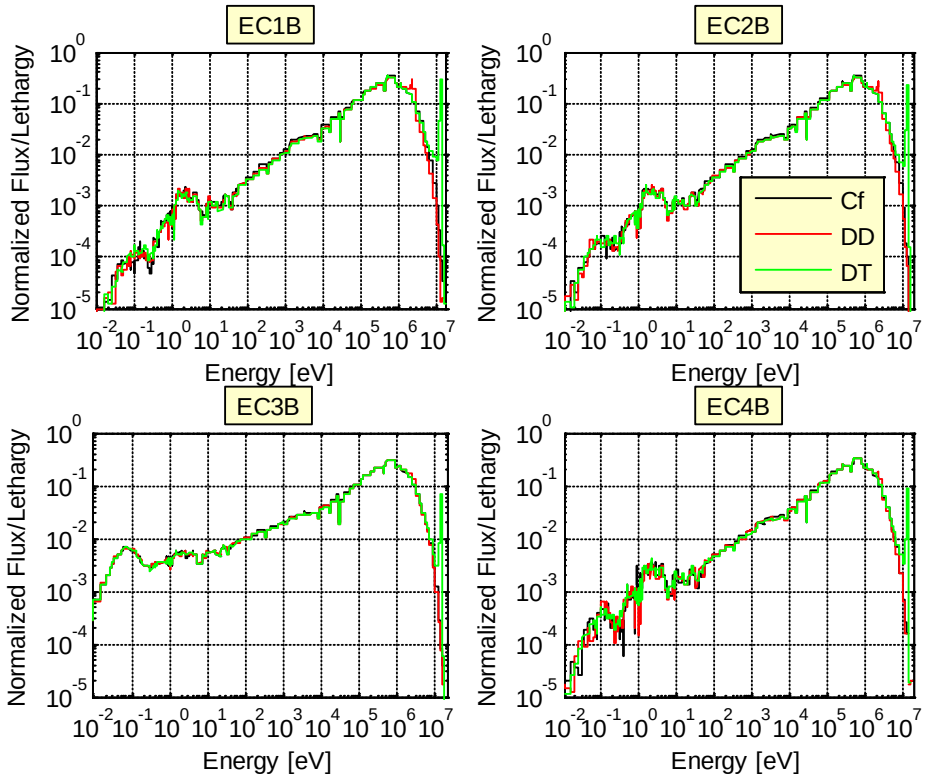

Figure 39. Neutron spectrum in fast zone for 36% enriched fuel

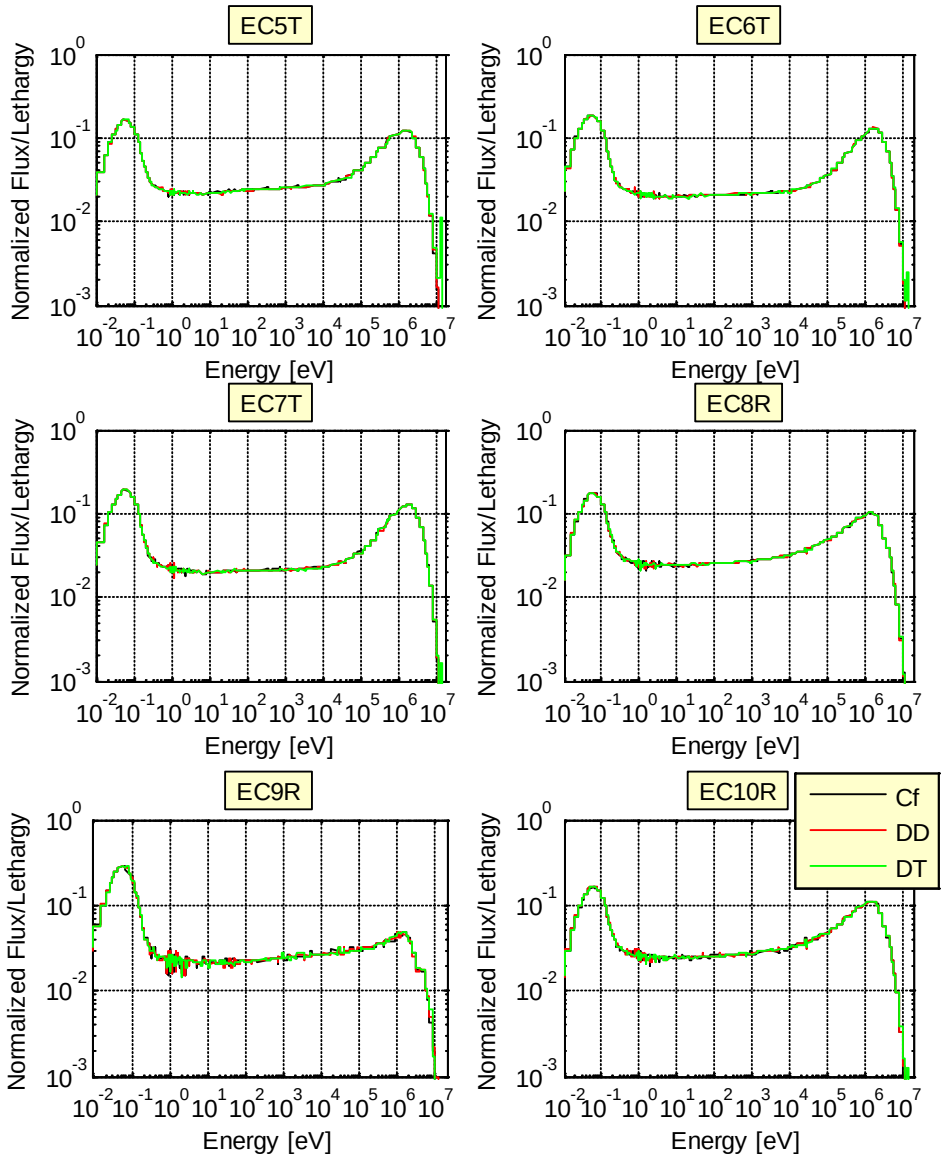

Figure 40. Neutron spectrum in thermal and reflector zones for 36% enriched fuel

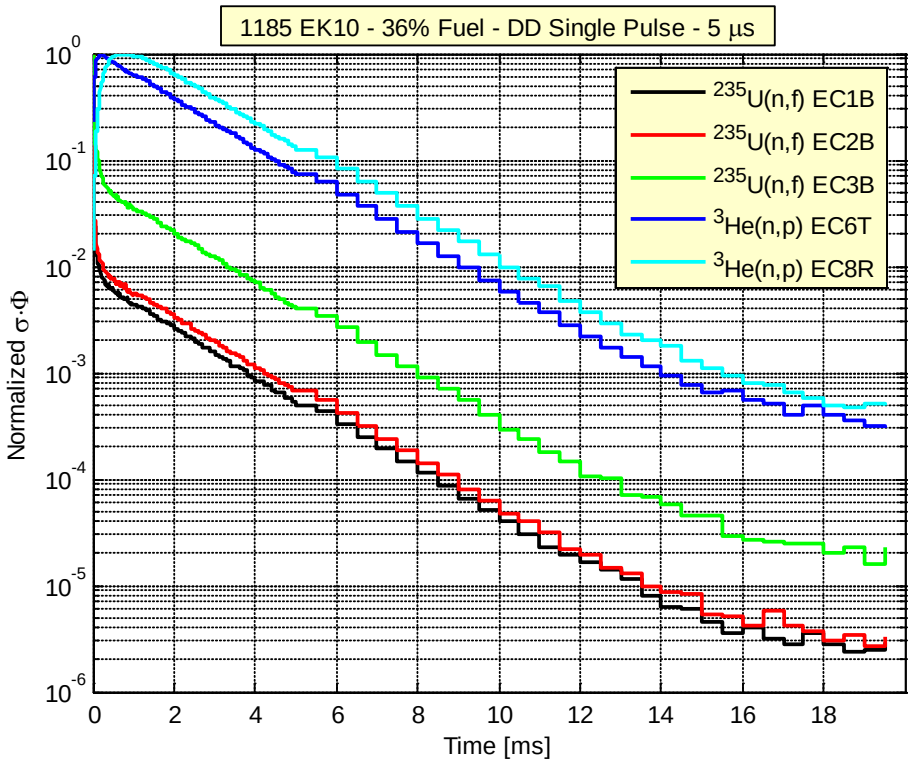

Figure 41. Normalized reaction rates for 36% enriched fuel and D-D neutron source

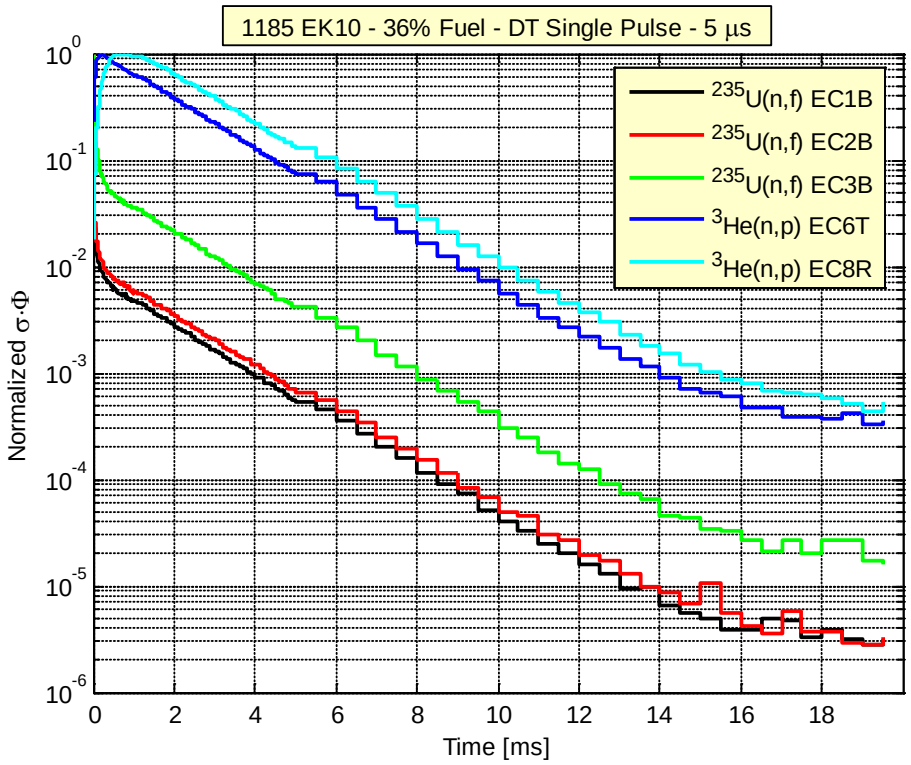

Figure 42. Normalized reaction rates for 36% enriched fuel and D-T neutron source

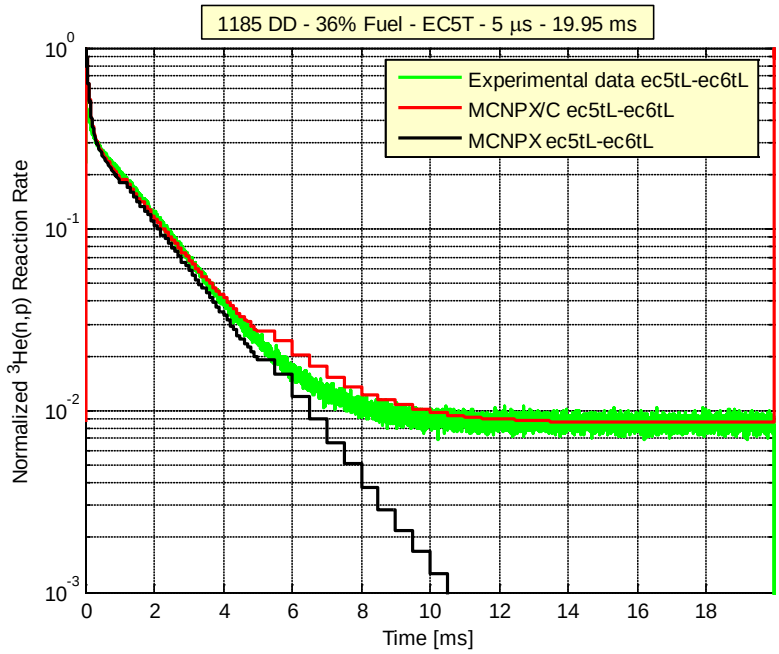

Figure 43. Normalized ^{3}He (n,p) reaction rate in EC5T for 36% enriched fuel; L refers to 25-cm long detectors; maximum of experimental data has been multiplied by 0.61; Δt = 2 and 10 μs for experiment and MCNP, respectively

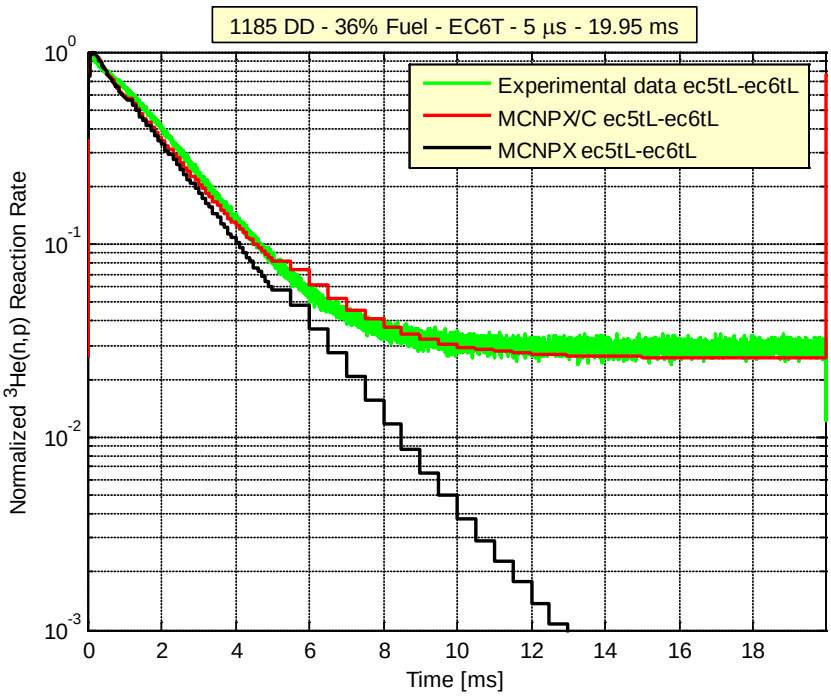

Figure 44. Normalized ^{3}He(n,p) reaction rate in EC6T for 36% enriched fuel; L refers to 25-cm long detectors; maximum of experimental data has been multiplied by 0.95; Δt = 2 and 10 μs for experiment and MCNP, respectively

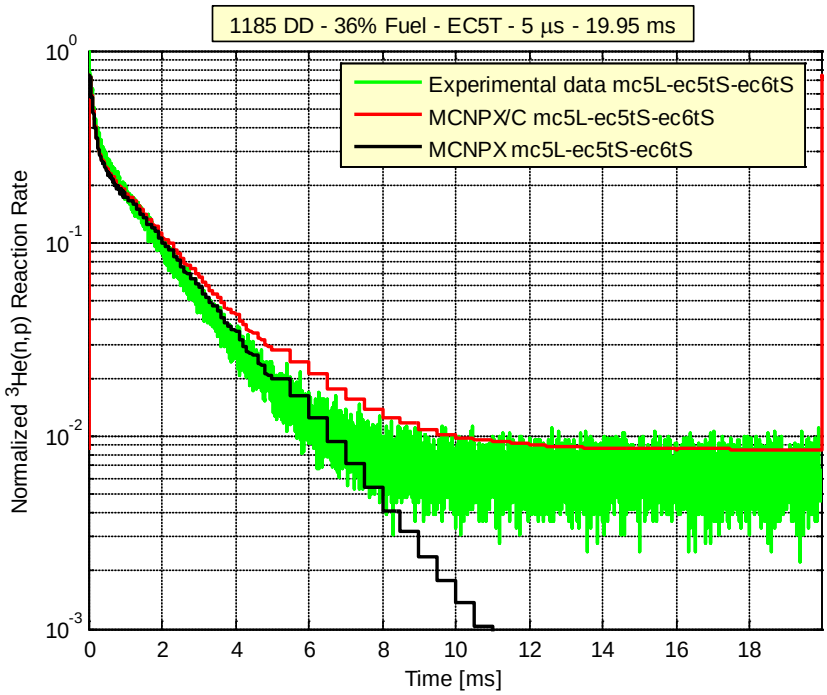

Figure 45. Normalized ^{3}He (n,p) reaction rate in EC5T for 36% enriched fuel; L and S refer to 25- and 1-cm long detectors, respectively; maximum of experimental data has been multiplied by 1.3; Δt = 2 and 10 μs for experiment and MCNP, respectively

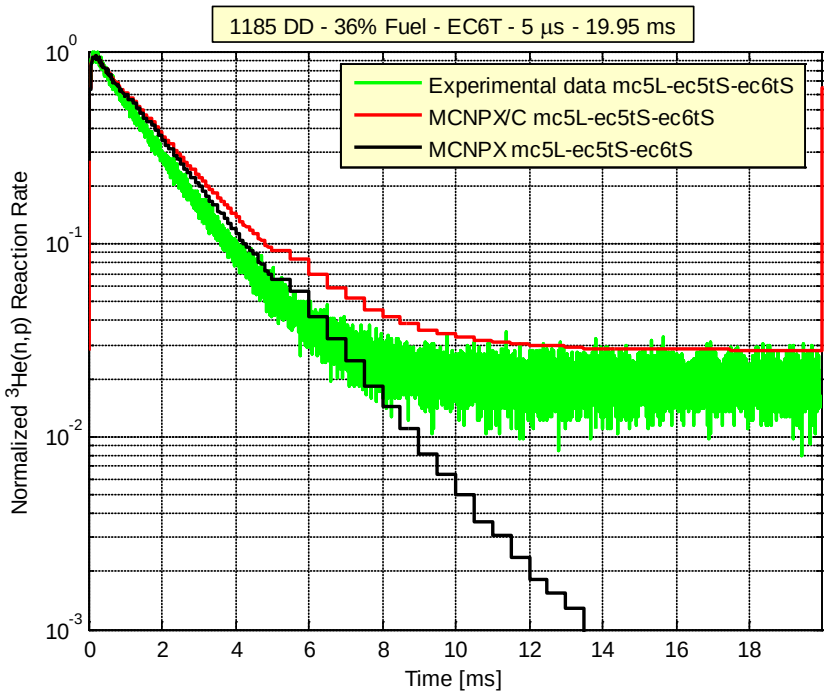

Figure 46. Normalized ^{3}He (n,p) reaction rate in EC6T for 36% enriched fuel; L and S refer to 25- and 1-cm long detectors, respectively; maximum of experimental data has been multiplied by 1.1; Δt = 2 and 10 μs for experiment and MCNP, respectively

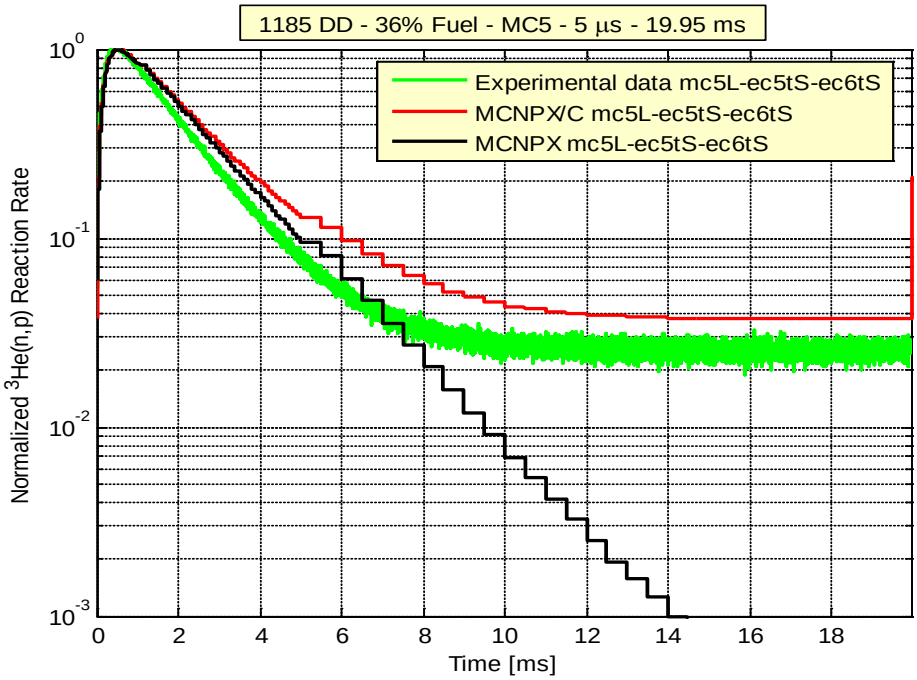

Figure 47. Normalized ^{3}He (n,p) reaction rate in measurement channel MC5 for 36% enriched fuel; L and S refer to 25- and 1-cm long detectors, respectively; maximum of experimental data has been multiplied by 1.05; Δt = 2 and 10 μs for experiment and MCNP, respectively

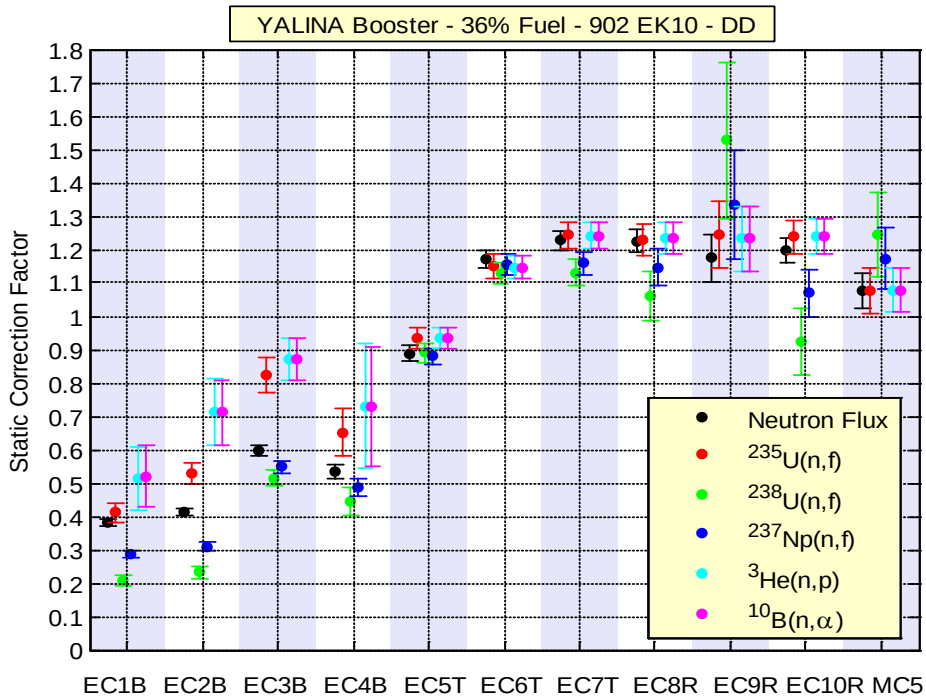

Figure 48. Correction factor for 36% enriched fuel from static MCNPX simulations with D-D neutron source and 902 EK10 fuel rods

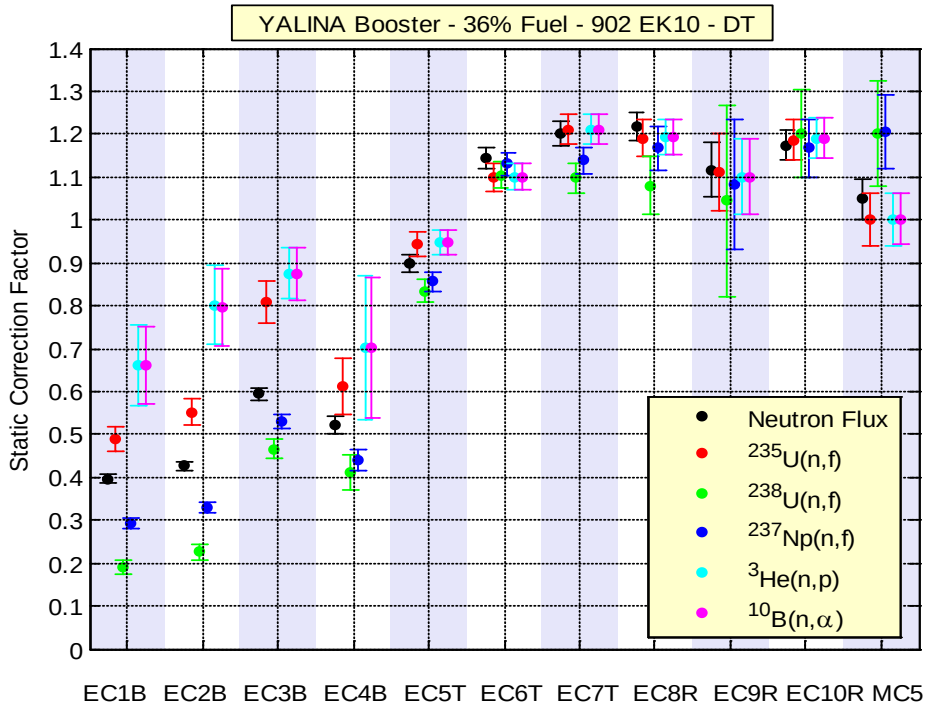

Figure 49. Correction factor for 36% enriched fuel from static MCNPX simulations with D-T neutron source and 902 EK10 fuel rods

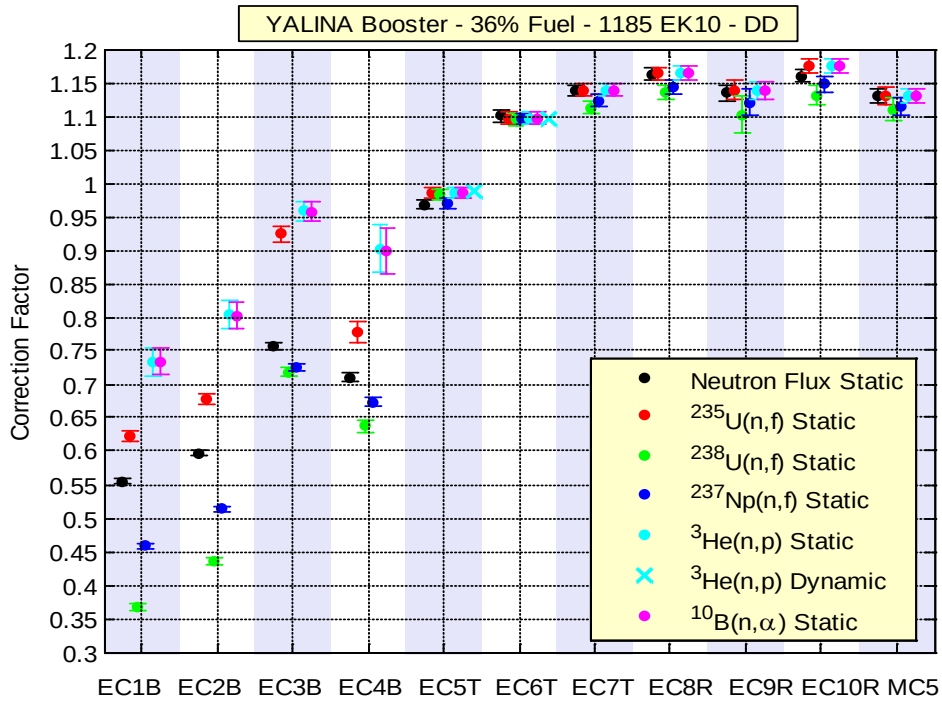

Figure 50. Correction factor for 36% enriched fuel from MCNPX simulations with D-D neutron source and 1185 EK10 fuel rods

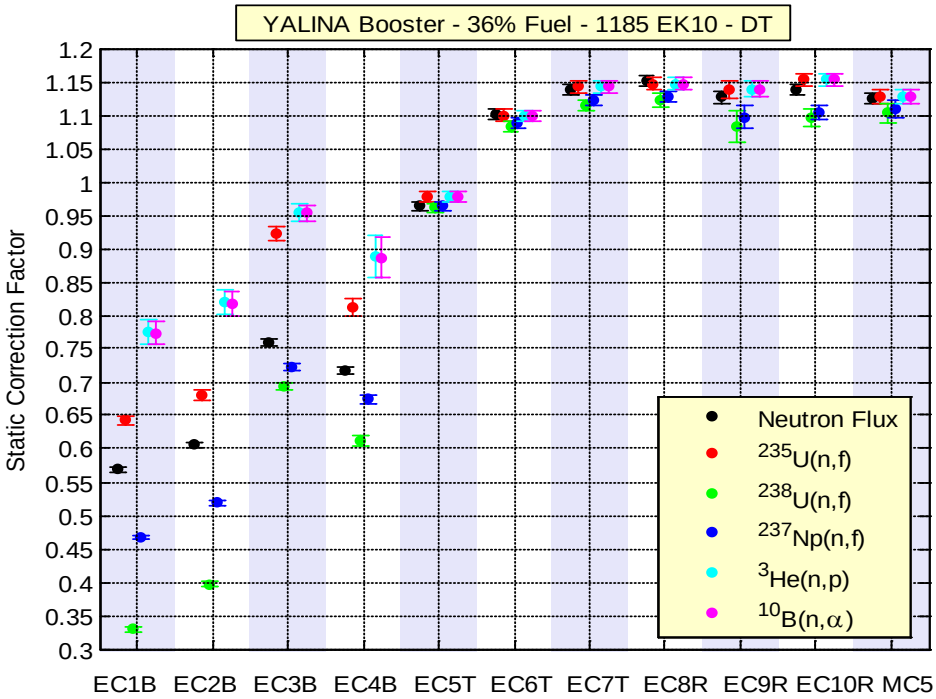

Figure 51. Correction factor for 36% enriched fuel from static MCNPX simulations with D-T neutron source and 1185 EK10 fuel rods

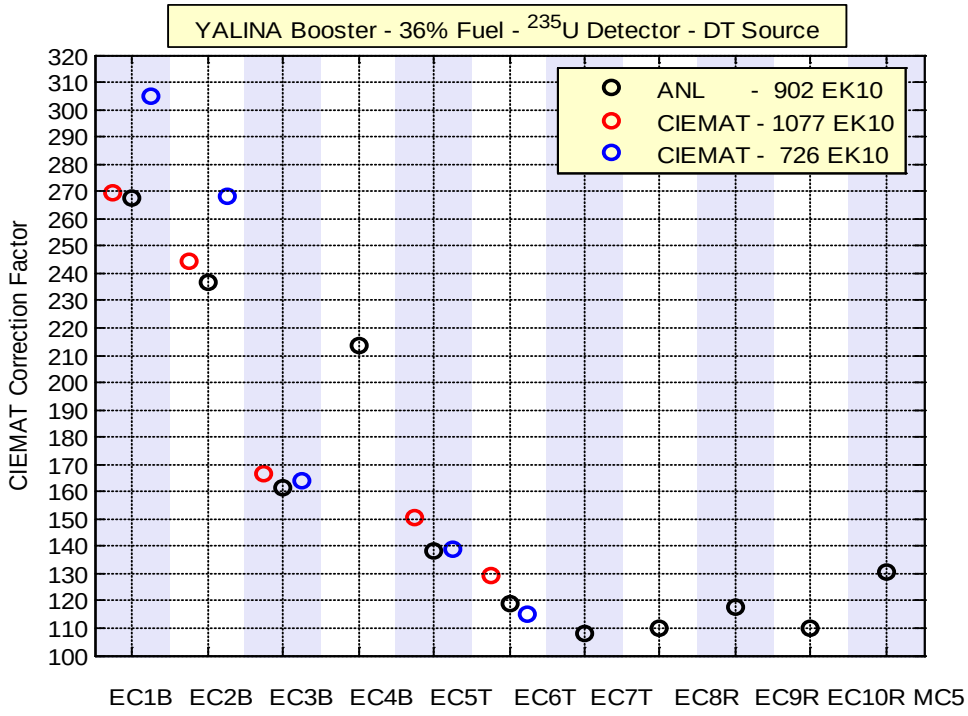

Figure 52. CIEMAT[16] and ANL correction factors for D-T neutron source in different EK10 fuel configurations; the results have been calculated using the CIEMAT definition of the correction factor[16]

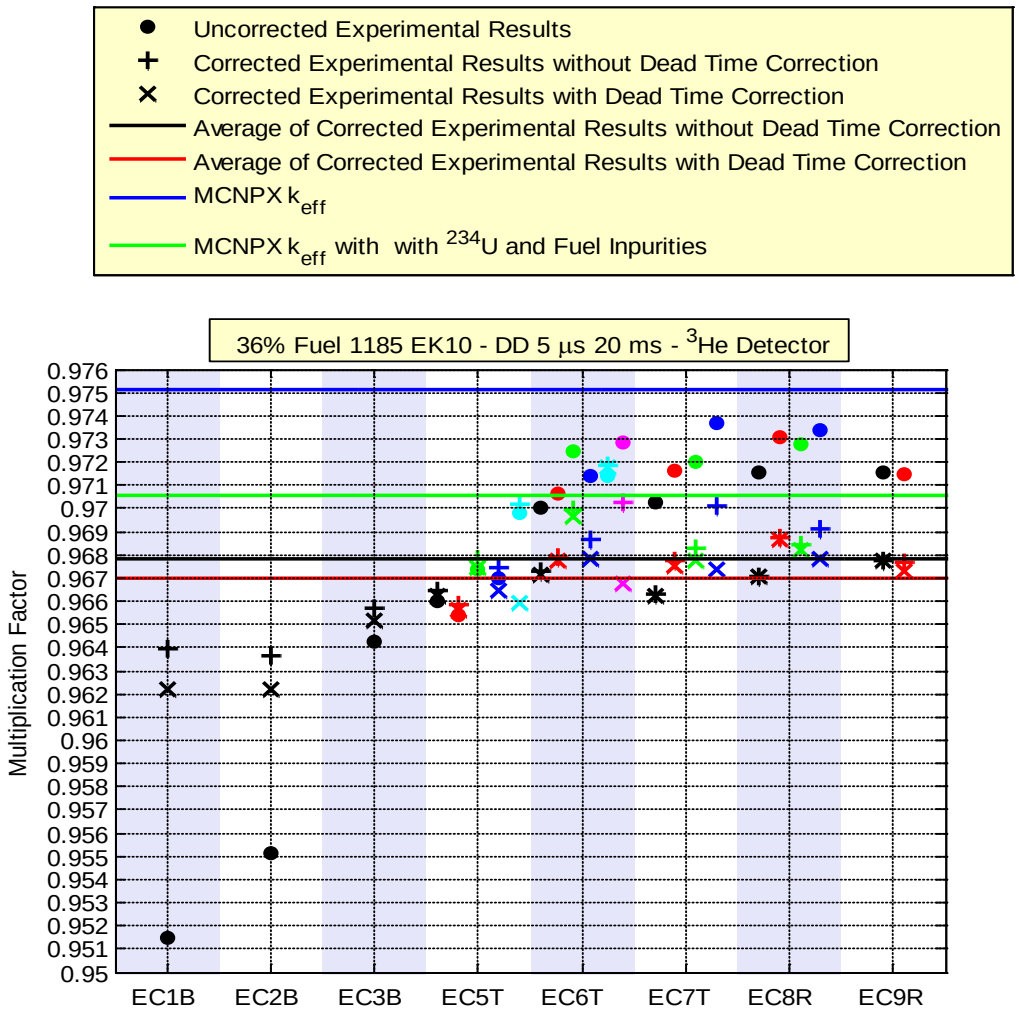

Figure 53. Corrected and uncorrected experimental multiplication factors and MCNPX multiplication factor obtained by criticality calculations for 36% enriched fuel configuration; the experimental reactivity has been corrected by the static correction factor. The colors of the experimental data in each channel follow the colors reported in the left column of Table V.

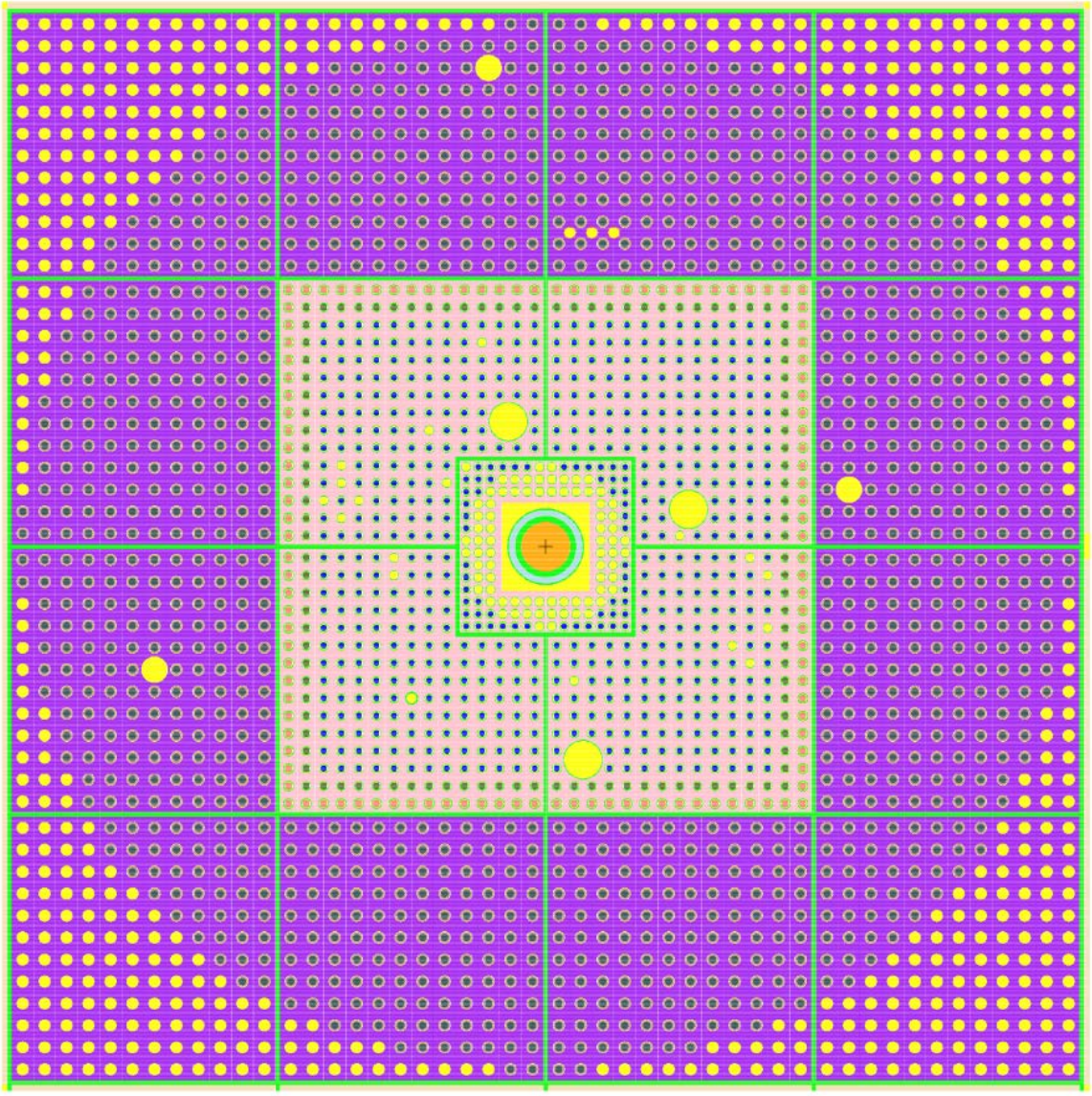

Figure 54. Horizontal section of YALINA Booster fuel zone with 21% enriched fuel in fast zone and 1185 EK10 fuel rods in thermal zone (Configuration 4)

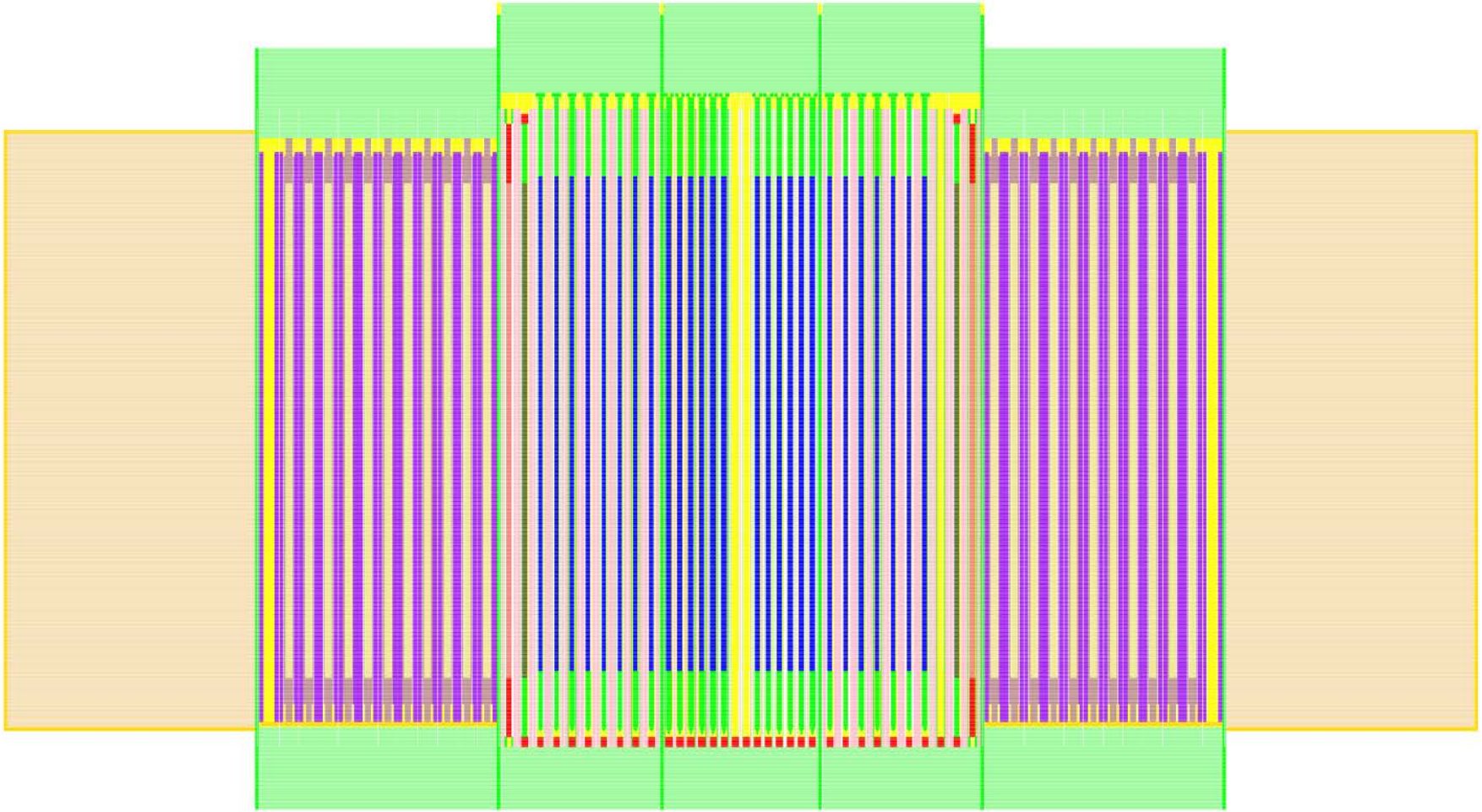

Figure 55. Vertical section of YALINA Booster subcritical assembly with 21% enriched fuel in fast zone

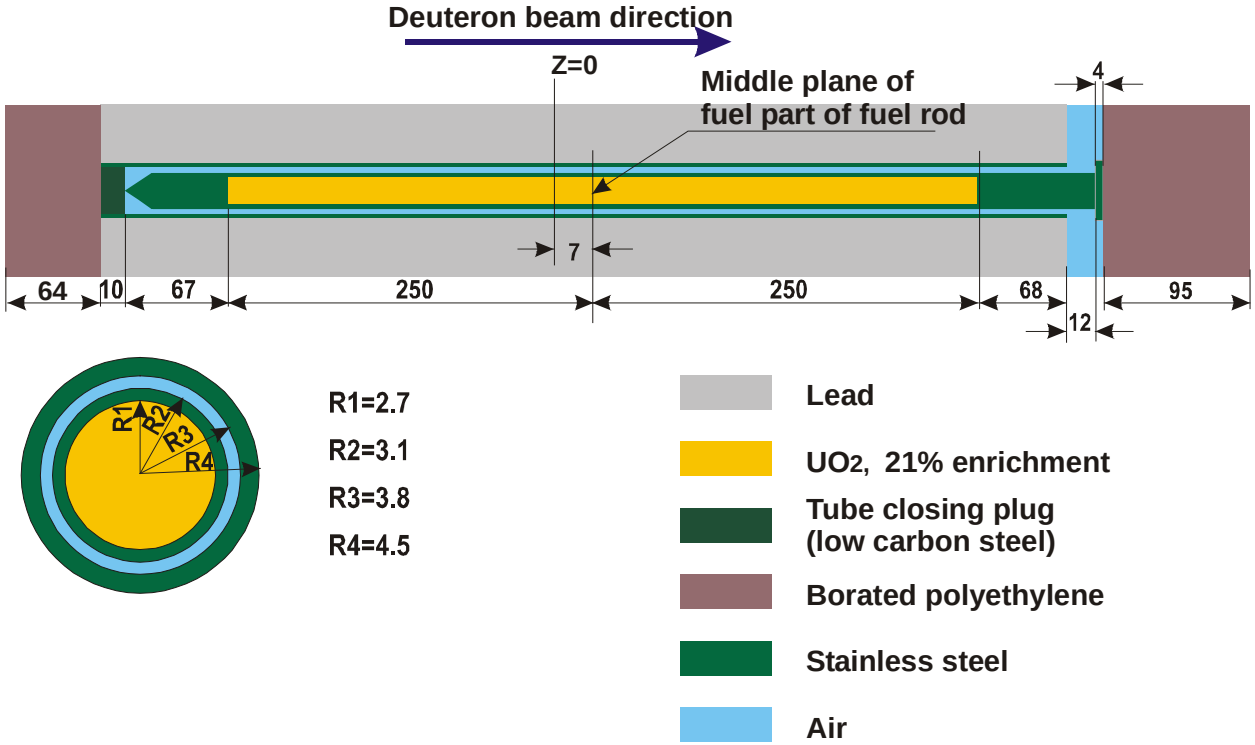

Figure 56. Technical specifications of the fuel rod with 21% enriched uranium oxide, dimensions in mm

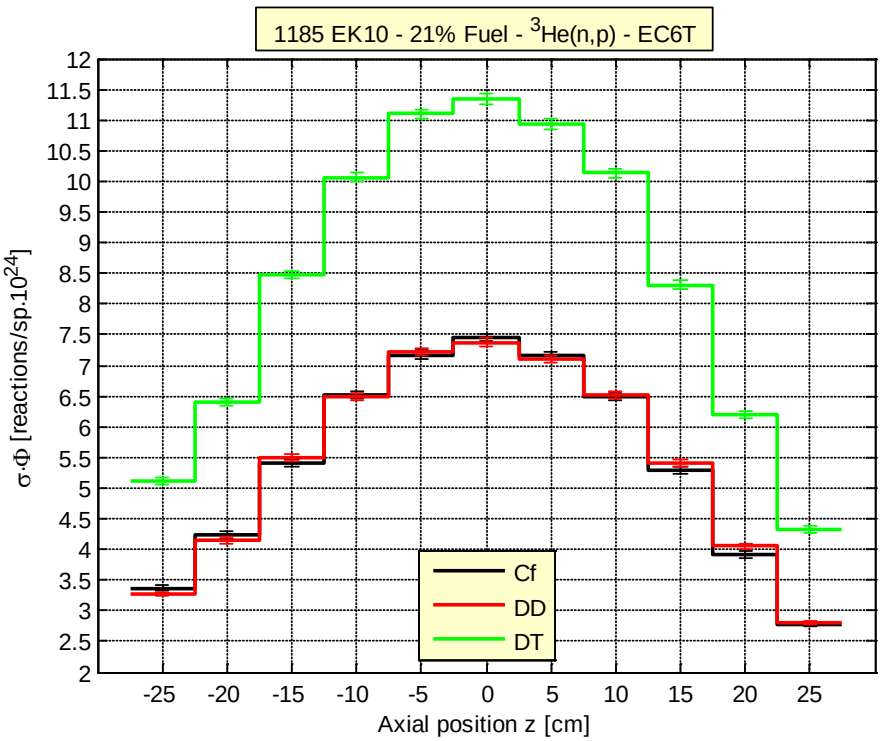

Figure 57. ^{3}He(n,p) reaction rate in EC6T for 21% enriched fuel

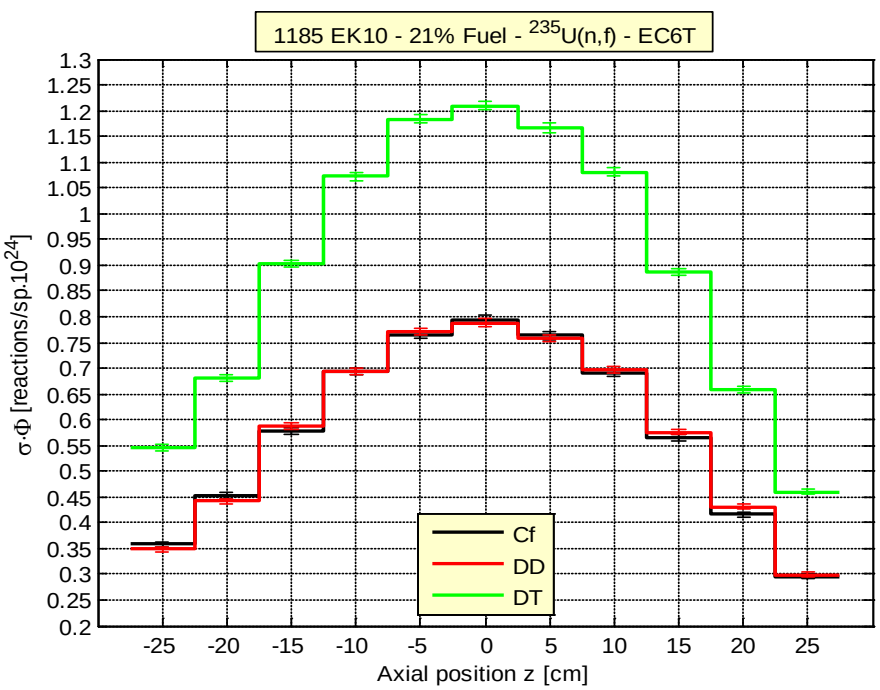

Figure 58. ^{235}U(n,f) reaction rate in EC6T for 21% enriched fuel

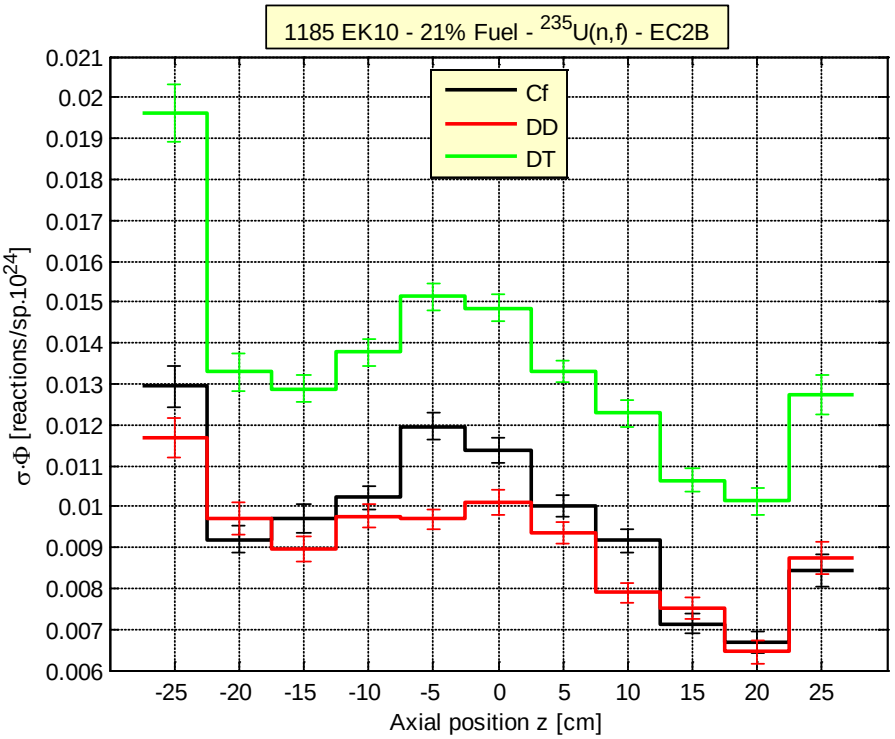

Figure 59. ^{235}U(n,f) reaction rate in EC2B for 21% enriched fuel

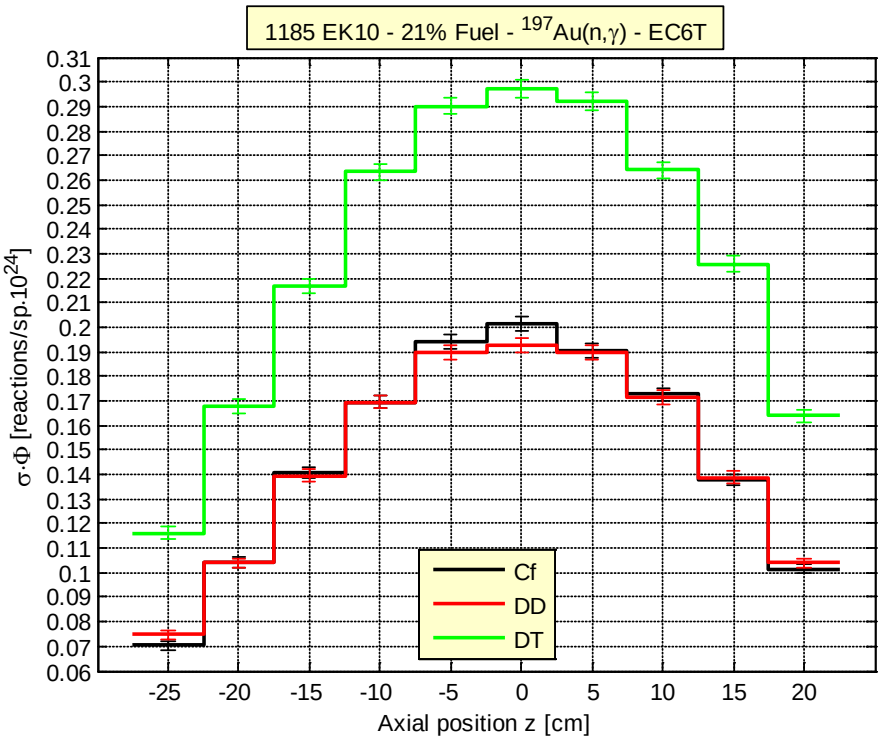

Figure 60. ^{197}Au(n,γ) reaction rate in EC6T for 21% enriched fuel

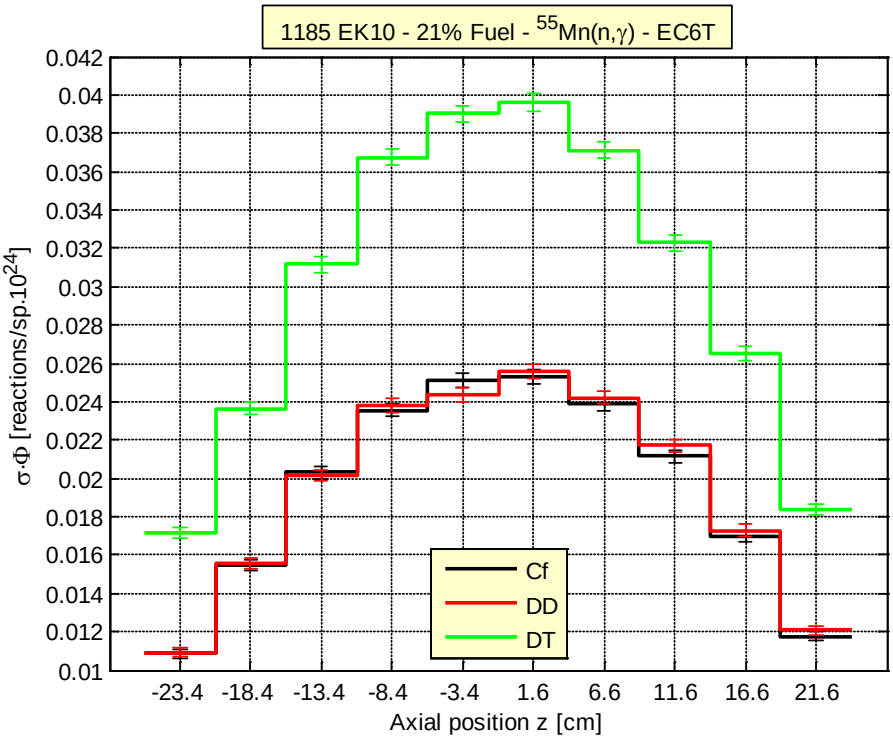

Figure 61. ^{55}Mn(n,γ) reaction rate in EC6T for 21% enriched fuel

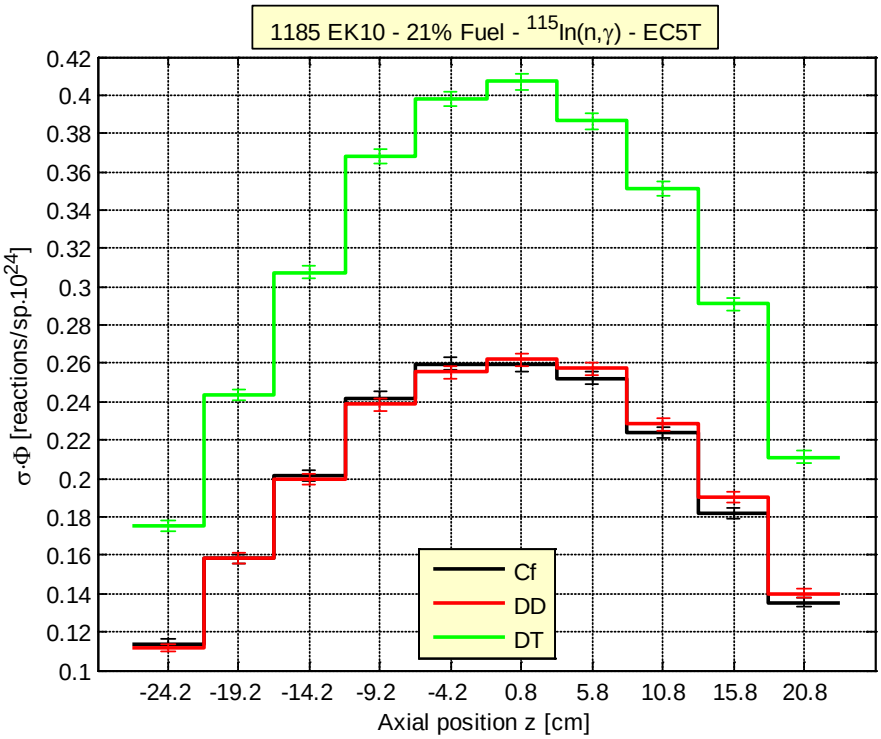

Figure 62. ^{115}In(n,γ) reaction rate in EC5T for 21% enriched fuel

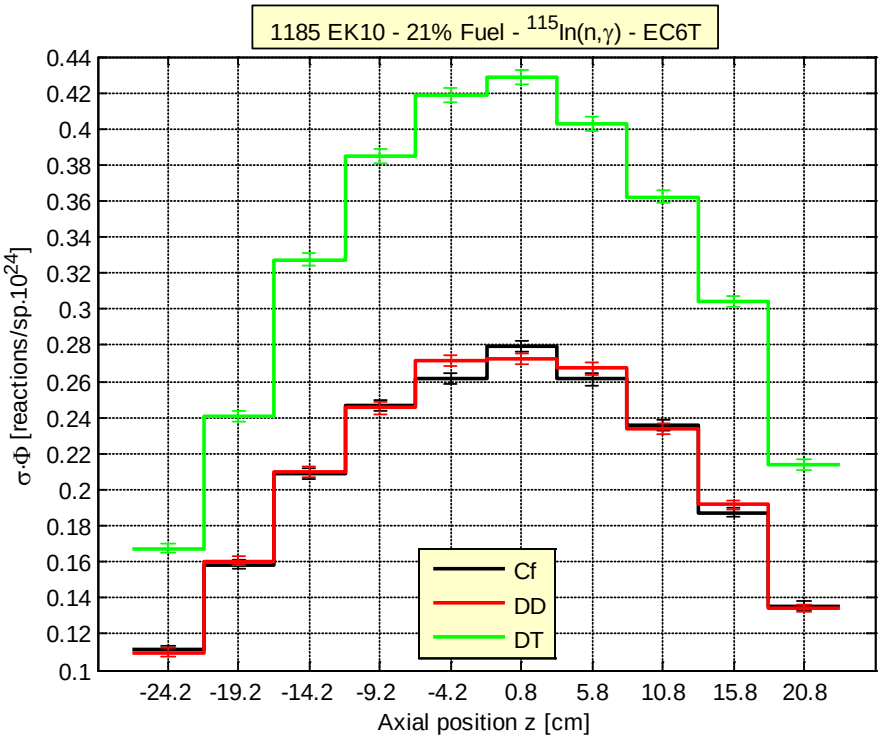

Figure 63. ^{115}In(n,γ) reaction rate in EC6T for 21% enriched fuel

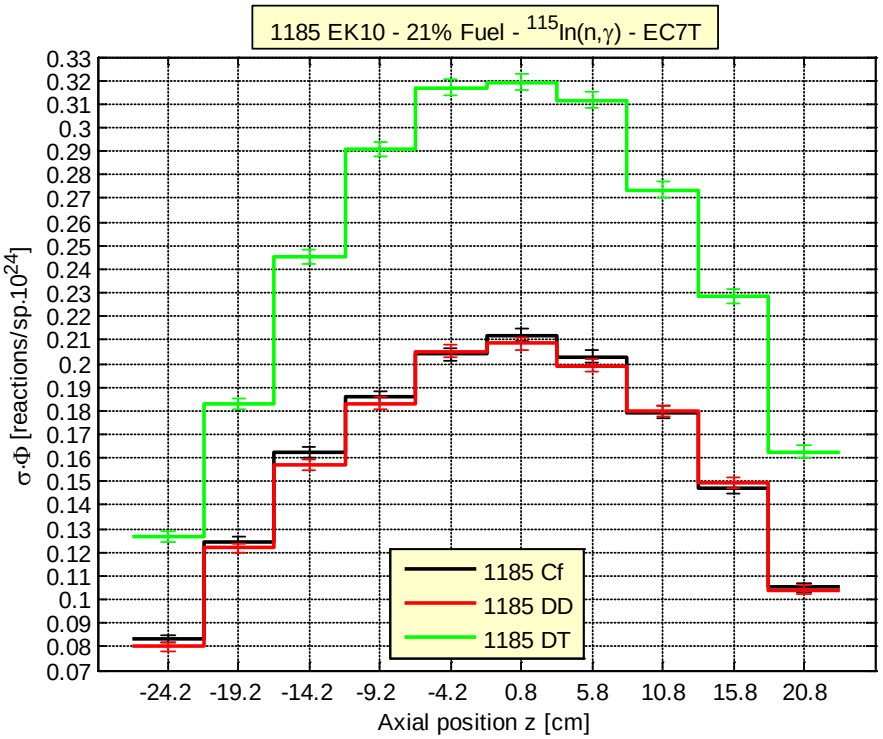

Figure 64. ^{115}In(n,γ) reaction rate in EC7T for 21% enriched fuel

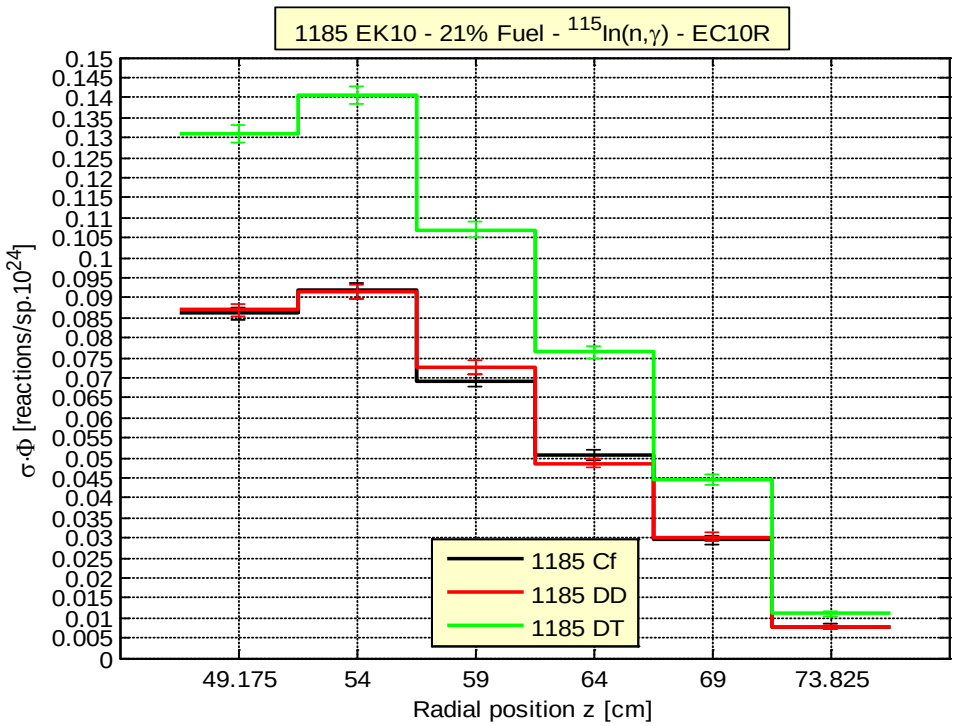

Figure 65. ^{115}In(n,γ) reaction rate in EC10R for 21% enriched fuel

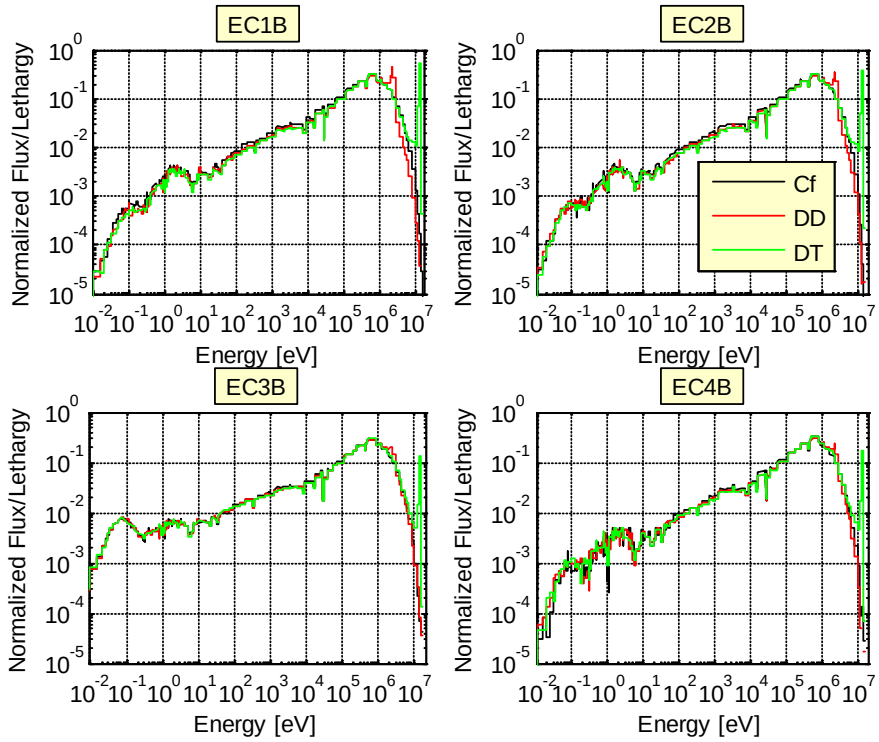

Figure 66. Neutron spectra in fast zone for 21% enriched fuel

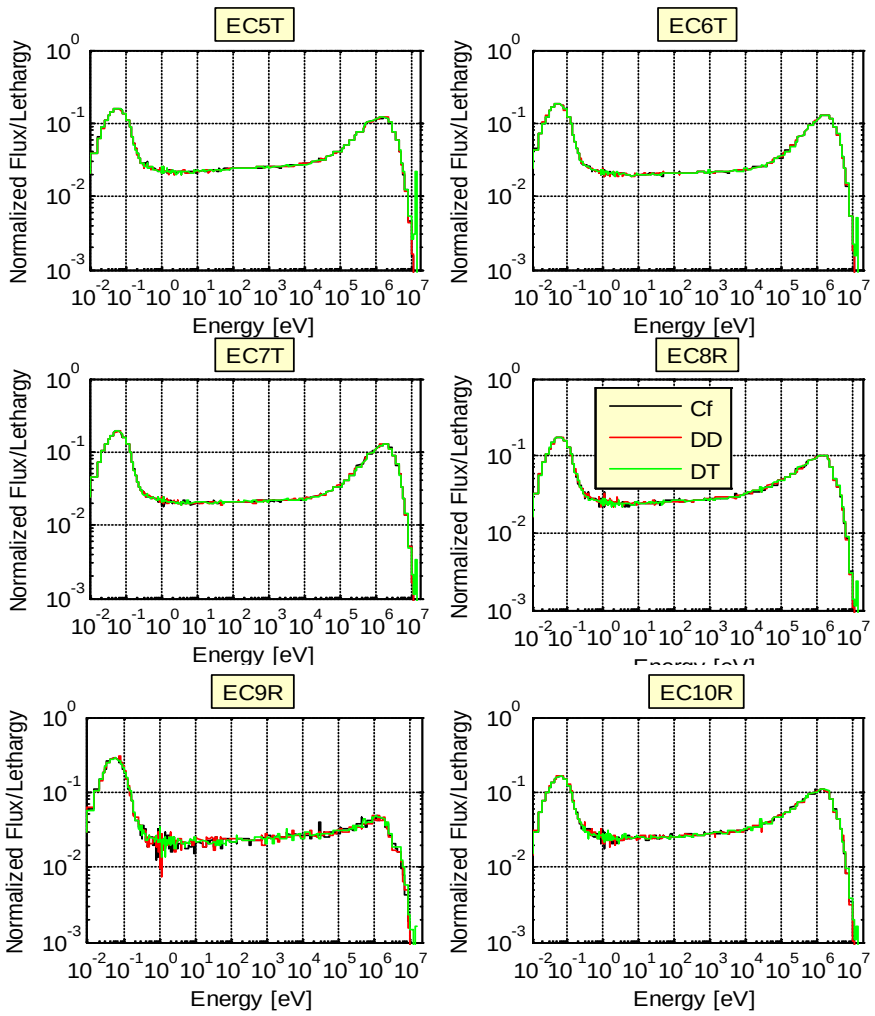

Figure 67. Neutron spectra in thermal and reflector zones for 21% enriched fuel

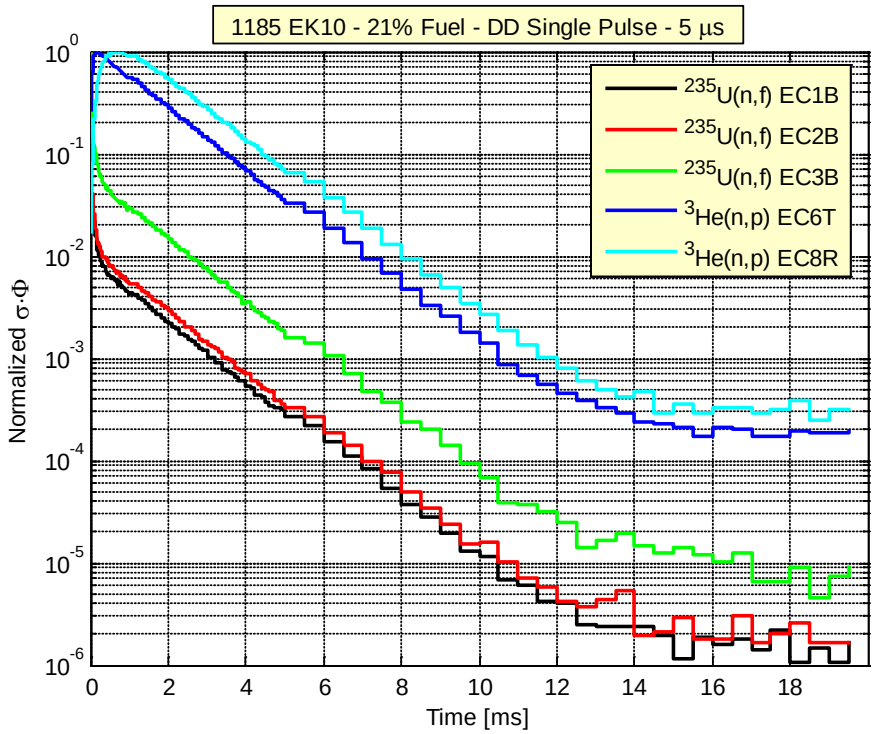

Figure 68. Normalized reaction rates for 21% enriched fuel and D-D neutron source

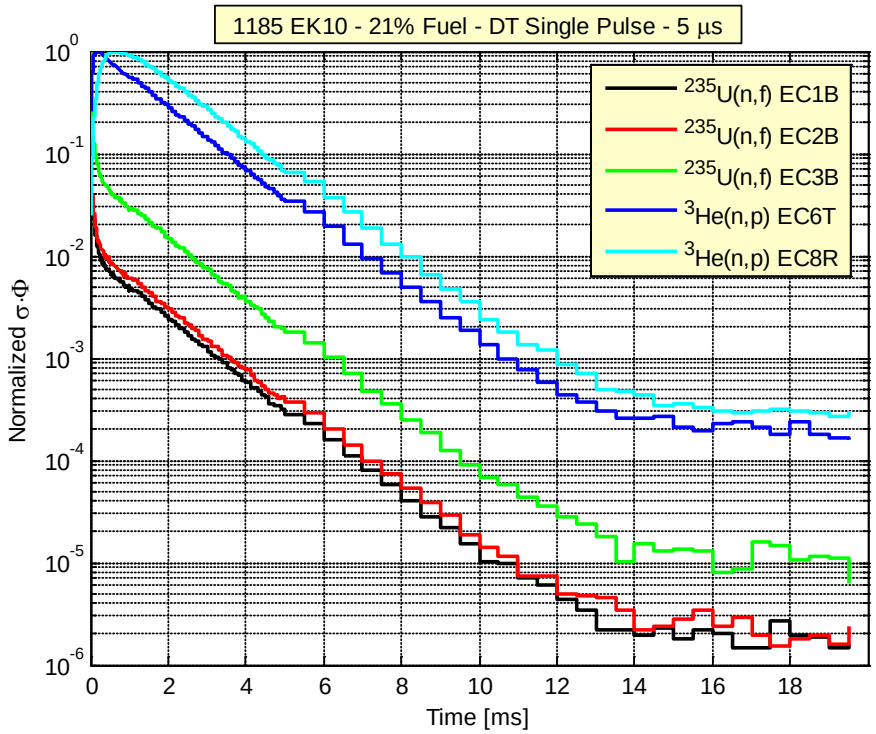

Figure 69. Normalized reaction rates for 21% enriched fuel and D-T neutron source

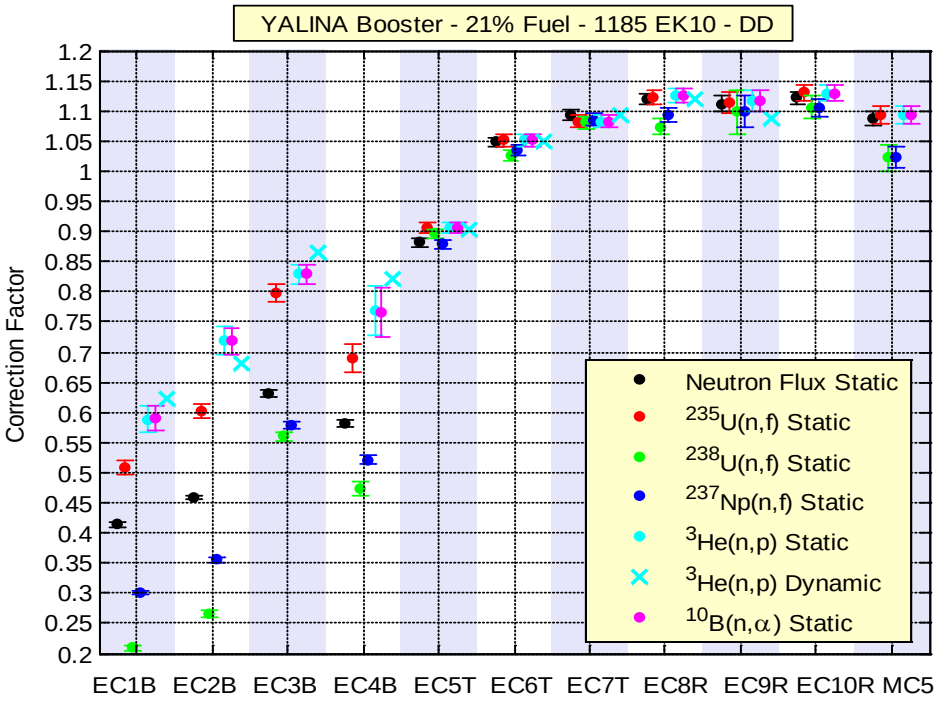

Figure 70. Spatial correction factor calculated with MCNPX simulations for 21% enriched fuel configuration and D-D neutron source

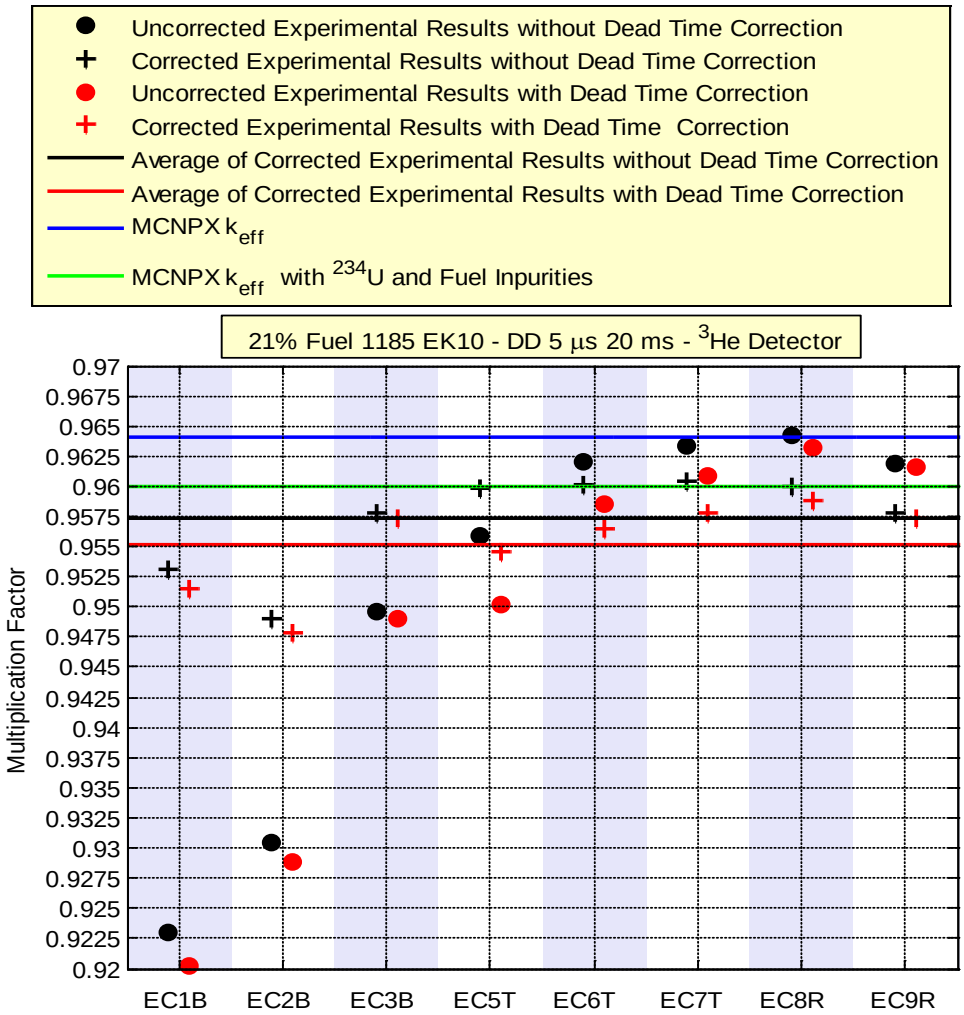

Figure 71. Corrected and uncorrected experimental multiplication factors and MCNPX multiplication factor obtained from criticality calculations for 21% enriched fuel configuration; the experimental reactivity has been corrected by the static correction factor Experiments were performed with D-D neutron source

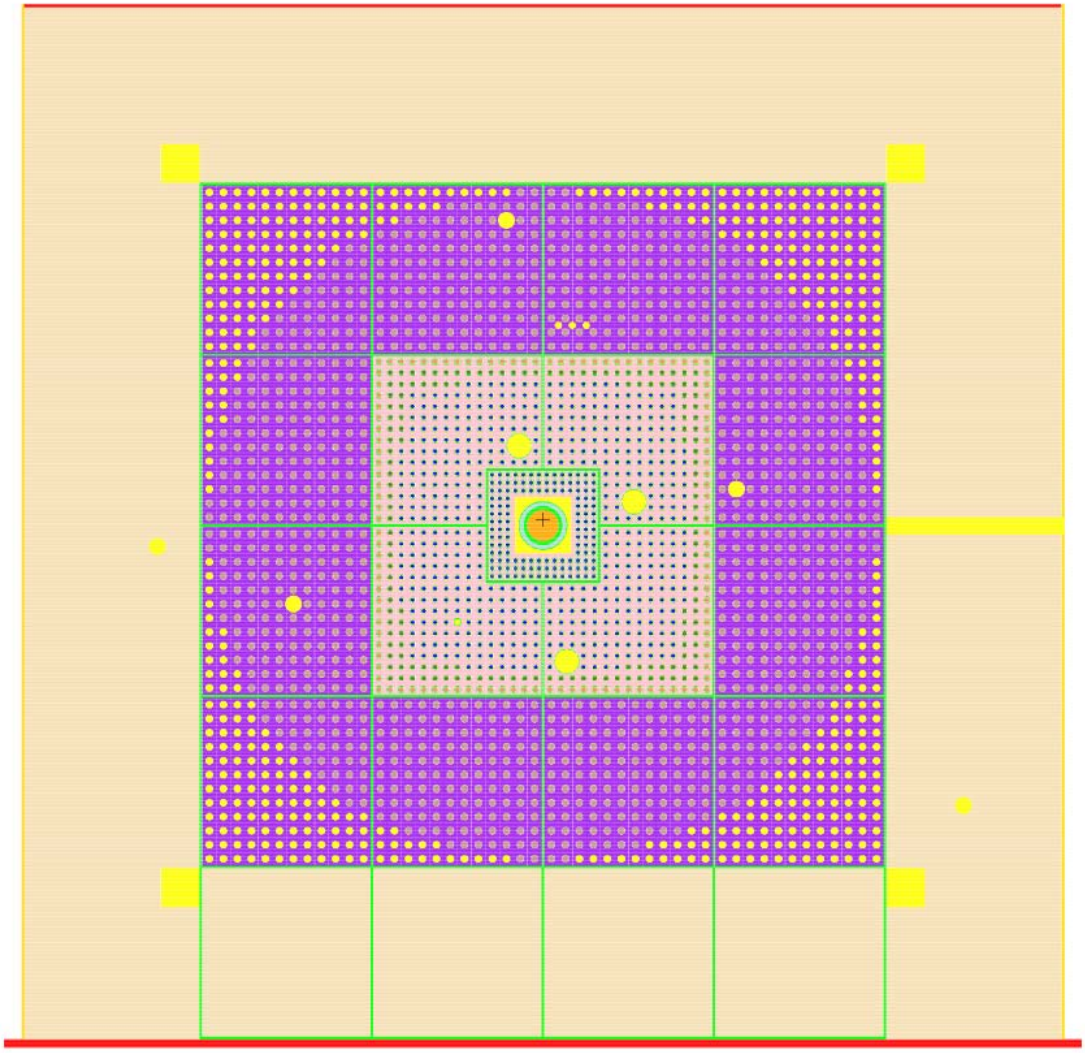

Figure 72. Horizontal section of configuration 5 of Table I

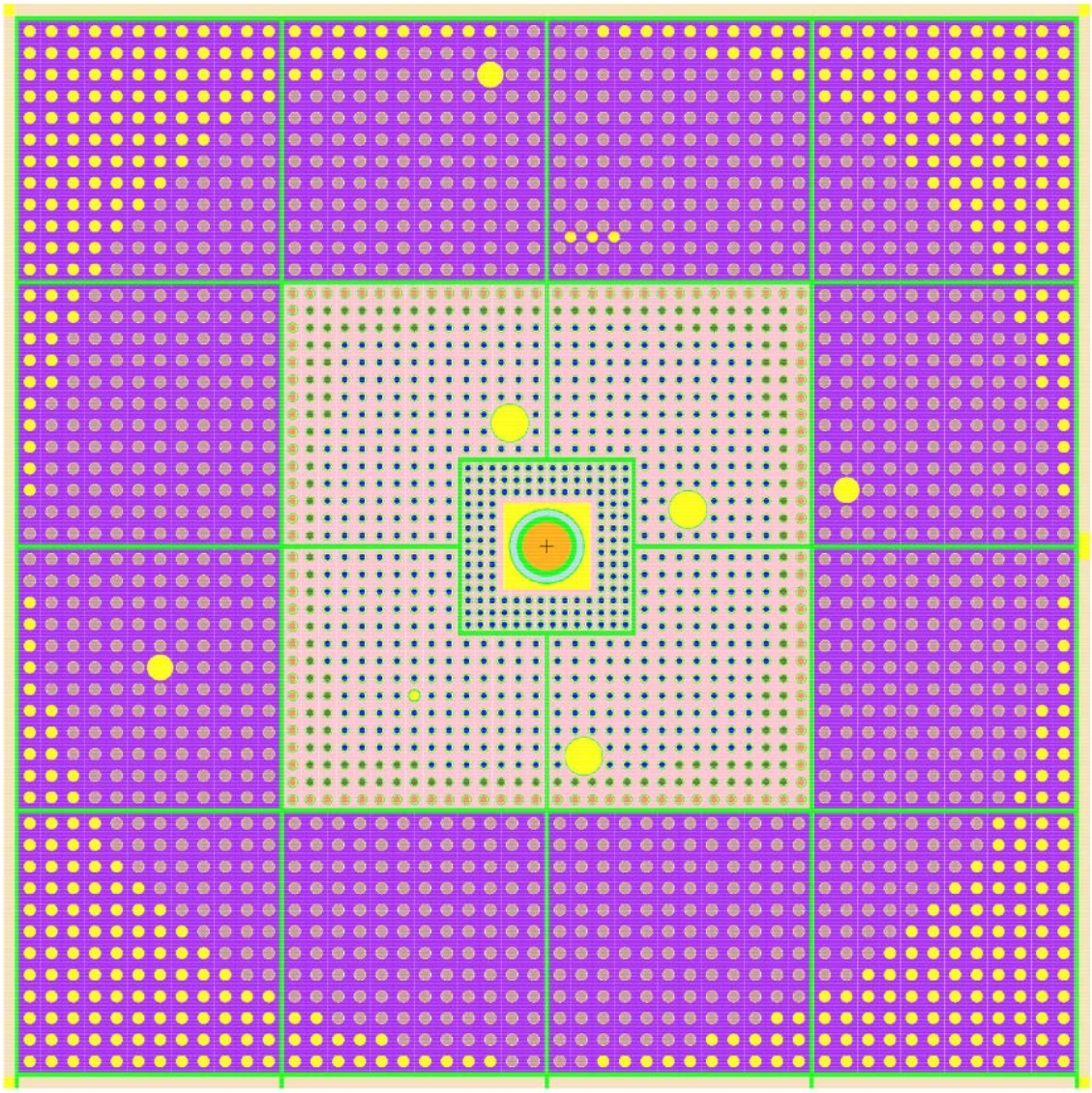

Figure 73. Fuel zone of configuration 5 of Table I

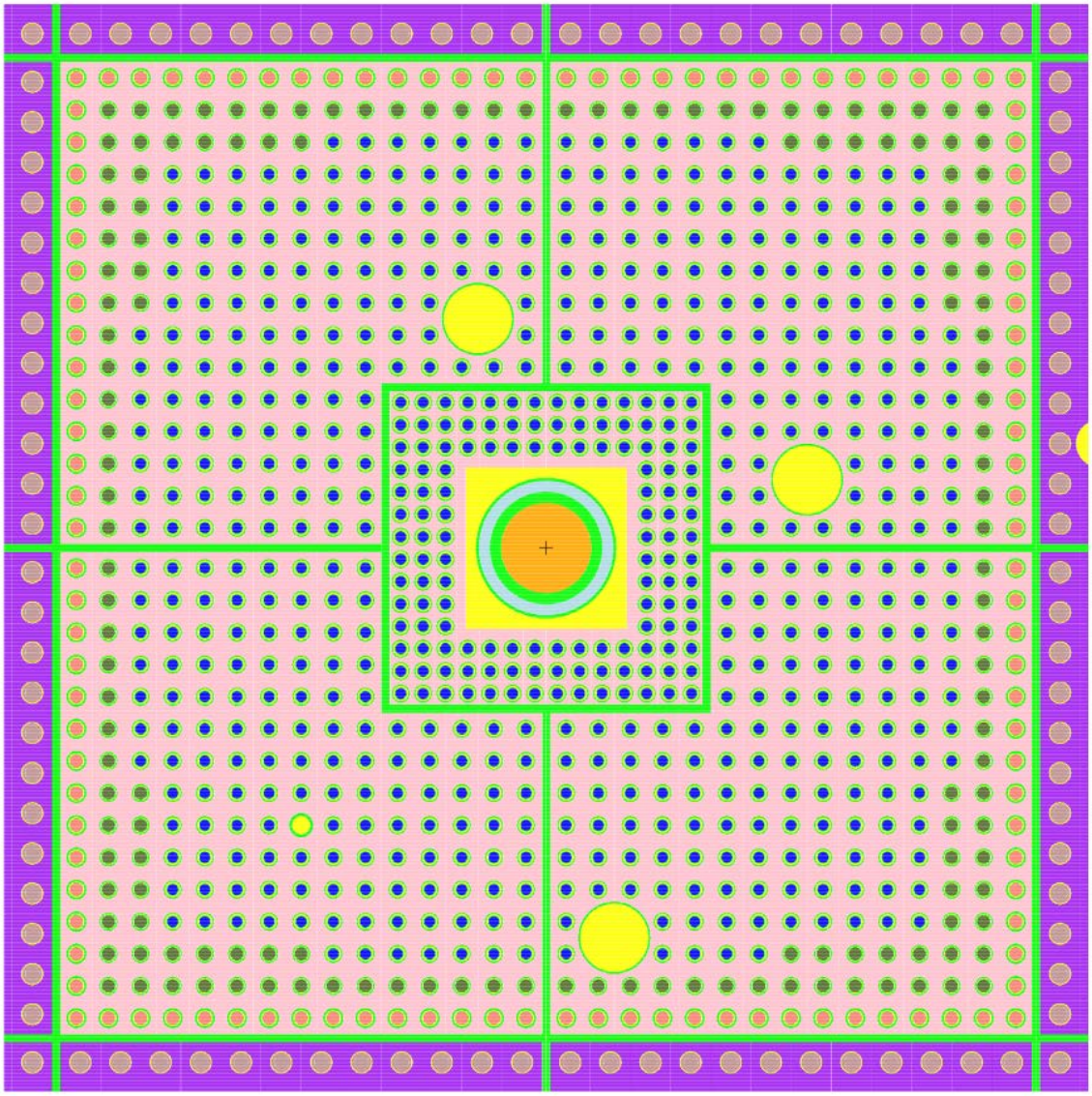

Figure 74. Fast zone of configuration 5 of Table I at z = 0 cm

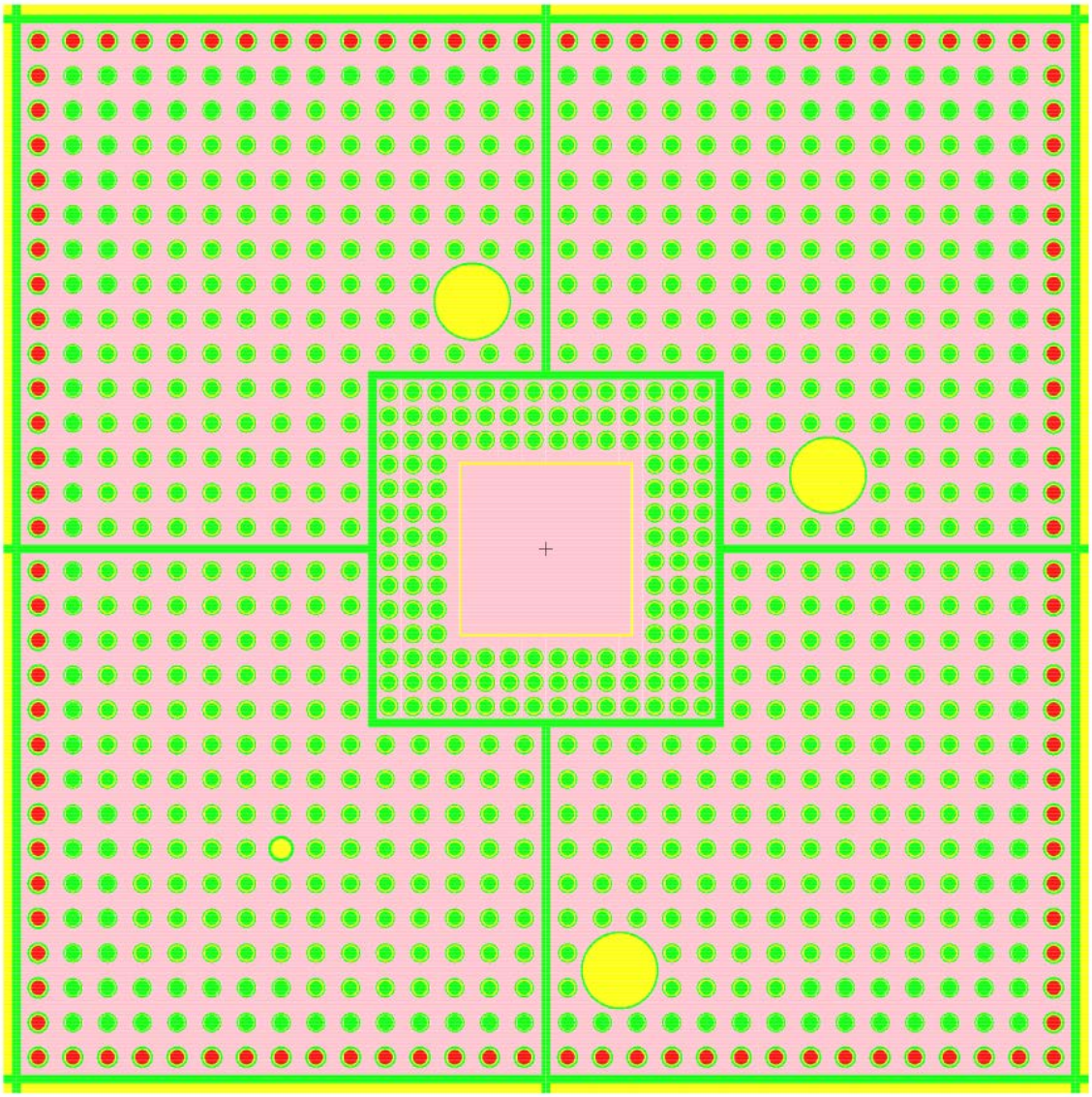

Figure 75. Fast zone of configuration 5 of Table I between z = 25 and z = 30.2 cm

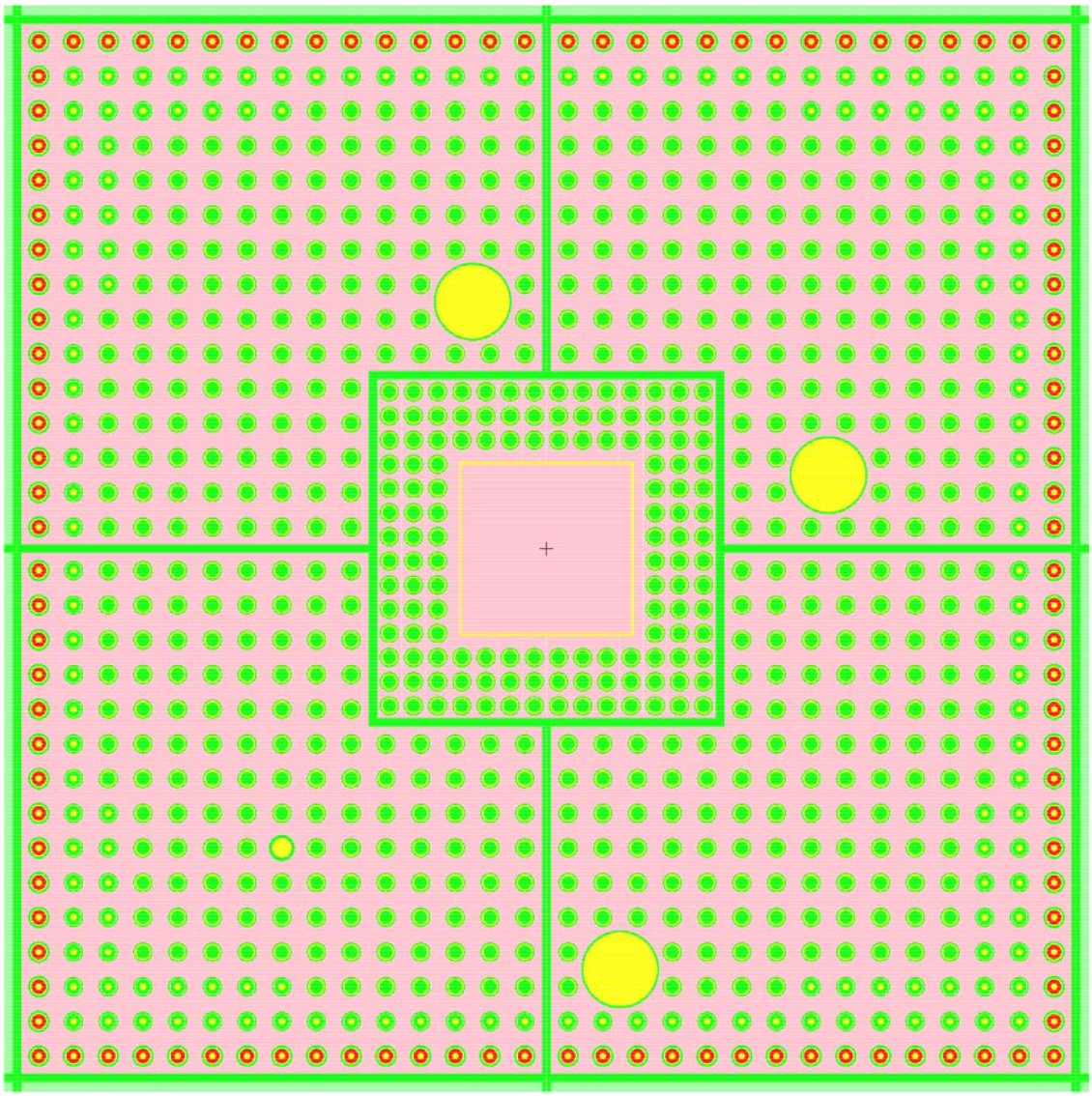

Figure 76. Fast zone of configuration 5 of Table I between z = 30.2 and z = 31 cm

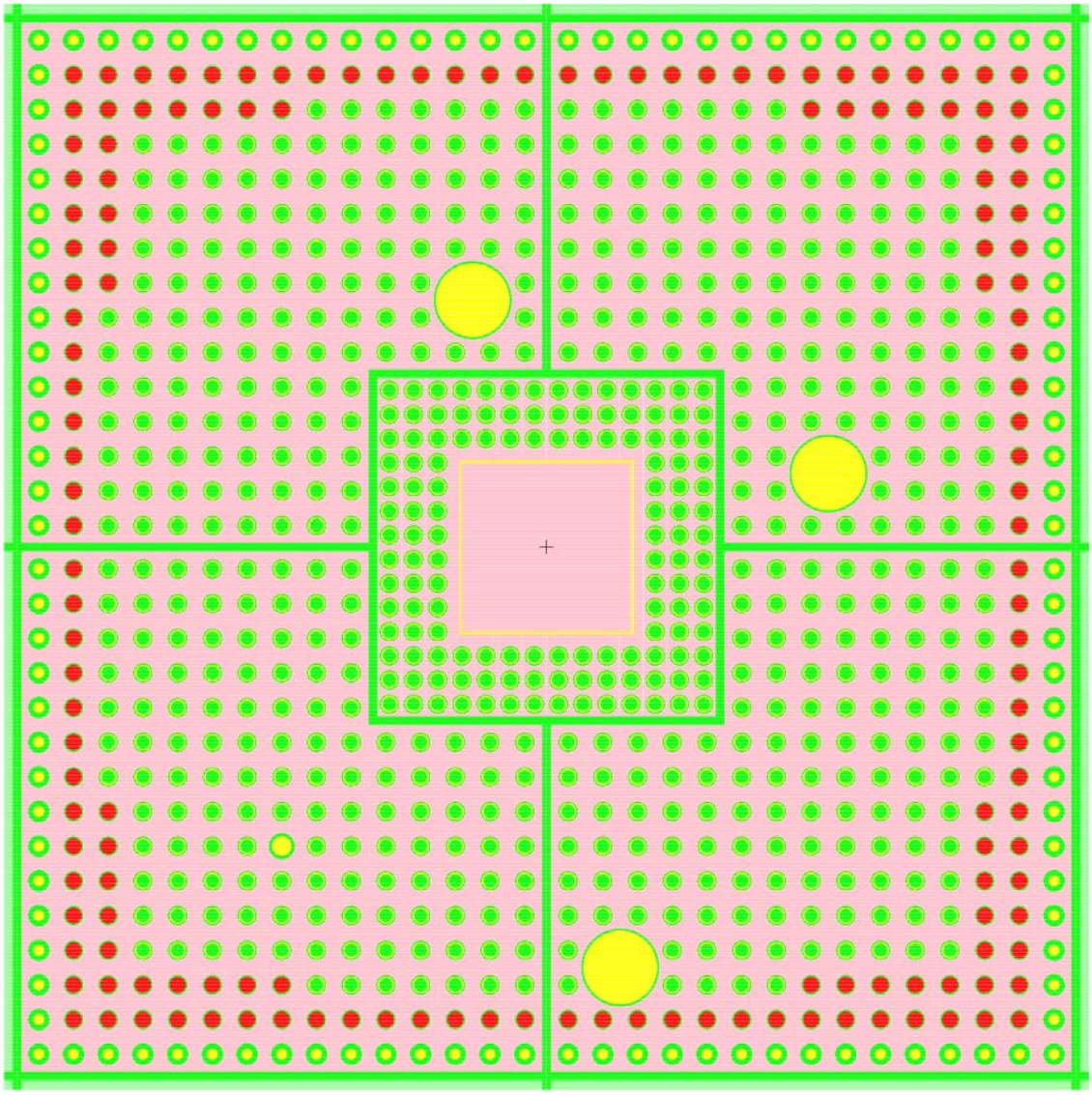

Figure 77. Fast zone of configuration 5 of Table I between z = 31 and z = 32 cm

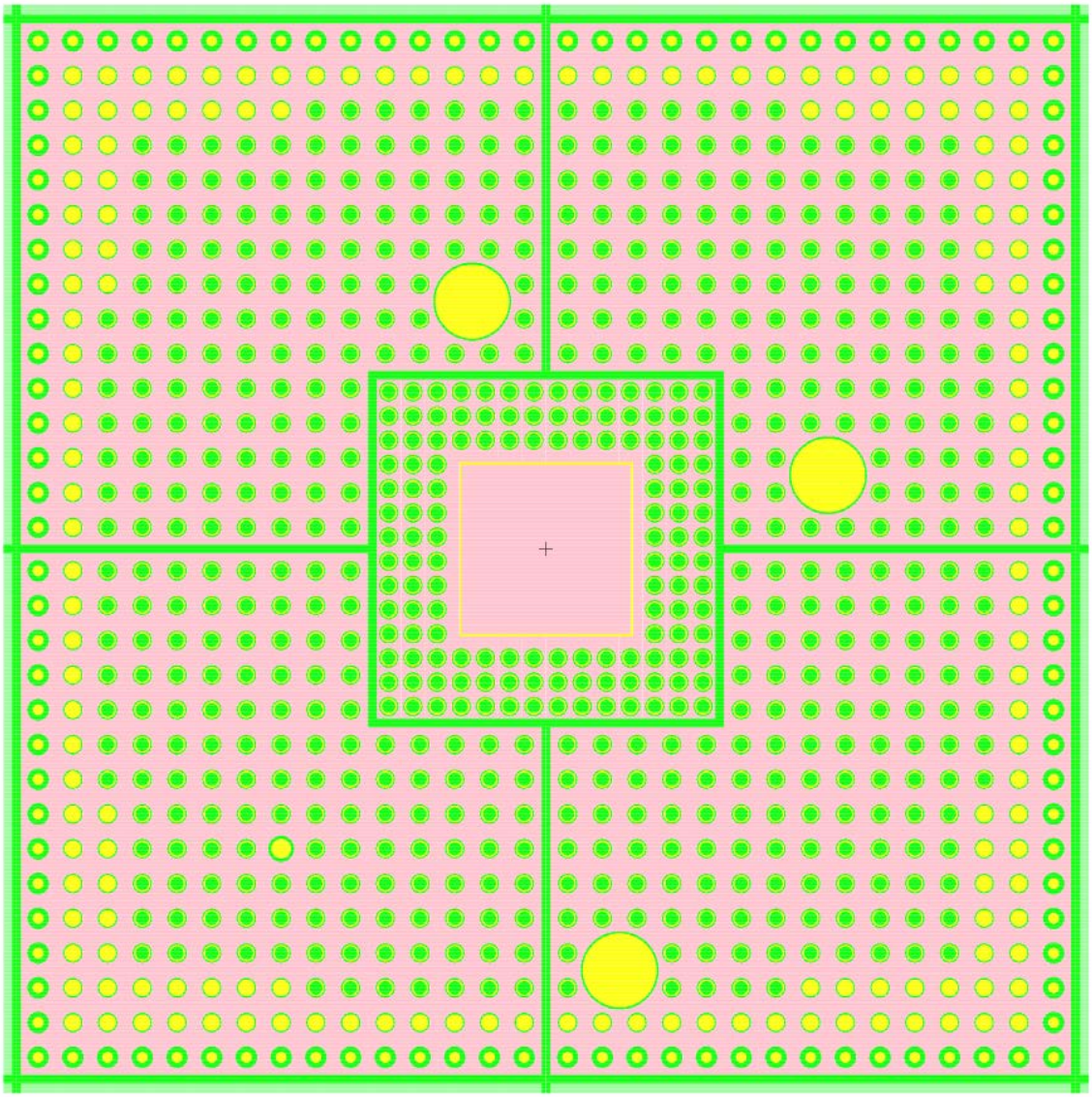

Figure 78. Fast zone of configuration 5 of Table I between z = 32 and z = 32.5 cm

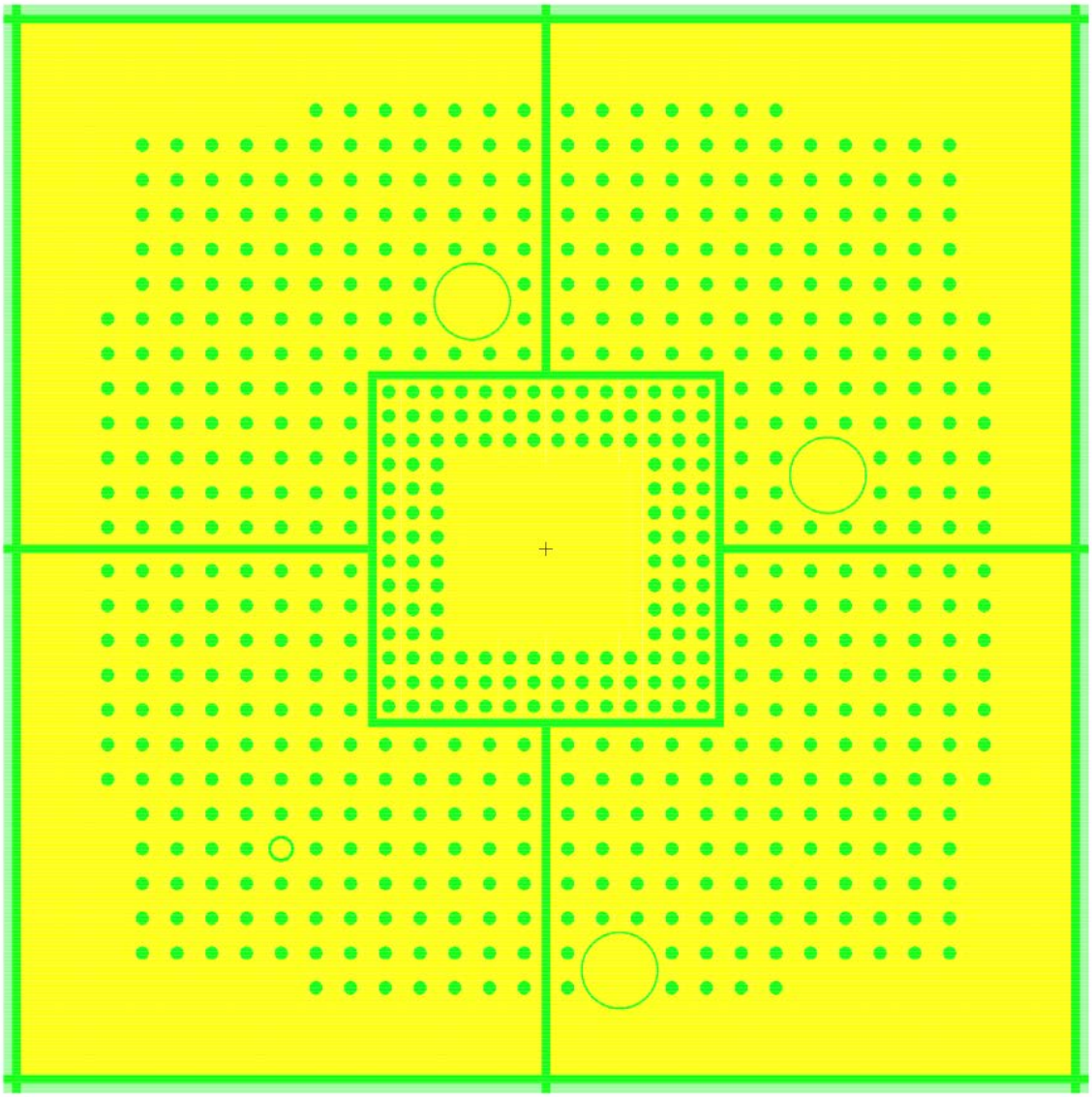

Figure 79. Fast zone of configuration 5 of Table I between z = 32.5 and z = 33.7 cm

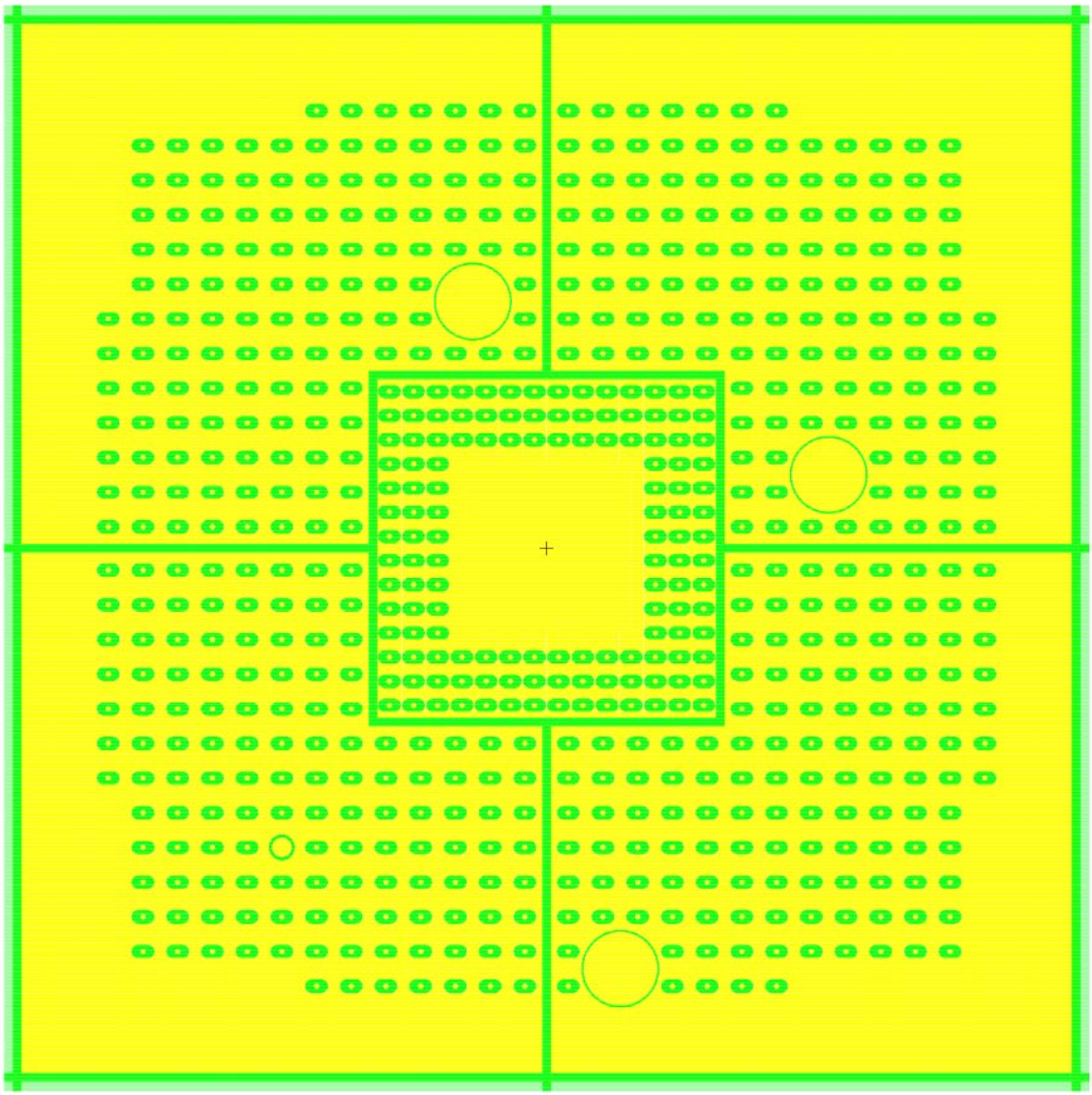

Figure 80. Fast zone of configuration 5 of Table I between z = 33.7 and z = 34.1 cm

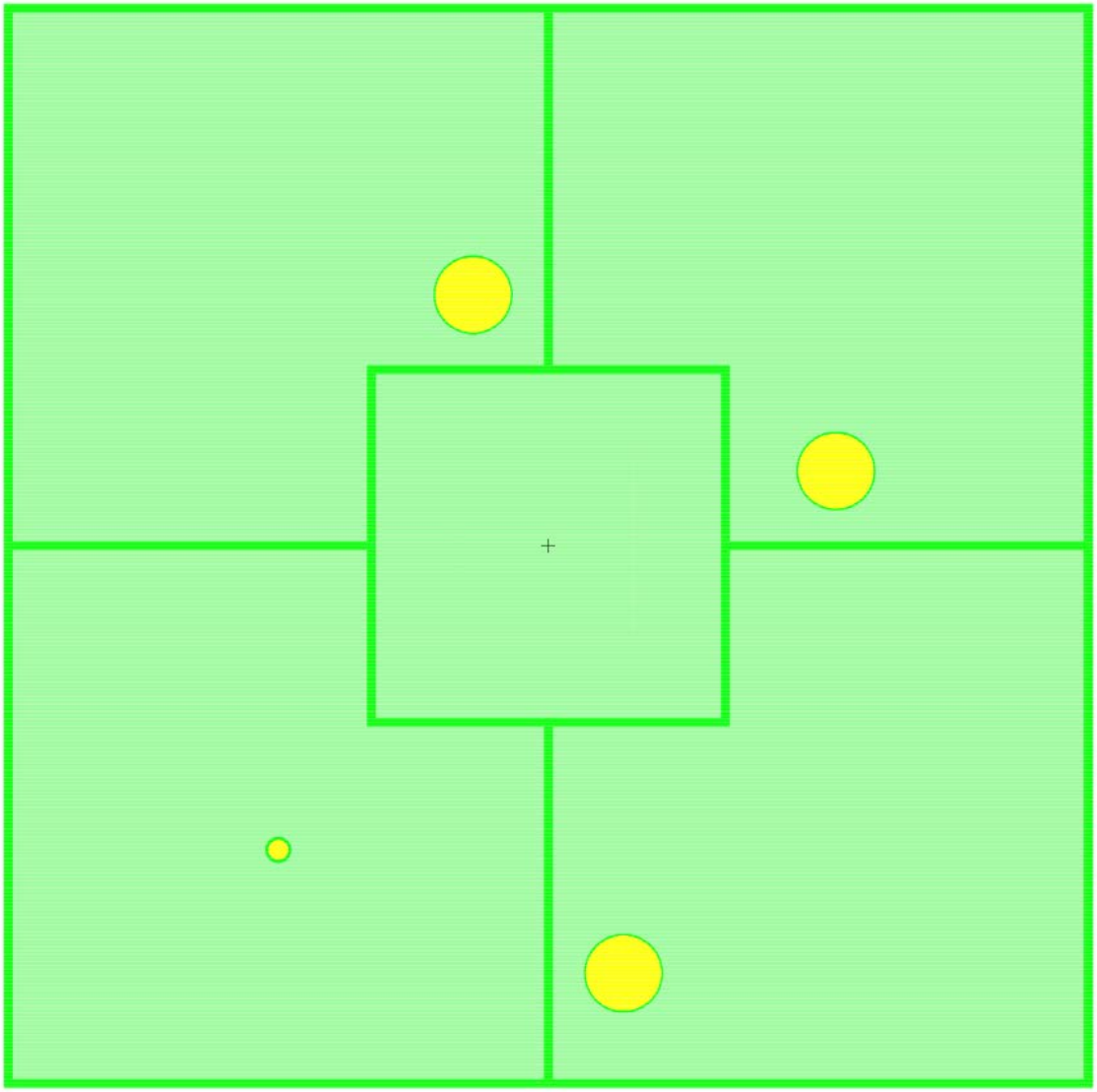

Figure 81. Fast zone of configuration 5 of Table I between z = 34.1 and z = 43.6 cm (steel grid ends at z = 42 cm)

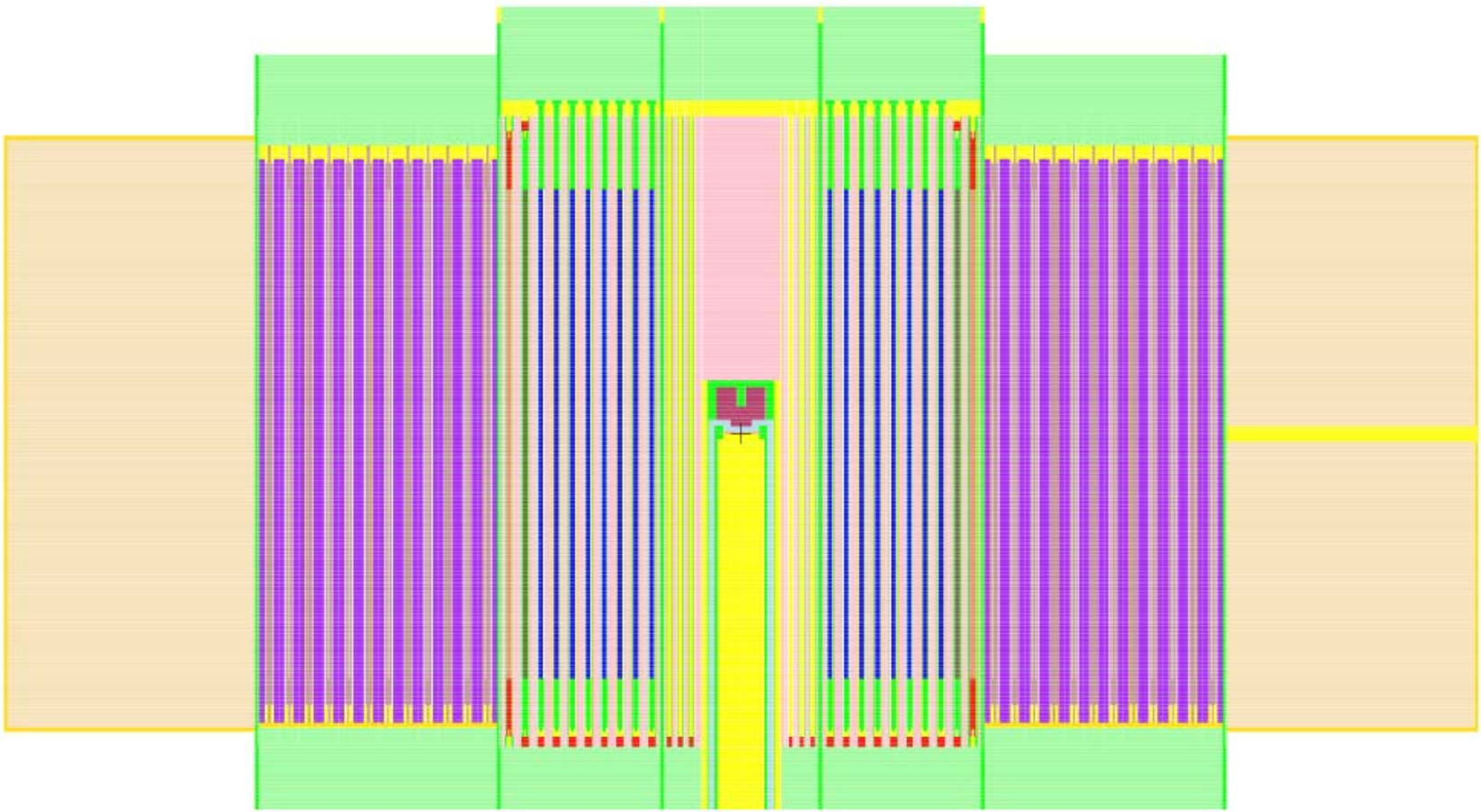

Figure 82. Vertical section of configuration 5 of Table I at y = 0.88 cm

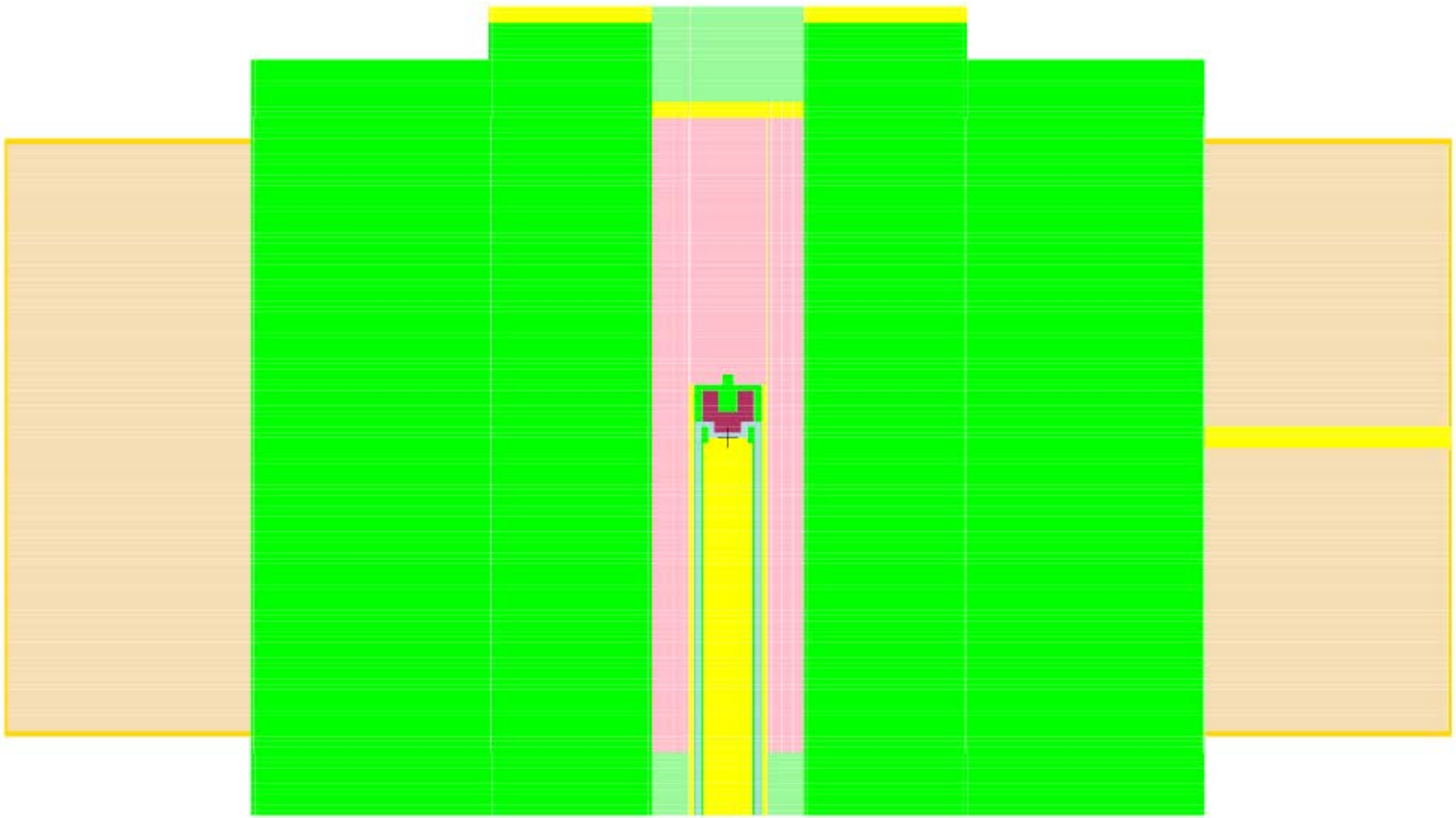

Figure 83. Vertical section of configuration 5 of Table I at y = 0 cm

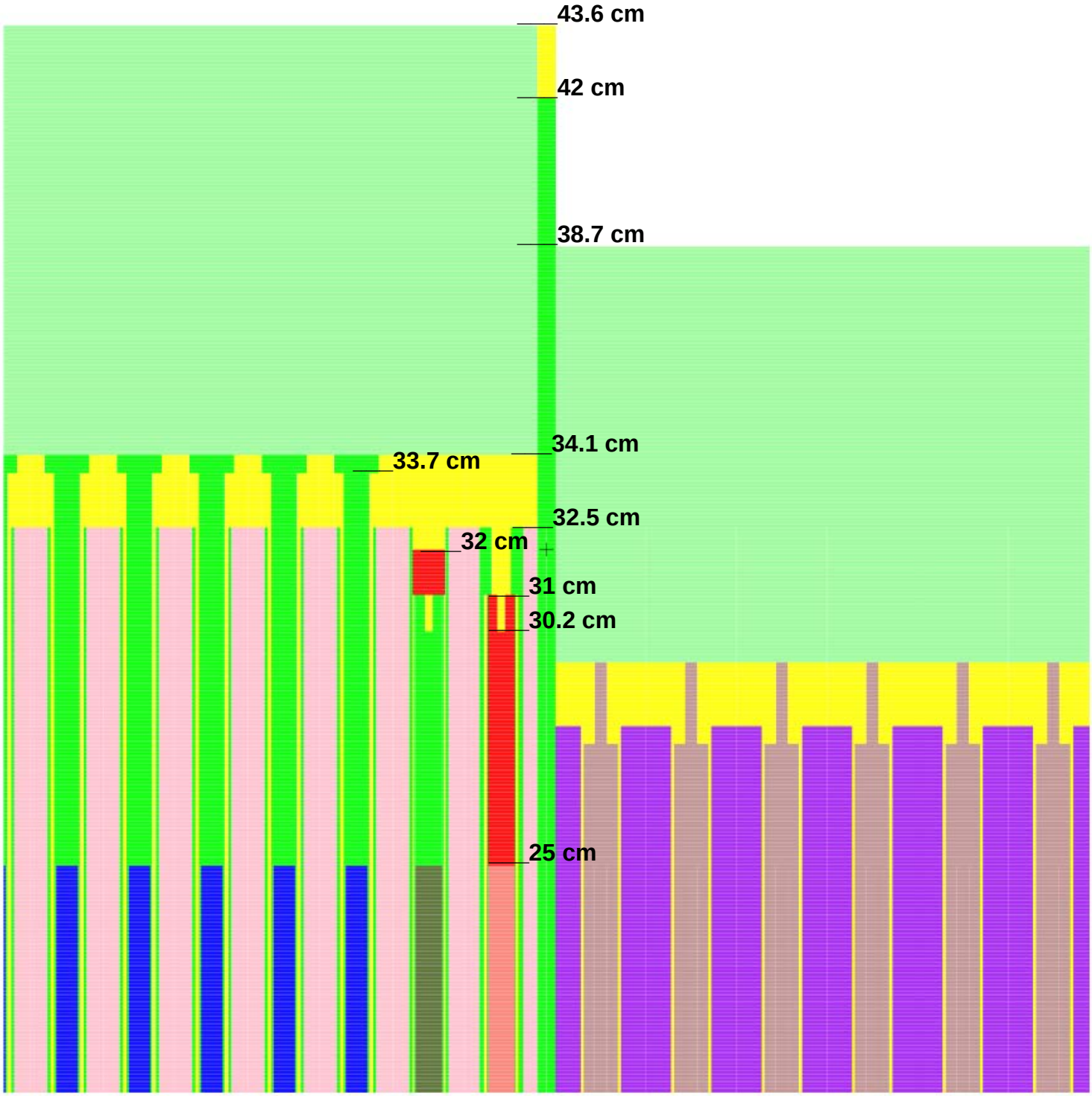

Figure 84. Top zoom of vertical section of configuration 5 of Table I; axial positions are relative at bottom surface of copper disk (z = 0 cm); in this configuration, offset (relative to bottom surface of copper disk) of active fuel length of 21% enriched fuel has not been taken into account

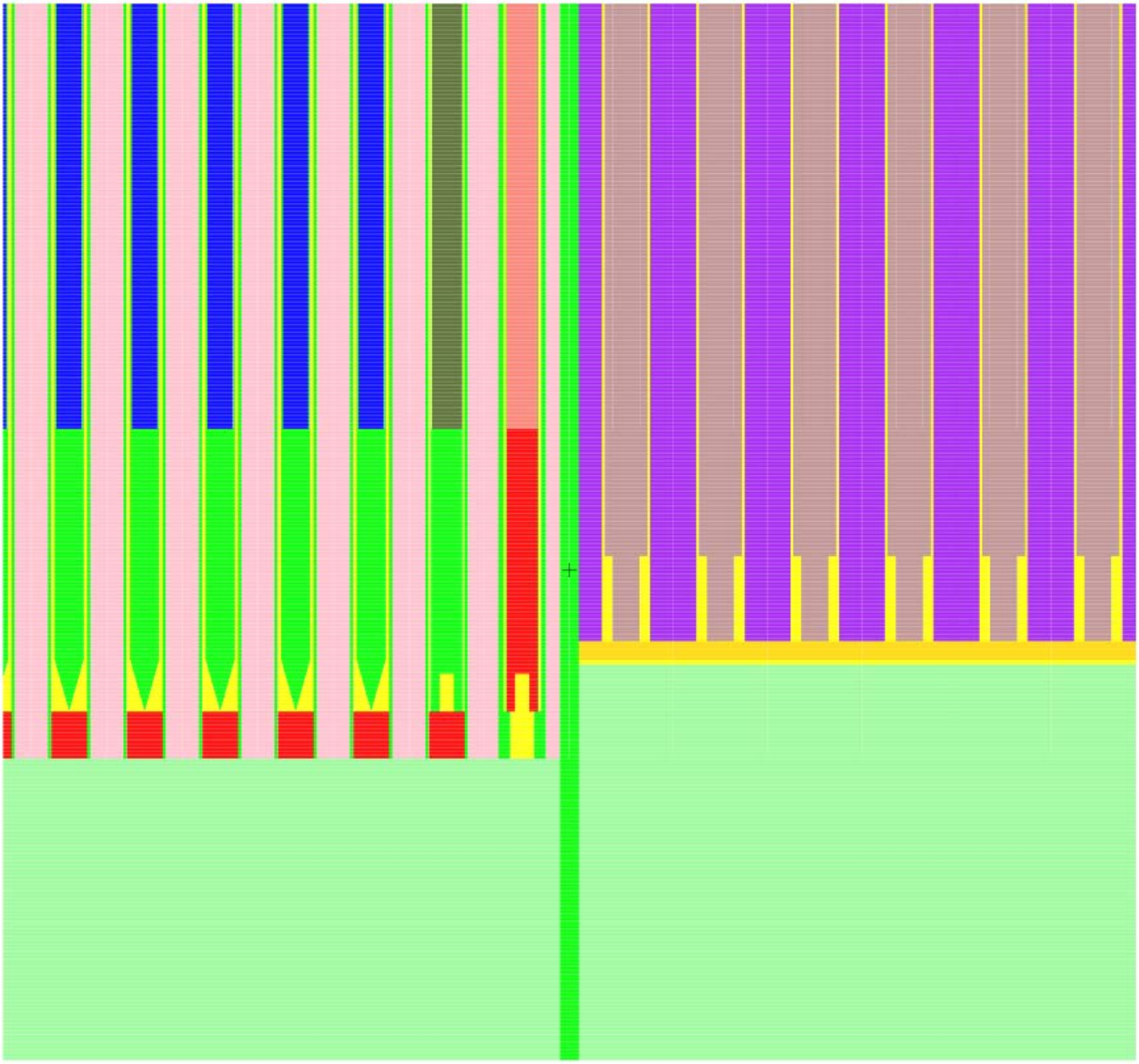

Figure 85. Bottom zoom of vertical section of configuration 5 of Table I

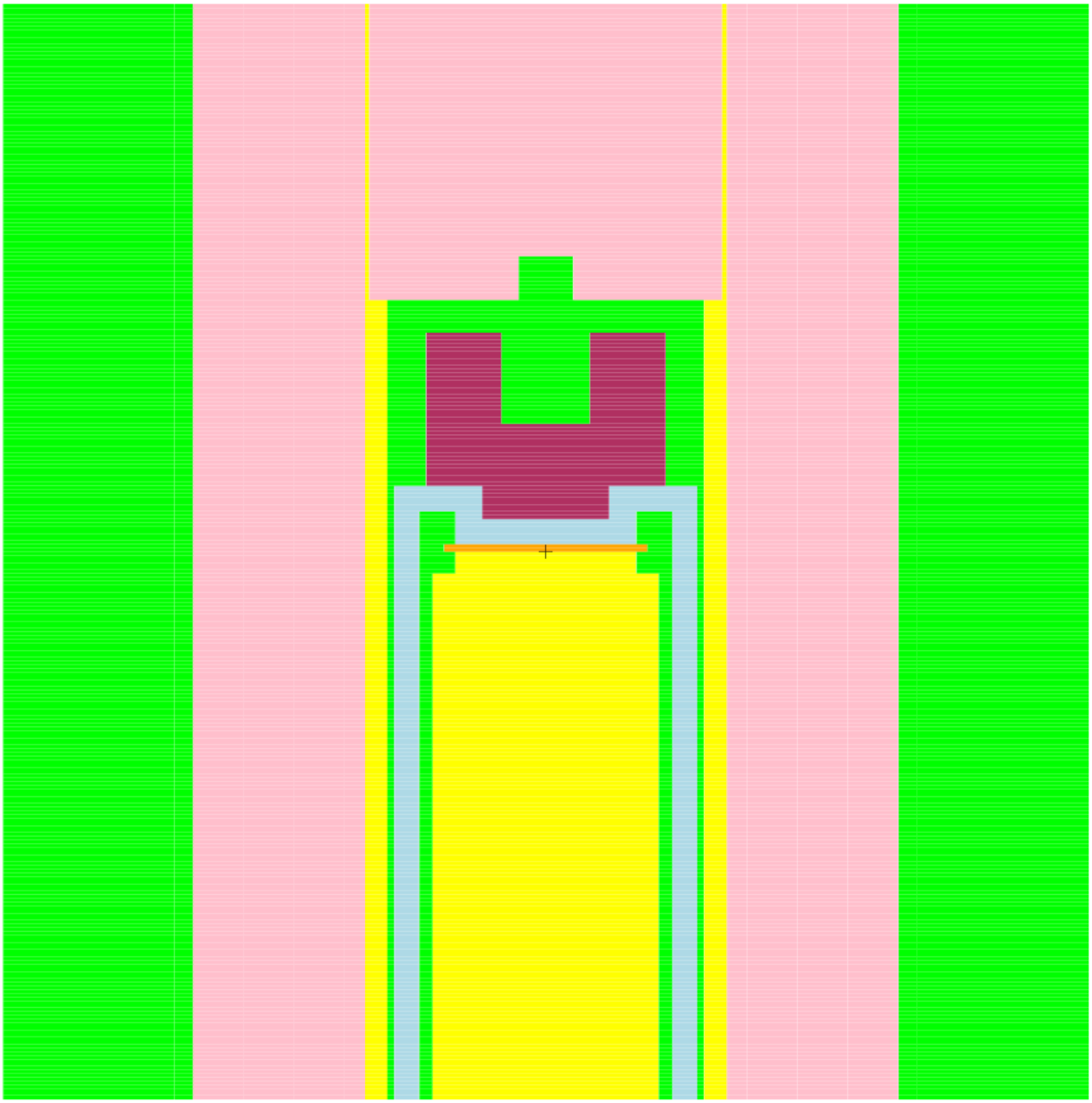

Figure 86. Zoom of target zone of configuration 5 of Table I

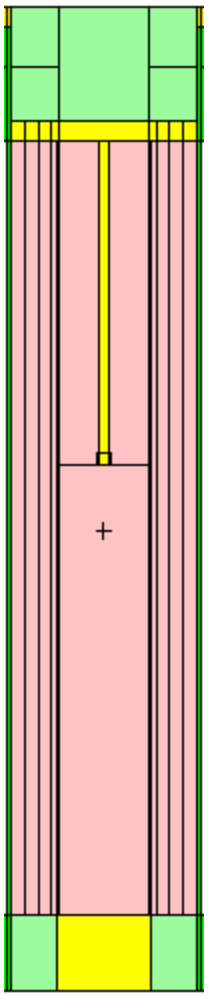

Figure 87. Vertical section of target zone (8 x 82 cm) of configuration 5 of Table I when the Cf beam tube is removed and replaced by a lead block; only the upper lead block has a hole; this arrangement was used only for calculations of Figures 123 and 124

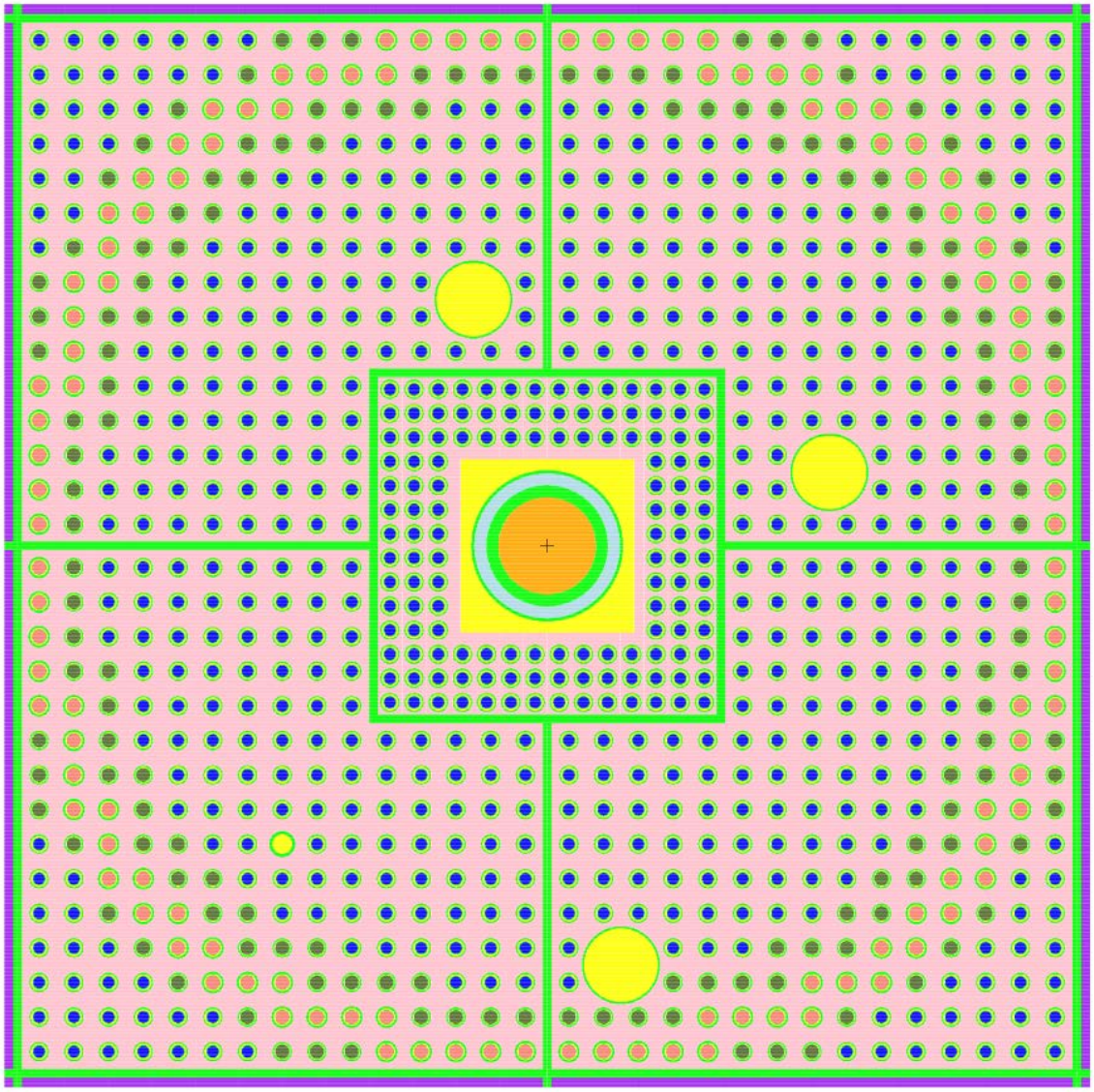

Figure 88. Fast zone of annular configuration 6 of Table I at z = 0 cm

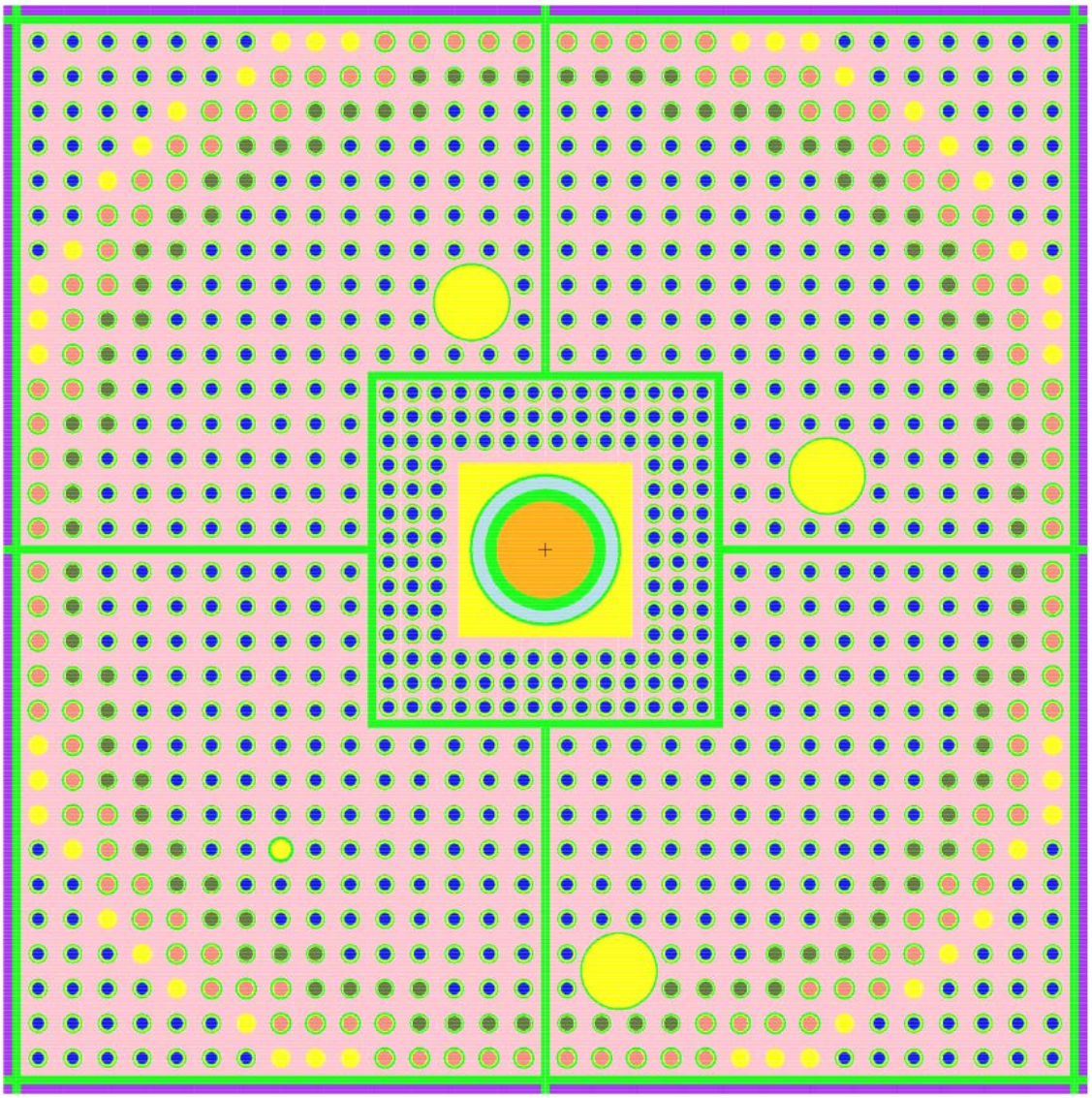

Figure 89. Fast zone of annular configuration 7 of Table I at z = 0 cm

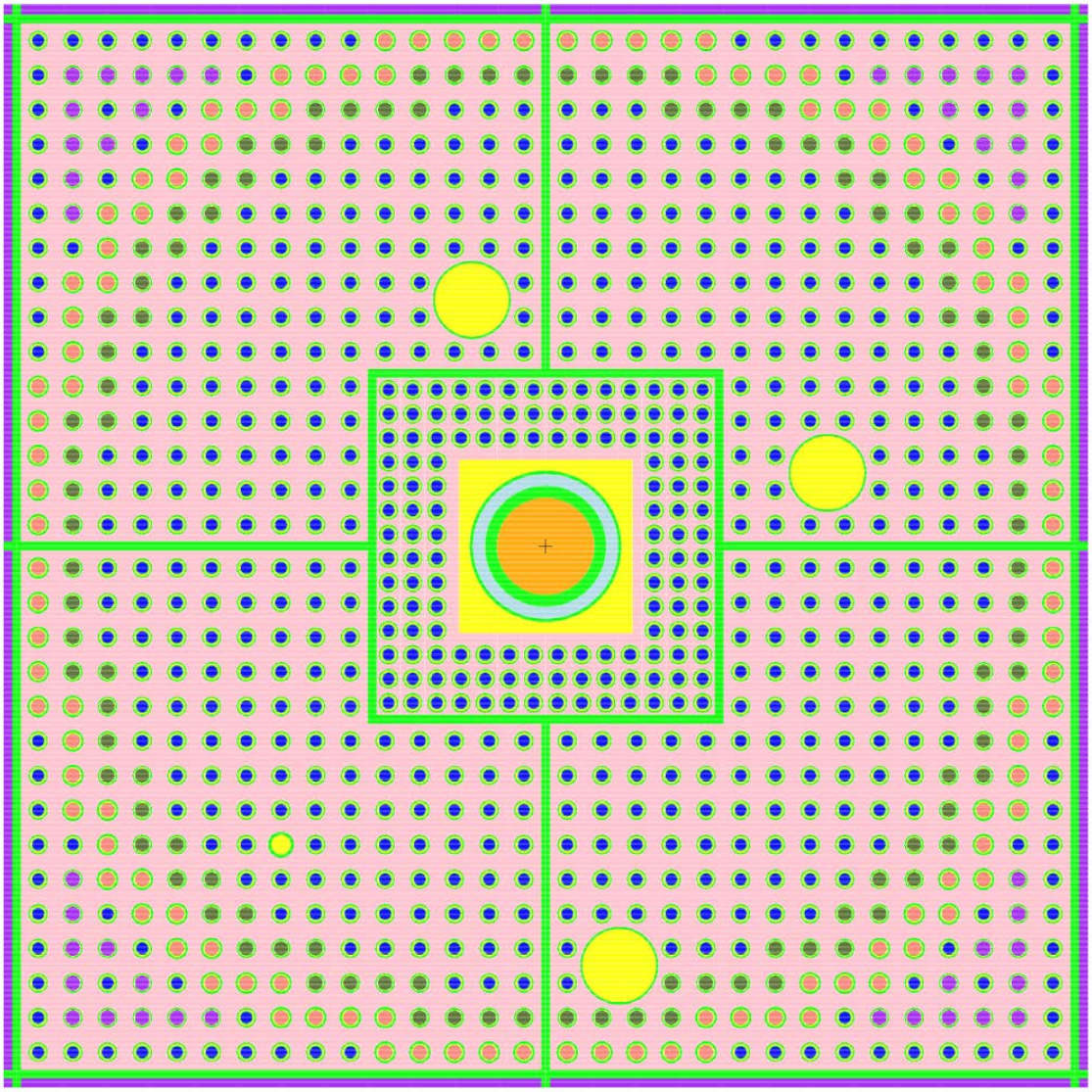

Figure 90. Fast zone of annular configuration 8 of Table I at z = 0 cm; 44 polyethylene rods in outer fast zone

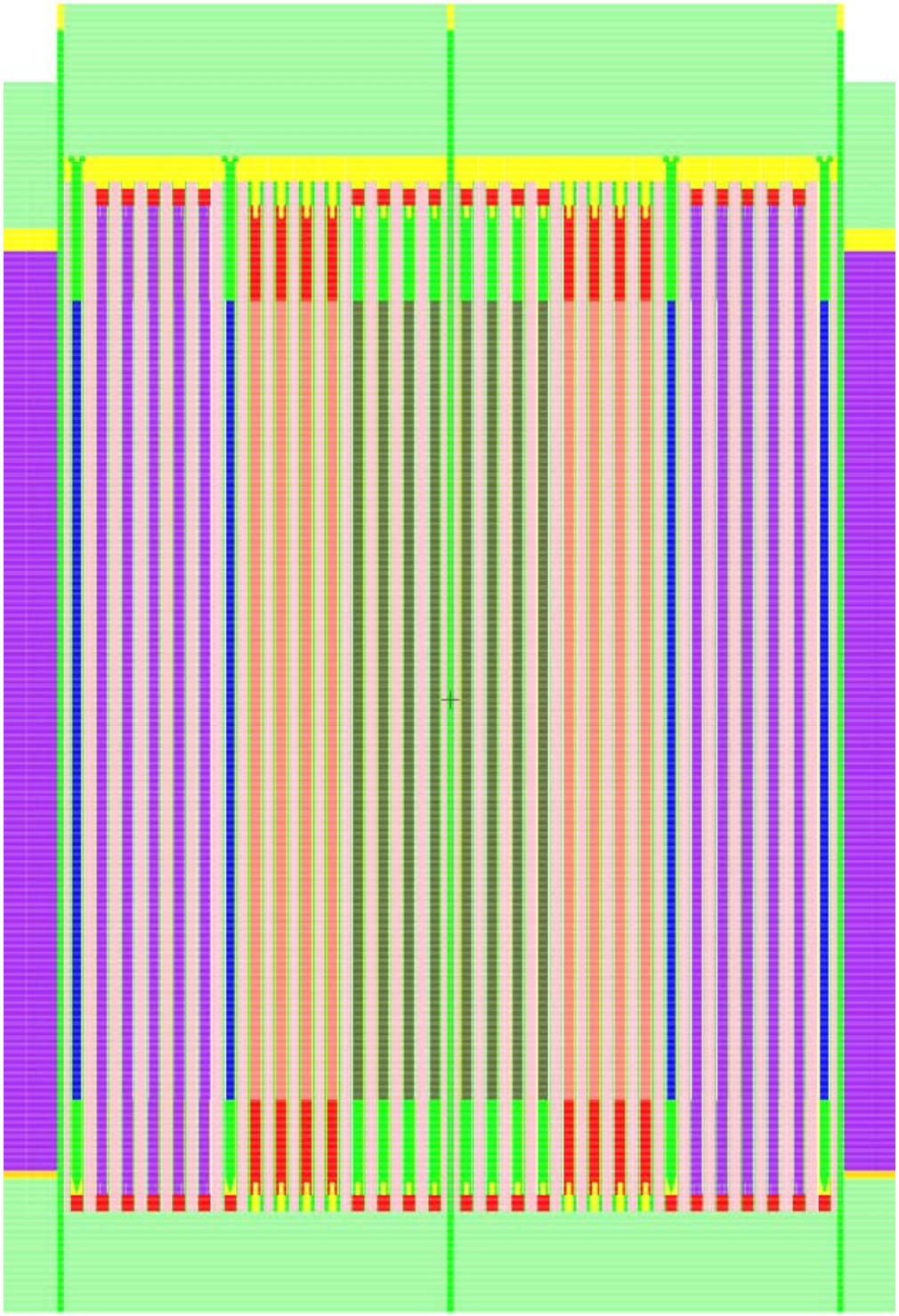

Figure 91. Vertical section of fast zone of annular configuration 8 of Table I; 44 polyethylene rods in outer fast zone

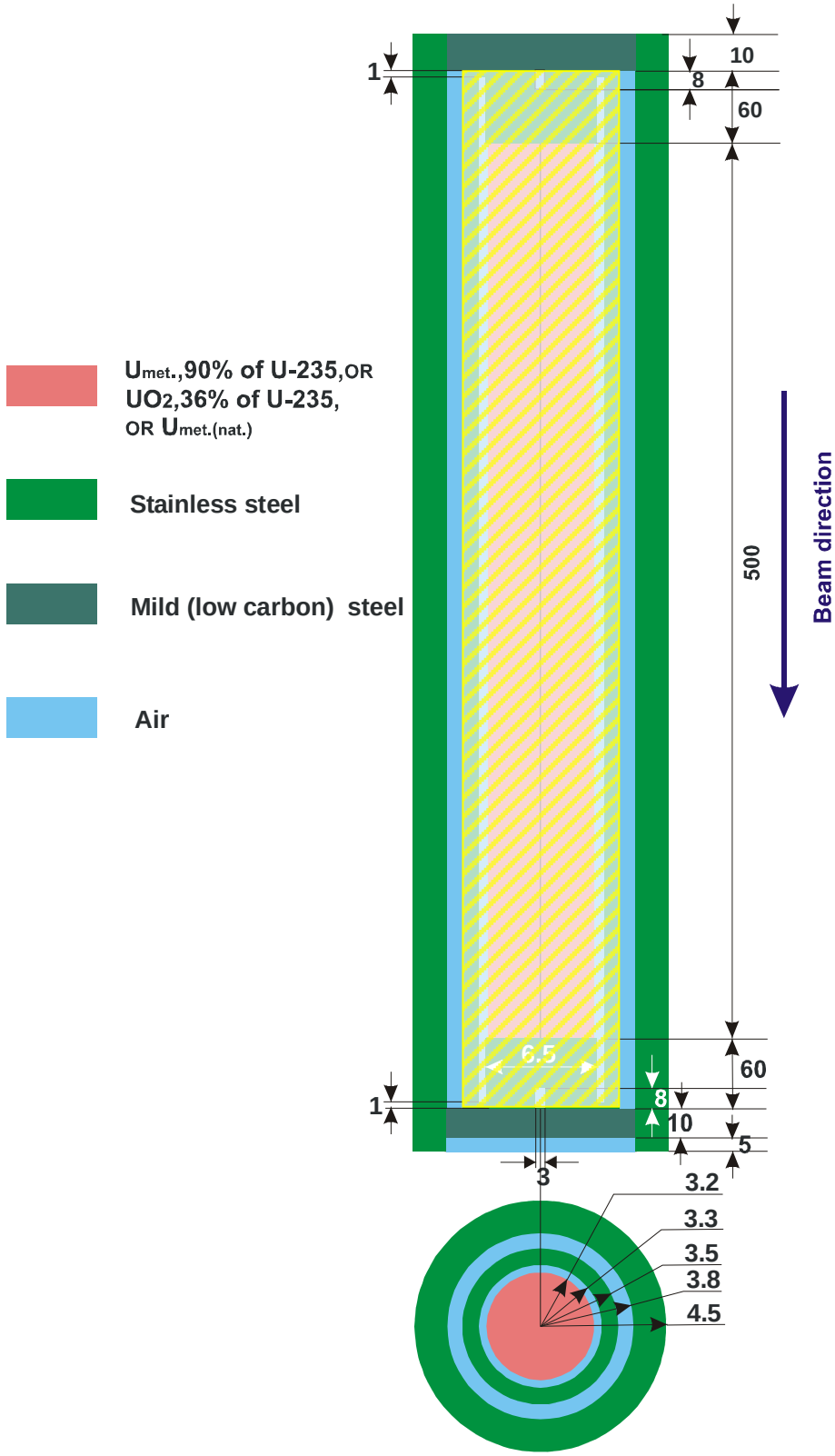

Figure 92. Geometry specifications of 90%, 36% enriched, and natural uranium fuel rods. Cross hatched yellow area highlights the polyethylene rod used in configuration 8 of Table I, dimensions in mm

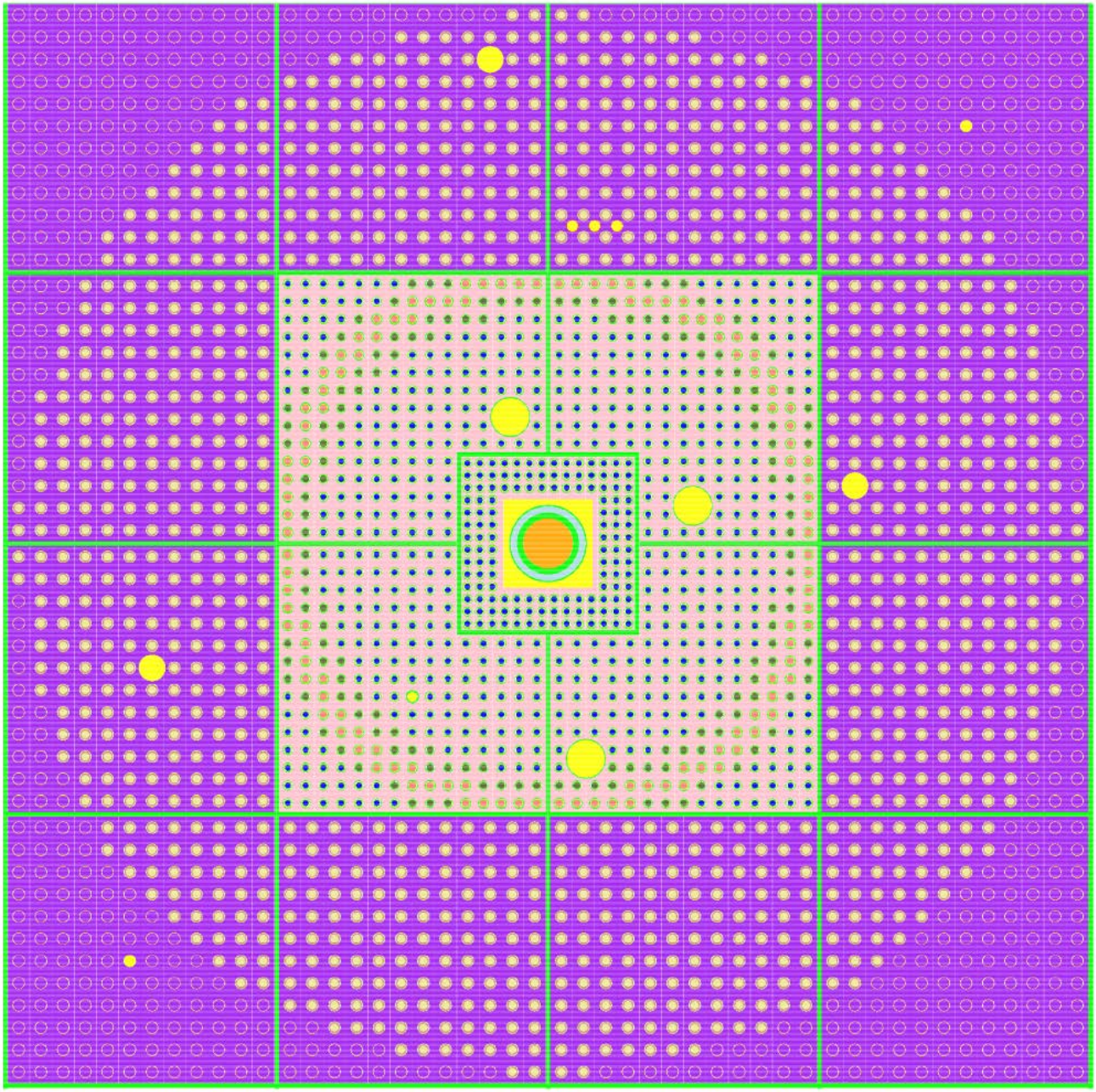

Figure 93. Fuel zone of (annular) configuration 9 of Table I at z = 0 cm; 538 polyethylene rods in thermal zone

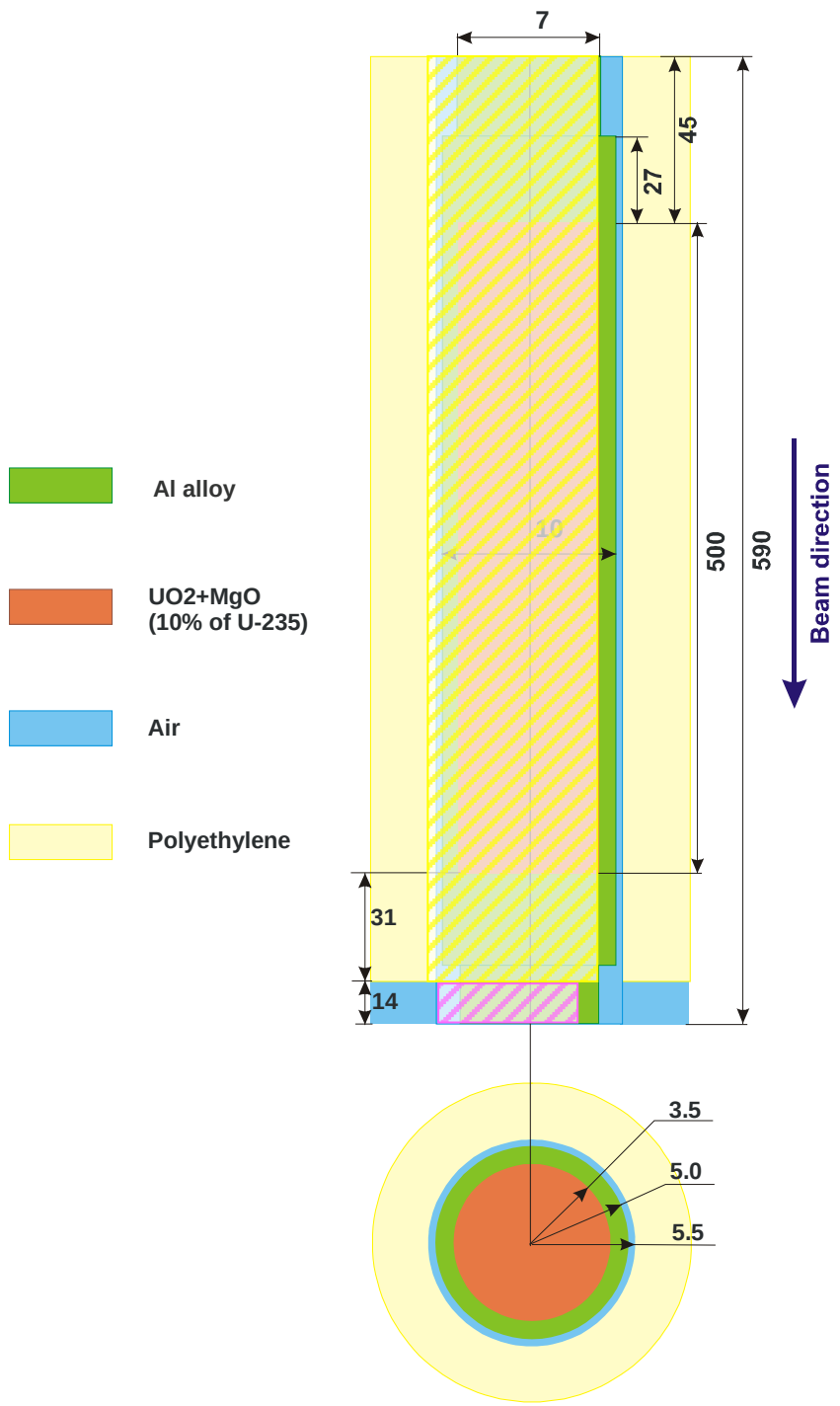

Figure 94. Geometry specifications of 10% enriched uranium rod. Cross hatched yellow area highlights the polyethylene rod used in configuration 9 of Table I. Cross hatched pink area highlights the steel region replaced by air when the polyethylene rod is used configuration 9 of Table I, dimensions in mm

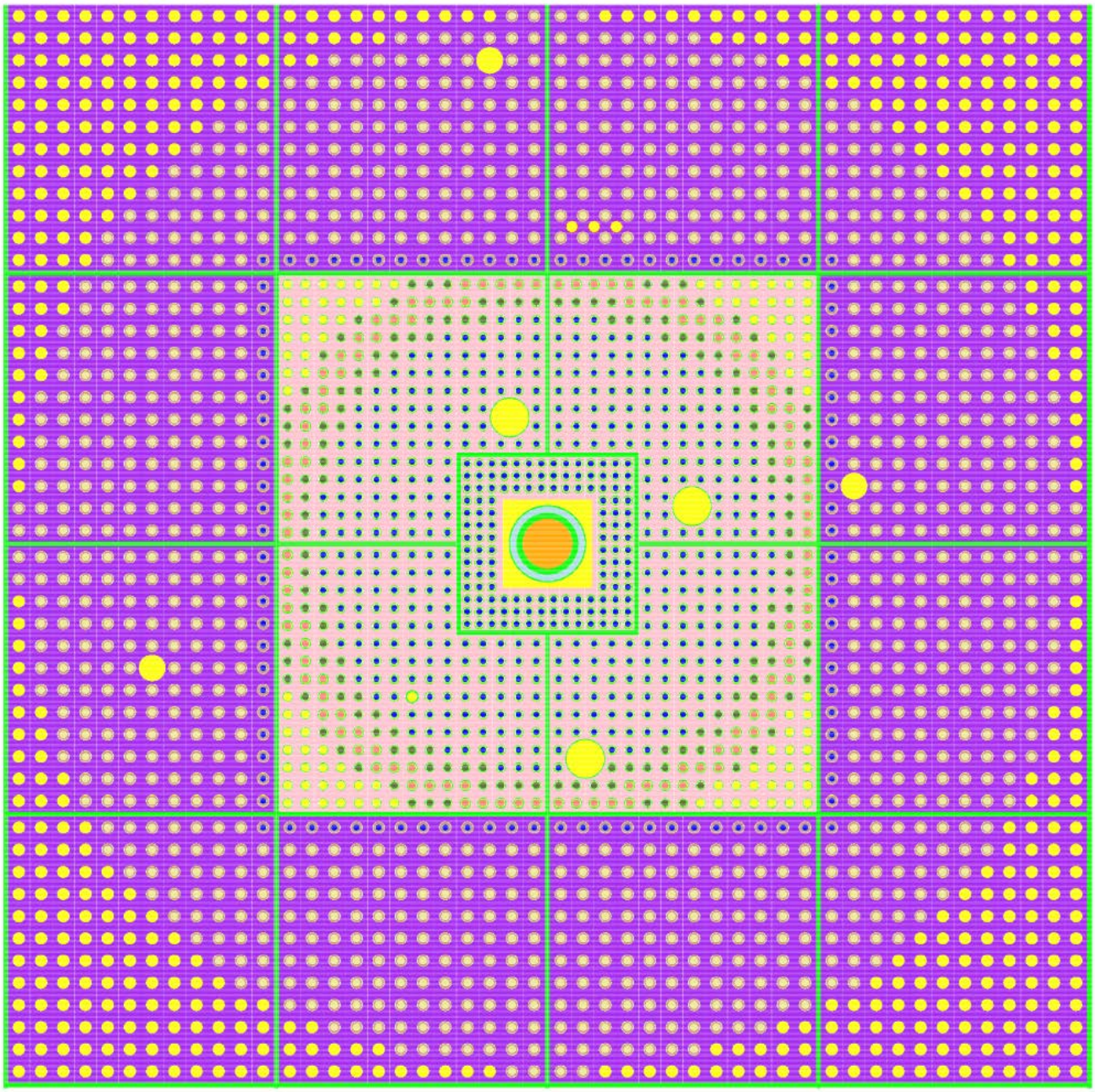

Figure 95. Fuel zone of annular configuration 10 of Table I at z = 0 cm; 100 21% enriched fuel rods in thermal zone

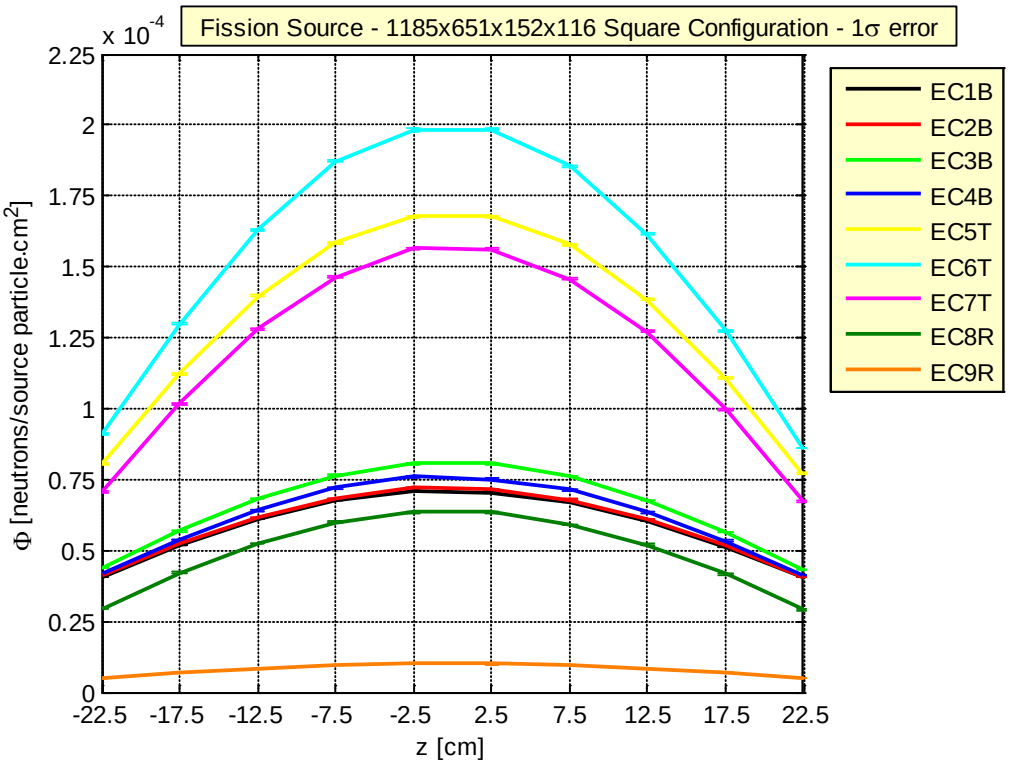

Figure 96. Axial flux distribution from criticality calculation for square configuration 5

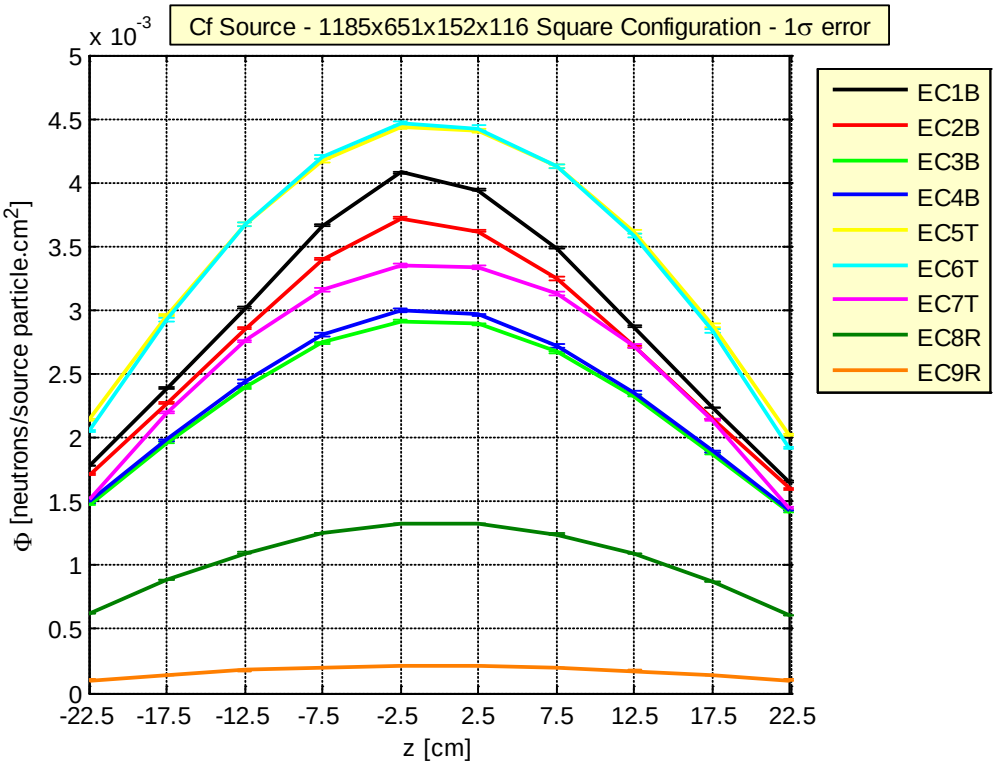

Figure 97. Axial flux axial distribution from Cf neutron source for square configuration 5

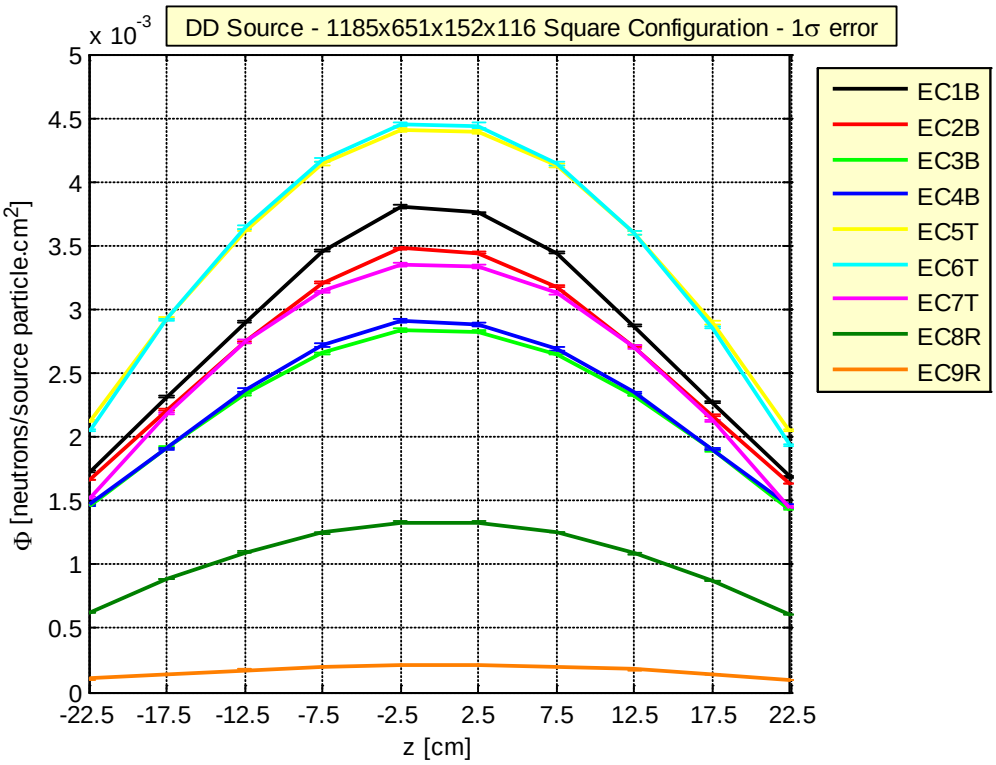

Figure 98. Axial flux profile from D-D neutron source for square configuration 5

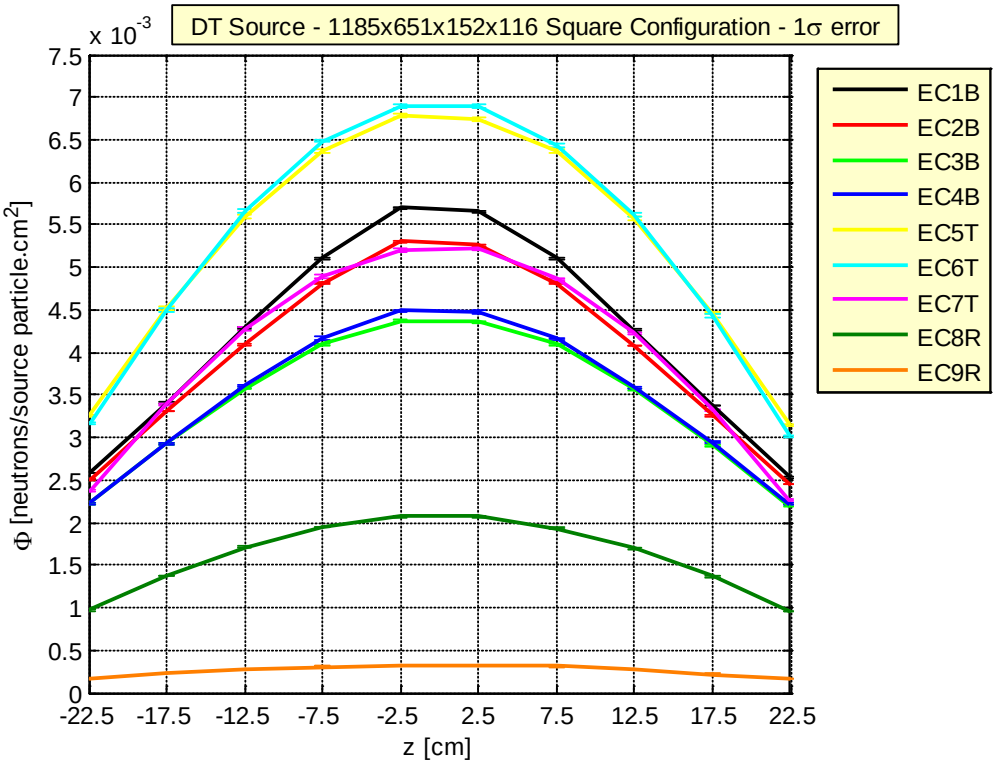

Figure 99. Axial flux distribution from D-T neutron source for square configuration 5

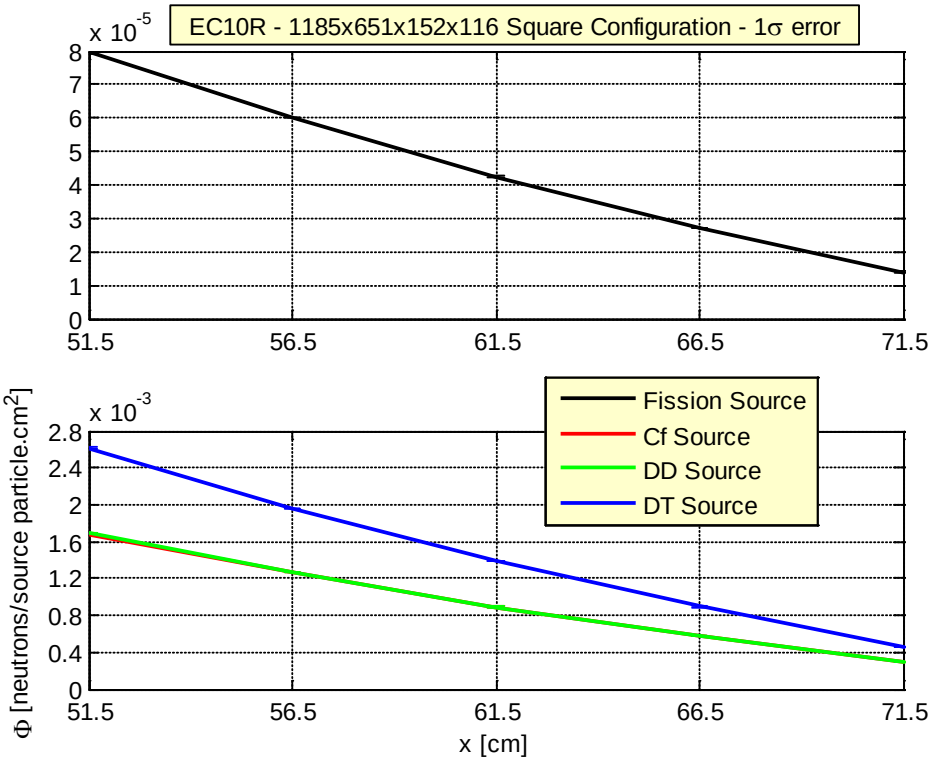

Figure 100. Radial flux distribution for square configuration 5

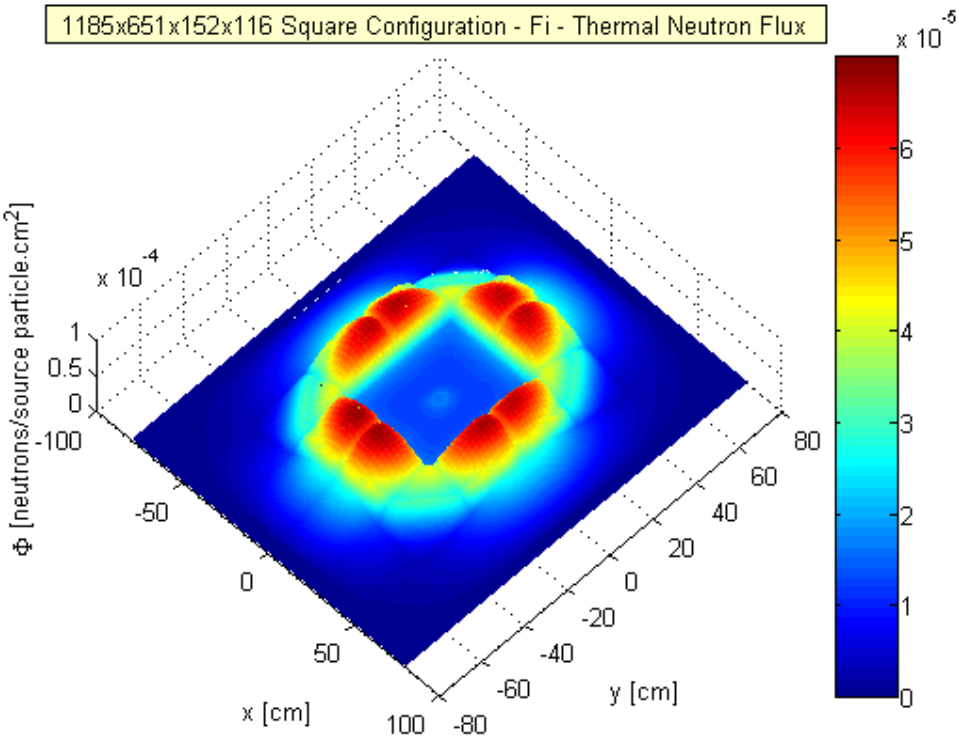

Figure 101. Thermal flux profile from criticality calculation for square configuration 5

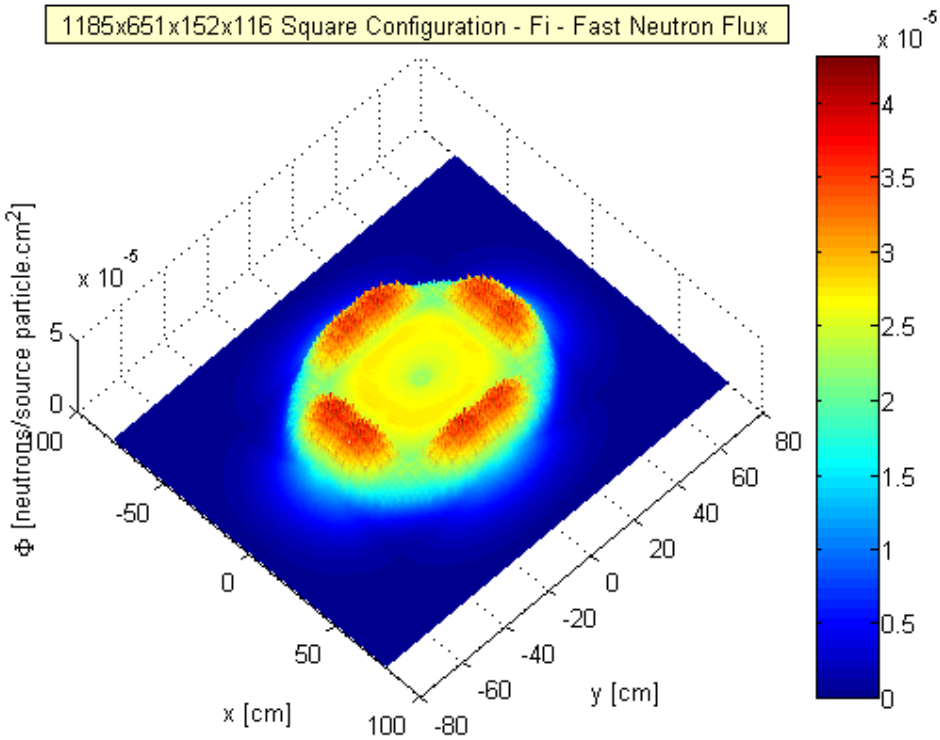

Figure 102. Fast flux profile from criticality calculation for square configuration 5

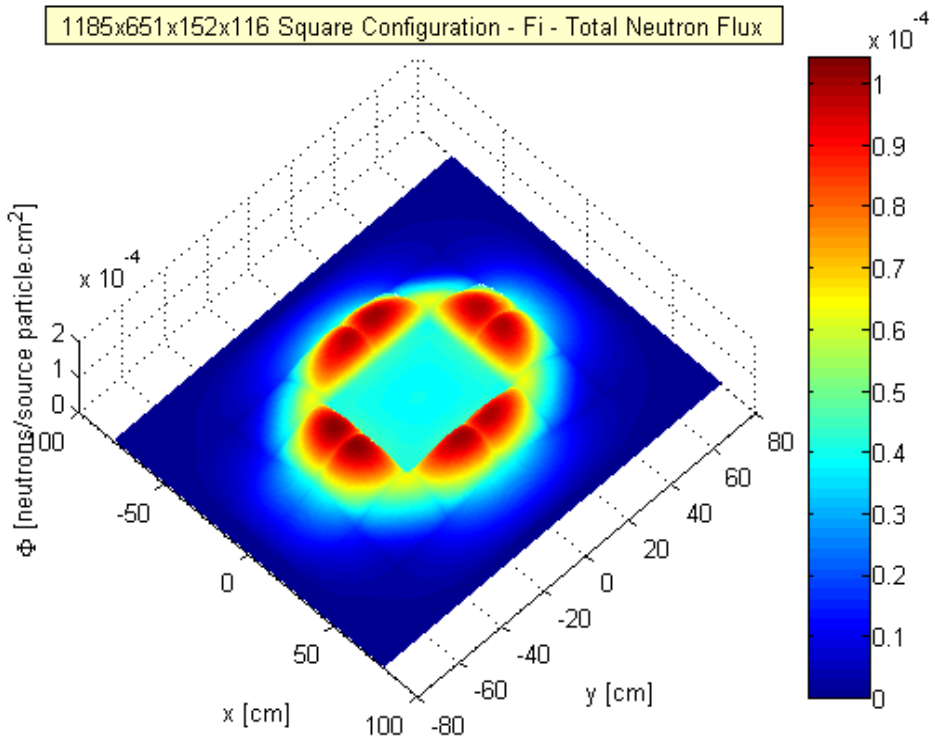

Figure 103. Total flux profile from criticality calculation for square configuration 5

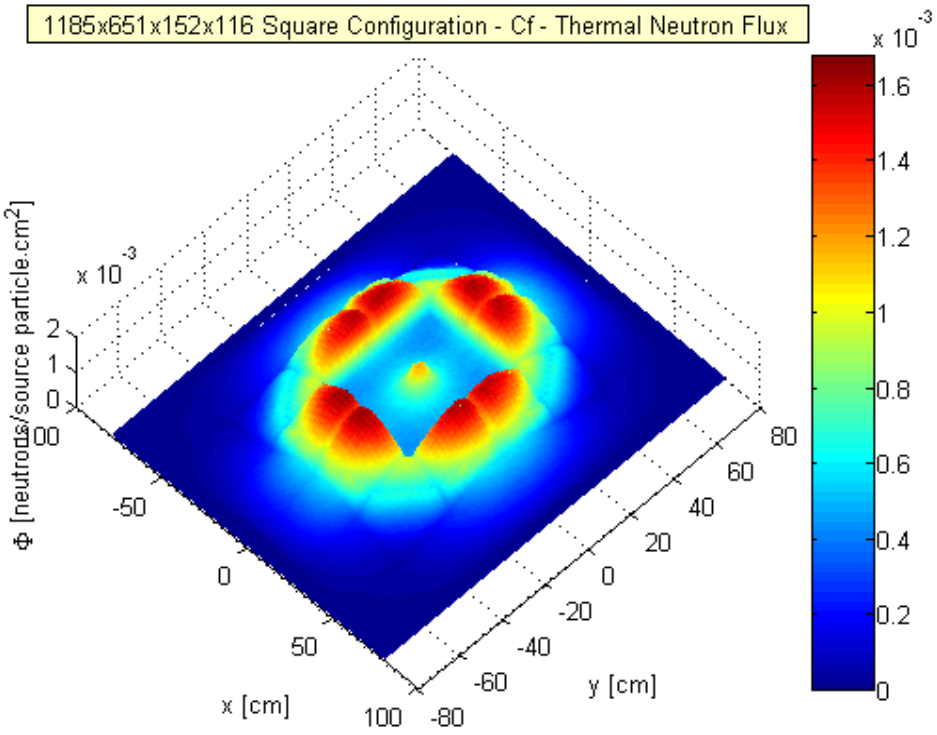

Figure 104. Thermal flux profile from Cf neutron source for square configuration 5

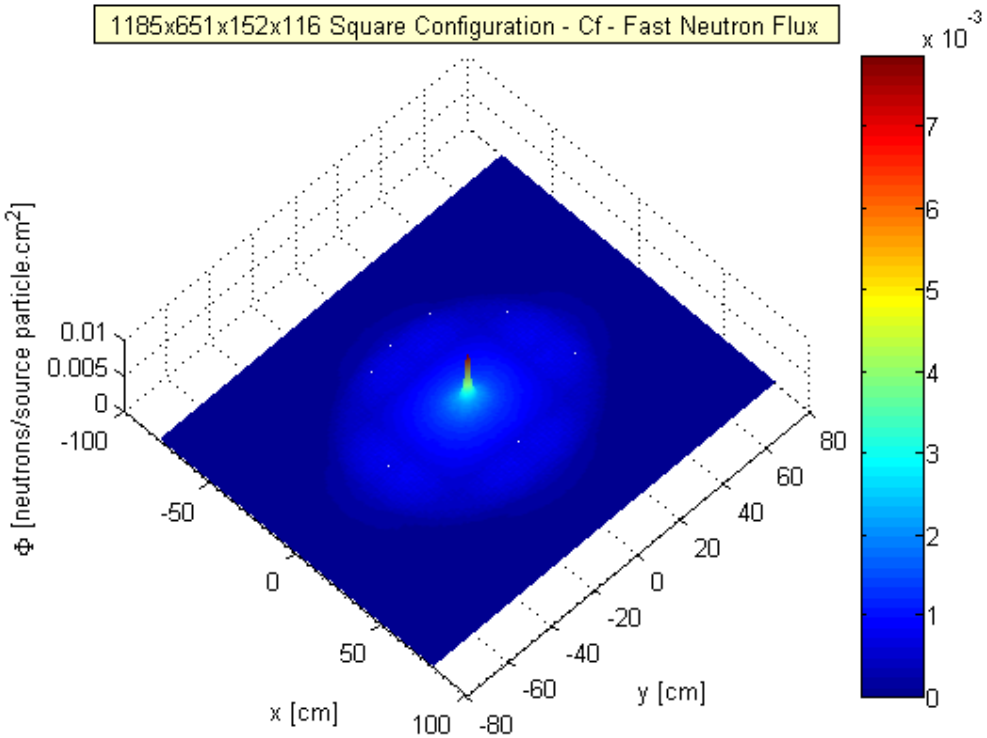

Figure 105. Fast flux profile from Cf neutron source for square configuration 5

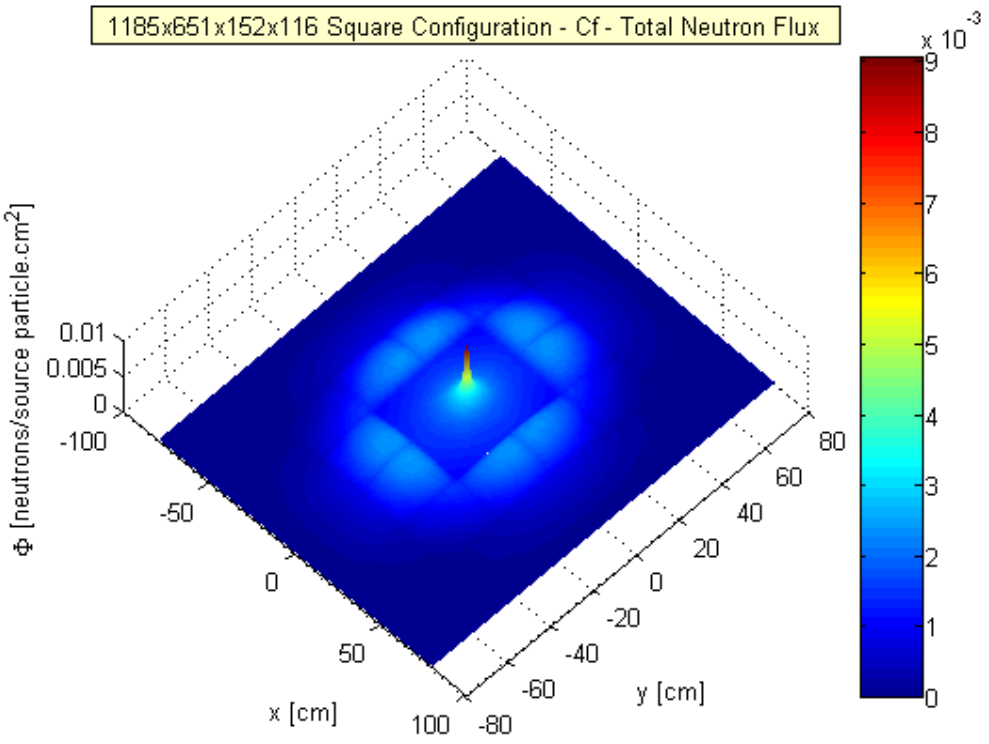

Figure 106. Total flux profile from Cf neutron source for square configuration 5

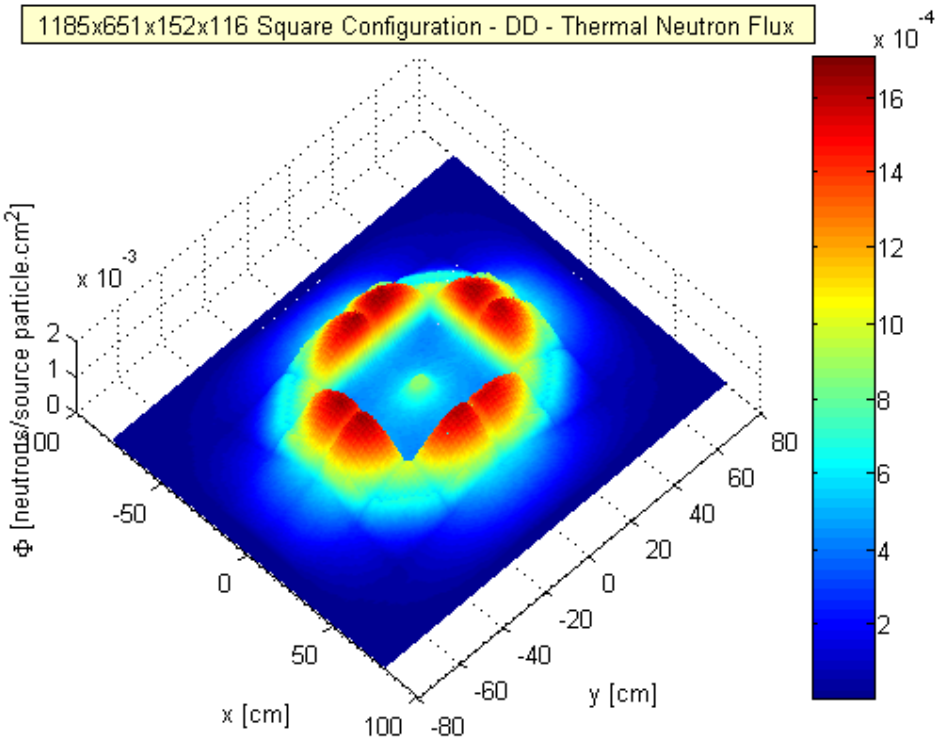

Figure 107. Thermal flux profile from D-D neutron source for square configuration 5

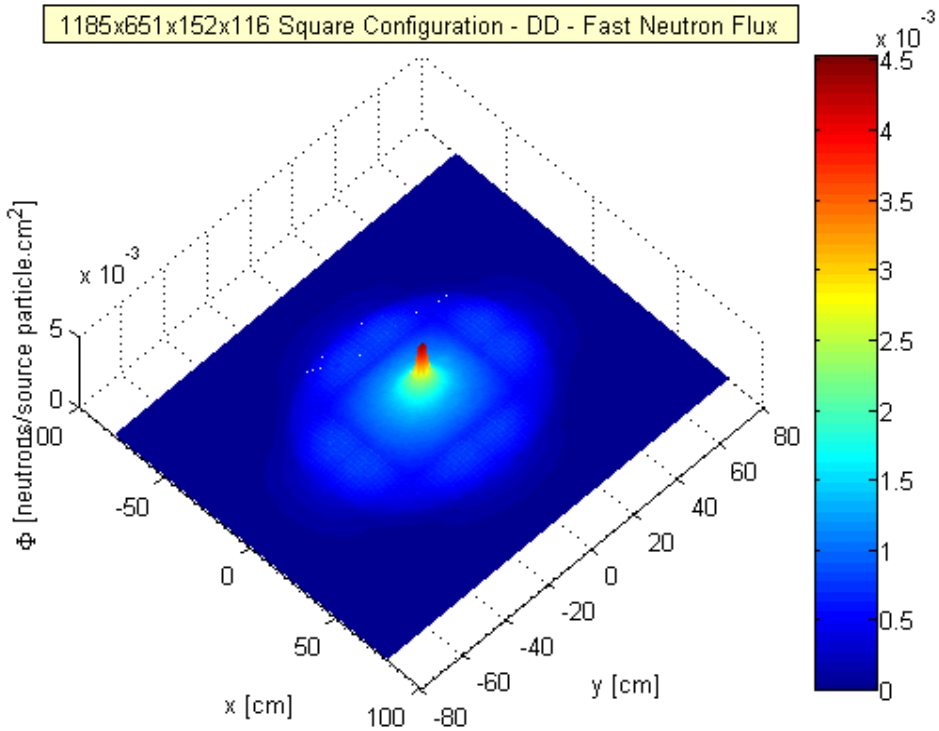

Figure 108. Fast flux profile from D-D neutron source for square configuration 5

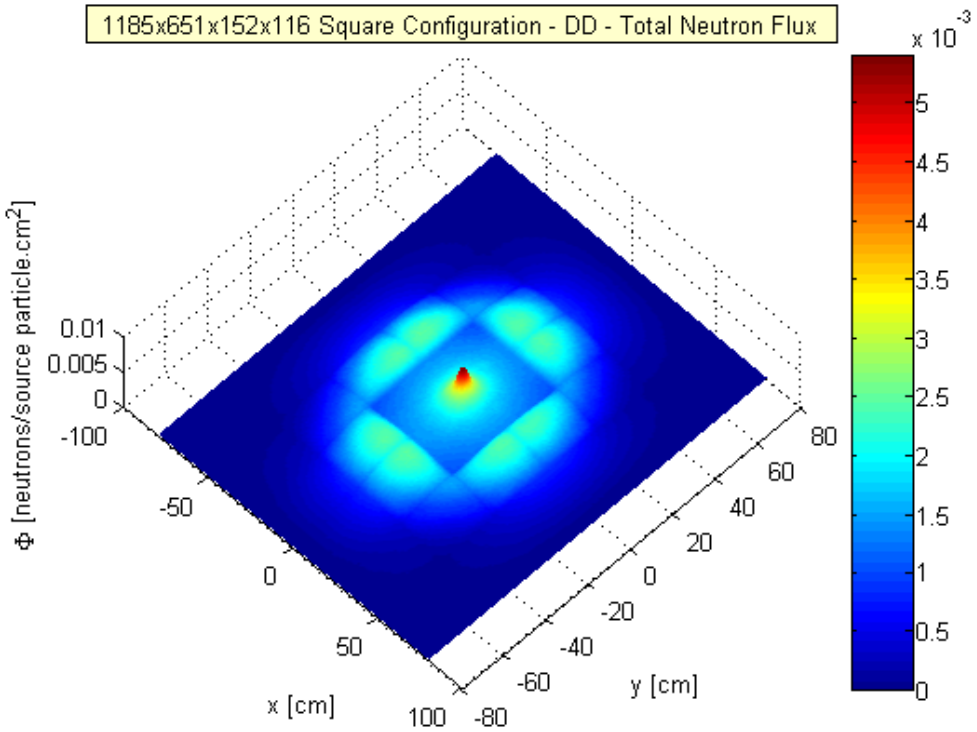

Figure 109. Total flux profile from D-D neutron source for square configuration 5

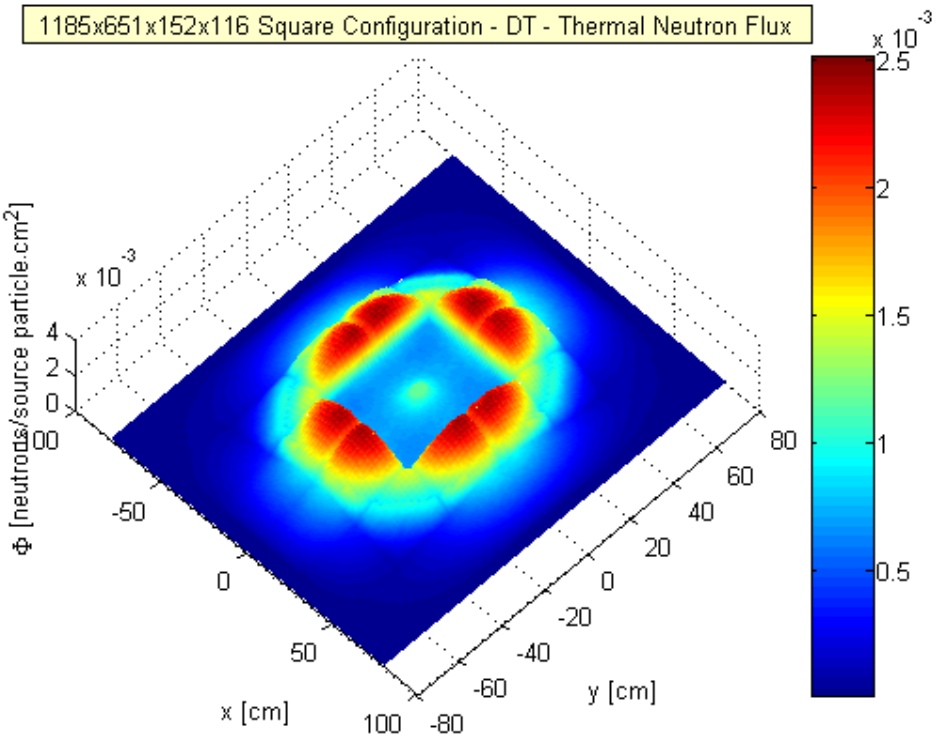

Figure 110. Thermal flux profile from D-T neutron source for square configuration 5

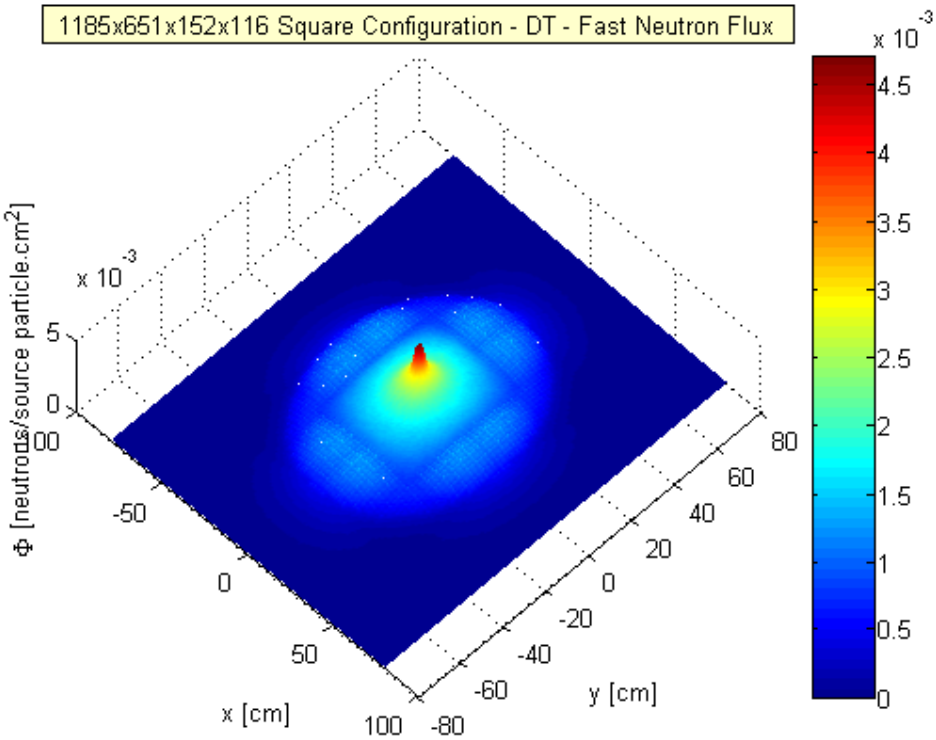

Figure 111. Fast flux profile from D-T neutron source for square configuration 5

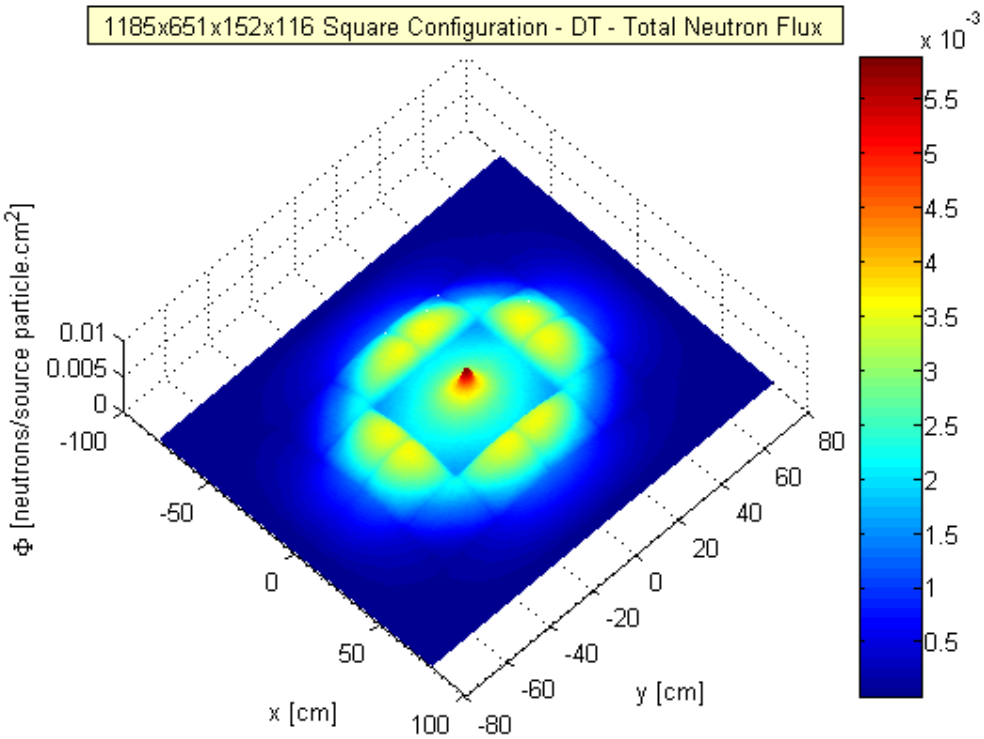

Figure 112. Total flux profile from D-T neutron source for square configuration 5

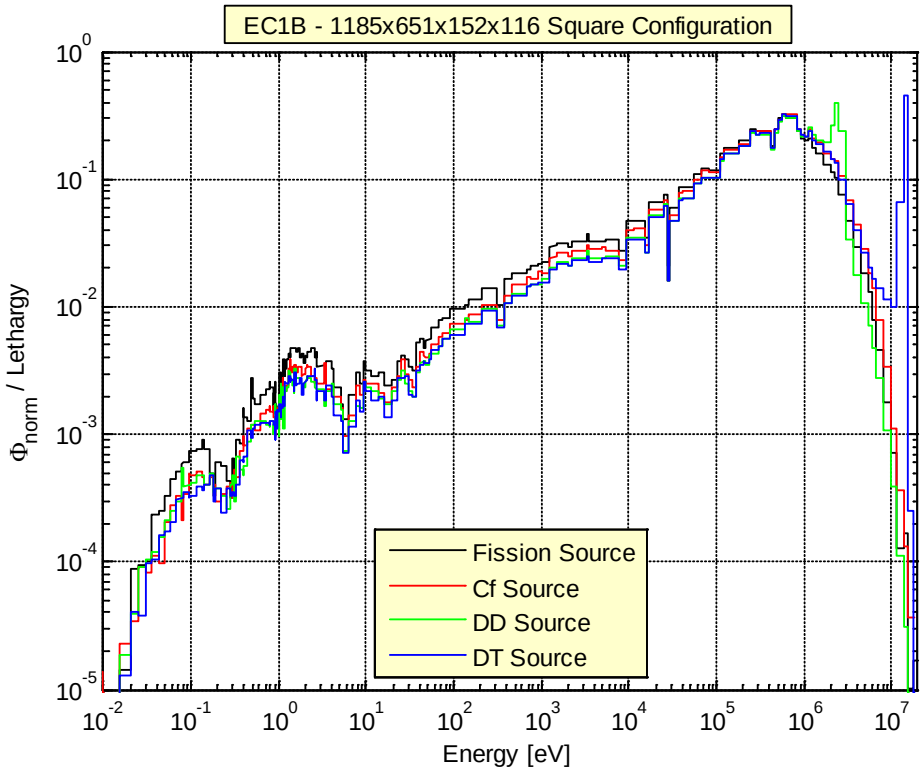

Figure 113. Normalized neutron spectrum in EC1B for square configuration 5

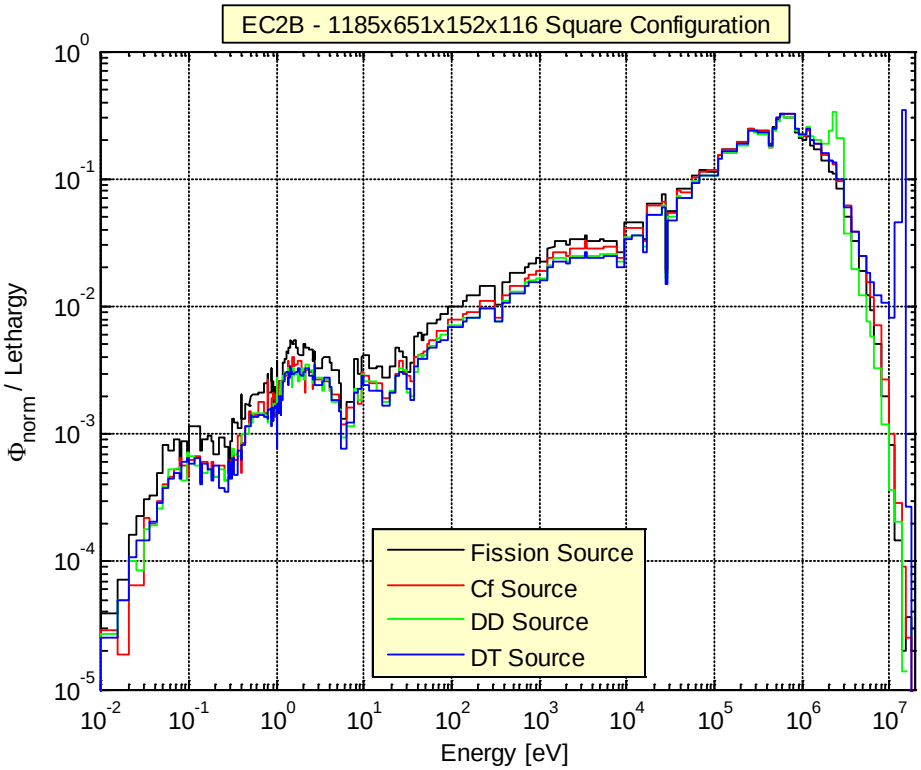

Figure 114. Normalized neutron spectrum in EC2B for square configuration 5

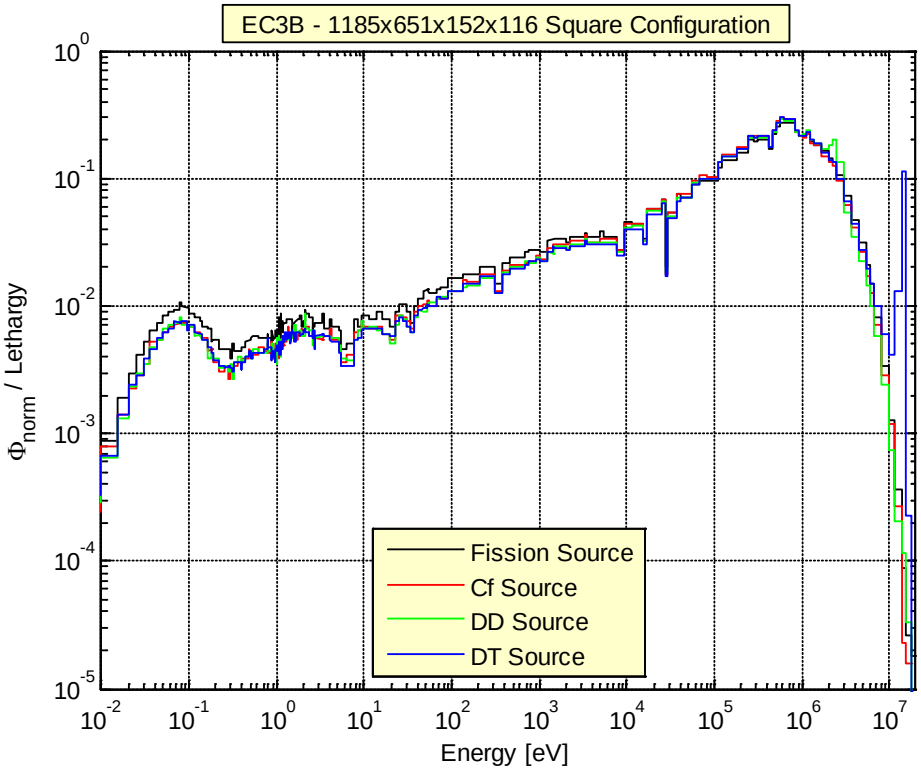

Figure 115. Normalized neutron spectrum in EC3B for square configuration 5

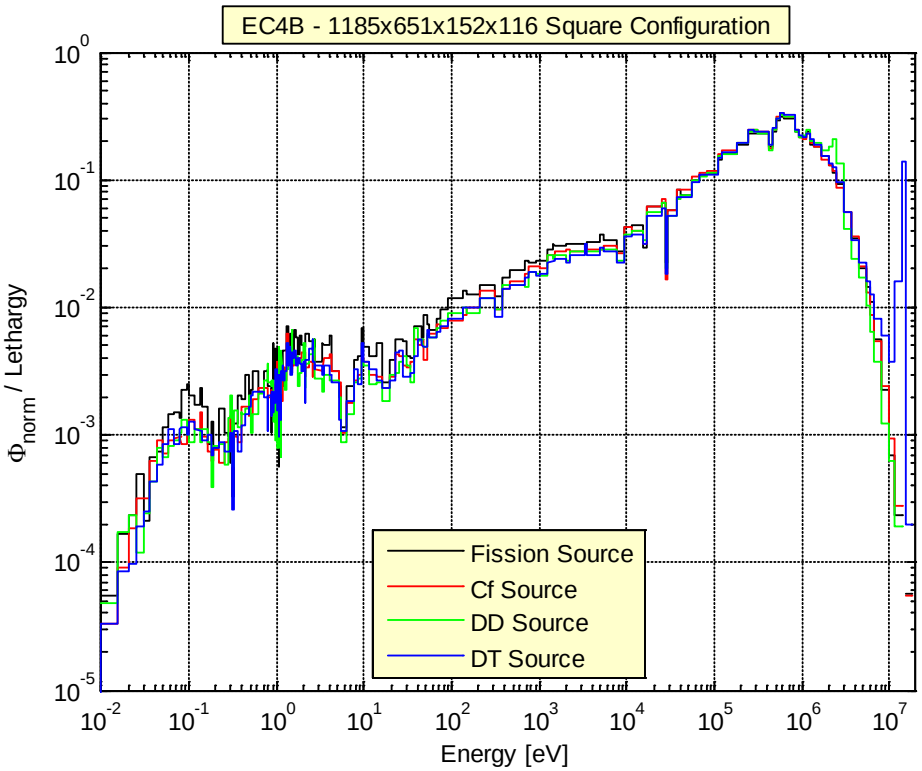

Figure 116. Normalized neutron spectrum in EC4B for square configuration 5

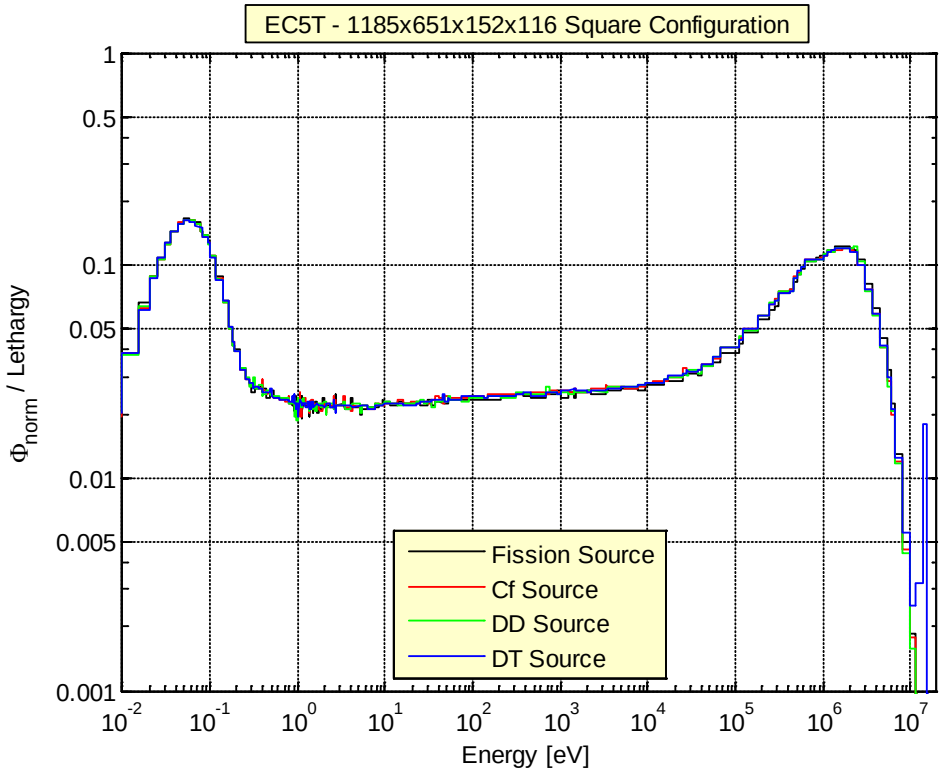

Figure 117. Normalized neutron spectrum in EC5T for square configuration 5

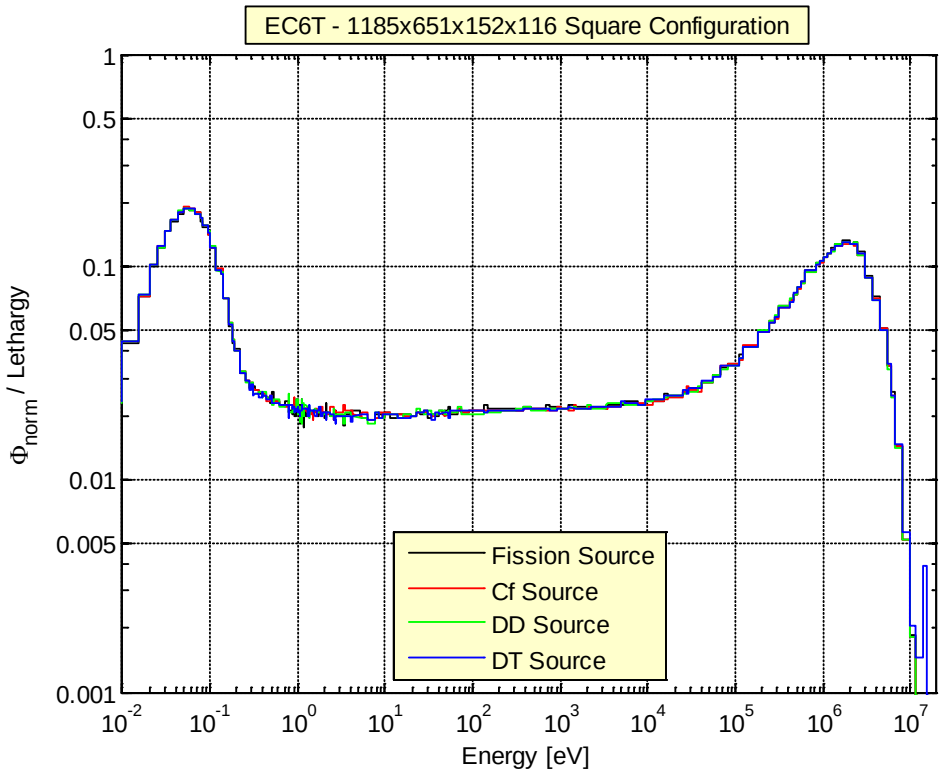

Figure 118. Normalized neutron spectrum in EC6T for square configuration 5

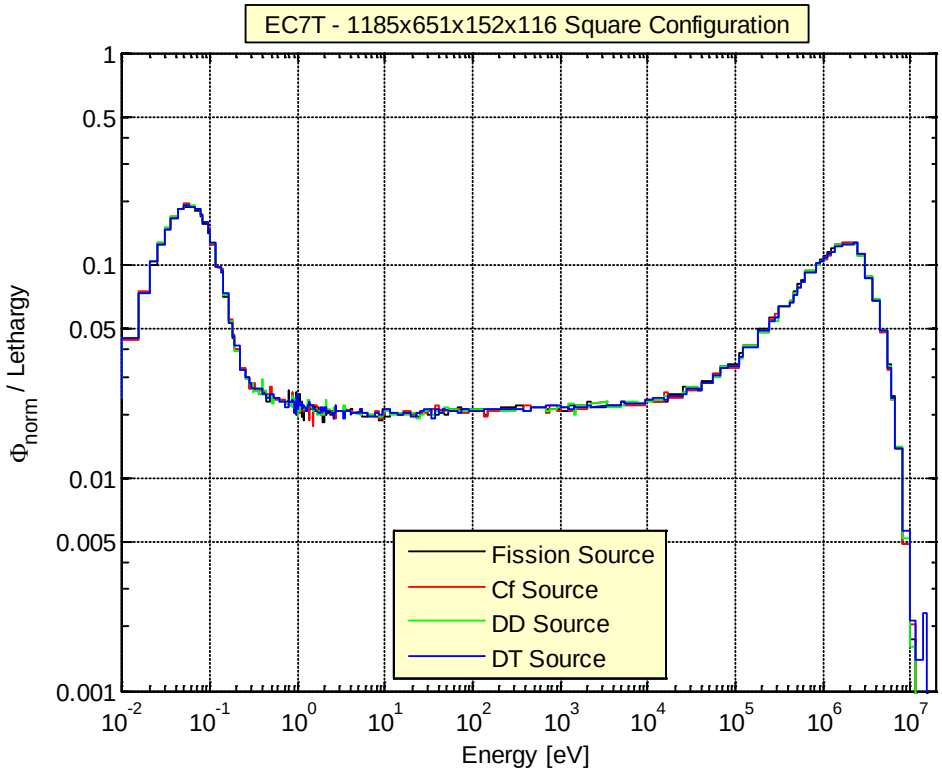

Figure 119. Normalized neutron spectrum in EC7T for square configuration 5

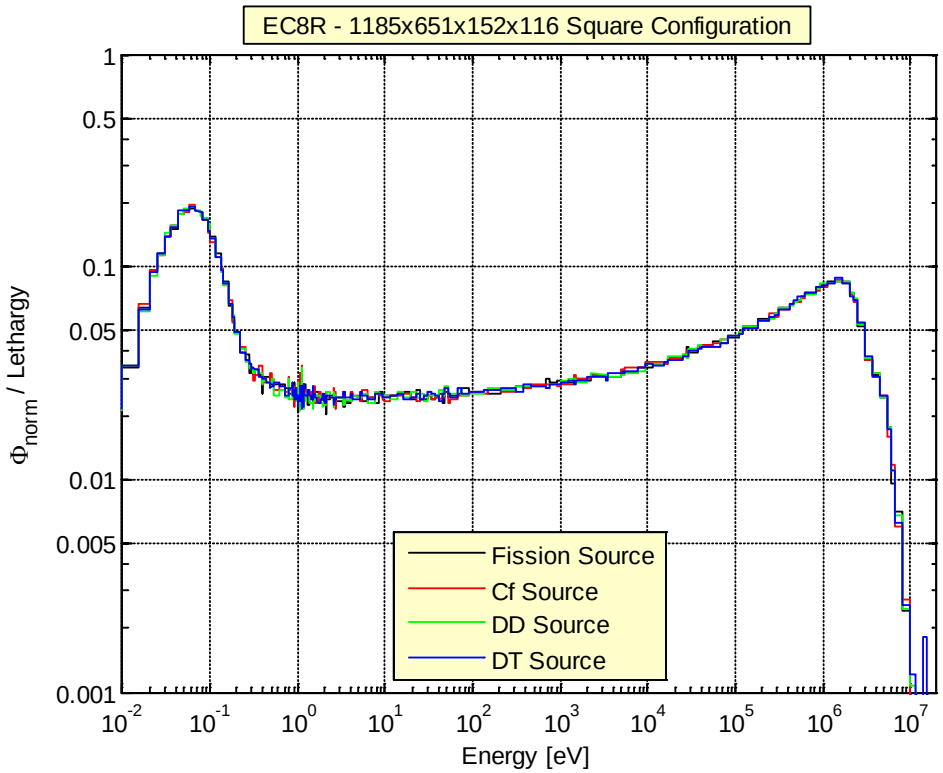

Figure 120. Normalized neutron spectrum in EC8R for square configuration 5

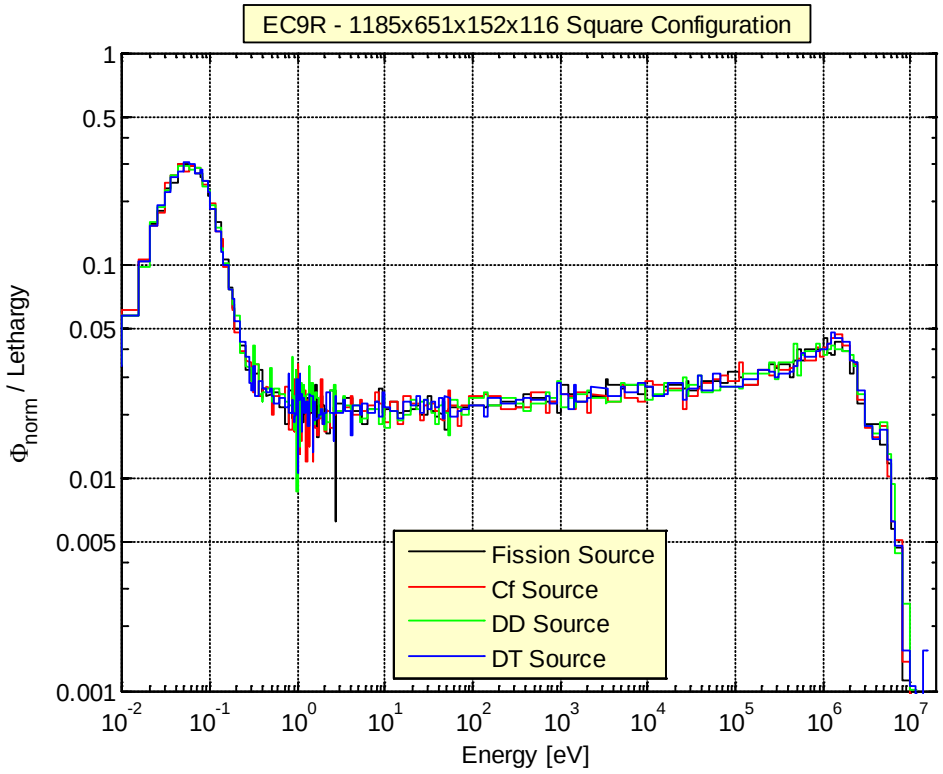

Figure 121. Normalized neutron spectrum in EC9R for square configuration 5

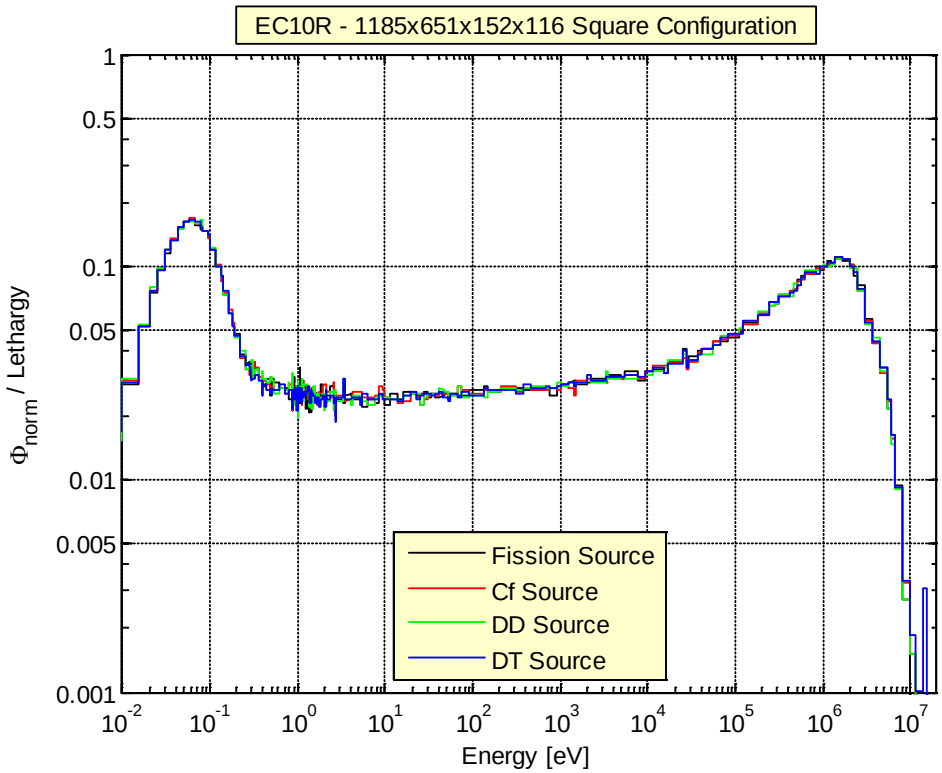

Figure 122. Normalized neutron spectrum in EC10R for square configuration 5

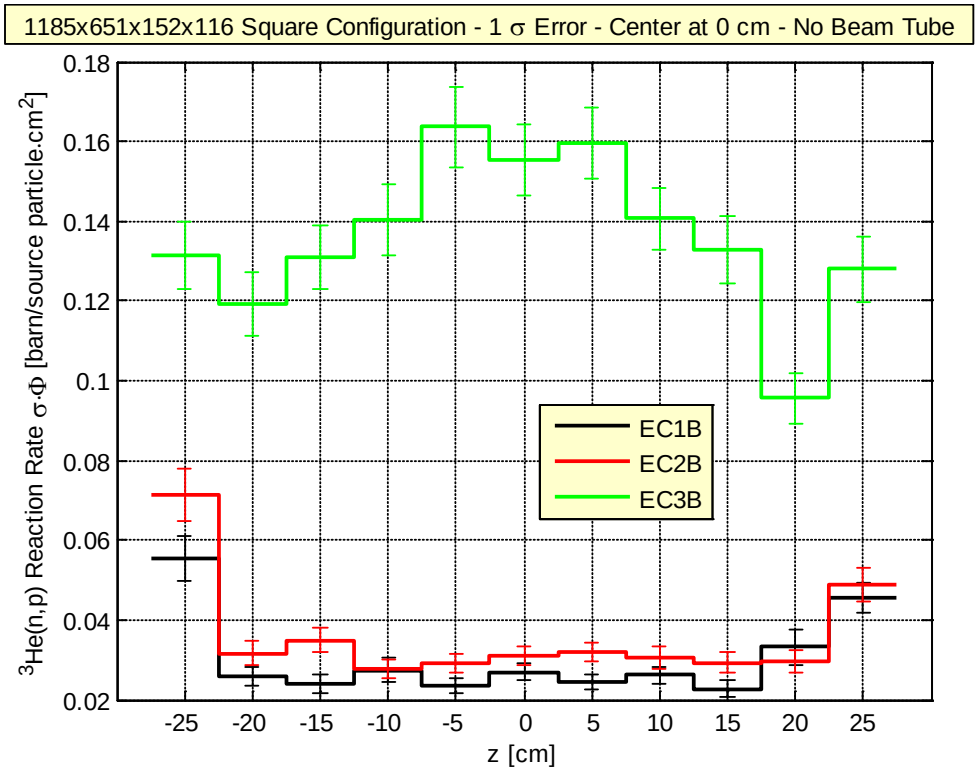

Figure 123. ^{3}He(n,p) reaction rate in experimental channels of fast zone for square configuration 5 from Cf neutron source; beam tube replaced by lead block

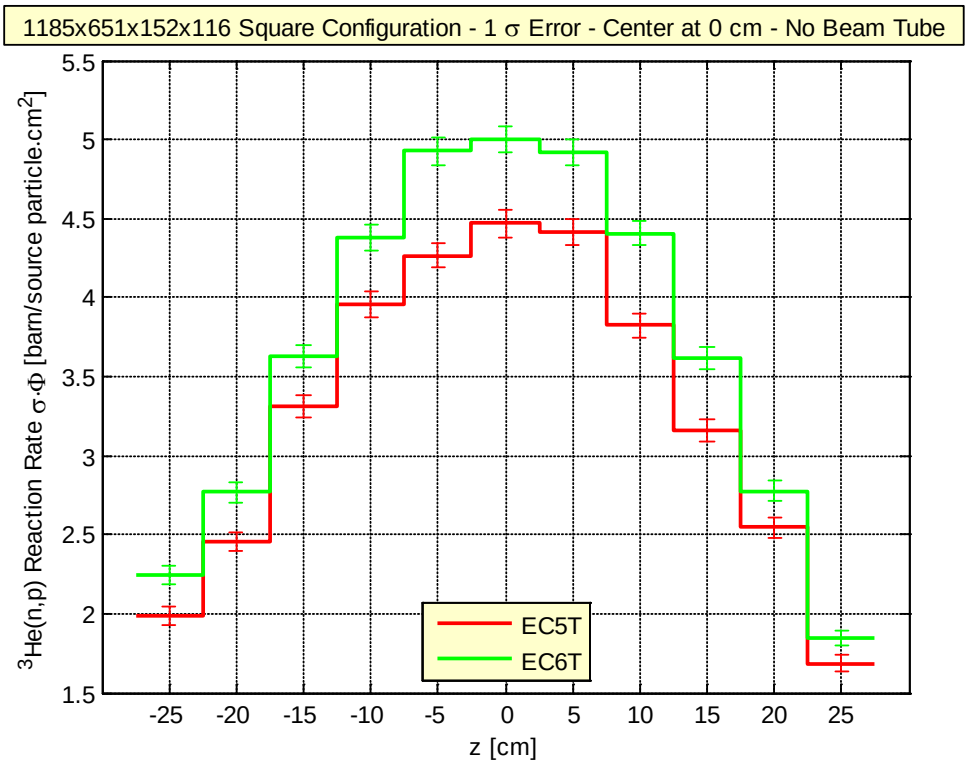

Figure 124. ^{3}He(n,p) reaction rate in experimental channels of thermal zone for square configuration 5 from Cf neutron source; beam tube replaced by lead block

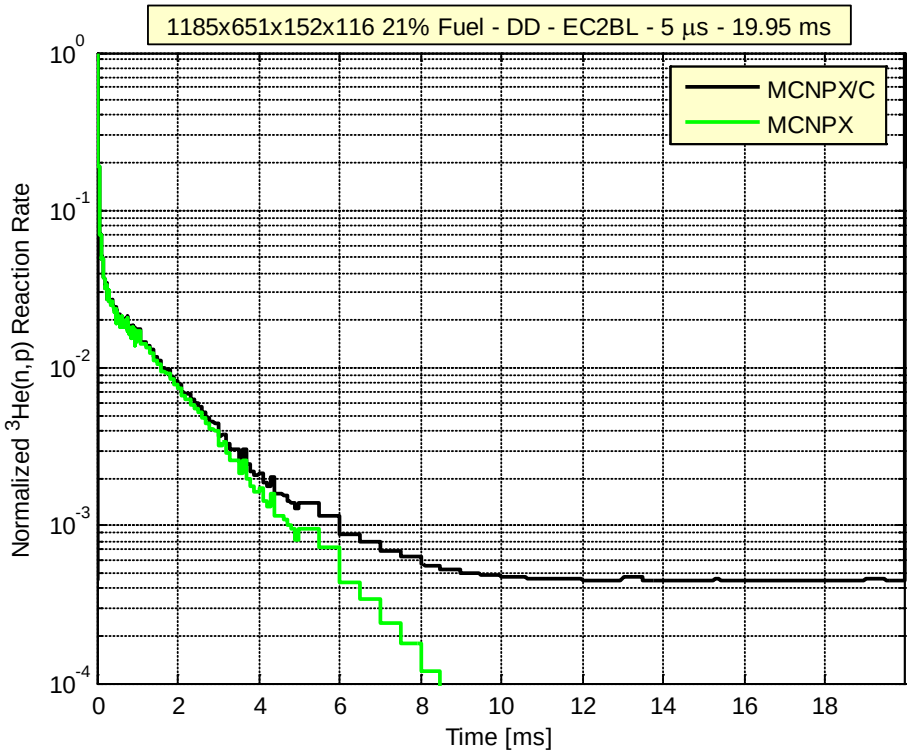

Figure 125. ^{3}He(n,p) reaction rate in the experimental channel EC2B (25-cm long detector) for square configuration 5 from D-D neutron source

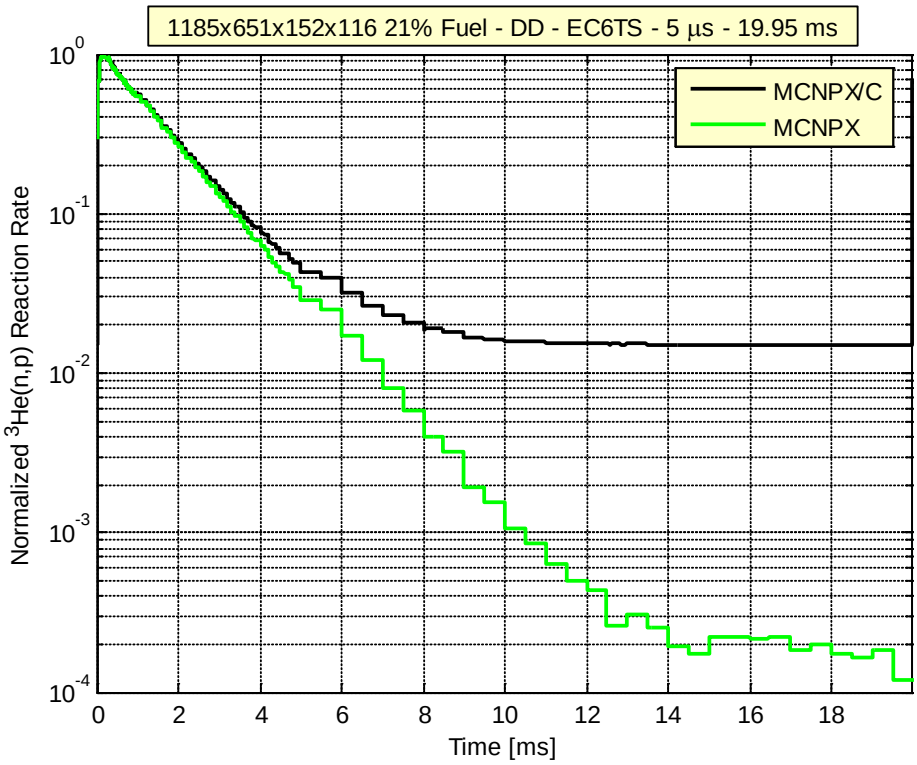

Figure 126. ^{3}He(n,p) reaction rate in the experimental channel EC6T (1-cm long detector) for square configuration 5 from D-D neutron source

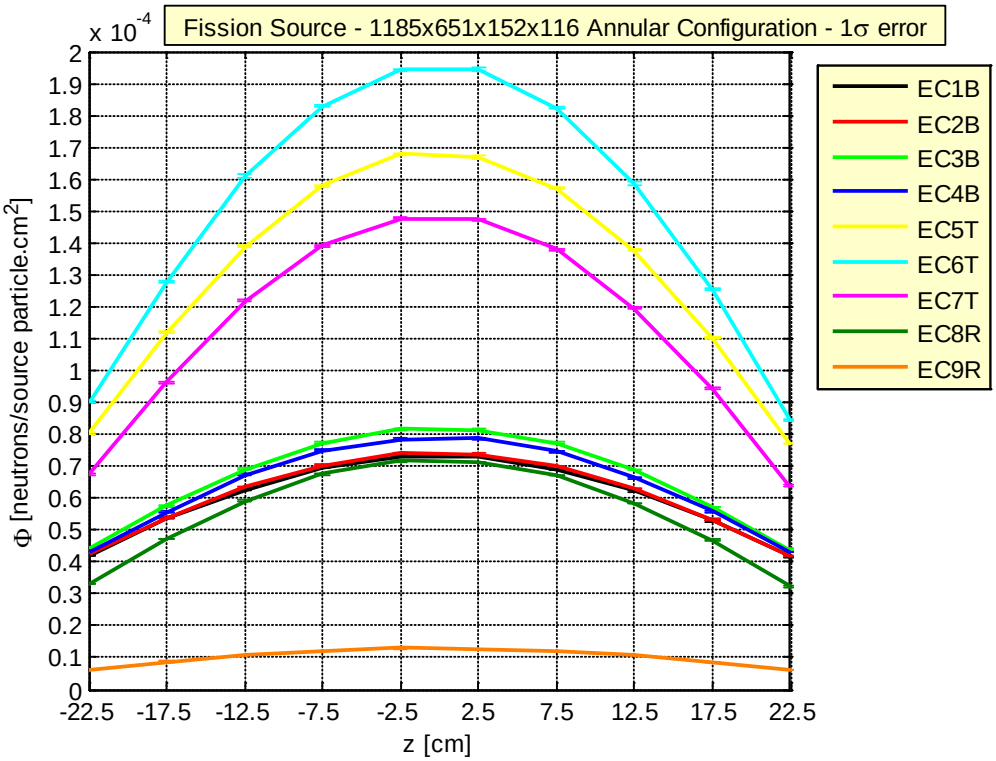

Figure 127. Flux axial distribution from criticality calculation for annular configuration 6

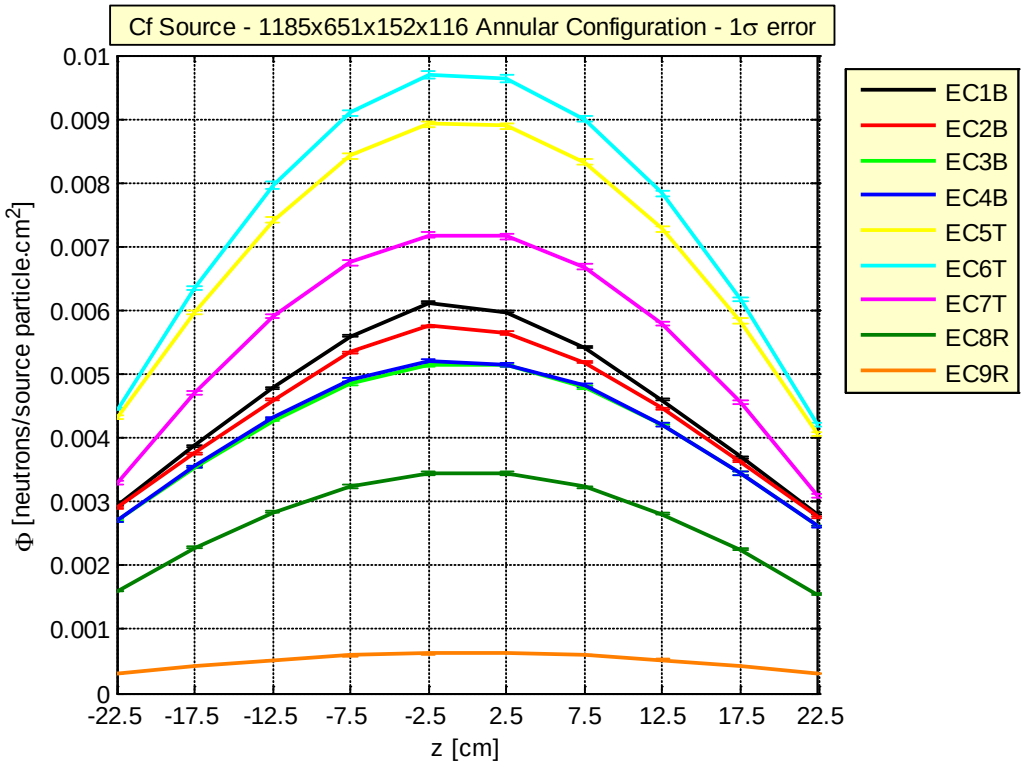

Figure 128. Flux axial distribution from Cf neutron source for annular configuration 6

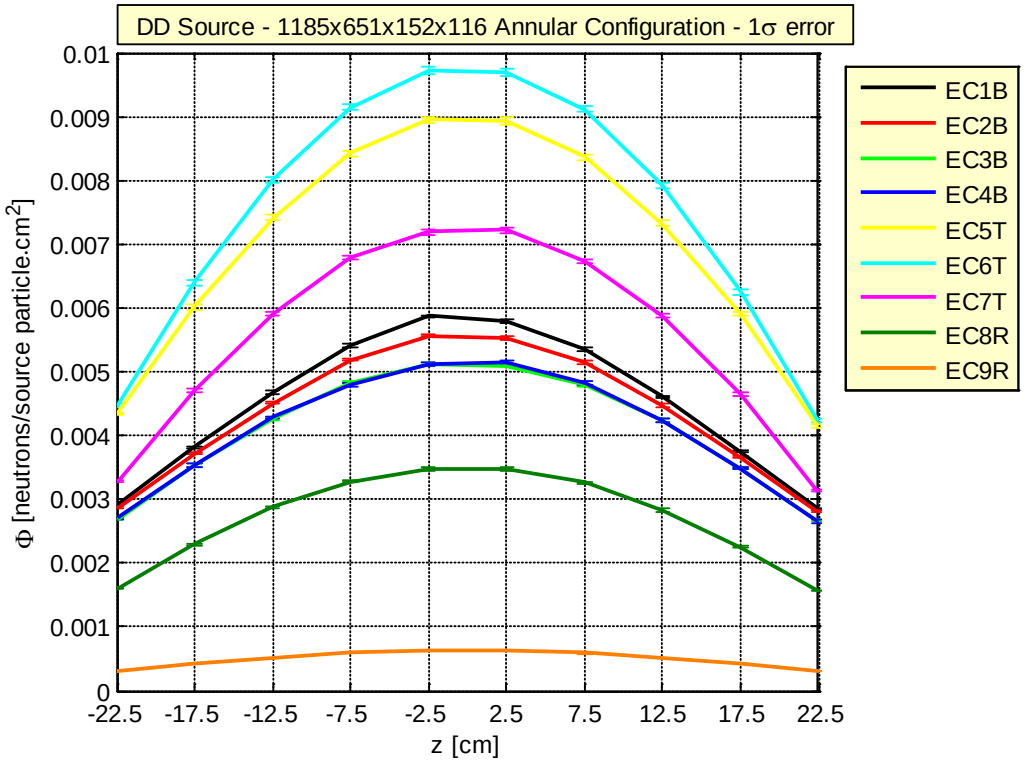

Figure 129. Flux axial distribution from D-D neutron source for annular configuration 6

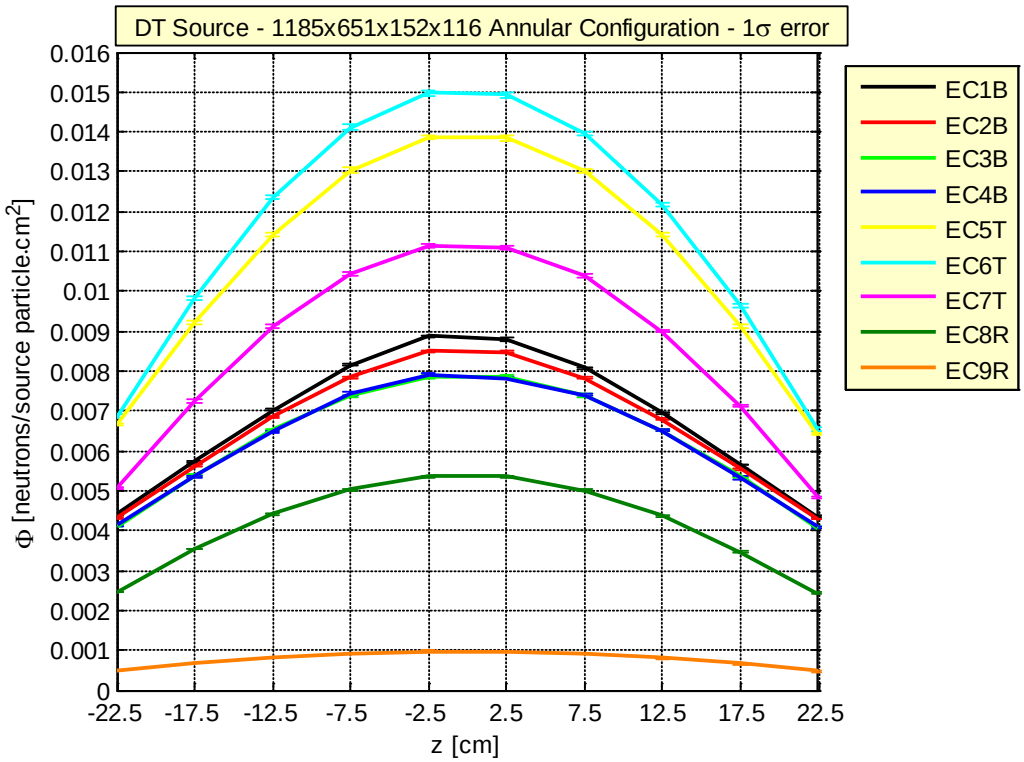

Figure 130. Flux axial distribution from D-T neutron source for annular configuration 6

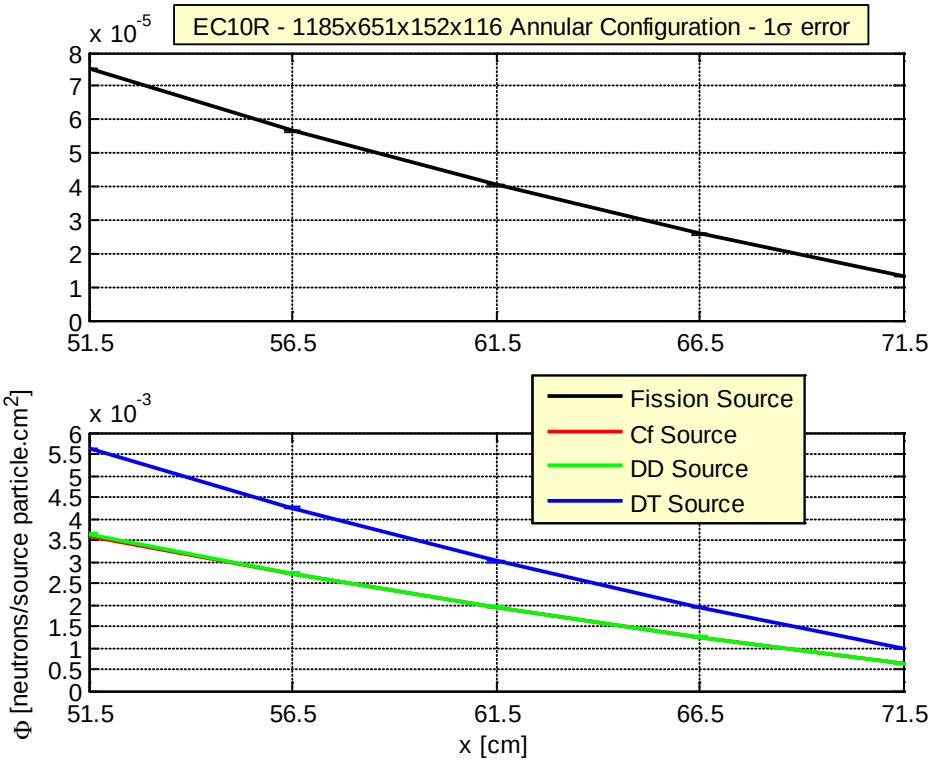

Figure 131. Flux radial distribution for annular configuration 6

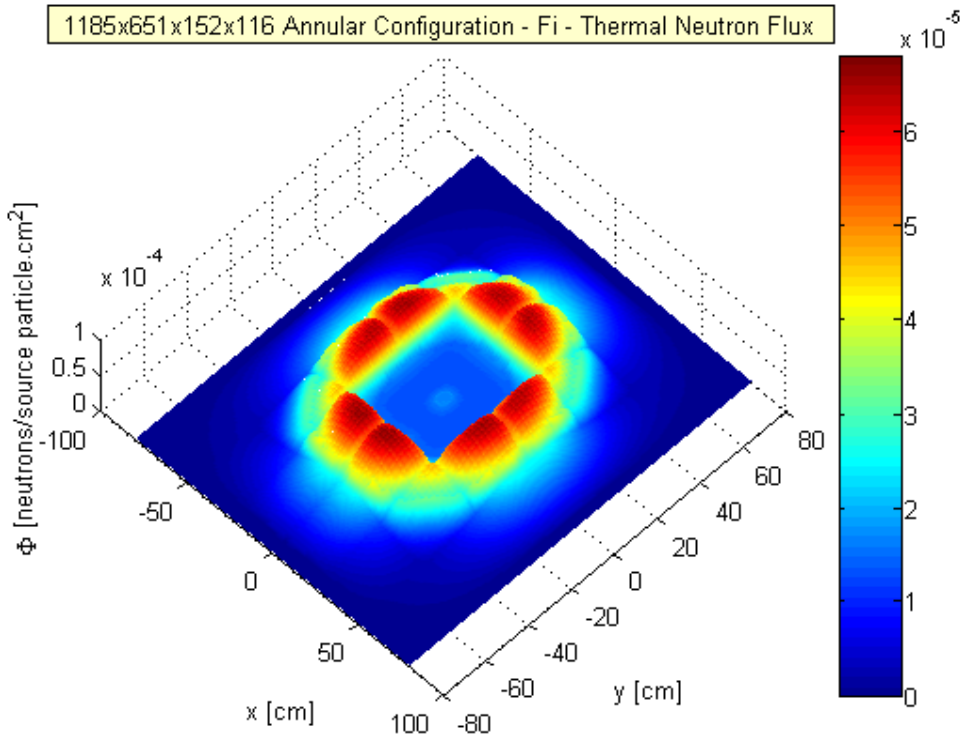

Figure 132. Thermal flux profile from criticality calculation for annular configuration 6

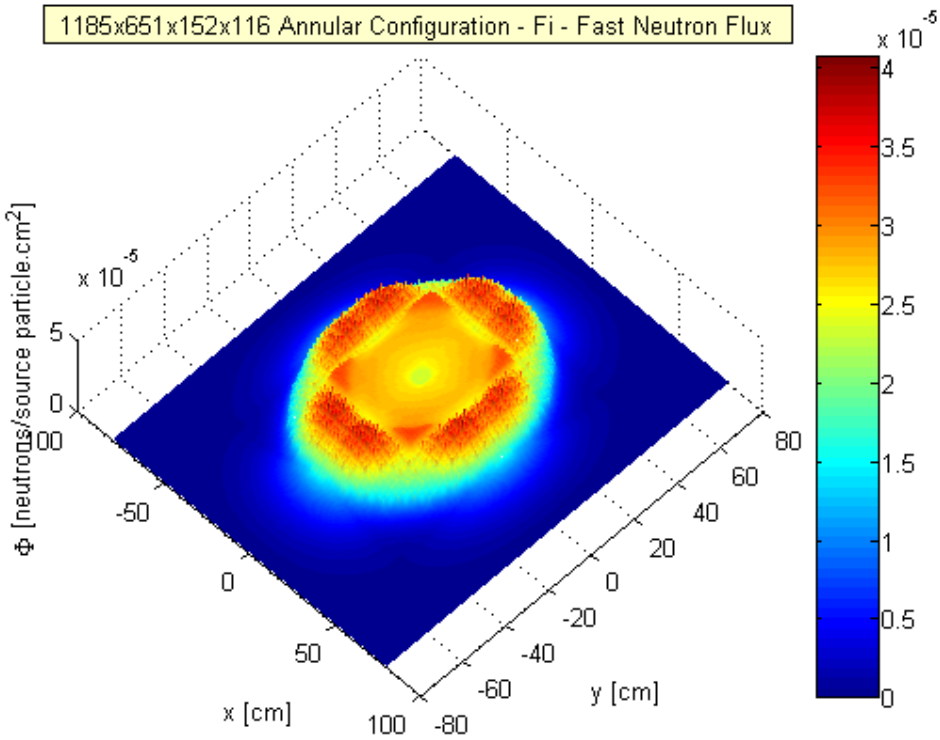

Figure 133. Fast flux profile from criticality calculation for annular configuration 6

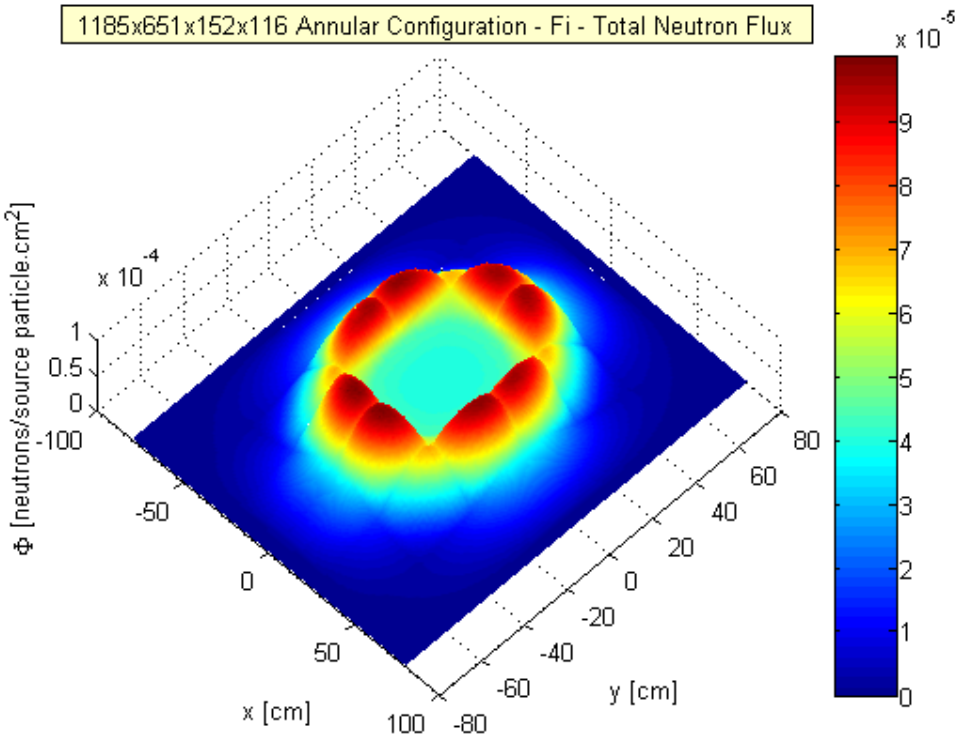

Figure 134. Total flux profile from criticality calculation for annular configuration 6

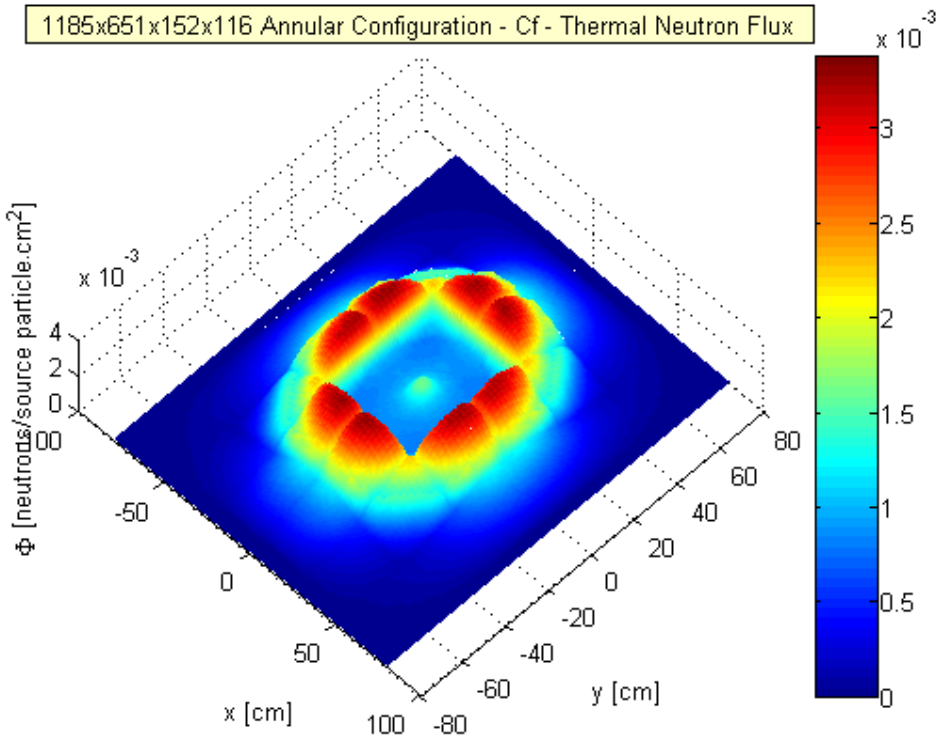

Figure 135. Thermal flux profile from Cf neutron source for annular configuration 6

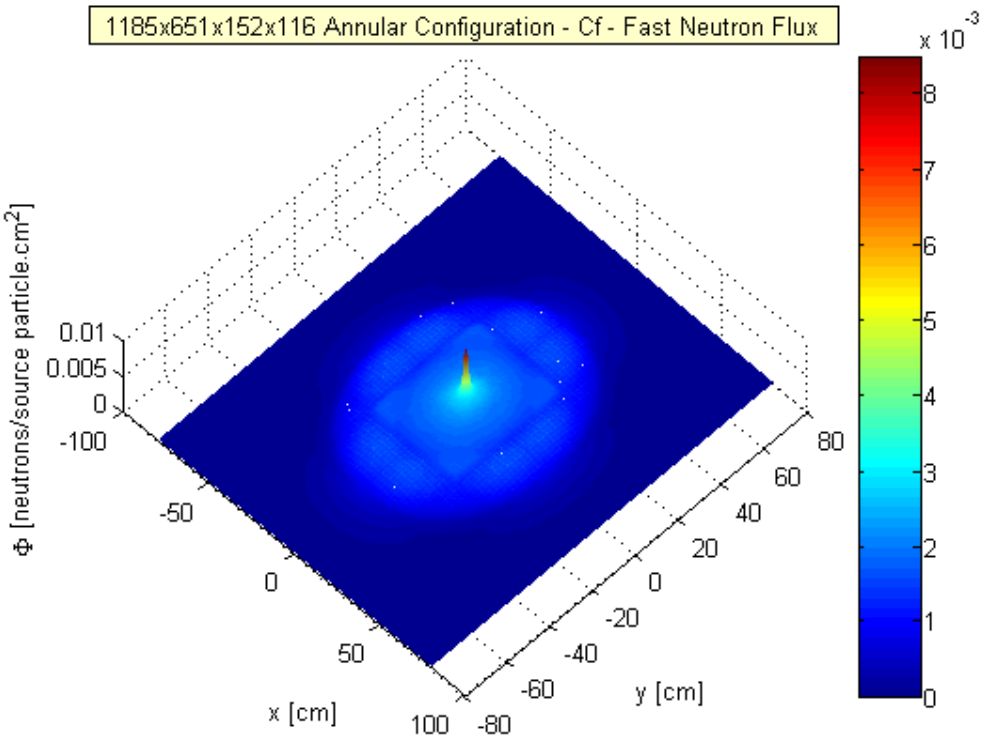

Figure 136. Fast flux profile from Cf neutron source for annular configuration 6

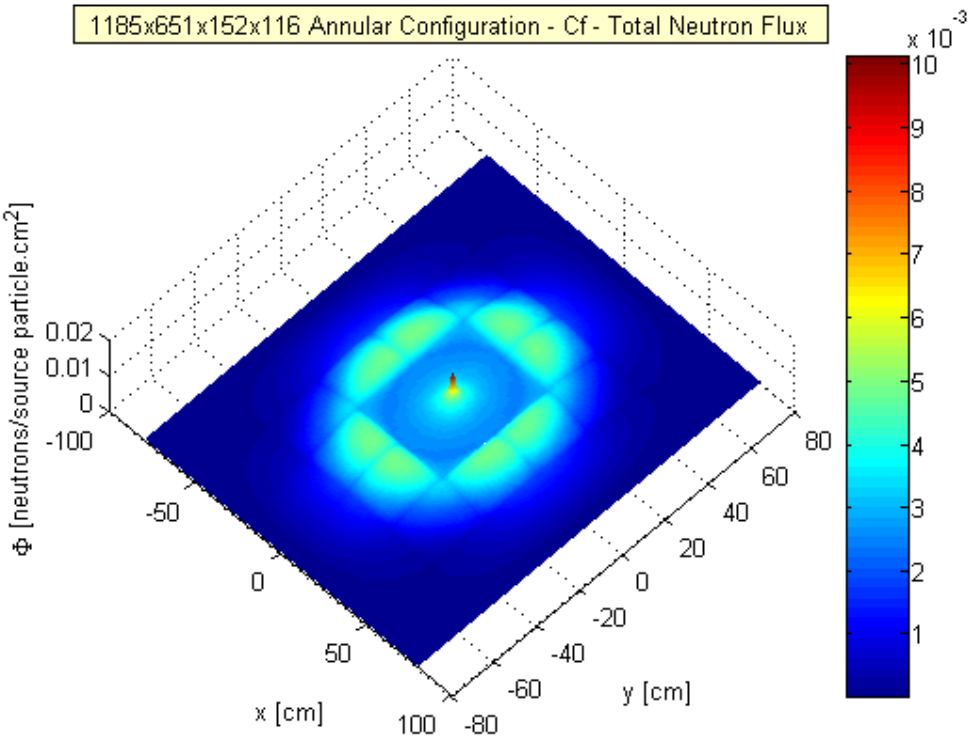

Figure 137. Total flux profile from Cf neutron source for annular configuration 6

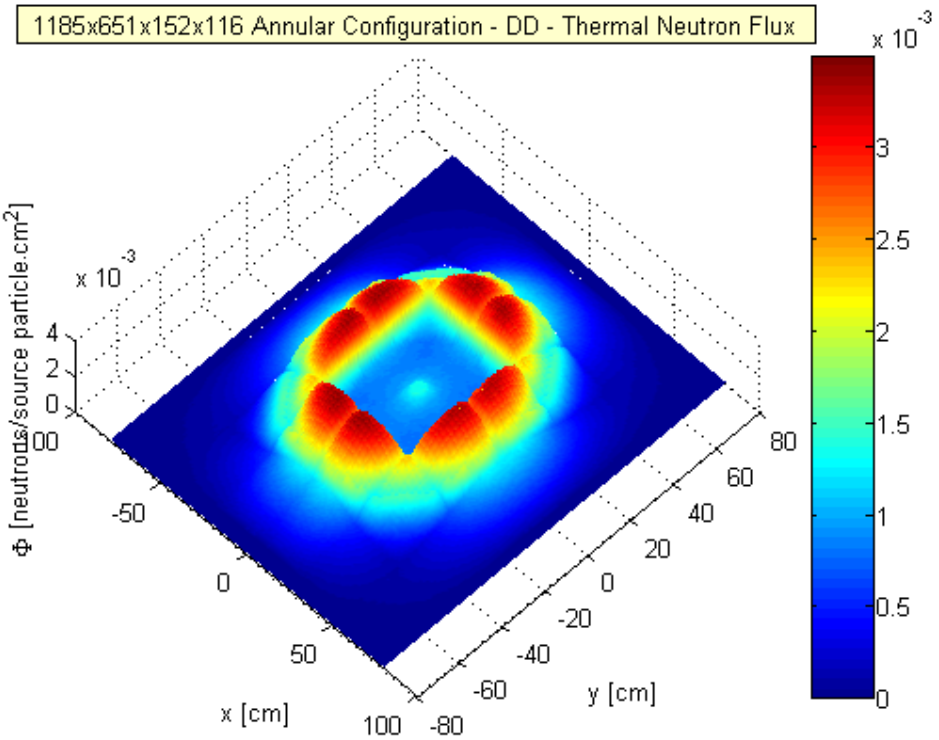

Figure 138. Thermal flux profile from D-D neutron source for annular configuration 6

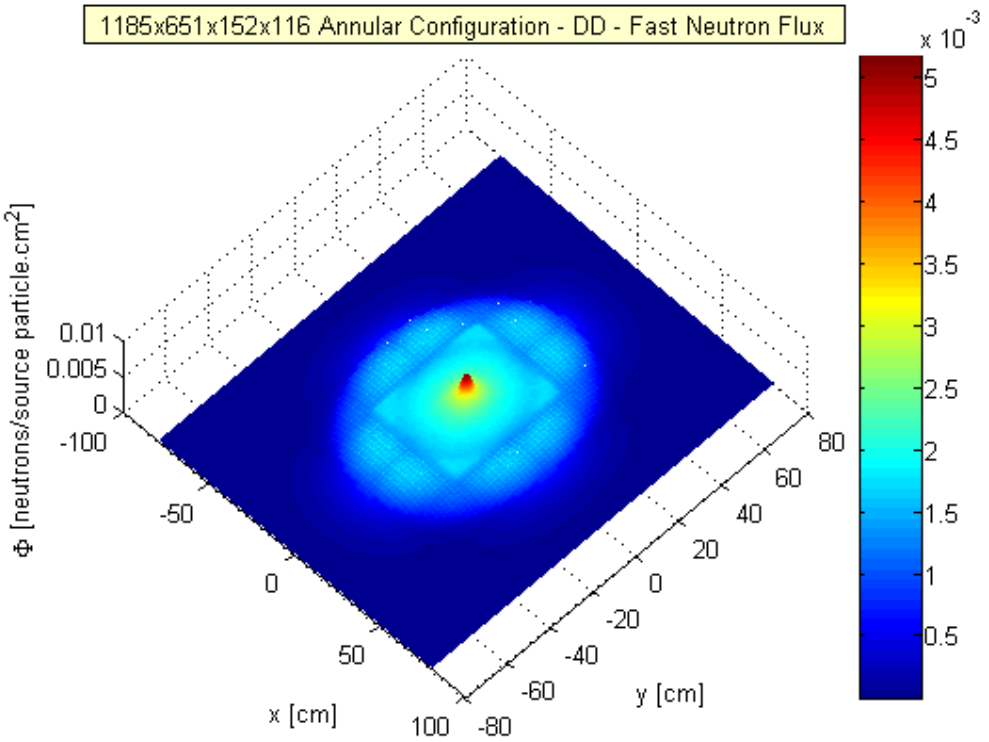

Figure 139. Fast flux profile from D-D neutron source for annular configuration 6

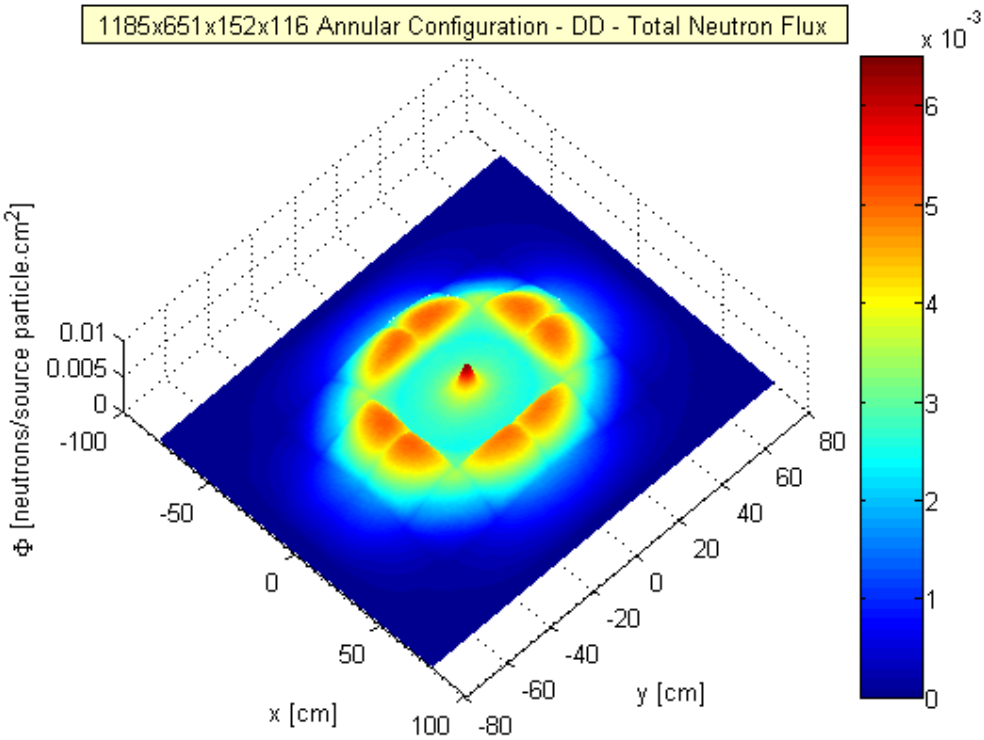

Figure 140. Total flux profile from D-D neutron source for annular configuration 6

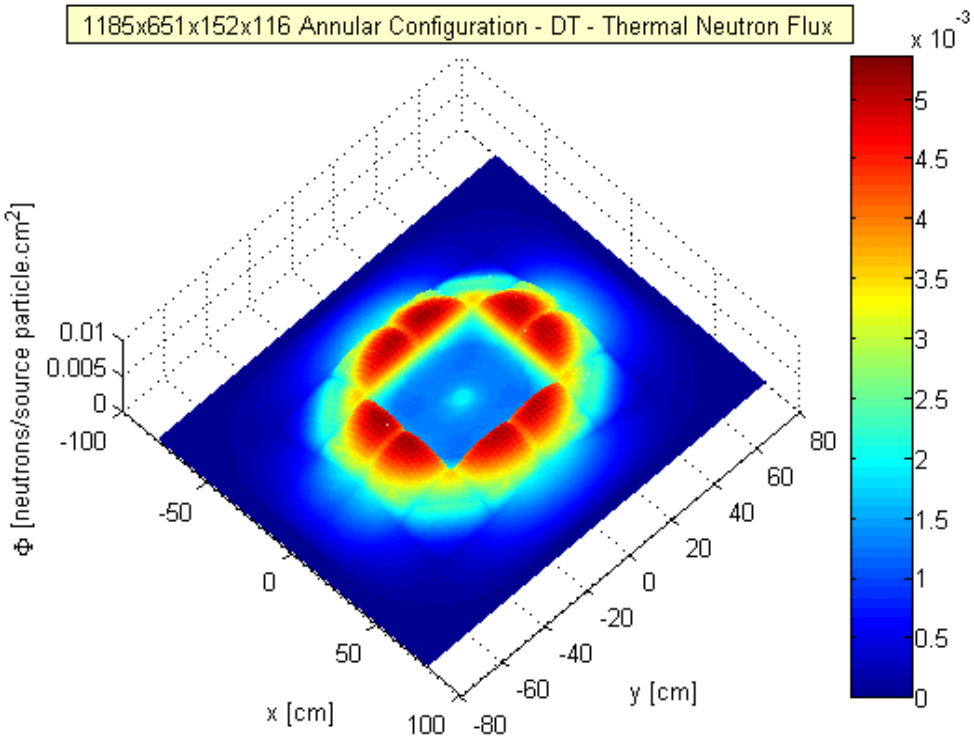

Figure 141. Thermal flux profile from D-T neutron source for annular configuration 6

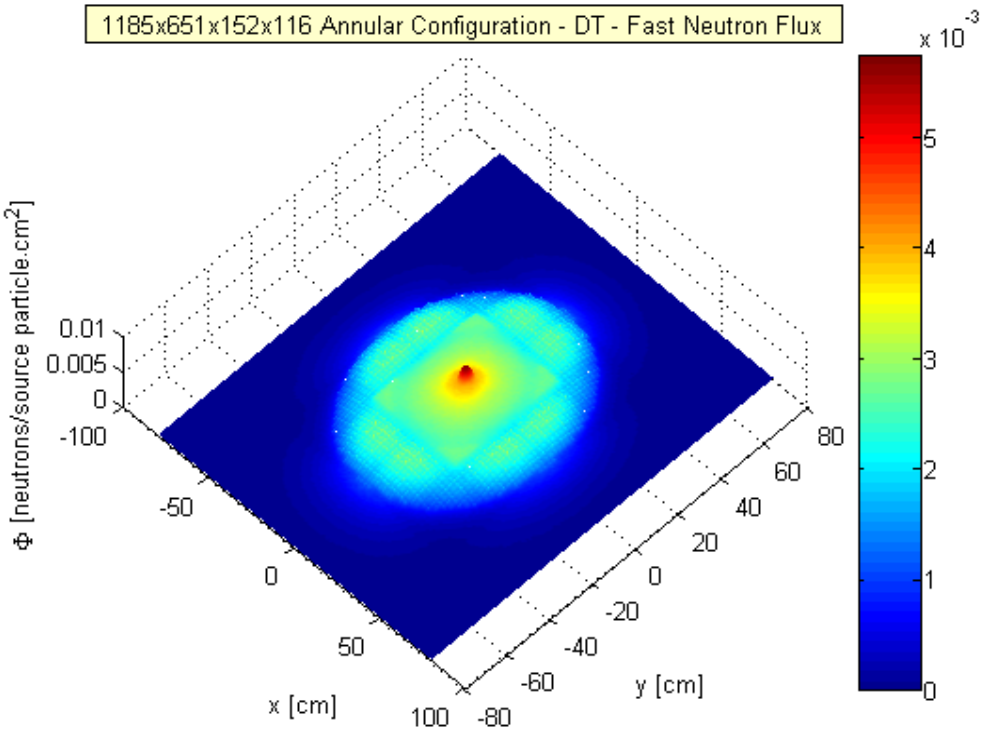

Figure 142. Fast flux profile from D-T neutron source for annular configuration 6

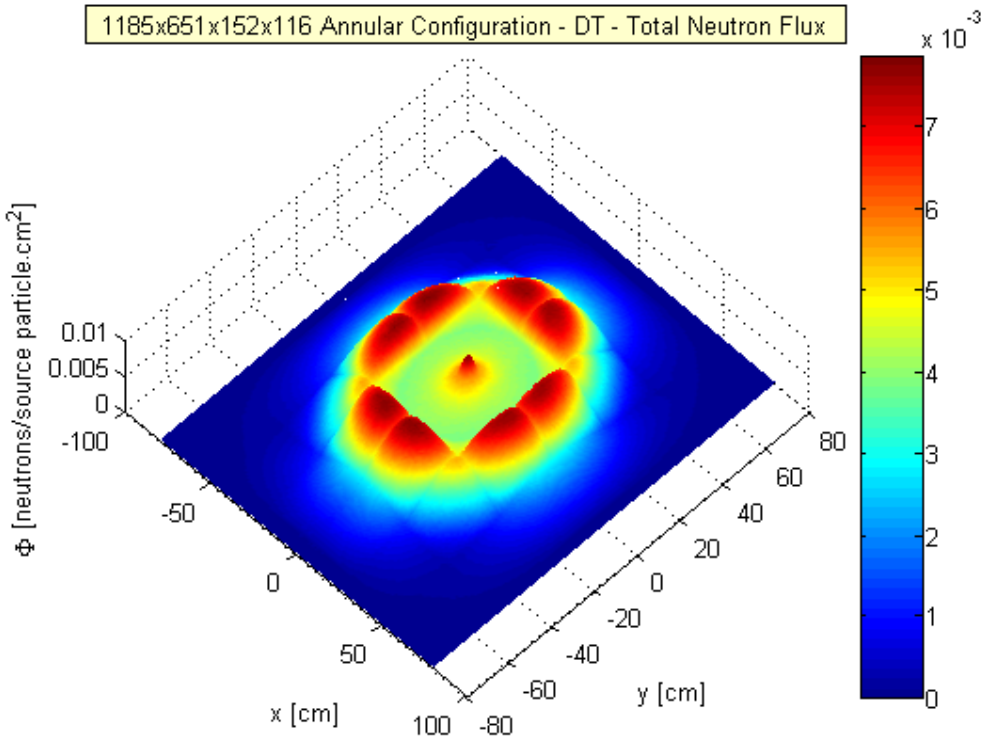

Figure 143. Total flux profile from D-T neutron source for annular configuration 6

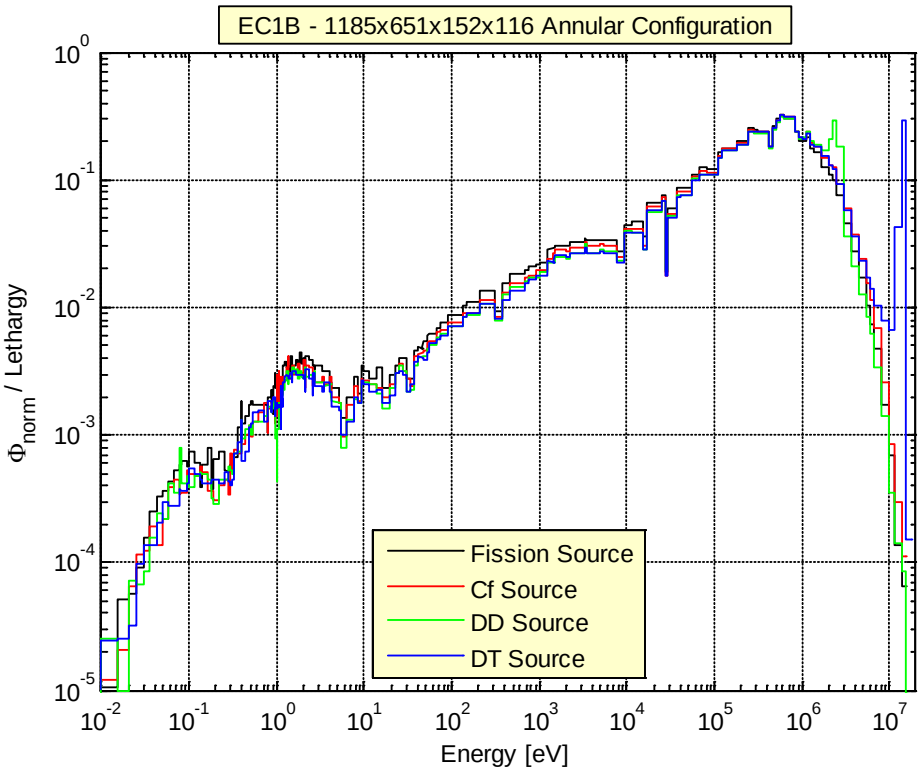

Figure 144. Normalized neutron spectrum in EC1B for annular configuration 6

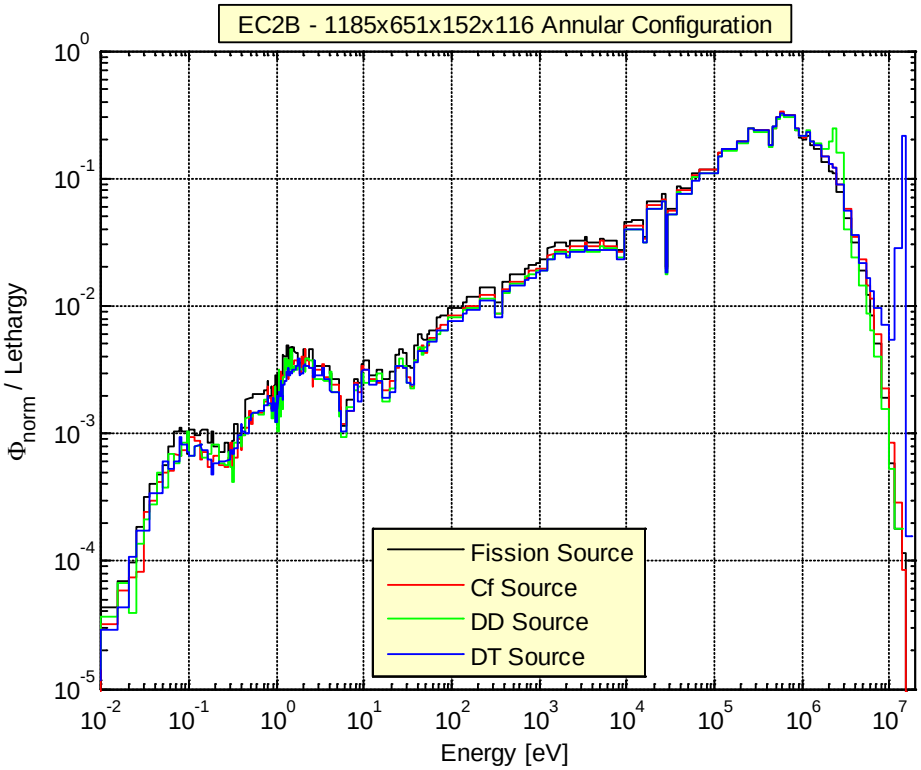

Figure 145. Normalized neutron spectrum in EC2B for annular configuration 6

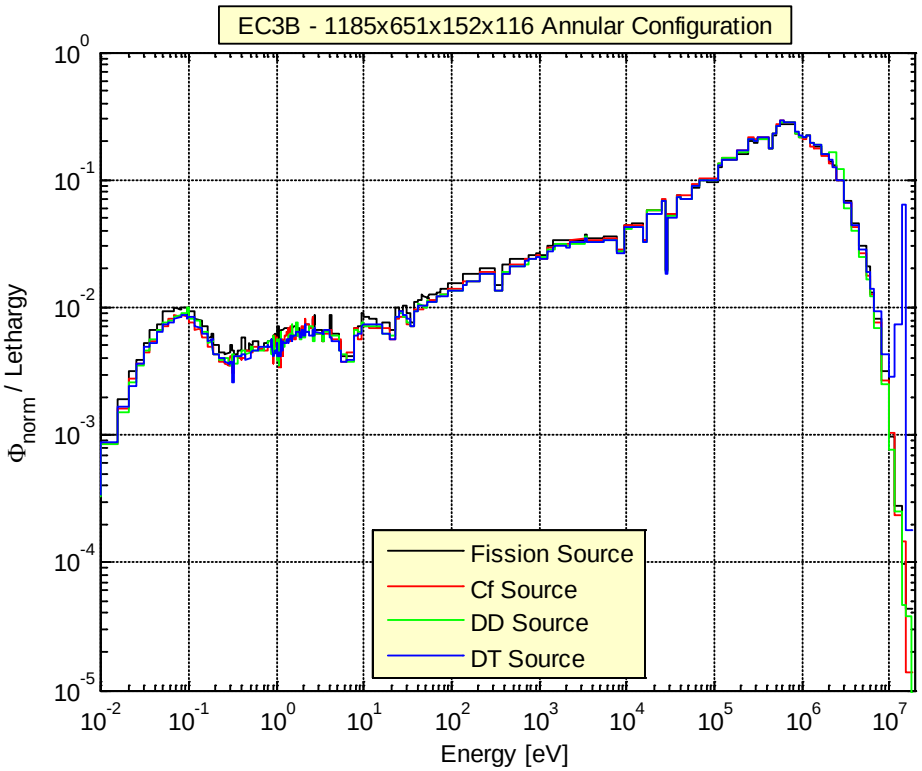

Figure 146. Normalized neutron spectrum in EC3B for annular configuration 6

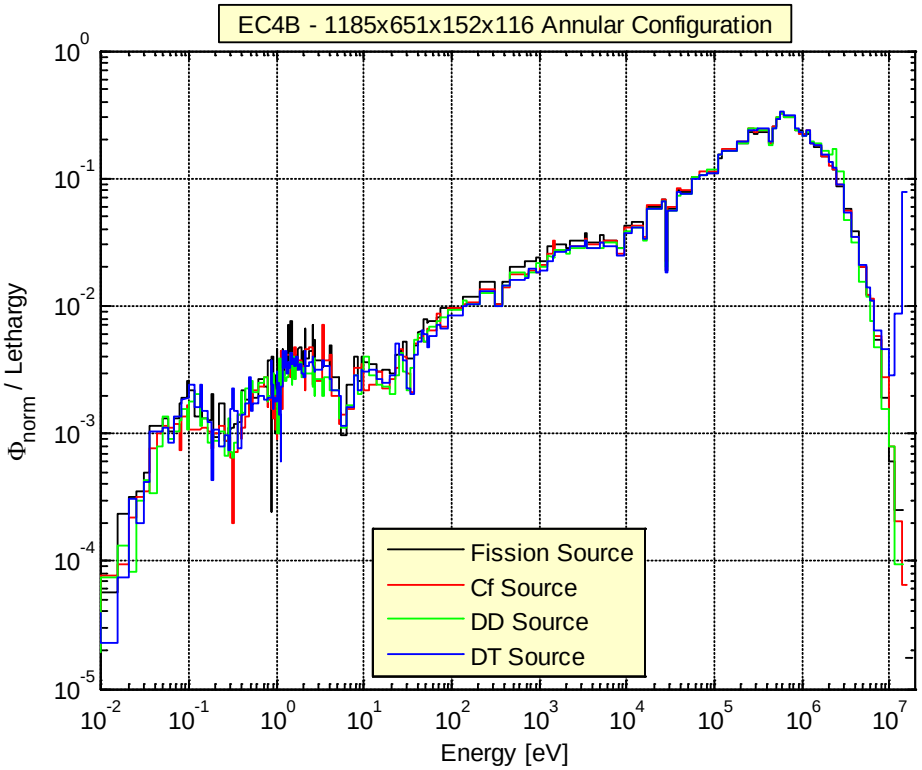

Figure 147. Normalized neutron spectrum in EC4B for annular configuration 6

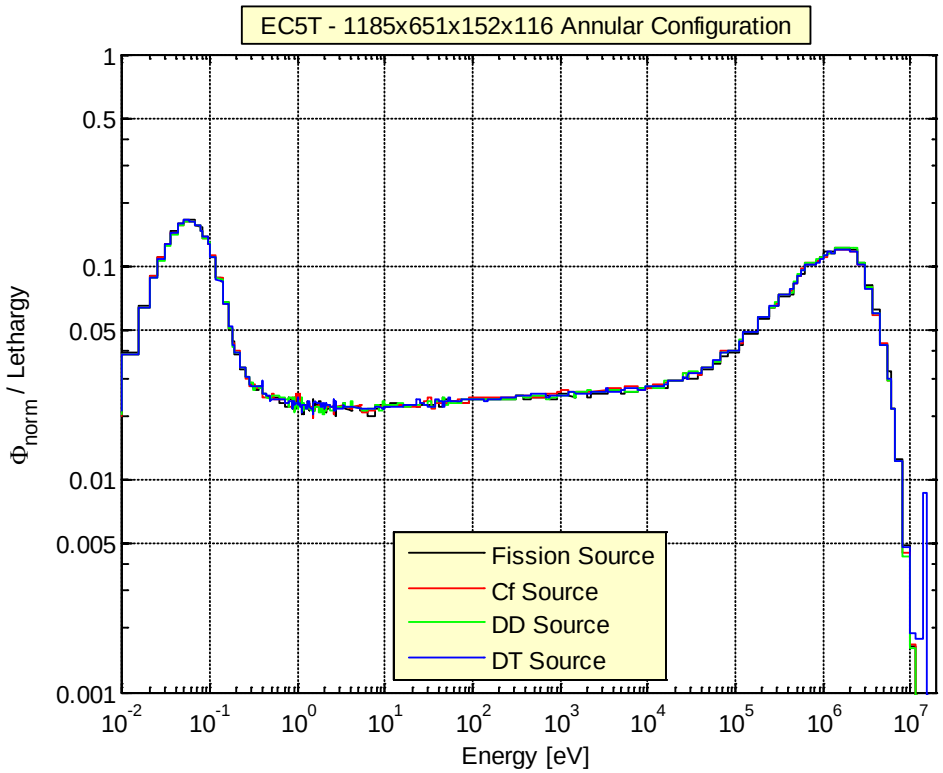

Figure 148. Normalized neutron spectrum in EC5T for annular configuration 6

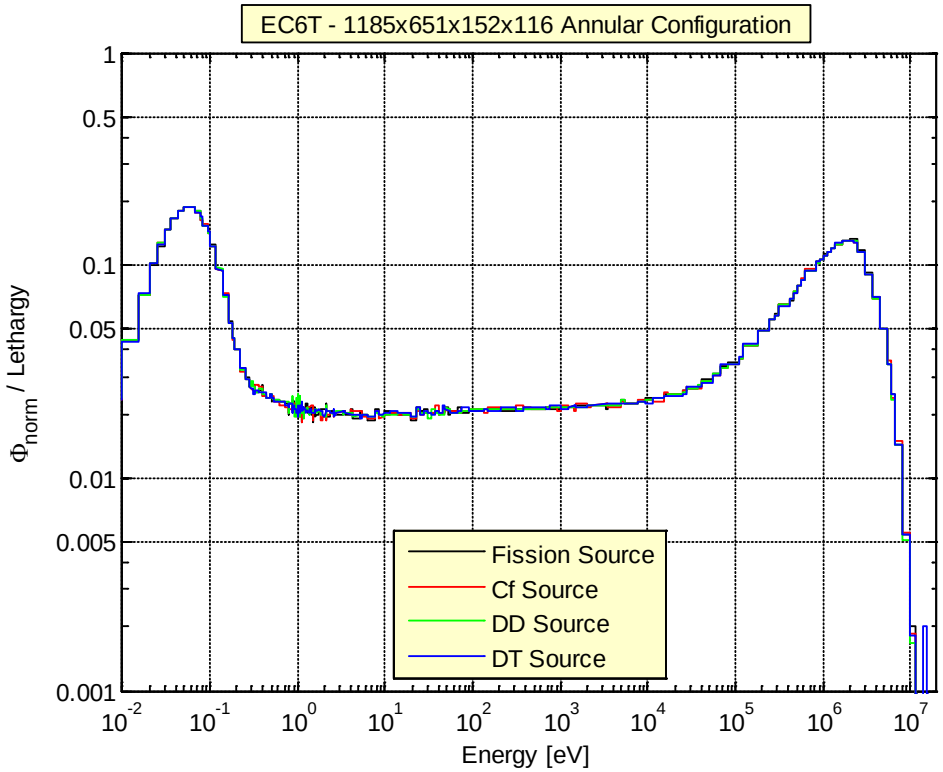

Figure 149. Normalized neutron spectrum in EC6T for annular configuration 6

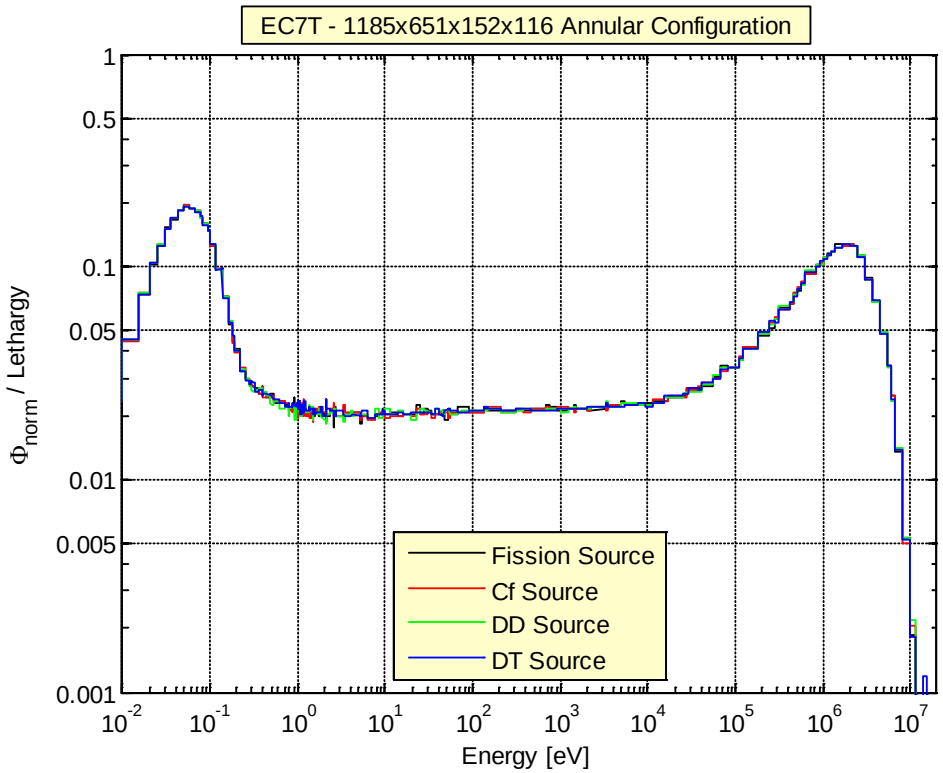

Figure 150. Normalized neutron spectrum in EC7T for annular configuration 6

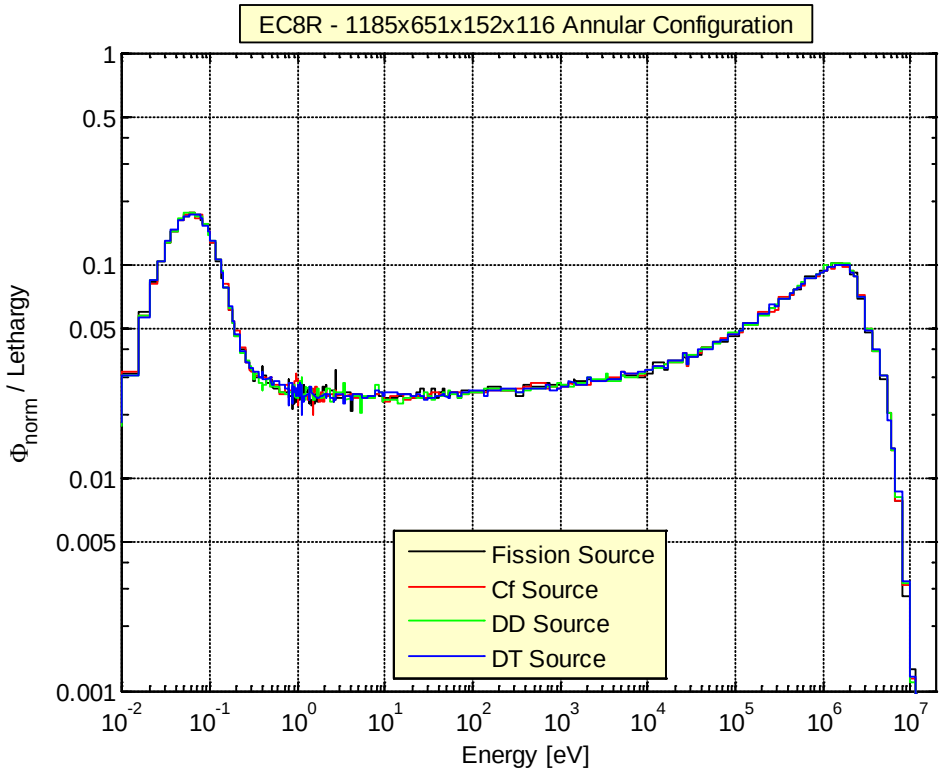

Figure 151. Normalized neutron spectrum in EC8R for annular configuration 6

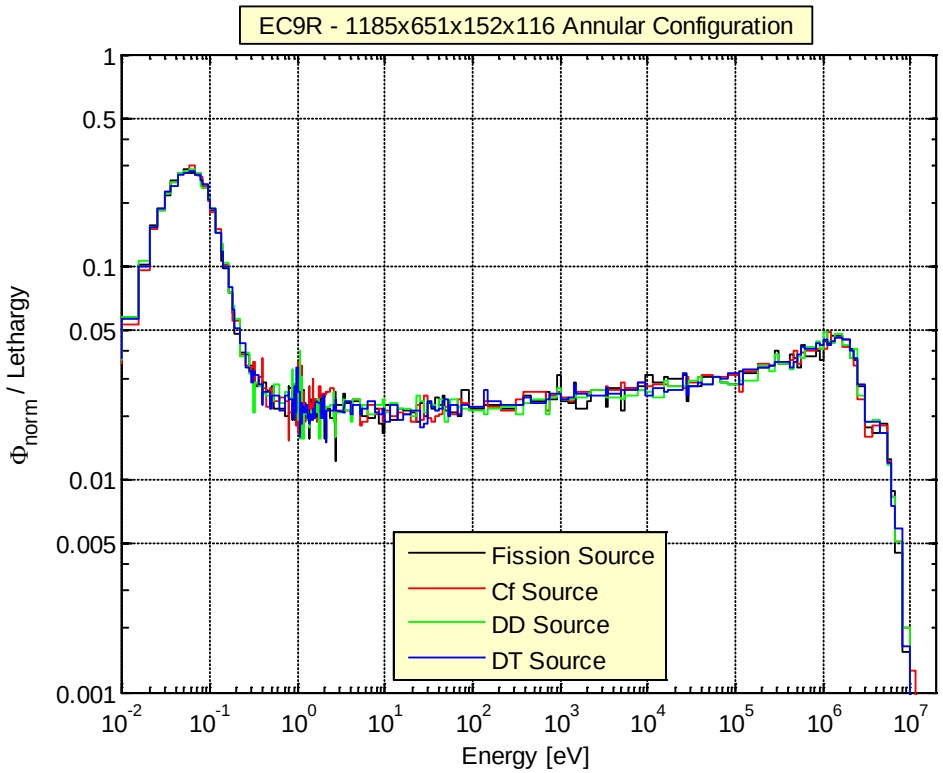

Figure 152. Normalized neutron spectrum in EC9R for annular configuration 6

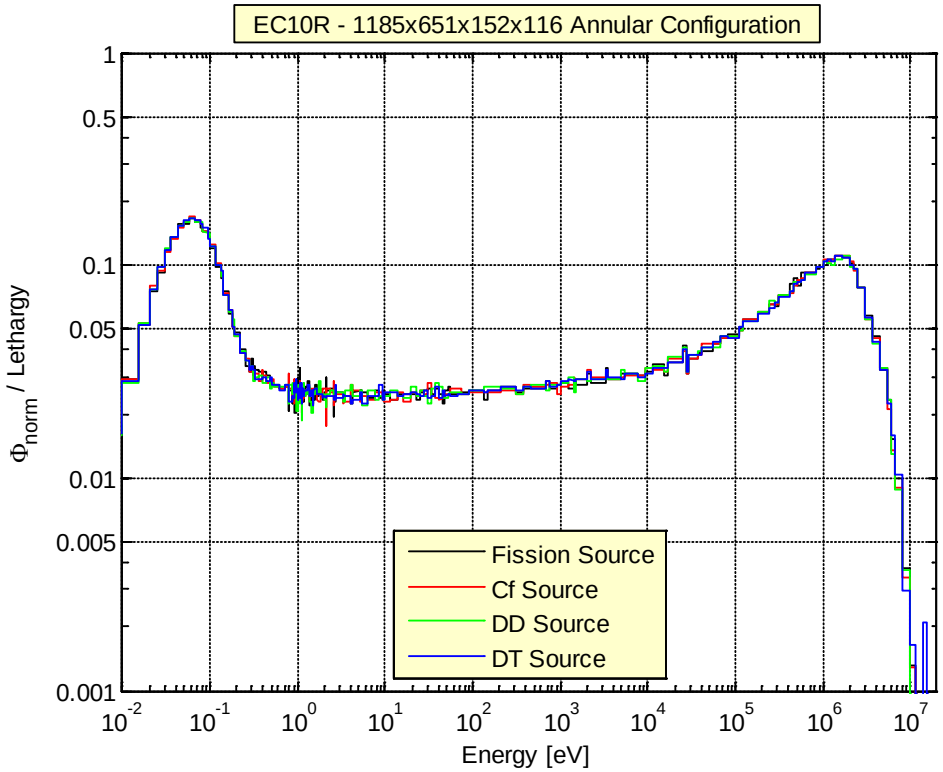

Figure 153. Normalized neutron spectrum in EC10R for annular configuration 6

Nuclear Engineering Division
Argonne National Laboratory
9700 South Cass Avenue
Argonne, IL 60439

www.anl.gov

A U.S. Department of Energy laboratory
managed by UChicago Argonne, LLC